

https://dspace.org/

# Inflammation-responsive self-oscillating polymeric gel to enhance dermal delivery of Neo-Geometric copper nanoparticles

**Murugan, Karmani**

**2017**

http://hdl.handle.net/10539/23152

Murugan, Karmani (2017) Inflammation-responsive self-oscillating polymeric gel to enhance dermal delivery of Neo-Geometric copper nanoparticles, University of the Witwatersrand, Johannesburg, <http://hdl.handle.net/10539/23152>

Downloaded from a DSpace repository. https://dspace.org/

# `INFLAMMATION-RESPONSIVE SELF-OSCILLATING POLYMERIC GEL TO ENHANCE DERMAL DELIVERY OF NEO-GEOMETRIC COPPER NANOPARTICLES

**KARMANI MURUGAN**

A thesis submitted to the Faculty of Health Sciences, University of the Witwatersrand, in fulfilment of the requirements for the degree of

Doctor of Philosophy

**Supervisor:**

Professor Viness

Department of Pharmacy and Pharmacology, Faculty of Health Sciences, University of the Witwatersrand, South Africa

**Co-Supervisors:**

Professor Yahya E. Choonara

Professor Lisa C. du Toit

Mr Pradeep Kumar

Department of Pharmacy and Pharmacology, Faculty of Health Sciences, University of the Witwatersrand, South Africa

**Johannesburg**
**2017**

## DECLARATION

I, Karmani Murugan, declare that this thesis is my own work. It has been submitted for the degree of Doctor of Philosophy in the Faculty of Health Sciences at the University of the Witwatersrand, Johannesburg, South Africa. It has not been submitted before for any degree or examination at this or any other University.

……..

Signed this ..... day of July 2017

## RESEARCH OUTPUTS

### Publications

1. Karmani Murugan, Yahya E. Choonara, Pradeep Kumar, Lisa C. du Toit, Viness Pillay. Parameters and characteristics governing cellular internalization and trans-barrier trafficking of nanostructures. International Journal of Nanomedicine, 2015, 10: 2191-2206 *[Review Article]. ISI; IF: 4.32*

2. Karmani Murugan, Yahya E. Choonara, Pradeep Kumar, Lisa C. du Toit, Viness Pillay. Surfactant directed synthesis and self-assembly of geometric cytotoxic copper nanocrystals. South African Pharmaceutical Journal, 2016, 83: 38-40 *[Research Article].*

3. Karmani Murugan, Yahya E. Choonara, Pradeep Kumar, Lisa C. du Toit, Viness Pillay. Neo-geometric copper nanocrystals by competitive, dual surfactant-mediated facet adsorption controlling skin permeation. Materials (MDPI), 2016, 9: 966-979 *[Research Article]. ISI; IF: 2.73*

4. Karmani Murugan, Yahya E. Choonara, Pradeep Kumar, Lisa C. du Toit, Viness Pillay. Cellular internalization kinetics and cytotoxic properties of statistically designed and optimized neo-geometric copper nanocrystals. Material Science and Engineering: C, September 2017*, ISI; IF: 3.42).*

5. Karmani Murugan, Yahya E. Choonara, Pradeep Kumar, Lisa C. du Toit, Viness Pillay. Transport of a novel geometric copper nanosystem across the skin barrier employing a self-oscillating polymeric network in the topical treatment of psoriasis. (Submitted to Nanomedicine -Future Medicine, November 2016, *ISI; IFI: 4.889*).

**APPENDIX 7.1**

## RESEARCH OUTPUTS

### Research Presentations

1. Karmani Murugan, Yahya E. Choonara, Pradeep Kumar, Lisa C. du Toit, Viness Pillay. Synthesis of superstable neo-geometric cytotoxic copper nanocrystals by competitive, dual surfactant-mediated facet adsorption. ***(Poster Presentation).*** *School of Therapeutic Sciences Research Day*, University of the Witwatersrand, Johannesburg, South Africa, September 08, 2015.

2. Karmani Murugan, Yahya E. Choonara, Pradeep Kumar, Lisa C. du Toit, Viness Pillay. Surfactant directed synthesis and self-assembly of geometric cytotoxic copper nanocrystals. ***(Podium Presentation).*** 36th Annual Conference of the Academy of Pharmaceutical Sciences of South Africa (APSSA) and the South African Association of Pharmacists in Industry (SAAPI), Ingelheim Boehringer Young Scientist Competition, CedarWood Conference Centre, Sandton, South Africa, September 18, 2015.

3. Karmani Murugan, Yahya E. Choonara, Pradeep Kumar, Lisa C. du Toit, Viness Pillay. Synthesis of superstable neo-geometric cytotoxic copper nanocrystals by competitive, dual surfactant-mediated facet adsorption. ***(Poster Presentation).*** 2015 American Association of Pharmaceutical Scientists – Annual Meeting and Exposition, Orange County Convention Centre, Orlando, Florida, United States of America, October 25, 2015.

4. Karmani Murugan, Yahya E. Choonara, Pradeep Kumar, Lisa C. du Toit, Viness Pillay. Ordered synthesis of geometric copper nanocrystals for enhanced drug delivery. ***(Poster Presentation).*** Molecular Biosciences Research Thrust Postgraduate Research Day 2015, University of the Witwatersrand, Johannesburg, South Africa, December 03, 2015.

5. Karmani Murugan, Yahya E. Choonara, Pradeep Kumar, Lisa C. du Toit, Viness Pillay. Dual surfactant-mediated synthesis of self-assembled geometric cytotoxic copper nanocrystals. **(Podium Presentation).** Wits 7th Postgraduate Symposium, University of the Witwatersrand, Johannesburg, South Africa, March 01, 2016.

6. Karmani Murugan, Yahya E. Choonara, Pradeep Kumar, Lisa C. du Toit, Viness Pillay. Surfactant directed synthesis and self-assembly of novel neo-geometric cytotoxic copper nanocrystals for enhanced cellular internalization. **(Poster Presentation).** 13th International Conference on Nanosciences & Nanotechnologies (NN16), Porto Palace Conference Centre, Thessaloniki, Greece, July 5, 2016.

**APPENDIX 7.2**

## ACCOLADES

1. Winner of the Boehringer Ingelheim Young Scientist Award: Surfactant directed synthesis and self-assembly of geometric cytotoxic copper nanocrystals. 36th Annual Conference of the Academy of Pharmaceutical Sciences of South Africa (APSSA) and the South African Association of Pharmacists in Industry (SAAPI), CedarWood Conference Centre, Sandton, South Africa, September 18, 2015.

2. Winner of the Young Researcher Award: Surfactant directed synthesis and self-assembly of novel neo-geometric cytotoxic copper nanocrystals for enhanced cellular internalization. 13th International Conference on Nanosciences & Nanotechnologies (NN16), Porto Palace Conference Centre, Thessaloniki, Greece, July 5, 2016.

**APPENDIX 7.3**

## ANIMAL ETHICS DECLARATION

I hereby confirm that the following study entitled "*In vivo* topical delivery of a neo-geometrical copper nanoparticle based system for psoriasis treatment in the BALB/c model" has received approval from the Animal Ethics Committee of the University of the Witwatersrand with ethics clearance number 2014/48/B.

**APPENDIX 7.4**

## PATENT FILED

Neo-geometric Copper Nanoparticles in the Treatment of Psoriasis. Karmani Murugan, Viness Pillay, Yahya E. Choonara, Pradeep Kumar, Lisa C. Du Toit. Patent filed.

## ACKNOWLEDGEMENTS

Over the course of this academic journey, there have been many who have assisted, guided and supported me, to whom I extend my heartfelt gratitude and appreciation.

Firstly, to The Almighty, for without Whom this would not be possible. My strength and successes come from the blessings of the Highest Power.

My pharmaceutical post-graduate career has culminated with the support of my most dear loved ones who formed the back-bone of my support structure. My deepest appreciation to my parents, Siva Murugan and Daisy Reddy, brother, Ravashin Murugan, and family. This work is a result of your love, sacrifices, support and motivation. Thank you for your belief in me and my dreams, being proud of me at every opportunity and for the existence of my life for it is who I am and what I have achieved thus far.

To my aunt, Tina Naicker, thank you for your support, more so in the last 8 years when I joined your nest. Your love and encouragement over and beyond this period most certainly superseded your undefined role as my “aunt”. I am grateful for the countless conversations about everything “life” and its boundless possibilities, my Sanguine.

To my love, my best friend and sounding board, Desigan Naicker, our 7 years together has been the most fulfilling and beautiful. May we continue to grow, build, learn, love and be kind to one another. A special thank you to the Naicker family, and Vineshree Govender and family for loving me as their own and for being my family away from home.

To my friends who became family, Trevor, Preston and Jason Naidoo, Urika Janghbahadur and our group of amazing friends. Thank you for introducing me to the quest for empowering myself, for making this journey a lighter one, sharing many laughs, late nights, board games and most importantly, love and support.

To my research supervisor, Prof. Viness Pillay, your expertise, passion, dedication and commitment to the science is admirable by far and has pushed me beyond my limits. My sincere gratitude extends to you for your mentorship in my research and providing the platform for young scientists to bring scientific theory to pass. May the Wits Advanced Drug Delivery Platform succeed at every opportunity.

To my co-supervisors, Prof. Yahya E. Choonara, Prof. Lisa C. du Toit and Mr Pradeep Kumar, your scientific advice, effort and time invested in my research is greatly appreciated. Thank you for your interest in me achieving my goals through my research. Prof. du Toit and Mr Kumar, a special thank you for your kindness, words of wisdom and vested concern in my research.

Finer aspects of my research were made possible by several entities which include:
-The Microscopy and Microanalysis Unit at the University of the Witwatersrand, my gratitude is expressed to Prof. Ziegler and Team for their time, teachings and use of their exceptional instruments.
-Mintek, for the use of their High-Resolution Transmission Electron Microscope which broadened my knowledge and view of beauty in crystals.
-The Central Animal Services Unit for their assistance during the *in vivo* investigations of my study and for their patience while I overcame my fear of our furry friends.

A special thank you to my long-time Wits friends, Bibi Fatima Choonara and Poornima Ramburrun for your friendship, company, advice and hour long conversations. Our academic step together has finally come to a fruitful end and I wish for you ellustrious careers in the sciences. To my colleagues, Az-Zamakhshariy Zardad, Famida Ghulam-Hoosain, Fatema Mia, Gretta Mbitsi-Ibouily, Jonathan Pantshwa, Kealeboga Mokolobate, Khadija Rhoda, Khuphukile Madida, Lara Freidus, Lusanda Mapela, Margaret Siyawamwaya, Mduduzi Sithole, Mershan Govender, Naeema Mayet, Nonhlanhla Masina, Olufemi Akilo, Pakama Mahlumba, Patrick Komane, Pierre Kondiah, Samson Adeyemi, Simphiwe Mavuso, Sunanina Indermun, Thashree Marimuthu and Zikhona Hayiyana for their assistance and support.

To Prof. Paul Danckwerts and the rest of the staff of the Department of Pharmacy and Pharmacology for their advice and motivation. Thank you to Mr Sello Ramarumo, Ms Pride Mothobi, Mr Kleinbooi Mohlabi and Mr Bafana Temba for their vital assistance with running of the laboratories. Mr David Bayever, my true gratitude to you for your mentorship during my years at Wits University. Your love for and pride in the Pharmacy profession is inspiring.

To my funders, the National Research Foundation (NRF) of South Africa and Pharmaceutical Society of South Africa (PSSA) for the financial assistance provided over the course of my post-graduate studies. Opinions expressed and conclusions arrived at, are those of the author and are not necessarily to be attributed to the NRF or PSSA.

## DEDICATION

This dissertation is dedicated to my father, Siva Murugan, for being my inspiration and my mother, Daisy Reddy, for being my motivation.

My successes are the result of your sacrifices.

And, to every scientist who acted upon a dream.

## ABSTRACT

*Psoriasis vulgaris is a chronic, hyper-proliferative skin condition which affects the patient's quality of life. The treatment strategy involves long term use of drugs that maintain the condition, however; playing a pivotal negative role in patient compliance. A constructive development in the design of treatment addressing the disease should focus on the challenges faced by current designs. Hence, cellular internalization and trans-barrier transport of nanoparticles can be manipulated on the basis of the physicochemical and mechanical characteristics of nanoparticles to enhance the treatment options of the condition by reducing dosing and increasing the healing due to intracellular drug delivery. Dictating these characteristics allows for the control of the rate and extent of cellular uptake, as well as delivering the drug-loaded nanosystem intra-cellularly which is imperative for drugs that require a specific cellular level to exert their effects, as is with psoriasis. Additionally, physicochemical characteristics of the nanoparticles should be optimal for the nanosystem to bypass the natural restricting phenomena of the body and act therapeutically at the targeted site.*

*Neo-geometric copper nanoparticles (CuNPs) in the biomedical application ascertained skin permeation and retention of the CuNPs as a drug delivery system. The approach to the use of the nanocrystal exploited the shape properties as a function of enhanced cellular uptake and the copper in the inflamed psoriatic environment acted as a cytotoxic agent against hyper-proliferating keratinocytes. A Self-Oscillating Polymeric Network (SOPN) served as a vehicle for the topical delivery of the geometric CuNPs in addition to its oscillating phenomenon to promote the permeation of the active nanoparticles across the rate limiting barrier of the skin, the stratum corneum. This twofold system adequately targets the key limitations in addressing psoriasis.*

*A statistical experimental design comprising a full factorial model for the optimization of the geometric CuNPs and Box-Behnken design applied on the SOPN served as a refining factor to achieve stable, homogenous, geometric nanoparticles using a one-pot method for the systematic optimization of the geometric CuNPs. The optimization of the SOPN involved amplitude and duration of the oscillations, permeation kinetics and cytotoxicity. After optimization of the nano-shapes and oscillations of the SOPN, extensive ex vivo cellular internalization studies were conducted to elucidate the effect of geometric CuNPs on uptake rates; in addition to the vital toxicity assays to further understand the cellular effect of geometric CuNPs as a drug delivery system. Complementing the geometry analysis; volume, surface area, orientation to the cell membrane and colloidal stability were also addressed. The SOPN was also investigated ex vivo for its biocompatibility to determine the $LD_{50}$ and permeation kinetics.*

*The in vivo study probed the nanosystem embedded in the innovative SOPN to stimulate the permeation of the CuNPs across the stratum corneum of the induced psoriasiform-plaque in a BALB/c mouse model. The results confirmed an optimized CuNPs-loaded SOPN topical system with promising plaque thickness reduction when compared with a commercial gold standard in the treatment of the skin condition. This novel system can be safely used with less frequent, lower dosing and no odour, therefore promoting patient compliance.*

## TABLE OF CONTENTS

DECLARATION.....i

PUBLICATIONS.....ii

RESEARCH PRESENTATIONS.....iii

ACCOLADES.....v

ANIMAL ETHICS DECLARATION.....vi

PATENT FILED.....vii

ACKNOWLEDGEMENTS.....viii

DEDICATION.....x

ABSTRACT.....xi

TABLE OF CONTENTS.....xii

LIST OF ABBREVIATIONS.....xxiii

LIST OF EQUATIONS.....xxv

LIST OF FIGURES.....xxvi

LIST OF TABLES.....xxx

## CHAPTER 1

## INTRODUCTION AND RATIONALE OF THE STUDY

1.1. Background to the Study ..... 1

1.2. Rationale and Motivation for this Study ..... 3

1.3. Possible Therapeutic Applications of the Study ..... 5

1.4. Novelty of the Study ..... 6

1.5. Aim and Objectives of this Study ..... 6

1.5.1. Neo-geometric copper nanoparticles ..... 7

1.5.2. Self-oscillating polymeric network ..... 8

1.6. Overview of the Thesis ..... 8

1.7. References ..... 9

## CHAPTER 2

## A REVIEW OF PARAMETERS AND CHARACTERISTICS GOVERNING CELLULAR INTERNALIZATION AND TRANSBARRIER TRAFFICKING OF NANOSTRUCTURES


2.1. Introduction ..... 13

2.2. Transport Mechanisms of Nanocarriers ..... 15

2.2.1. Intracellular endocytic delivery pathways ..... 15

2.2.2. Transcellular delivery pathway ..... 18

2.2.3. Paracellular delivery pathway ..... 18

2.3. Parameters and Characteristics of Nanostructures Governing Cellular Internalization ..... 19

2.3.1. Particle size ..... 19

2.3.2. Surface charge ..... 21

2.3.3. Particle shape ..... 22

2.3.4. Surface properties ..... 24

2.3.5. Proteins and ligand attachments ..... 26

2.4. Current Advances in Transbarrier Internalization ..... 28

2.5. Concluding Remarks ..... 31

2.6. References ..... 32

## CHAPTER 3

## NEO-GEOMETRIC COPPER NANOCRYSTALS BYCOMPETITIVE, DUAL SURFACTANT-MEDIATED FACET ADSORPTION CONTROLLING SKIN PERMEATION


3.1. Introduction ..... 49

3.2. Materials and Methods ..... 50

3.2.1. Synthesis of copper nanostructures ..... 50

3.2.2. Determination of the effect of surfactant concentration on particle morphology ..... 51

3.2.3. Crystallinity and composition characterization of synthesized copper ..... 51

3.2.4. Determination of the stability of the copper nanoparticles ..... 51

3.2.5. Molecular and structural transitional analysis of the surfactant-coated copper nanoparticles ..... 51

3.2.6. Determination of nanoparticle yield ..... 51

3.2.7. Thermal degradation analysis of the surface surfactant-coating of the copper nanoparticles ..... 52

3.2.8. *Ex vivo* permeation evaluation of five distinct nano-shapes ..... 52

3.2.9. Data analysis and confirmation of statistical significance of all assays performed ..... 52

3.3. Results and Discussion ..... 53

3.3.1. Influence of variation in surfactant concentration on copper nanoparticles shape ..... 53

3.3.2. Nanocrystal lattice spacing ..... 59

3.3.3. X-ray and electron diffraction analysis ..... 61

3.3.4. Surface charge analysis ..... 62

3.3.5. Yield analysis ..... 63

3.3.6. Evaluation of chemical and structural changes of the surfactant-coated copper nanoparticles ..... 64

3.3.7. Thermal degradation analysis of surfactant-coated copper nanoparticles ..... 65

3.3.8. Effect of nano-shape on skin permeation through excised mice skin ..... 66

3.4. Concluding Remarks ..... 68

3.5. References ..... 69

## CHAPTER 4

## CELLULAR INTERNALIZATION KINETICS AND CYTOTOXIC PROPERTIES OF STATISTICALLY DESIGNED AND OPTIMIZED NEO-GEOMETRIC COPPER NANOCRYSTALS


4.1. Introduction ..... 74

4.2. Materials and Methods ..... 75

4.2.1. Synthesis of geometric copper nanocrystals ..... 76

4.2.2. Experimental design and constraint optimization of neo-geometric copper nanoparticles ..... 76

4.2.3. Geometric and morphological characterization of the copper nanoparticles ..... 77

4.2.4. Zeta potential and stability analyses of copper nanoparticles ..... 77

4.2.5. Crystal and elemental analysis of the optimized copper nanoparticles ..... 77

4.2.6. Thermal degradation analysis of the surface surfactant-coating of the copper nanoparticles ..... 78

4.2.7. Optimization of the neo-geometric copper nanoparticles ..... 78

4.2.8. Cell culturing and copper nanoparticle-cell incubation ..... 78

4.2.9. Qualitative and quantitative cellular internalization studies ..... 78

4.2.10. Geometric dependency of copper nanoparticles on cell viability ..... 79

4.2.11. Lactate dehydrogenase activity ..... 79

4.2.12. Glutathione assay ..... 79

4.2.13. Lipid peroxidation activity ..... 80

4.2.14. Data analysis and confirmation of statistical significance of all assays performed ..... 80

4.3. Results and Discussion ..... 80

4.3.1. Geometric analyses of copper nanocrystals ..... 80

4.3.2. Analyses of the stability and aggregation potential of copper nanoparticles ..... 85

4.3.3. Evaluation of copper nanoparticle crystallinity and elemental composition of copper nanoparticles ..... 85

4.3.4. Investigation of surface surfactant-coating due by thermal degradation of copper nanoparticles ..... 87

4.3.5. Analysis of a full factorial response surface design ..... 88

4.3.6. Response surface analysis ..... 89

4.3.7. Response optimization of the neo-geometric copper nanoparticles ..... 93

4.3.8. Qualitative and quantitative analyses of cellular internalization studies based on nano-geometry ..... 95

4.3.9. MTT assay ..... 99

4.3.10. Lactate dehydrogenase activity ..... 103

4.3.11. Glutathione activity ..... 104

4.3.12. Lipid peroxidation activity ..... 105

4.4. Concluding Remarks ..... 106

4.5. References ..... 106

## CHAPTER 5

## TRANSPORT OF A NOVEL GEOMETRIC COPPER NANOSYSTEM ACROSS THE SKIN BARRIER EMPLOYING A SELF-OSCILLATING POLYMERIC NETWORK IN THE TOPICAL TREATMENT OF PSORIASIS


5.1. Introduction ..... 111

5.2. Materials and Methods ..... 113

5.2.1. Synthesis of cube-shaped copper nanocrystals ..... 113

5.2.2. Confirmation of cubic geometric copper nanocrystals ..... 113

5.2.3. Polymerization of self-oscillating cross-linked polymer ..... 113

5.2.4. Synthesis validation and investigation of the structural and molecular vibrations of the self-oscillating cross-linked polymer ..... 114

5.2.5. Fabrication of the polymeric network and incorporation of cube-shaped copper nanoparticles ..... 114

5.2.6. Application of a Box–Behnken design for the copper nanoparticle-loaded self-oscillating polymeric network ..... 114

5.2.7. Response surface analysis as per Box–Behnken design ..... 115

5.2.8. Lower critical solution temperature measurements of the self-oscillating cross-linked polymer ..... 115

5.2.9. Determination of the degree of crystallinity of synthesized and native polymers ..... 115

5.2.10. Measurement of optical vibrations to detect oscillations of the self-oscillating polymeric network ..... 116

5.2.11. *In vitro* studies in the determination of permeation rate controlled by the oscillations of the self-oscillating polymeric network ..... 116

5.2.12. *Ex vivo* analyses of the biocompatibility of the self-oscillating polymeric network via cell viability studies ..... 116

5.2.13. *In vivo* investigation of the cube-shaped copper nanocrystal-loaded self-oscillating polymeric network in the BALB/c induced-psoriasis model ..... 117

5.2.14. Data analysis and confirmation of statistical significance of all assays performed ..... 118

5.3. Results and Discussion ..... 118

5.3.1. Box-Behnken experimental design and constrained optimization of the copper nanoparticle-loaded self-oscillating polymeric network ..... 118

5.3.2. Response surface analysis ..... 120

5.3.3. Cube-shaped copper nanocrystals synthesized by dual surfactant mediated adsorption ..... 122

5.3.4. Chemical synthesis validation of the responsive synthesized self-oscillating polymeric network ..... 123

5.3.5. Lower critical solution temperature measurements of the oscillating polymer 124

5.3.6. X-Ray diffraction analysis to determine crystallinity changes ..... 126

5.3.7. Measurement of optical vibrations to detect oscillations ..... 127

5.3.8. Appraisal of nanoparticle permeation in relation to the self-oscillating polymeric network ..... 133

5.3.9. Cell toxicity and viability studies ..... 135

5.3.10. *In vivo* analysis of the geometric copper nanoparticle-loaded self-oscillating polymeric network in the psoriasis model ..... 137

5.4. Concluding Remarks ..... 146

5.6. References ..... 146

## CHAPTER 6

## CONCLUSIONS AND RECOMMENDATIONS

6.1. Conclusions ..... 150

6.2. Recommendations ..... 152

6.3. Future Outlook ..... 153

7. Appendices ..... 156

7.1. Research Publications ..... 156

7.1.1. Review Article 1 ..... 156

7.1.2. Research Paper 1 ..... 157

7.1.3. Research Paper 2 ..... 158

7.1.4. Research Paper 3 ..... 159

7.1.5. Research Paper 4 ..... 160

7.2. Research Presentations ..... 161

7.3. Research Awards ..... 167

7.3.1. Winner of the Boehringer Ingelheim Young Scientist Award, 2015, South Africa ..... 167

7.3.2. Winner of the Young Researcher Award, 2016, Greece ..... 168

7.4. Animal Ethics Certificate ..... 169

## LIST OF ABBREVIATIONS

ANOVA - Analysis of Variance
APP - protein aminopeptidase P
APS - ammonium persulfate
BALB/c – Bagg Albino (inbred research mouse strain)
BBB – blood brain barrier
BZ reaction - Belousov-Zhabotinsky reaction
CAMs - cell adhesion molecules
CARs - cell adhesion receptors
CAS – Central Animal Service
CMC - carboxymethyl cellulose
CPP - cell-penetrating proteins or peptides
CTAB - hexadecetyl trimethylammonium bromide
Cu- copper
CuNPs- copper nanoparticles
CuONPs - copper oxide nanoparticles
DMEM - Dulbecco's Modified Eagles Medium
DSC - Differential Scanning Calorimetry
DTNB - 5,5-dithio-bis-(2-nitrobenzoic acid)
EDS - Energy Dispersive Spectroscopy
FBS - foetal bovine serum
FCC – face-centred cube
FDC - Franz diffusion cell
FTIR - Fourier-Transform Infrared
GIT – gastro-intestinal tract
GSH - reduced glutathione
GSSG - glutathione disulfide
$H_2O_2$ - hydrogen peroxide
HeLa - human cervical cancer cells
HR-TEM- High Resolution Transmission Electron Microscope
ICP-OES - Inductively Coupled Plasma – Optical Emission Spectroscopy
$LC_{50}$ - median lethal concentration
LCST - lower critical solution temperature
LDH - lactate dehydrogenase
LPO – lipid peroxidation activity
MBAAm - N′-methylenebisacrylamide
MDA - malondialdehyde
NADPH - nicotinamide adenine dinucleotide phosphate
NHEK - normal human epidermal keratinocytes
NIPAAm - N-isopropylacrylamide
NLS - nuclear localization signal
NOSI - nitric oxide synthase
NP – nanoparticle
NSAIDS- non-steroidal anti-inflammatories
NTs – nanotubes

$O^{2-}$ - superoxide radical
$OH^{-}$ - hydroxyl radical
PASI - Psoriatic Area and Severity Index
PEG - Poly (ethylene glycol)
PLA - PEG-D-L-polylactide
PLGA - Poly (lactic-co-glycolic acid)
PNIPAM – Poly-N-isopropylacrylamide
PRINT - Particle Replication in Non-wetting Templates
PVP - poly-vinyl pyyrolidone
RBC - red blood cell
RES - reticulo endothelial system
RGD - Arg-Gly-Asp
ROS - reactive oxygen species
Ru – ruthenium
RVG - rabies virus glycoprotein
SAED - Selected Area Electron Diffraction
SDS - sodium dodecyl sulphate
SE – standard error
SOPN - Self-Oscillating Polymeric Network
TAT - trans-activating
TBA - thiobarbituric acid
TEM - Transmission Electron Microscope
Tf – transferrin
TGA - Thermo-Gravimetric Analysis
TJs - tight junctions
UV - Ultraviolet-Visible
WHO - World Health Organization
XRD - X-ray diffraction

## LIST OF EQUATIONS

**Equation 3.1:** Number of moles

**Equation 3.2:** Determination of theoretical yield of copper

**Equation 3.3:** Determination of actual yield of copper

**Equation 3.4:** Bragg equation

**Equation 3.5:** Determination of spacing between corresponding lattices of nanocrystals

**Equation 4.1:** Gibbs adsorption equation

**Equation 4.2:** Wulff's equation

**Equation 4.3:** Determination of the total curvature energy of the lipid bi-layer for internalization

**Equation 4.4:** Redox equation for the copper reaction

**Equation 5.1:** The Oregonator Model, reaction rate equation 1

**Equation 5.2:** The Oregonator Model, reaction rate equation 2

**Equation 5.3:** The Oregonator Model, reaction rate equation 3

**Equation 5.4:** The Schrodinger equation 1

**Equation 5.5:** The Schrodinger equation 2

**Equation 5.6:** *Ex vivo* cell viability determination

## LIST OF FIGURES

**Figure 1.1:** Copper nanoparticles of different shapes (ie. round, spherical, rod-like, elongated rod, cylindrical, filiform) to determine enhanced intracellular delivery to keratinocytes.

**Figure 1.2:** Schematic representation illustrates: a) the formulated neo-geometrical nanoparticles for enhanced cellular internalization suspended in the Self-Oscillating Polymeric Network; b) topical application of CuNPs dispersed within the inflammation-responsive SOPN system inclusive of adjuvants to reduce skin irritation; c) thermal activation of the BZ reaction results in a chemical reaction producing oscillations; d) oscillations promote enhanced penetration of CuNPs through thickened psoriatic plaque.

**Figure 2.1:** The transport mechanisms of a typical biological barrier: a) cellular internalization of nanoparticle into cell via endocytosis; b) transcellular transport of nanoparticles through cell; c) paracellular transport of nanoparticle between cells through the tight junction; d) receptor-mediated transcytosis.

**Figure 2.2:** Mechanisms of endocytosis sub-divided into categories of cell-uptake.

**Figure 2.3:** Mechanism of clathrin-mediated endocytosis of nanoparticles.

**Figure 2.4:** The mechanisms of caveolin-mediated endocytosis, macropinocytosis and phagocytosis.

**Figure 2.5:** Representation of the internalization potential dependent on particle size. The larger surface-area of the nanoparticle allows for increased surface contact with the cell membrane for higher internalization rates as described in the investigation of Nicolete *et al.* (2011).

**Figure 2.6:** Particle internalization based on orientation to the membrane. a) schematic showing the angle between the long axis of the particle and the bilayer normal; b) minimum driving forces required to guide the ellipsoid with different initial orientations of the long axis through the lipid bilayer; c) time evolution of particle orientations during the ellipsoid penetration processes with different initial orientations. (Reprinted with permission from Macmillan Publishers Ltd: Nature Nanotechnology (Yang and Ma, 2010)).

**Figure 2.7:** Pathway of uncoated hydrophobic nanoparticle: 1a) nanoparticle in blood circulation; 1b) opsonins recognise nanoparticle as foreign body due to hydrophobic surface;

1c) opsonization of nanoparticle; 1d) and 1e) phagocytosis by phagocyte and elimination of nanoparticle. Pathway of coated hydrophilic nanoparticle: 2a) hydrophilic polymer-coated nanoparticle in blood circulation; 2b) steric hindrance maintains repulsive forces between opsonins and nanoparticle; 2c) nanoparticle continues to circulate until target site reached; 2d) and 2e) endocytosis by target cell.

**Figure 2.8:** Stimulating endocytosis through CPP- and antibody-conjugation of nanoparticles.

**Figure 3.1:** a) sample S1, spherical nanoparticles (90 nm); b) sample S2, combination of spheres and rods; c) sample S3, combination spheres and rods with predominant rods; d) sample S4, rod-like nanoparticles; e) sample S5, cubic-shaped nanoparticles; f) sample S6, pyramidal nanoparticles; g) sample S7, irregular spherical particles; h) sample S8, combination of neo-geometrical nanoparticles; i) sample S9, combination of neo-geometrical nanoparticles at reduced size range; j) sample S10, irregular nanospheres; k) sample S11, spherical nanoparticles (250–300 nm); l) sample S12, spherical nanoparticles (10 nm).

**Figure 3.2:** Schematic of growth of homogenous shapes according to surfactant variation: a) growth of a rod structure from the decahedral precursor; b) tetrahedral precursor geometry; c) polyhedral precursor geometry; d) cuboctahedral precursor geometry growing from the (100) and (111) planes.

**Figure 3.3:** 1a) rod-shaped nanoparticle and inset showing 5-fold center of the decahedral geometry at (111); 1b) lattice fringes and spacing of rod-shaped nanoparticle; 1c) uniform SAED patterns; 2a) Cube-shaped nanoparticle; 2b) lattice fringes and spacing of cube-shaped nanoparticle 2c) uniform SAED patterns; 3a) Pyramid-shaped nanoparticle; 3b) lattice fringes and spacing of pyramid-shaped nanoparticle; 3c) uniform SAED patterns; 4a) Spherically-shaped nanoparticles; 4b) lattice fringes and spacing of spherical nanoparticles; 4c) uniform SAED patterns.

**Figure 3.4:** a) powder X-Ray diffraction patterns of synthesized copper nanocrystals; b) energy dispersive spectra showing pure elemental copper.

**Figure 3.5:** FTIR spectra of: a) ascorbic acid; b) sample S1; c) CTAB; d) SDS; e) sample S4; f) sample S5.

**Figure 3.6:** TGA curves of: a) sample S1 showing degradation of reducing agent; b) sample S2 showing degradation of surfactants on the nanoparticle surface.

**Figure 3.7:** *Ex vivo* permeation profiles of geometric copper nanoparticles through excised BALB/c mice dermal tissue (*n* = 3).

**Figure 4.1:** TEM images of the nanoparticles synthesized from 12 formulations as per the Full Factorial Design.

**Figure 4.2:** Precursor nuclei and geometric structures from which nanocrystals arise.

**Figure 4.3:** a) XRD patterns of the neo-geometric nanosystems; b) energy dispersive spectra indicating elemental analysis.

**Figure 4.4:** TGA analysis confirming the surfactant adsorption on the CuNPs.

**Figure 4.5:** Residual plots: a) shape uniformity per sample; b) zeta potential.

**Figure 4.6:** a) main effects; b) interaction plot for shape uniformity.

**Figure 4.7:** a) main effects; b) interaction plot for zeta potential.

**Figure 4.8:** Contour plot and response surface plots. a) shape uniformity per sample; b) zeta potential.

**Figure 4.9:** Phase contrast images of geometric CuNP internalization over a 24 hour incubation period.

**Figure 4.10:** Quantitative analysis of cell internalized CuNPs over 1, 4, 8 and 24 hours.

**Figure 4.11:** Cell viability after 24 hour neo-geometric CuNP exposure to a) NHEK cells and b) HeLa cells. Lactate dehydrogenase leakage after after 24 hour neo-geometric CuNP exposure to c) NHEK cells and d) HeLa cells. Glutathione levels after 24 hour neo-geometric CuNP exposure to e) NHEK cells and f) HeLa cells. Malondialdehyde levels after 24 hour neo-geometric CuNP exposure to g) NHEK cells and h) HeLa cells. Data presented are mean ±SE of 3 experiments performed in duplicate. *$p \leq 0.05$ versus control.

**Figure 5.1:** Optimization plot for the response optimization of the SOPN formulation.

**Figure 5.2:** Residual and surface plots of a) average oscillation amplitude; b) duration of oscillations; c) permeation rate; d) cell toxicity.

**Figure 5.3:** a) cube-shaped copper nanocrystals; b) lattice fringes and spacing of 1.811Å (100).

**Figure 5.4:** FTIR spectra of the synthesized SOPN and native polymers.

**Figure 5.5:** DSC thermograms of the synthesized SOPN and comparative polymers.

**Figure 5.6.** XRD spectra of a) NIPAM; b) PNIPAM; c) SOPN

**Figure 5.7:** Redox function of the BZ reaction creating an oscillatory action within the polymer.

**Figure 5.8:** Self-oscillating vibrational frequency of the 15 Box-Behnken Design formulations. Data presented are mean ±SE of 3 experiments performed in duplicate. *$p$ ≤0.05 versus control.

**Figure 5.9:** SOPN potentiated diffusion of CuNPs diffusion through a membrane barrier. Data presented are mean ±SE of 3 experiments performed in duplicate. *$p$ ≤0.05 versus control.

**Figure 5.10:** Cell viability analysis of the SOPN on NHEK cells. Data presented are mean ± SE of 3 experiments performed in duplicate. *$p$ ≤0.05 versus control.

**Figure 5.11:** Macrological transition in the psoriasis model: a) healthy skin; b) imiquimod-induced psoriasis; c) over the 3 phases during treatment interventions for Group1 (CuNPs), Group 2 (aqueous cream), Group 3 (CuNPs-loaded SOPN), Group 4 (SOPN) and Group 5 (corticosteroid cream).

**Figure 5.12:** Histology pictographs comparing mice skin samples from a) Group A (CuNPs-loaded aqueous cream); b) Group B (Unmedicated aqueous cream); c) Group C (CuNPs-loaded SOPN); d) Group D (Unmedicated SOPN); e) Group E (commercial product) at days 3, 7 and 14.

**Figure 5.13:** Copper retention in a) blood; b) skin. Data presented are mean ± SE of 3 experiments. *$p$ ≤0.05 versus control.

## LIST OF TABLES

**Table 2.1:** Key terms.

**Table 2.2:** Overview of biological barriers and nanoparticle advances to overcome physiological limitations.

**Table 3.1:** Surfactant variations corresponding to physicochemical characteristics of synthesized CuNPs, Data presented are mean ± SE of three experiments performed in duplicate. *$p \leq 0.05$.

**Table 3.2:** Zeta potential data collated from all CuNPs samples.

**Table 3.3:** Copper nanoparticle flux and associated permeability coefficients for the geometric copper nanoparticles through excised BALB/c mice dermal tissue ($n = 3$).

**Table 4.1:** Formulation variables and responses applied in the Full Factorial design.

**Table 4.2:** Statistically generated formulations obtained from a Full Factorial Design of optimization.

**Table 4.3:** Measured responses as per a Full Factorial Design.

**Table 4.4:** Optimized formulations outputting homogenous samples of stable neo-geometric CuNPs.

**Table 5.1:** 15 Formulations generated by Box–Behnken design.

**Table 5.2:** Experimental design formulation analysis of the oscillating phenomenon and biocompatibility of the SOPN. Data presented are mean ± SE of 3 experiments performed in duplicate. *$p \leq 0.05$ versus control.

**Table 5.3:** PASI scoring evaluation at 3 phase time points on day 3, 7 and 14 of treatment.

# CHAPTER 1

# INTRODUCTION AND RATIONALE OF THE STUDY

## 1.1. Background to the Study

Dermal psoriasis is a chronic, inflammatory condition which is characterized by plaques on the flexor surfaces of the body (Kilfoyle *et al*., 2012). In the pathophysiology of the disease, cytokine production is up-regulated resulting in the hyper-proliferation of keratinocytes and T-cell pathogenesis found in the basal layer of the epidermis (Tzu *et al*., 2006). The psoriasis plaque is the result of the accompanying inflammatory process (Tzu *et al*., 2006). The disease affects the patients' quality of life socially and psychologically and improved therapy would substantially reduce discomfort and the augment patients' quality of life (Raddadi *et al*., 2011). Current therapeutic interventions include topical corticosteroids, vitamin D analogues, tacrolimus, salicylic acid, coal tar and combination therapy (Raddidi *et al*., 2011). Studies show that these drugs have been successively incorporated into topical nanosystems such as biodegradable nanoparticles, tyrosine-derived nanospheres (Kilfoyle *et al*., 2012), lipid nanocarriers (Agrawal *et al*., 2012), activated nanogels (Singka *et al*., 2010) and drug-loaded mesoporous nanoparticles (Vadia and Rajput, 2012) which focus on keratolytic processes. However, these interventions do not allow for the delivery of active agents intracellularly or the enhanced permeation of anti-psoriatic dugs through the stratum corneum and thick psoriatic plaque by a direct mechanism. Epidermal hyperplasia as the key component in this immune response and maintenance of the psoriatic plaque (Griffiths and Barker, 2007) and the highly implicated stratum corneum significantly affects permeability of foreign substances (Elias and Menon, 1990). In the treatment of psoriasis, surpassing these barriers may significantly enhance the treatment prognosis.

Studies to specifically determine the effect of nanoparticle shape on cellular internalization are limited (Gould, 2006) yet necessary in order to enhance biomedical technology and inform toxicity studies. The various pathways for cellular internalization of nanoparticles includes 1) clathrin-mediated endocytosis in which membrane invagination occurs due to the clathrin protein, 2) clathrin-independent endocytosis, 3) caveolae-mediated endocytosis where caveolin proteins induce plasma invaginations, 4) dynamin-dependent endocytosis causes vesicle scission at the plasma membrane, and 5) clathrin- and caveolae-independent pathways (Musyanovych *et al*., 2011). Nanoparticles for enhanced internalization may use the same mechanism and mimic the structural parameters of natural peptides such as proteins or hormones which internalize readily. Factors affecting cellular internalization

include the nanoparticle size, shape, surface charge, chemical composition, surface morphology, functionality and stability (Gratton *et al*., 2008). For example, dermal psoriasis of which there is no cure would have an increased prognosis factor if therapeutic interventions targeted intracellular components in its treatment strategy.

Therefore, this study focuses on improved cell uptake via a smart nanosytem of neo-geometric copper nanoparticles (CuNPs) embedded in a vehicle to promote the delivery of the copper as a model drug. The field of nanomedicine is characterized in drug delivery in terms of nanoparticle shape, size, type, chemical composition and use (Li *et al*., 2008). The scope for further research into this ever-advancing concept has immense potential to progress medical care by decreasing side-effect profiles due to specific and targeted drug release, improving bioavailability and bypassing first-pass metabolism of drugs (Nomura *et al*., 2009). Nanoparticle shape can impact the cellular internalization process and may enhance the performance of nano-polymer drug carriers (Kuntsche *et al*., 2010). Gratton and co-workers (2008) undertook a study which proved that cylindrical nanoparticles enhanced the internalization of HeLa cells. However, this internalization was dependent on the appropriate orientation of the nanoparticles to the targeted cells. In this study, the shape effect of internalization will be ascertained and when coupled with the cytotoxic potential of the copper, this novel drug delivery system may prove to be at the forefront of psoriatic treatment innovations.

In the synthesis of the Self-Oscillating Polymeric Network (SOPN) vehicle, utilising the Belousov-Zhabotinsky (BZ) reaction provides a dynamic system of redox oscillations which can be applied to transdermal drug delivery (Yoshida and Ueki, 2014). This phenomenon promotes periodic, mechanical, macroscopic waves when applied to gels and polymers, in acidic solution with required substrates. The automatic mechanical oscillation of the polymer gel will be induced by the covalently coupled BZ reaction encouraged by ionic charge oscillations of the required substrates. Also known as tunnelling, the quantum mechanical occurrence allows for a particle to penetrate and cross a barrier that it typically cannot without external control. Providing the additional energy supplied by the macroscopic waves of the BZ reaction, the anti-psoriatic drug will be stimulated to cross the skin barrier into the hyper-keratinized layer. The chemical process produces mechanical and physical change within the system resulting in biomedical and therapeutic benefits.

The inflamed environment of the psoriasis, after application of the gel system, serves as the external stimuli controlling the activation of the reaction to create the periodic oscillations, hence the use of a stimuli-sensitive polymer activator. Thus, the rhythmic and spatial

patterns produced by the reaction stimulate the movement of the nanoparticles and enhances penetration through the psoriatic skin. Applying this concept to drug delivery and overcoming the limitation of drug transport through the stratum corneum, especially the thickened psoriatic plaque, will serve as an innovative strategy in the treatment of various dermal syndromes. Increasing drug content to penetrate this layer will significantly reduce therapeutic time and dosing periods.

### 1.2. Rationale and Motivation for this Study

According to the World Health Organization (WHO) (2013), studies in developed countries have an estimated psoriasis prevalence of 4.6% and 90% of these cases is plaque psoriasis (Al Raddadi *et al*., 2011). Psoriasis is incurable and due to the nature of the skin disorder, is a challenge to treat. Making use of a nanosystem with enhanced intracellular delivery and a delivery vehicle to stimulate penetration of anti-psoriatic drug through the stratum corneum allows for increased drug permeation, reduced duration of treatment and a decreased drug concentration required for application. Delivering drug at the intended dermal target site provides a direct means to treat dermal conditions allowing for the avoidance of hepatic metabolism and systemic side effects (Alexander *et al*., 2012).

When considering psoriasis, first-line therapy consists of topical agents (Al Raddadi *et al*., 2011); hence, maximising the efficacy of topical treatment should be a priority focus in psoriasis research. Topically applied CuNPs between 15-100nm have been evaluated to penetrate skin pores and induce necrosis in the epidermal layer where cellular vitality is significantly affected (Cohen *et al*., 2013). Copper has an anti-proliferative and cytotoxic effect by inducing apoptosis and has been reported to improve anti-cancer therapy (Jose *et al*., 2011), properties which make it suitable for use as an agent to therapeutically target psoriasis and will therefore be used as a model drug compound in this study. Most drugs used in the treatment strategy for psoriasis are cytotoxic (Tzu *et al*., 2006). By designing shape-specific CuNPs for enhanced cellular internalization, the cytotoxicity to surrounding tissue is reduced and targeted for the cells associated with the pathophysiology of the disease. Copper will be used as the drug model as it confers apoptotic properties and the shape of the metal nanoparticles, using varying surfactant concentrations, can be manipulated to conduct this study (Figure 1.1).

In the course of the BZ reaction of the SOPN vehicle, the transition metal catalyst periodically changes between the reduced state and the oxidised state creating the macroscopic vibrations. The reaction will be activated upon application of the CuNPs-loaded

SOPN to the psoriatic plaque in response to the change in pH provided by the mediators of psoriasis by varying the reaction substrates, altering its lower critical solution temperature values and employing the use of a thermo-responsive polymer with sensititivity to hydrophobic changes initiated by the BZ reaction. The inflammation-responsive SOPN will promote periodic, mechanical, macroscopic waves when applied to gels and polymers with required substrates in an area of inflammation which corresponds with low pH. The response will allow for the resulting BZ reaction to produce mechanical oscillating waves and stimulate the delivery of the CuNPs to permeate the stratum corneum barrier of the skin. Automatic mechanical oscillations of the polymer-gel will be induced by the covalently coupled BZ reaction encouraged by ionic charge oscillations of the required substrates. Providing the additional energy supplied by the macroscopic waves of the BZ reaction, the CuNPs will be stimulated to penetrate the skin barrier, hair follicles and skin pores (Figure 1.2). Once the CuNPs bypass the stratum corneum, the shape-specific CuNPs for enhanced cellular internalization into keratinocytes will confer its directed cytotoxicity and minimize effects on surrounding tissue by targeting for the cells associated with the pathophysiology of the disease. The importance of shape-specificity plays its role in the cellular uptake kinetics and cytotoxic potential of psoriasis drugs; and maintaining the integrity of the surrounding healthy tissue.



**Figure 1.1:** Preliminary surfactant –coated copper nanoparticles of different shapes (ie. round, spherical, rod-like, elongated rod, cylindrical, filiform) to determine enhanced intracellular delivery to keratinocytes.

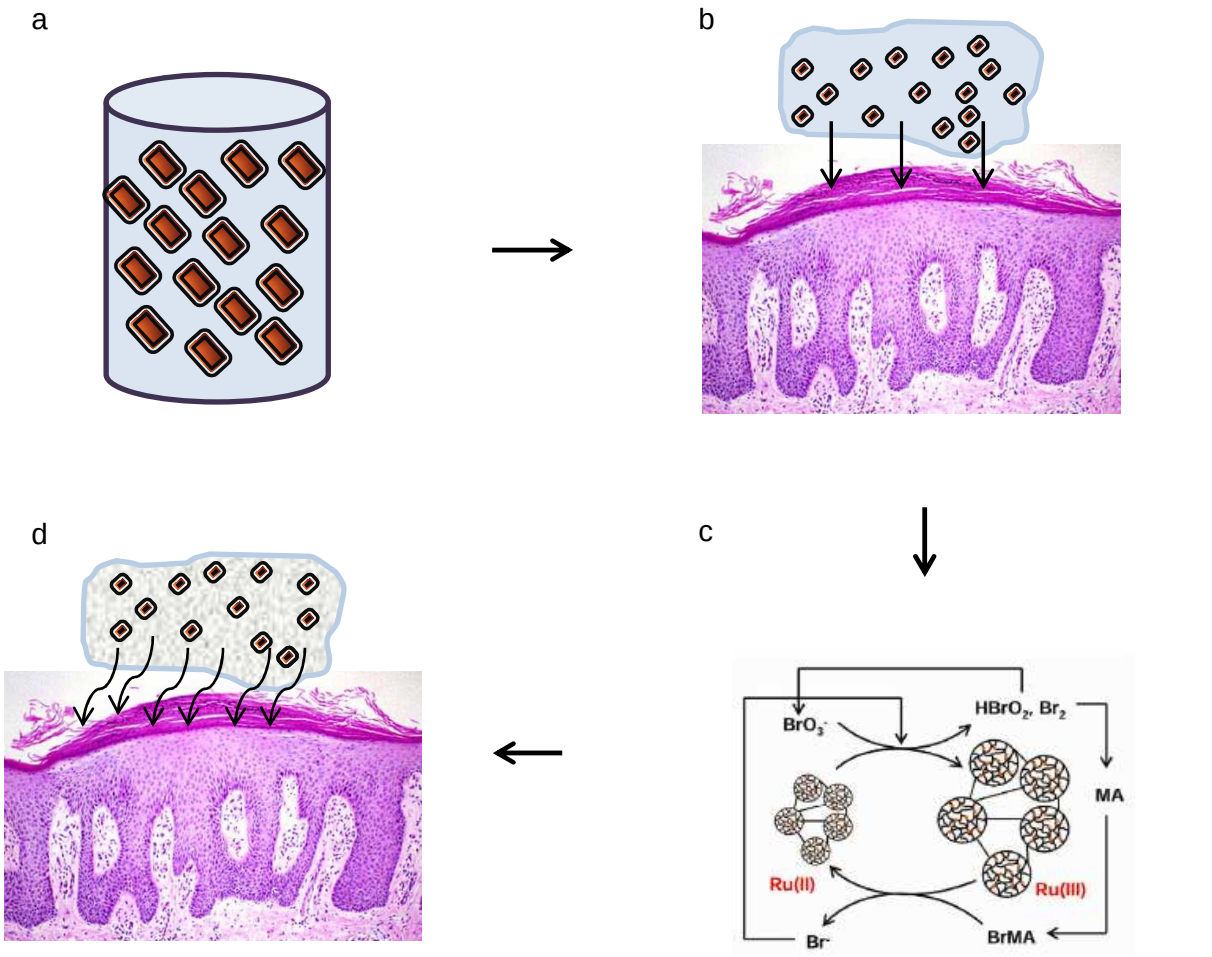


**Figure 1.2:** Schematic representation illustrates: a) the formulated neo-geometrical nanoparticles for enhanced cellular internalization suspended in the Self-Oscillating Polymeric Network; b) topical application of CuNPs dispersed within the inflammation-responsive SOPN system; c) low pH activation of the BZ reaction results in a chemical reaction producing mechanical oscillations; d) oscillations promote enhanced penetration of CuNPs through thickened psoriatic plaque.

### 1.3. Possible Therapeutic Applications of the Study

- Local treatment of skin disorders (e.g. squamous cell carcinoma, bacterial/fungal infections, atopic dermatitis) by directly applying gel to targeted area.
- Drugs that induce systemic side effects (e.g. tretinoin, NSAIDs) will bypass hepatic metabolism if delivered via the transdermal route and will not affect other physiological processes.
- Skin disorders with hyper-keratosed characteristics and for application to body parts with thickened skin.

- Drug-free SOPN can be applied to any dermal condition with the inclusion of appropriate drug.
- Dermal infection sites – copper has shown to confer antibacterial properties, utilising this phenomena and targeted delivery to the target site will result in enhanced drug delivery and shorter duration of therapy.

### 1.4. Novelty of the Study

- Shape-specific nanoparticles offer enhanced cell targeting from the intracellular component.
- Selective accumulation of the CuNPs in the epidermis should eliminate adverse side effects associated with systemic exposure.
- This formulation will control the over-proliferation of keratinocytes, dose-control the delivery of the CuNPs, and ease skin irritation caused by psoriasis.
- It will be incorporated into a self-oscillating gel formulation that allows enhanced skin contact, this also ensures that the CuNPs limited to area of application and ease of application.
- Use of the BZ reaction and its resulting mechanical oscillations in its application for topical therapy.
- Use of the acidic environment provided by the psoriasis to control the activation of the BZ reaction.
- Suspension of neo-geometrical CuNPs in the stimuli-responsive SOPN to enhance the permeability of the CuNPs through the skin barrier.

### 1.5. Aim and Objectives of this Study

The aim of this study was to synthesize CuNPs of various geometries to ascertain the effect of shape on cellular internalization. Upon completion of this aim and its relevant objectives, formulation advances were made to develop, enhance and evaluate a stimuli-responsive self-oscillating polymeric dermal delivery system that has the capability to activate mechanical oscillations by means of a chemical reaction after responding to the low pH generated by the psoriatic skin. The synthesized CuNPs is suspended in the SOPN gel which also serves as the delivery vehicle. The ultimate goal of the system was to synthesise a smart, dermal device to mechanically enhance the delivery of drugs through the skin barrier whereby the advantageous properties of both systems may be combined.

This study focused on designing a system with the following design criteria:

- For the purpose of topical administration, the BZ reaction formed part of polymer-gel complex for ease of administration and familiarity to the patient in a conventional physical form.
- The system consists of a polymeric gel system that is composed of a stimuli-responsive polymer such as N-isopropylacrylamide to ensure activation of the BZ reaction upon exposure to the skin affected and reaction substrates to precede the reaction, creating mechanical oscillations.
- Suspended within this polymeric gel network is the synthesized neo-geometric CuNPs for enhanced cellular internalization to promote optimal therapeutic responses.
- Activation of the SOPN will occur only upon exposure to the site of application enstipulating stimuli-responsive behaviour ensuring the maintenance of the reaction until after topical application of the SOPN.

The afore-mentioned objectives were met as determined through the completion of Design of Experiments statistical approach.

The following objectives were also undertaken to ensure pragmatic fulfilment of the study:

### 1.5.1. Neo-geometric copper nanoparticles

a. The selection of appropriate materials and polymers to complement the synthesis of various copper nano-particulates using an adapted microemulsion, reverse micelle and thermal reduction method.
b. Physicochemical and physicomechanical characterization of nano-shaped particulates will include size analysis, zeta potential tests and Transmission Electron Microscopy (TEM) for the shape identification of the nanoparticles, crystallinity and elemental composition by High Resolution Transmission Electron Microscope (HR-TEM) analysis, X-ray diffraction (XRD), Selected Area Electron Diffraction (SAED), Energy Dispersive Spectra (EDS), degradation of copper and stabilising coat by Thermo-Gravimetric Analysis (TGA) and molecular transitions by Fourier-Transform Infrared (FTIR).
c. *Ex vivo* studies will investigate the cytotoxic potential and intracellular delivery of nanoparticles by incubating keratinocytes and cervical cancer cells with CuNPs.

### 1.5.2. Self-oscillating polymeric network

a. The selection of appropriate materials, polymers and methods to complement the synthesis of the inflammation-sensitive self-oscillating polymer-gel for neo-geometric CuNPs.
b. Synthesis of the thermo-responsive SOPN polymer-gel blend and incorporation of CuNPs will be conducted.
c. Physicochemical characterization of oscillating polymer-gel blend will include Ultraviolet-Visible (UV) Spectroscopy, FTIR, and Differential Scanning Calorimetry (DSC).
d. *Ex vivo* permeation studies will be carried out on excised mice skin to ascertain transport of the CuNPs from the SOPN through the stratum corneum.
e. *Ex vivo* cytotoxicity studies will determine the biocompatibility of the system.
f. The clinical potential of the system will be determined by conducting *in vivo* research upon a suitable animal model whereby the response of the SOPN will be tested on exposure to psoriatic skin upon completion of *in vitro* studies. Plaque thickness reduction and histological evaluation will be included in *in vivo* analyses.

## 1.6. Overview of the Thesis

**Chapter 1** of this thesis provides an introduction and background to this study and highlights the rationale, aim, objectives and potential benefits of this study.

**Chapter 2** is a critical review of nano-characteristics affecting cellular internalization and transbarrier transport. Drug delivery systems using these techniques have also been addressed in addition to the current nanobiotechnology advances in application of the various biological barriers of the body.

**Chapter 3** of the thesis describes the preliminary synthesis parameters in the growth of neo-geometric CuNPs. Analysis of the effect of dual surfactants creating a cationic complex evaluates the shape formation during synthesis of the nanocrystals. Physicochemical properties are also investigated for further analysis into the geometric nanocrystals.

**Chapter 4** highlights the investigation of synthesizing homogenous, stable geometric CuNPs through institution of a statistical experimental Full Factorial Design. The design, development and optimization are detailed. Using the key optimized geometric CuNPs, cellular uptake and toxicity studies on two cells lines are extensively investigated.

**Chapter 5** focuses on the synthesis of a SOPN system and is optimized through a Box-Behnken template for formulary analysis whereby 15 formulations are obtained. The optimized formulations are further characterized to elucidate its physicochemical and physicomechanical properties. The *in vivo* performances of the CuNPs and SOPN as independent and combined systems are investigated in the induced-psoriasis Bagg Albino (inbred research mouse strain) (BALB/c) mouse model in the determination of healing of the psoriasiform plaque.

**Chapter 6** concludes this thesis, discussing the limitations and recommendations for future use of the system.

### 1.7. References


Agrawal, Y., Petkar, K.C. and Sawant, K.K., 2010. Development, evaluation and clinical studies of Acitretin loaded nanostructured lipid carriers for topical treatment of psoriasis. *International journal of pharmaceutics*, *401*(1), pp.93-102.

Al Raddadi, A.A., Fatani, M.I., Shaikh, Y.H., Thaci, D., Al Reshaid, A.A., Al-Eisa, A.M., Alghamdi, W.A., Abdulfattah, H.Y., Al Belbisi, Z.M., Atawi, A.C. and Alajroush, W.A., 2011. Adopted guidelines of care for the topical management of psoriasis from American and German guidelines. *Journal of the Saudi Society of Dermatology & Dermatologic Surgery*, *15*(1), pp.5-13.

Alexander, A., Dwivedi, S., Giri, T.K., Saraf, S., Saraf, S. and Tripathi, D.K., 2012. Approaches for breaking the barriers of drug permeation through transdermal drug delivery. *Journal of Controlled Release*, *164*(1), pp.26-40.

Chen, I.C., Kuksenok, O., Yashin, V.V., Balazs, A.C. and Van Vliet, K.J., 2012. Mechanical resuscitation of chemical oscillations in Belousov–Zhabotinsky gels. *Advanced Functional Materials*, *22*(12), pp.2535-2541.

Cohen, D., Soroka, Y., Ma'or, Z., Oron, M., Portugal-Cohen, M., Brégégère, F.M., Berhanu, D., Valsami-Jones, E., Hai, N. and Milner, Y., 2013. Evaluation of topically applied copper (II) oxide nanoparticle cytotoxicity in human skin organ culture. *Toxicology in vitro*, *27*(1), pp.292-298.

De, S. and Mandal, S., 2013. Surfactant-assisted shape control of copper nanostructures. *Colloids and Surfaces A: Physicochemical and Engineering Aspects*, *421*, pp.72-83.

Dubey, V., Mishra, D., Dutta, T., Nahar, M., Saraf, D.K. and Jain, N.K., 2007. Dermal and transdermal delivery of an anti-psoriatic agent via ethanolic liposomes. *Journal of Controlled Release*, *123*(2), pp.148-154.

Eeckman, F., Moës, A.J. and Amighi, K., 2002. Evaluation of a new controlled-drug delivery concept based on the use of thermoresponsive polymers. *International journal of pharmaceutics*, *241*(1), pp.113-125.

Elias, P.M. and Menon, G.K., 1991. Structural and lipid biochemical correlates of the epidermal permeability barrier. *Advances in lipid research*, *24*, pp.1-26.

Gould, P., 2006. Size matters to cell uptake–but so does shape: Nanoparticles. *Nano Today*, *1*(2), p.15.

Gratton, S.E., Napier, M.E., Ropp, P.A., Tian, S. and DeSimone, J.M., 2008. Microfabricated particles for engineered drug therapies: elucidation into the mechanisms of cellular internalization of PRINT particles. *Pharmaceutical research*, *25*(12), pp.2845-2852.

Griffiths, C.E. and Barker, J.N., 2007. Pathogenesis and clinical features of psoriasis. *The Lancet*, *370*(9583), pp.263-271.

Ikai, K., 1999. Psoriasis and the arachidonic acid cascade. *Journal of dermatological science*, *21*(3), pp.135-146.

Ito, Y., Nogawa, M. and Yoshida, R., 2003. Temperature Control of the Belousov− Zhabotinsky Reaction Using a Thermoresponsive Polymer. *Langmuir*, *19*(23), pp.9577-9579.

Jose, G.P., Santra, S., Mandal, S.K. and Sengupta, T.K., 2011. Singlet oxygen mediated DNA degradation by copper nanoparticles: potential towards cytotoxic effect on cancer cells. *Journal of nanobiotechnology*, *9*(1), p.9.

Kilfoyle, B.E., Sheihet, L., Zhang, Z., Laohoo, M., Kohn, J. and Michniak-Kohn, B.B., 2012. Development of paclitaxel-TyroSpheres for topical skin treatment. *Journal of controlled release*, *163*(1), pp.18-24.

Kuntsche, J., Koch, M.H., Steiniger, F. and Bunjes, H., 2010. Influence of stabilizer systems on the properties and phase behavior of supercooled smectic nanoparticles. *Journal of colloid and interface science*, *350*(1), pp.229-239.

Li, P., Dai, Y.N., Zhang, J.P., Wang, A.Q. and Wei, Q., 2008. Chitosan-alginate nanoparticles as a novel drug delivery system for nifedipine. *Int J Biomed Sci*, *4*(3), pp.221-228.

Musyanovych, A., Dausend, J., Dass, M., Walther, P., Mailänder, V. and Landfester, K., 2011. Criteria impacting the cellular uptake of nanoparticles: a study emphasizing polymer type and surfactant effects. *Acta biomaterialia*, *7*(12), pp.4160-4168.

Nomura, T., Mori, T., Arima, H. and Konishi, Y., 2009. Shape and size control of barium chromate nanoparticles using reverse micelle. *Advanced Powder Technology*, *20*(1), pp.101-105.

Pileni, M.P., Tanori, J. and Filankembo, A., 1997. Biomimetic strategies for the control of size, shape and self-organization of nanoparticles. *Colloids and Surfaces A: Physicochemical and Engineering Aspects*, *123*, pp.561-573.

Pullela, S.R., Wang, Q. and Cheng, Z., 2013. Self-oscillating structural polymer gels. *Advances in Nanoparticles*, 2, pp94-98.

Shah, P.P., Desai, P.R., Patel, A.R. and Singh, M.S., 2012. Skin permeating nanogel for the cutaneous co-delivery of two anti-inflammatory drugs. *Biomaterials*, *33*(5), pp.1607-1617.

Singka, G.S.L., Samah, N.A., Zulfakar, M.H., Yurdasiper, A. and Heard, C.M., 2010. Enhanced topical delivery and anti-inflammatory activity of methotrexate from an activated nanogel. *European Journal of Pharmaceutics and Biopharmaceutics*, *76*(2), pp.275-281.

Tzu, J., Mamelak, A.J. and Sauder, D.N., 2006. Current advancements in the treatment of psoriasis: Immunobiologic agents. *Clinical and Applied Immunology Reviews*, *6*(2), pp.99-130.

Vadia, N. and Rajput, S., 2012. Study on formulation variables of methotrexate loaded mesoporous MCM-41 nanoparticles for dissolution enhancement. *European Journal of Pharmaceutical Sciences*, *45*(1), pp.8-18.

Valodkar, M., Rathore, P.S., Jadeja, R.N., Thounaojam, M., Devkar, R.V. and Thakore, S., 2012. Cytotoxicity evaluation and antimicrobial studies of starch capped water soluble copper nanoparticles. *Journal of hazardous materials*, *201*, pp.244-249.

van der Fits, L., Mourits, S., Voerman, J.S., Kant, M., Boon, L., Laman, J.D., Cornelissen, F., Mus, A.M., Florencia, E., Prens, E.P. and Lubberts, E., 2009. Imiquimod-induced psoriasis-like skin inflammation in mice is mediated via the IL-23/IL-17 axis. *The Journal of Immunology*, *182*(9), pp.5836-5845.

Yoshida, R. and Ueki, T., 2014. Evolution of self-oscillating polymer gels as autonomous polymer systems. *NPG Asia Materials*, *6*(6), p.e107.

# CHAPTER 2

# A REVIEW OF PARAMETERS AND CHARACTERISTICS GOVERNING CELLULAR INTERNALIZATION AND TRANSBARRIER TRAFFICKING OF NANOSTRUCTURES

## 2.1. Introduction

The emergence of nanomedicine provides a strategic, therapeutic tool which aims to increase drug targeting to site-specific areas within the body. Nanoparticle research has identified the crossing of mucosal barriers and cellular uptake to support nanoparticle utilization, as well as nanoparticle surface properties that affect these phenomena (Alonso, 2004). In the design of nanoparticles for biological use, significant factors to overcome limitations associated with insufficient drug delivery to targeted sites are inclusive of nanoparticle size, surface charge, nanoparticle shape, chemical composition and stability (Gratton *et al*., 2008a; Parveen *et al*., 2012). Manipulating these pertinent nanoparticle characteristics may facilitate various applications and enhanced cellular and transbarrier internalization of nanoparticles into the target sites. These sites innately have a biological barrier to prevent the entry of foreign objects, thus resulting in decreased drug concentrations at the intended site. Ideally, nanomedicine should circumvent the biological barriers and enhance drug targeting and nanoparticle uptake (Brzoska *et al*., 2004).

Figure 2.1 illustrates different transport mechanisms across and into the biological membrane for the internalization of nanoparticles and key terms related to nanoparticle internalization and transbarrier are provided in Table 2.1. According to Kumari and co-workers (2010a), nanoparticle internalization occurs mainly through intracellular, paracellular and transcellular pathways. However, endocytosis pathways are poorly understood regardless of their clinical significance and continued research (Parveen *et al*., 2012). Continued research in this paradigm, coupled with nanoparticulate internalization and characterization will provide immense insight into an ideal pharmaceutical formulation design.

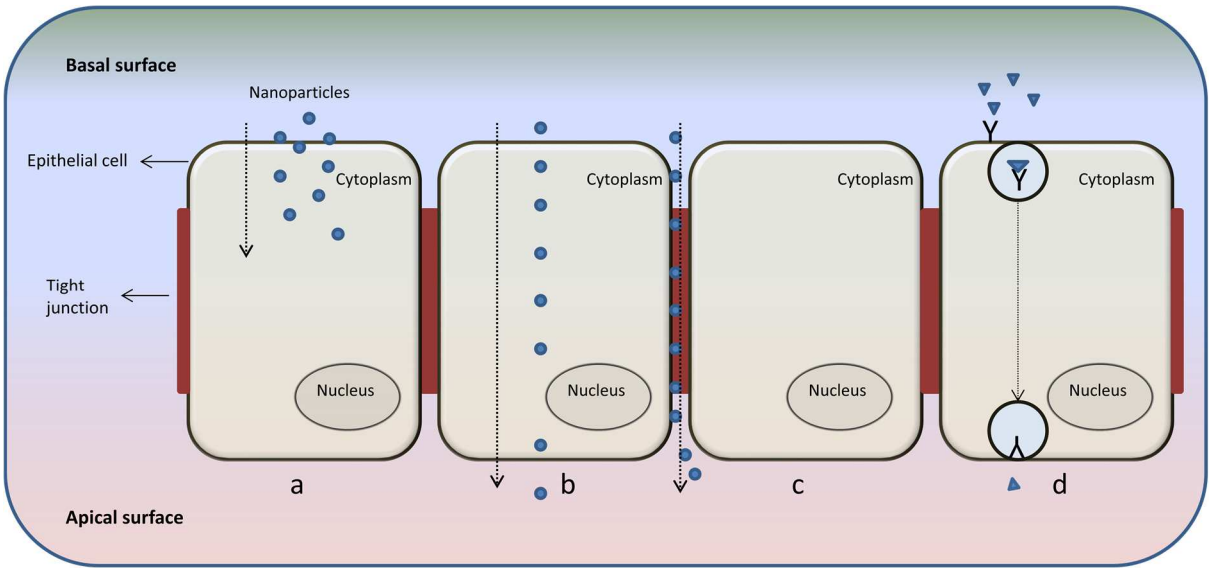


**Figure 2.1:** The transport mechanisms of a typical biological barrier: a) cellular internalization of nanoparticle into cell via endocytosis; b) transcellular transport of nanoparticles through cell; c) paracellular transport of nanoparticle between cells through the tight junction; d) receptor-mediated transcytosis.

Current studies on nanomedicine are encouraged in order to structure a framework that enables efficient, safer drug delivery and to eliminate many of the disadvantages posed by conventionally delivered drugs. Studies to specifically determine the effect of nanoparticle internalization are limited yet necessary in order to enhance biomedical technology and inform toxicity studies. Elucidating the parameters of nanoparticles that enable them to target cells in response to disease-specific signals could significantly improve therapeutic care of complex diseases. The current review therefore discusses nanoparticle properties and characteristics such as size, shape, charge, shape, hydrophobicity and ligand attachments that influence its uptake into target cells and through biological barriers. Intracellular pathways and current mechanisms employed to augment nanoparticle uptake and biological-barrier transport are also discussed in detail.

**Table 2.1:** Key terms

| Term | Definition |
|---|---|
| Cellular internalization | Process by which biological and foreign matter is taken up by cells. |
| Endocytosis | Energy or enzyme-dependent mechanism of cellular internalization. |
| Transbarrier | Refers to transport of nano- and micro-substances through cells from extracellular fluid through the apical and basolateral membrane. |
| Opsonization | Biological phenomenon whereby opsonin molecules adsorb onto the surface of foreign particles to enhance Reticulo Endothelial System (RES) recognition and phagocytosis. |

| | |
|---|---|
| PRINT particles | Particles fabricated using a lithographic technique of Particle Replication in Non-wetting Templates (PRINT) to produce monodisperse, shape-controlled particles. |

## 2.2. Transport Mechanisms of Nanocarriers

### 2.2.1. Intracellular endocytic delivery pathways

Various receptor-mediated pathways exist for cellular internalization of biological substances such as hormones and enzymes that require internalization to exert an effect at a cellular level (Figure 2.2). By adopting these mechanisms, drugs and nanoparticles can be delivered to the necessary cell type. Cellular uptake mechanisms need to be understood in order to enhance internalization and identify nanoparticle characteristics that promote specific mechanisms (Alonso, 2004). The mechanisms of different endocytic pathways as illustrated in Figure 2.1a are thoroughly described in the subsequent discussions.

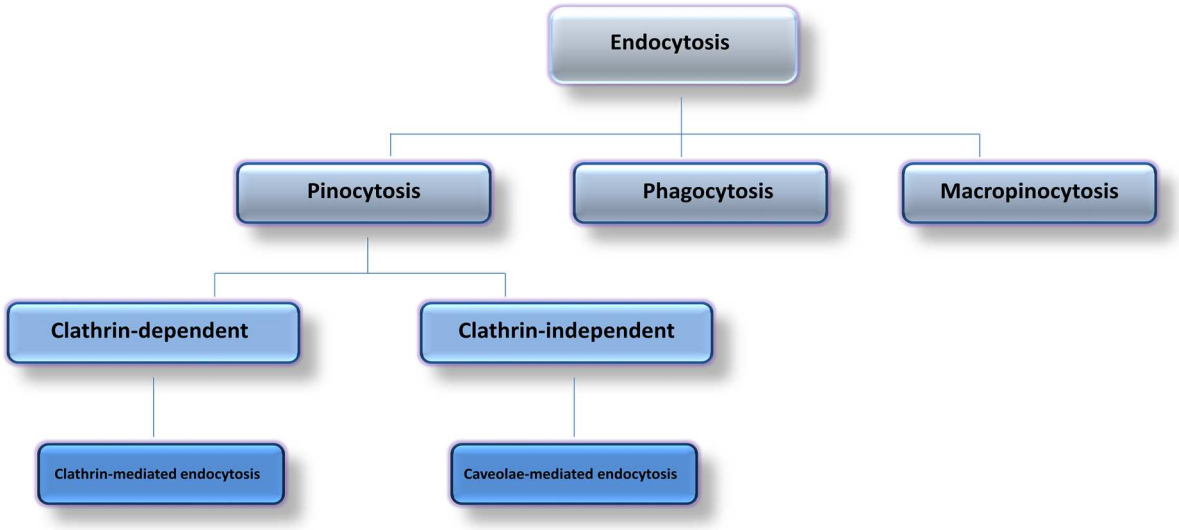


**Figure 2.2:** Mechanisms of endocytosis sub-divided into categories of cell-uptake.

#### 2.2.1.1. Pinocytosis

Included in the pinocytosis classification are clathrin-mediated endocytosis, caveolae-mediated endocytosis and macropinocytosis. Clathrin-mediated endocytosis involves clathrin-coated vesicle formation in the presence of adaptor and accessory proteins. Endocytic event cascade is activated by the signalling of the nanoparticle on the cell surface (Xiang *et al*., 2012), which aligns surface proteins to prompt clathrin recruitment from the cytosol to begin clathrin-coating on the inner membrane of the cell. An adaptor protein, Epsin, is involved in the initial stages of membrane curvature and pit formation and accessory proteins such as dynamin (GTPase) affect vesicle formation from shallow to deep

invagination by inducing deformation of the membrane (Mousavi *et al*., 2004). With the aid of dynamin, a clathrin-coated vesicle with a size of 100-150nm is formed due to polymerization of the coat complex and the nanoparticle -containing clathrin-coated vesicle then internally detaches from the donor membrane (Xiang *et al*., 2012). Once within the cell, clathrin and adaptor proteins uncoat to allow fusing of the vesicle within the cell to release the endocytosed nanoparticles (Figure 2.3).

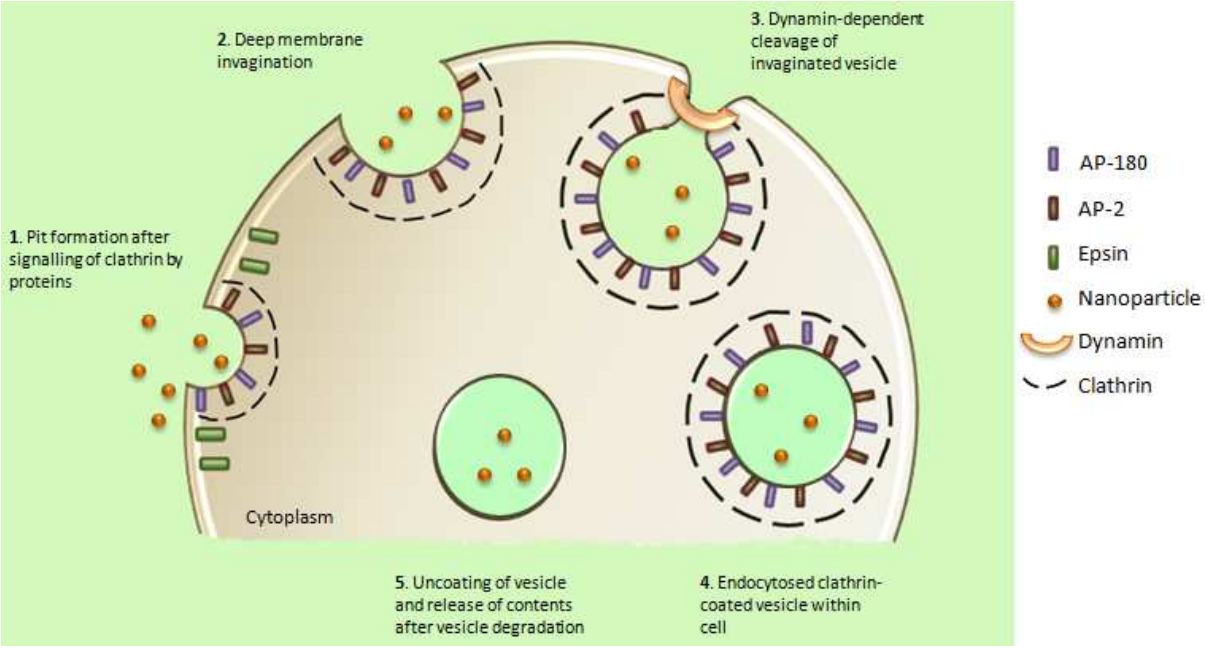


**Figure 2.3:** Mechanism of clathrin-mediated endocytosis of nanoparticles.

Caveolae-mediated endocytosis is a pathway dependent on membrane cholesterol, dynamin and cell receptor mediation (Xu *et al*., 2013). Caveolae are formed by a cluster of caveolin proteins (caveolin-1, -2, -3) that bind directly to membrane cholesterol (Kumari *et al*., 2010b), as shown in Figure 2.4. Complex signalling is driven by the cell-membrane bound nanoparticles to be endocytosed which induces actin re-organization and dynamin recruitment from the cytosol (Pelkmans *et al*., 2002) to stimulate membrane invagination and further on, vesicle budding. The uncoated invagination initially assumes a flask shape with a body diameter of 60-80nm and a neck diameter of 10-15nm (Wang *et al*., 2009). Similar to clathrin-mediated endocytosis, dynamin regulates vesicle budding of the caveolae to internalize cell membrane segments that contain the cargo and the caveolae membrane fuses into the acceptor compartment to release its contents.

#### 2.2.1.2 Macropinocytosis

Macropinocytosis is a clathrin-, caveolin and dynamin independent process, which involves uptake of a larger volume of the membrane, also allowing for larger sized particles of sizes

>1 µm to be internalized (Sahay *et al*., 2010). The pathway proceeds by forming protrusions due to actin polymerization from the cell membrane which then encapsulates the substance to be internalized and once again fuses back with the cell membrane (Kumari *et al*., 2010b). The process is initiated by activation of tyrosine kinases which signals a cascade of changes in the actin cytoskeleton and the formation of membrane protrusions. The random macropinocytic extensions enclose the material in the extracellular environment for cellular uptake (Figure 2.4), and collapses to fuse with the cell membrane generating an internalized macrosome vesicle of an average of ~10µm (Kerr *et al*., 2009; Sahay *et al*., 2010). The uncoated membrane of the macrosome either acidifies and shrinks or fuses with the lysosomal compartment consequently releasing the nanoparticles or contents into the intracellular compartment (Hillaireau and Couvreur, 2009).

#### 2.2.1.3. Phagocytosis

Similar to macropinocytosis, phagocytosis is also a clathrin-, caveolin- and dynamin-independent process and is proficient in **i**nternalizing larger particles inclusive of drug nanocarriers and pathogens (Hillaireau and Couvreur, 2009). It involves sequential instigation of receptors as a result of cell-surface recognition of cargo leading to internalization by encircling it into triggered cup-shaped cell membrane deformations, forming a phagosome (Kumari *et al*., 2010b). The pathway begins with opsonization of the nanoparticles which then attach to the cell-surface via Fc receptors and complement receptors (Groves *et al*., 2008), marking the beginning of actin polymerization and rearrangement and membrane extension to form surface extensions that encapsulate the opsonized nanoparticles for internalization (Hillaireau and Couvreur, 2009; Park and Cox, 2009) (Figure 2.4). A reduction and contraction of actin at the base of the cup allows for closure of the phagosome and the entire actin-lined phagosome is then internalized with its contents (Groves *et al*., 2008). In a macropinocytotic manner, the vesicle undergoes degradation after transporting the opsonized particle into the cell.

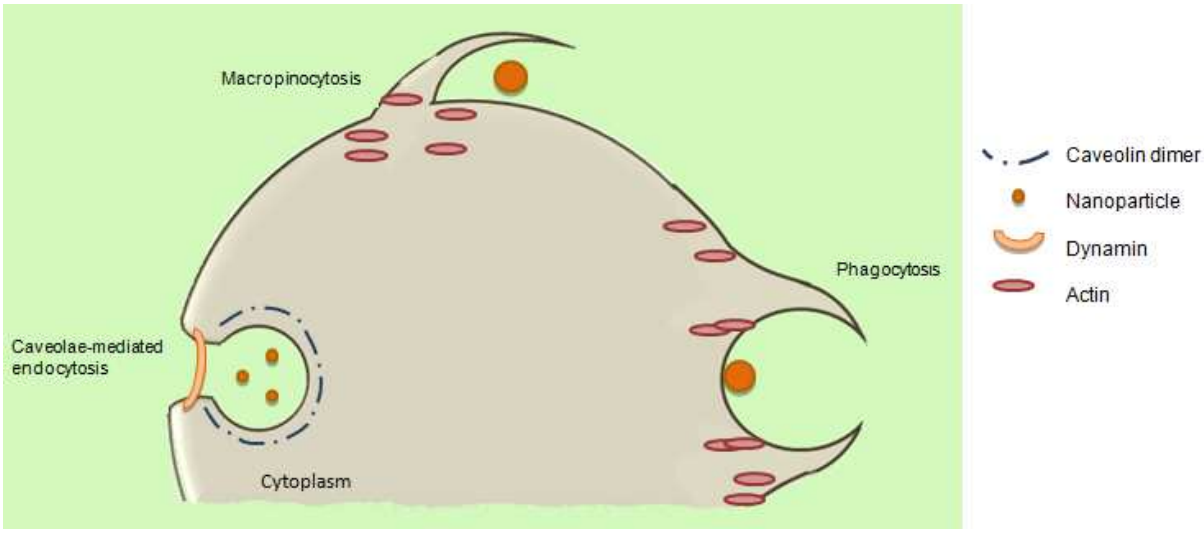


**Figure 2.4:** The mechanisms of caveolin-mediated endocytosis, macropinocytosis and phagocytosis.

### 2.2.2. Transcellular delivery pathway

As described by clathrin-dependent and clathrin-independent internalization, post-uptake, the vesicle undergoes degradation. However, through other pathways, the vesicle can be transported to the other end of the cell surface where its contents can be expelled into the extracellular environment as shown in Figure 2.1b (Bornsel *et al*., 1989). This pathway allows for lipophilic nanoparticles and molecules to move efficiently through the transcellular route by partitioning into and out of lipid bi-layers via vesicular carriers due to its lipidic nature (Gonzalez-Mariscal *et al*., 2008). The cargo to be transported binds to cell-membrane receptors to form a complex. Membrane invagination is then initiated and the deep pit is internalized as a vesicle containing nanoparticles (Mostov, 1994; Lu *et al*., 2012). Following internalization, the endocytosed vesicle is sorted into a transcytotic vesicle to prevent typical endosome degradation. The transcytotic vesicle is then transported to the other end of the cell where the vesicle membrane fuses with the cell membrane and the content of the vesicle is secreted externally (Mostov, 1994; Ferrati *et al*., 2014).

### 2.2.3. Paracellular delivery pathway

Paracellular delivery of drugs is a passive process that occurs between adjacent cells via tight junctions through the intercellular space and not through the cell as described by transcellular delivery (Figure 2.1c) (Hayashi *et al*., 1997). This route is specific for hydrophilic nanoparticles and molecules since hydrophilic molecules cannot cross biological membranes and aqueous pathways that normally absorb nutrients, vitamins or cofactors (Gonzalez-Mariscal *et al*., 2008). Hydrophilic molecules are unable to cross biological membranes in the manner of lipophilic molecules due to the lipid properties of the cell bi-layer membrane; therefore, targeting the paracellular pathway can significantly affect their

transepithelial transport. Transit through this route is regulated by tight junctions (TJs) that have heterogeneous pores with a variety of diameters of up to 15Å (Hayashi *et al*., 1997) and charges of which the overall charge of the TJ is negative and is therefore more responsive to positively charged nanoparticles for paracellular permeation (Salamat-Miller and Johnston, 2005).

## 2.3. Parameters and Characteristics of Nanostructures Governing Cellular Internalization

The need for understanding the fundamental physicochemical characteristics of nanoparticles and their pivotal role in cellular uptake is essential when designing smart nanosystems. Ascertaining nanoparticle functionality provides basic and necessary information to influence the rational design of optimal nanocarriers by selectively delivering drug to targeted tissue to increase the rate of cellular uptake and effectively reduce drug-induced side-effects (Mohanraj and Chen, 2006; Reddy *et al*., 2006; Moghimi *et al*., 2012). Other determining factors relating to cellular uptake are 1) variation in the uptake pathways (Barua and Rege, 2009), 2) cell-specificity (Snijder *et al*., 2009), 3) nanoparticle interaction with cell-surface receptors (Reddy *et al*., 2006) and 4) nanoparticle interaction with plasma proteins leading to nanoparticle-protein complex formation (Aggarwal *et al*., 2009).

### 2.3.1. Particle size

An important consideration regarding particle size is the 4µm diameter of the smallest blood vessels of which a micrometer particle may cause an embolism. Acknowledging size should therefore not be limited to its internalization ability but also for its physical effects once inside the body (Gunaseelan *et al*., 2010; Torrano *et al*., 2013). Cells within the human body vary from 1-100µm and therefore have a low probability of internalizing particles of ~100µm. This particle size range for intracellular delivery is limited to the cells with a large enough capacity to host the particle. In addition to the higher rates of endocytosis of smaller sized nanoparticles (<100nm) (Luo *et al*., 2006; des Rieux *et al*., 2006; Sahay *et al*., 2010), experimental data also promotes higher bioavailability of the endocytosed drug-carrier at 100-1000nm (Acosta, 2009; Patel *et al*., 2011). Various studies revealed that within a 1-100nm range, 50nm nanoparticles shows maximum cellular uptake with 14-20nm nanoparticles having a higher endocytotic rate than the 100nm nanoparticles (Chithrani *et al*., 2006; Jin *et al*., 2009; Awaad *et al*., 2012). No significant difference in cellular uptake has been shown by the nanoparticles of the size range between 25-130nm (Roger *et al*., 2009) while some reports postulate that nanoparticles have higher internalization between 50-100nm (Torchilin, 2006). On the contrary, from a cellular uptake research experiment using

thio-organosilica nanoparticles of 50nm-500nm, Awaad and associates (2012) concluded that 95-200nm is the ideal size for increased cellular uptake.

In an *in vitro* study undertaken by Nicolete and co-workers (2011), after 4 hours of being culture-incubated, 6.5±3.9µm Poly (lactic-co-glycolic acid) (PLGA) microparticles were still attached to the cell surface and required more time for endocytosis to occur. Simultaneously, PLGA nanoparticles of size 389nm (polydispersity index=0.2) had already, within the same time period, been encapsulated in vesicles and endocytosed into the intracellular compartment (Figure 2.5). These results were coherent with the study conducted by Loh and co-workers (2012) which demonstrated poor internalization capability of chitosan particles that were >1µm, much unlike the extensive uptake of nanoparticles of sizes 110-390nm. Interestingly, Sahay and co-workers (2010) stated that microparticles also enter cells but not as rapidly as nanoparticles and concluded that Poly (ethylene glycol) (PEG) particles <5µm can gain entry into cells via pinocytosis. Likewise, considering the possibility of the aggregation of nanoparticles, the size of an aggregated nanocluster is larger than a single nanoparticle and will affect the internalization rate accordingly. *In vitro*, the stability of the nanoparticles should be controlled to promote a consistent nanosystem.

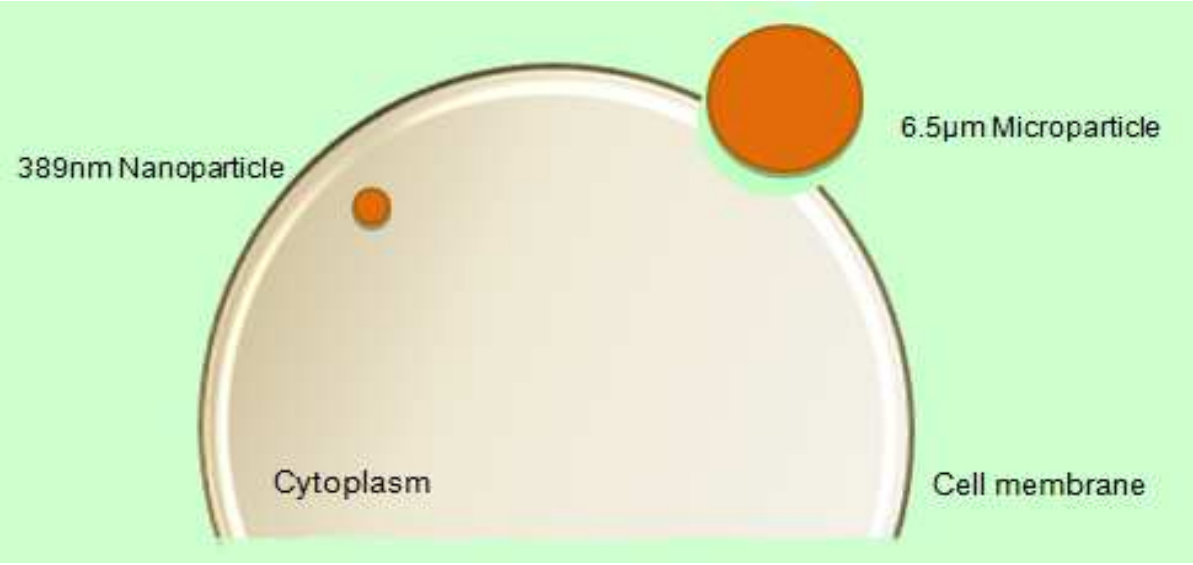


**Figure 2.5:** Representation of the internalization potential dependent on particle size. The larger surface-area of the nanoparticle allows for increased surface contact with the cell membrane for higher internalization rates as described in the investigation of Nicolete *et al*. (2011).

A research review compiled by Acosta (2009) predominantly concluded that nanoparticles with a size of 500nm and below produced higher cellular uptake than nanoparticles of a bigger size. These results, however, were also coherent with the penetration abilities of the

systems that housed the nanoparticles, which is evident that the nanocarrier system also impacted internalization profiles. The uptake of nanoparticles with a size of 500nm has a lower viability but may be promoted with the use of a constructive, complementary delivery system. Essentially, an assisting delivery system would have lipophilic properties or a suitable surface charge for enhanced internalization.

Despite several studies promoting the use of smaller nanoparticles (<100nm), disparities exist in other studies providing evidence that particle size affects internalization as significantly as its complementary system. The variation in internalization profiles and nanoparticle size demonstrates that the influence of nanoparticle size is also dependent on the type of cells and the chemical composition of the nanomaterial (Sahay *et al*., 2010; Loh *et al*., 2012).

### 2.3.2. Surface charge

Charge parameters are vital in the characterization of nanoparticles as they determine aggregation in the blood or interaction with oppositely- and like-charged cell-membrane surfaces. A plethora of studies concluded that cationic and neutral particles show the highest transport efficiency compared to negatively charged particles due to the charge attraction between the positive nanoparticles and negative cell-membrane surface therefore increasing the rate and extent of internalization (des Rieux *et al*., 2006; Harush-Frenkel *et al*., 2008; Nan *et al*., 2008; Ilina *et al*., 2012). These electrostatic forces are long-range forces and can act across intervening aqueous space (Rand, 1981).

#### 2.3.2.1. Cationic and neutral nanoparticles

In the study by Jallouli and associates (2007), the uptake of 60nm neutral and cationic maltodextrin porous nanoparticles with a phospholipid core were investigated in brain capillary endothelial cells. Neutral nanoparticles were endocytosed in the caveolae-mediated pathway while the cationic nanoparticles were found to utilise the paracellular pathway due to the rich anionic sites found on the luminal surface of the endothelial cells. The cationic nanoparticles had a stronger charge affinity to the collagen fibres on the surface of the endothelial cells, thus impeding drug delivery while the neutral nanoparticle sample showed better transcytosis into the targeted cells.

#### 2.3.2.2. Cationic nanoparticles

Karlsson and co-workers (1999) showed that cationic particles had a 2.5-fold higher uptake than neutral particles and a 25-fold higher uptake than anionic particles concluding that cationic particles are transported using the paracellular pathway to a greater degree than

neutral or anionic particles. This study contradicts Lin and associates (2012) who concluded from their experimental study that cationic and neutral gold-coated nanoparticles were internalized via endocytosis while anionic nanoparticles showed lesser permeability and trafficked through the paracellular pathway.

#### 2.3.2.3. Anionic nanoparticles

Contrary to the above mentioned research, many studies prove the successful internalization of negatively charged nanoparticles. An interesting study conducted by Harush-Frenkel and associates (2008) concluded that both anionic and cationic PEG-D-L-polylactide (PLA) nanoparticles accumulated within MDCK and human cervical cancer (HeLa) cells. The internalized anionic nanoparticles underwent a degradative lysosomal process and were unable to undergo further transcytosis, rendering cationic nanoparticles more suitable for cellular drug delivery. Likewise, negatively charged quantum dot nanoparticles were, in fact, endocytosed through a caveolae-mediated pathway and cationic quantum dot nanoparticles used a clathrin-mediated pathway, internalizing human epidermal keratinocyte cells (Zhang and Monteiro-Riviere, 2009). Both charged quantum dots were internalized via endocytosis with no specific rationalization to endocytic preference.

Despite the hypothesis of nanoparticles with a negative charge having a slower uptake rate due to repulsive forces, research has shown that certain anionic nanoparticles internalize more readily. From this discussion, it can be deduced that anionic nanoparticles have the ability to undergo internalization via caveolae-pathways, whereas cationic nanoparticles commonly use the clathrin-pathways (Harush-Frenkel *et al*., 2008; Zhang and Monteiro-Riviere, 2009). Highly charged negative nanoparticles also favour good stability since the Columbic repulsion forces arising from their surface charge can overcome the Van der Waals attractive forces between them and prevent aggregation (Muthu and Singh, 2008).

### 2.3.3. Particle shape

Functional behaviour and internalization of particles in drug delivery is strongly influenced by its shape (Champion *et al*., 2007). Although few researchers have focused on shape, those who have made noteworthy contributions, but with contradicting results (Hao *et al*., 2012). In many of the following studies, nanoparticle shape was the key factor for enhanced internalization, proving its pivotal role in nanoparticle fabrication. Chithrani and co-workers (2006) investigated the uptake of gold spherical and rod-shaped nanoparticles. The 74nm and 14nm spherical nanoparticles had a higher uptake when compared to 74x14nm rod-shaped nanoparticles by 500 and 375%, respectively, which support their claim that spherical particles have a higher internalization probability. The speculation is that the

difference in curvature between the two shapes determines cell surface binding. When the longitudinal axis of the rod-shaped nanoparticle is in contact with the cell surface, it has a larger area of contact with the cell-membrane receptors than compared to spherical nanoparticles and therefore blocks the remaining available membrane receptors, reducing the number of nanoparticles being internalized. Han and associates (2006) have reported similar results which prove that spherical particles internalize substantially quicker than asymmetrically-shaped particles. Champion and Mitragotri (2006) reported on the correlation between contact angle and particle internalization concluding that rod-shaped nanoparticles have a higher likelihood of internalization when their major axis is perpendicular to the cell membrane. The long axis of the rod aligned perpendicular to the cell will increase the internalization rate and the rate will decrease as ø (angle of orientation to the perpendicular) increases (Figure 2.6). This theory is based on the orientation of the nanoparticle to the cell membrane and could further dictate the synthesis of nanoparticle shapes with several short aspects to enhance internalization.

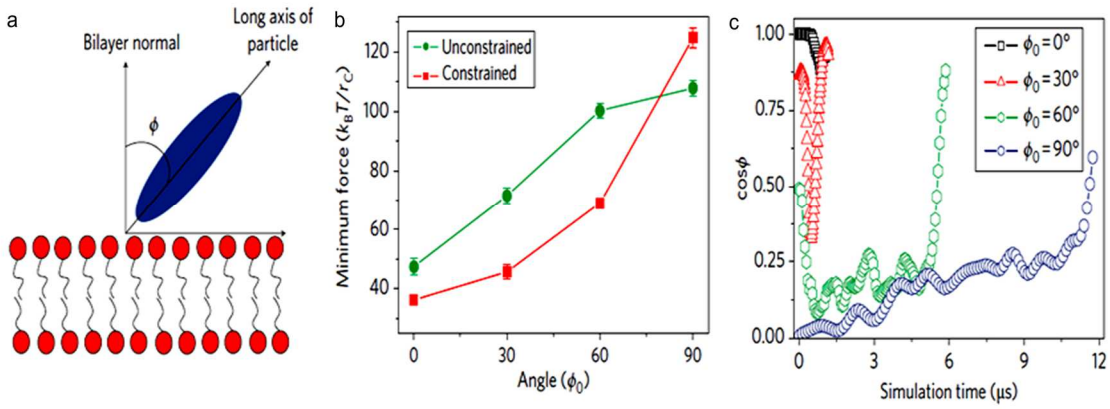


**Figure 2.6:** Particle internalization based on orientation to the membrane. a) schematic showing the angle between the long axis of the particle and the bilayer normal; b) minimum driving forces required to guide the ellipsoid with different initial orientations of the long axis through the lipid bilayer; c) time evolution of particle orientations during the ellipsoid penetration processes with different initial orientations. (Reprinted with permission from Macmillan Publishers Ltd: Nature Nanotechnology (Yang and Ma, 2010)).

Another theory was reported by Gratton and co-workers (2008b) through a study using various shaped PEG-based PRINT particles. Among different shapes investigated, nano-cylinders were internalized to a considerably larger extent than micro-cylinders and nano-cubes. The higher cell uptake was speculated due to the larger surface area allowing for more multivalent ionic interactions with the cell membrane which then undergo endocytosis and phagocytosis (Gratton *et al*., 2008b). This theory was supported by Sadeghi and co-workers (2012) who based the highest antibacterial activity of silver nano-plate nanoparticles compared to nano-spheres and nano-rods on the larger surface area that binds with the

bacterial cells, as well as by Hao and co-workers (2012) who proved that mesoporous silica long-rod nanoparticles had higher internalization and retention than spheres and short-rods. In addition, various nano-shaped particles have also shown to have diverse accumulation capabilities in different organ systems. Decuzzi and associates (2010) identified the shape-effect of silicon nanoparticles and their accumulation in specific tissue, which they evaluated from their bio-distribution data that in the lung, discoidal-shaped nanoparticles tended to internalize more than spherical, cylindrical and quasi-hemispherical nanoparticles. In the liver, cylindrical nanoparticles accumulated more than the other three shapes, discoidal-shaped nanoparticles accumulated most in the heart and discoidal and quasi-hemispherical nanoparticles had the highest internalization in the spleen tissue. These results were further corroborated by Park and co-workers (2009) who demonstrated that nano-worms had a higher tumour uptake in a fibro-sarcoma and breast cancer cell line compared with spherical nanoparticles and Devarajan and co-workers (2010) who showed preferential accumulation of irregular spherical nanoparticles in the spleen while regular spherical nanoparticles accumulated in the liver.

Contrary to the above mentioned observations that promote non-spherical nanoparticles as possessing higher internalization, we cannot deduce that spherical nanoparticles are less conducive for internalization as several studies attest to their dynamic characteristics and unmatched high surface area to volume ratio. In fact, if considering therapeutic potential of nanoparticles then spheres would be superior to non-spherical nanoparticles due to their excellent drug loading capacity. Many researchers claim hypothetical theories on the internalization kinetics based on nanoparticle shape, however, we cannot deny that all of these nanoparticles investigated do not have constant additional nanoparticle parameters, and these would also impact on the rate of cellular uptake.

### 2.3.4. Surface properties

The surface properties of nanoparticles are as fundamental as the other key characteristics that dictate internalization. For targeted drug delivery, high circulation time of nanoparticles in the body is required for the nanoparticles to recognise its specific site of interest. Opsonins adsorbing to the surface of hydrophobic nanoparticles decrease circulation time by initiating the immune response cascade which allows phagocytosis of the nanoparticles following recognition as foreign objects. If the drug is unnecessarily taken up by the RES, drug bioavailability is reduced and undesirable effects are exerted on the immune system and pose the threat of toxicity within the host (Howard and Peer, 2013; Naahidi *et al*., 2013). Nanoparticle hydrophobicity may instigate redundant interaction with plasma proteins, phagocytic internalization, immune cell stimulation and particle clearance (Dobrovolskaia

and McNeil, 2007). Minimizing the recognition of nanoparticles by the RES and subsequent immune system will enhance the probability of uptake by the target cells. Hence, recent research is focused on modifying conventional hydrophobic nanoparticle surfaces with a hydrophilic protective layer. This layer creates a cloud of chains at the nanoparticle surface to cause steric repulsive forces against plasma proteins and increase the blood circulation half-life of targeted nanocarriers as shown in Figure 2.7 (Brigger *et al*., 2002; Mohanraj and Chen, 2006; Owens and Peppas, 2006; Chiu *et al*., 2010).Hydrophilic-coated nanoparticles can be fabricated by making use of polymer types such as PEG, PEG-based copolymers and poly-vinyl pyyrolidone (PVP) (Owens and Peppas, 2006; Gomes-da-Silva *et al*., 2013).

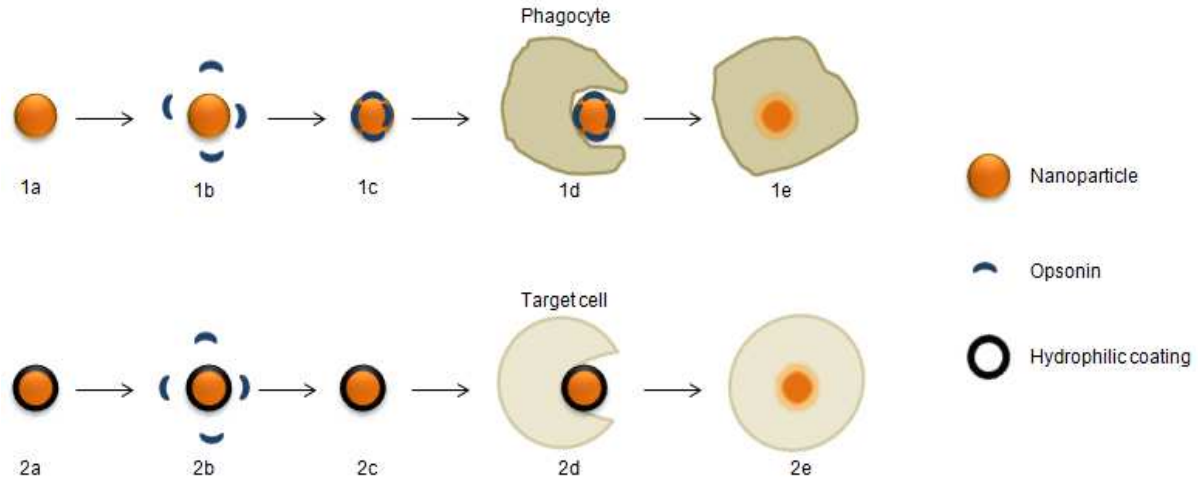


**Figure 2.7:** Pathway of uncoated hydrophobic nanoparticle: 1a) nanoparticle in blood circulation; 1b) opsonins recognise nanoparticle as foreign body due to hydrophobic surface; 1c) opsonization of nanoparticle; 1d) and 1e) phagocytosis by phagocyte and elimination of nanoparticle. Pathway of coated hydrophilic nanoparticle: 2a) hydrophilic polymer-coated nanoparticle in blood circulation; 2b) steric hindrance maintains repulsive forces between opsonins and nanoparticle; 2c) nanoparticle continues to circulate until target site reached; 2d) and 2e) endocytosis by target cell.

Physicochemical surface parameters can affect cellular uptake as reported in the recent study conducted by Loh and co-workers (2012). The study ascertained the theory of concentration-dependent chitosan molecules increasing nanoparticle transport through membranes by disrupting the integrity of intercellular tight junctions involved in paracellular transport (Sonaje *et al*., 2011).Chitosan redistributes cytoskeleton proteins such as actin and tubulin found in the apical membrane resulting in the opening of tight junctions (Sambruy *et al*., 2001). Using chitosan-coating as a surface modification for nanoparticles could optimize paracellular transport and deliver a higher amount of drug-loaded nanocarriers to the targeted site.

An interesting recent advance in research shows the coating of a polymeric nanoparticle core with red blood cell (RBC) membranes. Luk and co-workers (2014) synthesized a cloaked nanoparticle utilizing the RBC membranes to evade the immune response cascade resulting in a prolonged *in vivo* circulation time. This bio-inspired nano-system enhances the probability of nanoparticle uptake and if coupled with other nanoparticle factors to promote increased cellular uptake may prove to be yet another breakthrough drug delivery system. Therefore, modulating surface characteristics can control internalization rate, extent and even transport pathways. However, in order to achieve the desired outcome, the selection as well as manipulation of appropriate biomaterials for coating is imperative.

### 2.3.5. Proteins and ligand attachments

Cell-penetrating proteins or peptides (CPP) can increase cellular uptake of surface-modified drug-loaded nanoparticles by employing direct cell penetration or receptor-mediated endocytic pathways and localising nanoparticles at the required site (Lin *et al*., 2013; Loureiro *et al*., 2014). CPPs are small amphipathic or cationic polypeptides (10-30 amino acids long) inclusive of trans-activating (TAT) peptide, penetratin, transportan, toxins, poly-arginine and rabies virus glycoprotein (RVG) (Patel *et al*., 2007; Jones, 2008). A possible mechanism of the TAT protein is that it binds to cell surface heparin sulphate proteoglycans and is then internalized through receptor-mediated uptake (Figure 2.8).

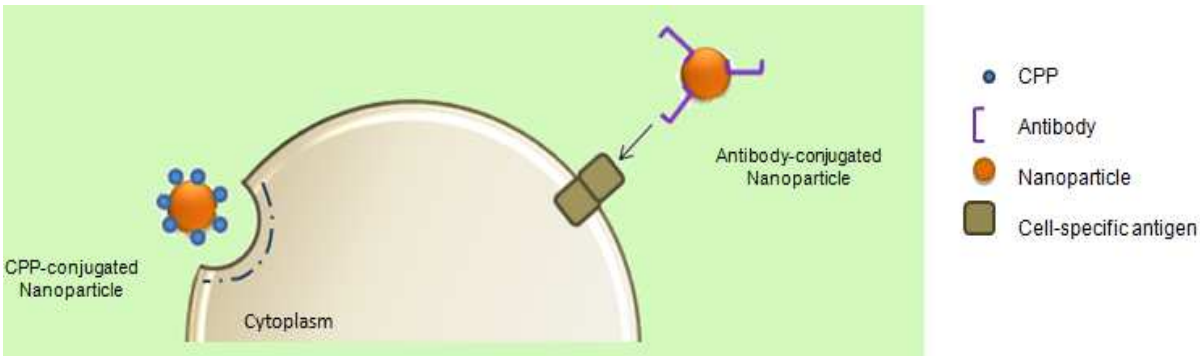


**Figure 2.8:** Stimulating endocytosis through CPP- and antibody-conjugation of nanoparticles.

Bareford and Swaan (2007) reviewed cell adhesion molecules (CAMs) which form part of the subfamily of immunoglobulins. CAMs bind to cell adhesion receptors (CARs) on cell-surfaces and stimulate clathrin-mediated uptake. Peptides such as Arg-Gly-Asp (RGD) bind to CARs and have been used extensively to promote the uptake of drug-loaded nanoparticles. Furthermore, the cationic proteins have a higher affinity to the negatively charged cell membranes which further promotes cellular internalization (des Rieux *et al*.,

2006; Bareford and Swaan, 2007). Ligands for enhanced cellular uptake include folic acid, albumin and cholesterol, which are internalized using caveolae-mediated uptake, and are common, attractive methods to stimulate spontaneous uptake through receptors (Bareford and Swaan, 2007). In contrast, Pujals and Giralt (2008) reviewed the highly improved internalization efficiency of fatty acids or silaproline, which is a hydrophobic derivative of proline-rich, amphipathic CPPs. Targeting tissue specific receptors and molecules by using antibodies has also proven to be useful for enabling internalization of drug-carriers intended for site-specific delivery. This strategy requires the conjugation of receptor-specific ligands and proteins to the nanoparticle coat. The potential for the binding to the target tissue is dependent on the abundance of the ligand and its specificity and affinity for binding to the target cell membrane (Parveen *et al*., 2012).

By targeting the monoclonal antibody to the protein aminopeptidase P (APP) in the lung, *in vivo* transport across the endothelial barrier to lung tissue occurs within seconds (Oh *et al*., 2007). Nanoparticles that are surface modified with cyclic RGD peptide binds to $\alpha_v\beta_3$ integrin receptors internalize more readily into HeLa cells than unmodified nanoparticles (Oba *et al*., 2008). This concept can be applied to tumour cells that contain specific membrane antigens where the surface of the drug-carrier is modified with the corresponding antibody for increased binding and uptake. This is experimentally shown by targeting prostate specific membrane antigen (Liu *et al*., 2009), transferrin-conjugated nanoparticles that demonstrated higher cellular uptake in a prostate cancer cell line (Sahoo *et al*., 2004), and monoclonal antibody-conjugated PLGA nanoparticles for increased tumour cell uptake (Kocbek *et al*., 2007). In contrast, quantitative and bio-distributive data from the study conducted by Huang and co-workers (2010) showed that three different ligands (single-chain variable fragment, amino terminal fragment and cyclic RGD peptide) only marginally improved gold nanoparticle accumulation in tumour tissue in comparison with non-targeted controls (Huang *et al*., 2010). Similarly, Temsamani and Vidal (2004) reviewed the construct of phosphopeptides linked with penetratin as having inhibitory effects on ligand-dependent transduction pathways in various cell lines, even though individually, these CPPs promote internalization. The use of serum protein attachments on gold nanoparticles where shown to improve their uptake half life, rate and extent (Chithrani *et al*., 2006). α- and β-globulin proteins are known to be internalized by cells and increasing the diversity of protein attachments may allow entrance into cells via the receptor-mediated pathways. However, another study reported that serum protein attachments inhibited the uptake of polyvalent gold nanoparticles, and that instead; uptake is dependent on scavenger receptors (Patel *et al*., 2010).

Taking note of the use of a cationic mixed monolayer of CPPs and PEG, Liu and co-workers (2007) proved its efficiency on internalization rates of gold nanoparticles by combining these factors. The multifunctional nanoparticles show superior uptake as compared to nanoparticles synthesized exclusive of the addition of CPP or having an anionic surface charge. Thus, drug delivery scientists have capitalized on the knowledge of receptors and ligands as targeting moieties for specific cellular organelle targeting (Bareford and Swaan, 2007; Fortier *et al*., 2014). This principle is not only applied to general cells but also can be adopted for the specific targeting to tumours for increasing the bioavailability of drug to the target site.

### 2.4. Current Advances in Transbarrier Internalization

It has been discussed how the inherent physical and chemical properties of nanoparticles such as size, shape, surface charge, solubility, surface characteristics and ligand complexes can dictate the nanoparticles degree of biocompatibility and internalization kinetics, as well as the selectivity of these factors for specific cell types. The additional key parameter for consideration in the uptake of nanoparticles is the environment the nanosystem comes into contact with (Aggarwal *et al*., 2009), and the manner in which we can engineer these parameters to trigger different biological responses (Sonaje *et al*., 2011). As discussed by Brannon-Peppas and Blanchette (2012), the size of nanoparticles for crossing biological barriers is dependent on the tissue, target site and circulation. Likewise, all other nanoparticle characteristics need to be fabricated in consideration of inherent target-tissue requirements for cellular internalization. Barrier capacity and trans-compartment transport of particles vary considerably between different tissue types (Vllasaliu *et al*., 2011). Limited transport across the epithelia is one of the prime obstacles for therapeutic agents and nanomedicines reaching the adequate biological compartment (Alonso, 2004) as barrier systems are unable to evaluate and differentiate drug delivery systems for translocation from foreign particles and therefore restrict the entry of the drug-carriers, rendering the system invaluable and reducing its efficacy.

The delivery of therapeutic agents requires successful negotiation of these barriers in order to attain a sufficient therapeutic index (Ferrari, 2010). To transverse these barriers using smart nanosystems, the development of efficient nanomedicines requires a thorough understanding of the characteristics of the body systems, biological barriers and mechanisms to evade foreign particle interactions in the body. Once the characteristics of the biological systems are defined, we can identify nanoparticle parameters that enhance trans-membrane transport or cellular uptake (Table 2.2). From the data reported in Table

2.2, it is evident that various nanosystems contributing different parameters and characteristics are able to transverse biological barriers dictated by the barrier's set of limitations and specific nanoparticle criteria for internalization.

**Table 2.2:** Overview of biological barriers and nanoparticle advances to overcome physiological limitations.

| Organ system | Barriers to Internalization | Physicochemical Nanoparticle modification | (Trans)-Epithelial transport mechanisms | Reference |
|---|---|---|---|---|
| Skin | Insoluble corneocytes and tight junctions in viable epidermis | Chemical enhancers (oleic acid, ethanol, PEG) to surface-coat | Pores, trans/inter cellular, follicular penetration | Masaoka *et al*., 2006; Kuo *et al*., 2009 |
| | | 215.2nm anionic quercetin-loaded lipid NPs | Intercellular permeation | Chen-yu *et al*., 2012 |
| | Pilosebaceous (10-70mm) and sweat glands (60-80mm) | <10nm metal maghemite NPs | Lipidic matrix, follicular penetration | Baroli *et al*., 2007 |
| | | Hydrophilic 40nm irregular, spherical PEG-b-copolymer NPs | Follicular penetration | Baroli *et al*., 2007; Shim *et al*., 2004 |
| | Intercellular lipidic matrix | 18nm hydrophobic cationic/neutral 18nm ellipsoid/spherical quantum dots | Pores, follicular penetration | Ryman-Rasmussen *et al*., 2006 |
| Blood | Complement system, phagocytosis | Heparin-complexed cerium oxide NPs for monocyte drug delivery | | Wang *et al*., 2012; Ting *et al*., 2013 |
| | White blood cells | Cell membranes contain regions of +ve and –ve charge, NPs of either charge can be internalized | | Ting *et al*., 2013 |
| Ocular | Blood-aqueous barrier | 180nm anionic sparfloxacin-loaded PLGA NPs | Nasolacrimal drainage system | Gupta *et al*., 2010; Freddo, 2013 |
| | Blood-retinal barrier | 3.46µm surfactant-complexed multilamellar acetazolamide niosomes | | Freddo, 2013; Guinedi *et al*., 2005 |
| | Precorneal tear film (3-10µm) | 161nm PEG-coated poly-ε-caprolactone nanocapsules | Transcytosis | de la Fuente *et al*., 2010 |
| Spinal cord | Blood-spinal cord barrier (BSCB) | 2-5nm cerium oxide NPs | | Mautes *et al*., 2000; Das *et al*., 2007 |
| | | Ideal properties for penetrating BSCB/astrocytic foot processes | | Mautes *et al*., 2000 |
| | Astrocytic foot processes | NP size (<50nm), cationic, hydrophilic, CPP-complexed | | Sahay *et al*., 2010; Chithrani *et al*., 2006 Ilina *et al*., 2012; Patel *et al*., 2007; Brigger *et al*., 2002 |
| Brain | BBB, blood-cerebrospinal fluid barrier | Hydrophilic PEG-coated polyhexadecylcyanoacrylate | Caveolae-mediated endocytosis | Garcia-Garcia *et al*., 2005; Costantino |

| | | | | |
|---|---|---|---|---|
| | | | | and Boraschi, 2012 |
| | | Chemical/biological/physical modulators for opening BBB | Trans/Paracellular | Hynynen, 2008; Stam, 2010 |
| | Enzymatic BBB | MAb 5C6, to CR3 receptor-a $\beta_2$-integrin present on microglia | Receptor-mediated transcytosis | Reid *et al*., 1993 |
| | | RMP-7 (bradykinin analogue)-coated 50nm NPs | | Kuo and Lee, 2012 |
| | | Polyether-copolyester dendrimers | Clathrin/caveolae-mediated uptake | Dhanikula *et al*., 2008 |
| | High transendothelial electrical resistance of 1500–2000V/cm$^2$ | Cationization of antibodies to undergo active transport | Absorptive mediated transcytosis | Reid *et al*., 1993 |
| | | Anionic, 90nm transferrin(Tf)-conjugated polymersomes | Tf Receptor-mediated transcytosis | Pang *et al*., 2011 |
| | | Anionic, ≤200nm SLNs | | Martins *et al*., 2012 |
| | | Cationic, 190-210nm nano-lipid emulsion | Caveolae-mediated end/macropinocytosis | Wen *et al*., 2011 |
| | Brain extracellular space of 38-64nm | Anionic, 154nm PLGA-NPs via inner ear administration | Pinocytosis | Thorne and Nicholson, 2006; Zhang *et al*., 2013 |
| | | 80nm $TiO_2$ NPs administered through intranasal instillation | Transcytosis | Mistry *et al*., 2009 |
| Liver | | Filo-shaped micelles with high aspect ratios and cylindrical | Clathrin/caveolae-mediated endocytosis | Geng *et al*., 2007; Decuzzi *et al*., 2010; Jacobs *et al*., 2010 |
| | Tight junctions, 5-10µm wide blood vessels (BVs) | 20nm carboxylated-polystyrene | | Johnston *et al*., 2010 |
| | | 147.2nm cationic chitosan NPs of irregular shape modified with glycyrrhizin complexation | Receptor-mediated endocytosis | Lin *et al*., 2008 |
| | Phagocytic properties of juxtaposed Kupffer cells | CPPs conjugated on <90nm cationic NPs to target AGP receptors on hepatocytes for direct drug delivery | Receptor-mediated endocytosis | Kim *et al*., 2004 |
| | | Saturating Kupffer cells with excess of drug-loaded NPs | | Jacobs *et al*., 2010 |
| | | Particles of 1-3µm evade ruffled surface of Kupffer cells | | Doshi *et al*., 2010 |
| | Protective mucin layer | Neutral, hydrophobic NPs <200nm | | Lai *et al*., 2009 |
| Oral cavity | Non-keratinized epithelia, saliva mucus, membrane coating granules of buccal mucosa | NPs entrapped within solid lozenges, chewing gum, flexible adhesive patches, and viscous liquids to coat mucosa | | Madhav *et al*., 2009; Teubl *et al*., 2013 |
| GIT | Tight junction barriers, cell composition | Coating drug-loaded NPs with bacterial invasive ligands to target M cell surface components | Receptor-mediated endocytosis | Masaoka *et al*., 2006; Kochut *et al*., 2013 |
| | Low pH gradients | pH-sensitive cationic 343nm trimethylchitosan and 212nm PLGA-PEG mannose NPs | Receptor-mediated endocytosis | Ferrari, 2010; Coco *et al*., 2013 |
| | Thick, anionic mucus layer | 154nm cationic poly-6-cationic amphiphilic cyclodextrin-DNA complex internalized by intestinal epithelial cells | Macropinocytosis | Yang *et al*., 2011; O'Neill *et al*., 2011 |

| | | | | |
|---|---|---|---|---|
| | Macrophages | Hydrophobic, neutral aminated NPs | Transcytosis | des Rieux *et al*., 2005 |
| Lungs | | 15-100nm gold NPs | Transcytosis | Brandenberger *et al*., 2010 |
| | Alveolar-capillary barrier, complex tight junctions | Commercial multi-walled carbon-NTs disrupt tight junctions | Paracellular | Rotoli *et al*., 2008 |
| | | Hydrophilic, surfactant-coated, enzymatic 20nm PEI-PLGA NPs in 1.6µm microgel | | Wanakule *et al*., 2012 |
| | | Discoidal-shaped NPs | | Decuzzi *et al*., 2010 |
| | Alveolar lining fluid | 200nm NPs complexed with Fc portion of IgG | Receptor-mediated endocytosis | Vllasaliu *et al*., 2012 |
| | Macrophages | 235nm protein-based NPs (serum albumin and transferrin) | Receptor-mediated transcytosis | Brzoska *et al*., 2004; Wanakule *et al*., 2012 |
| Kidney | 200-300nm thick glycocalyx layer | 78-100nm spherical PLGA NPs | Caveolae-mediated endocytosis | Haraldsson *et al*., 2008; He *et al*., 2013 |
| | Phagocytic mesangial cells | Albumin/streptavidin as ligands targeting renal tubular cells | Receptor-mediated endocytosis | Kocbek *et al*., 2007; Kerr *et al*., 2009; Roger *et al*., 2009 |
| | Cationic decomplexation | Anionic derivatives carboxylated, co-dimethyl maleic acid, acetylated low molecular weight chitosan or PVP as NP coating | Receptor-mediated endocytosis | Kodaira *et al*., 2004; Yamamoto *et al*., 2004 Yuan *et al*., 2008 |

## 2.5. Concluding Remarks

The scope for further research into this concept has immense potential to progress medical care by decreasing side effect profiles due to specific and targeted drug release, improving bioavailability and bypassing first pass metabolism. The use of sophisticated nanomedicines as effective vectors of drugs exerts beneficial effects at the molecular level providing targeted drug delivery. The forefront of nanomedicine research comprises diagnosis, treatment, monitoring and management of biological conditions. Independently, nanotechnology has surfaced as one of the most successful drug delivery concepts to date and it is obvious that applications for biomedical nanotechnology are broad. This review encompasses possible techniques of nanoparticle manipulation to furthermore improve intracellular delivery of drugs. The benefits of enhanced cellular internalization have been extensively motivated and the scope for further research in this domain is constant. Therapeutic advantages can be demonstrated by increasing nanoparticle cellular uptake, targeting site-specific organ systems by increasing selectivity and even altering the drug release kinetics of the nanosystem and bio-distribution. Taking this concept into consideration also allows for a single nanoparticle of ideal characteristics to encapsulate

several drugs for delivery to enhance efficacy and possibly reduce resistance. Furthermore, the diversity of nanoparticle parameters with regards to targeting ligands can be studied thoroughly to assist with the internalization of macromolecule drugs that primarily have difficulty penetrating the cell membrane.

Apart from cellular internalization, focus has been placed on nuclear targeting via a nuclear localization signal (NLS) (Tkachenko *et al*., 2003; Chen *et al*., 2009; Narayanan *et al*., 2013). At a complex level, drug delivery targeting intracellular organelles post cellular internalization may prove to be a research area of high interest. Included in this paradigm is the possibility of the multistage drug targeting of nanoparticles from bypassing the cellular membrane to organelle level of therapeutics. By combining many physicochemical and mechanical nanoparticle parameters specific to certain cells types or organ systems, an optimal level of cellular uptake can be achieved. Research proves several nanoparticle characteristics that are pertinent for efficient internalization; however it is immensely limited on more detailed trans-barrier uptake kinetics that would crucially improve nanoparticle efficacy and intracellular targeting while maintaining stability and non-toxicity. Nano drug-carriers can be greatly exploited provided *ex vivo* and *in vivo* research is extensively conducted.

Pertinent to the above mentioned nanoparticle factors, we need to understand that by optimizing nanoparticle parameters and characteristics that support internalization theories and studies for enhanced intracellular delivery, these designed systems may not promote optimal drug entrapment or have adequate drug release. The issue of drug delivery design can be addressed but other *in vivo* requirements such as adequate clearance from systemic circulation, release of drugs from non-targeted sites, drug release from the nanosystem and elimination of the nanocarrier from the body need to be adhered to. As the knowledge of physico-chemical and physiological *in vivo* processes improves, nanomedicine can be further specialised to attain the absolute effect intended.

### 2.6. References


Acosta, E., 2009. Bioavailability of nanoparticles in nutrient and nutraceutical delivery. *Current opinion in colloid & interface science*, *14*(1), pp.3-15.

Aggarwal, P., Hall, J.B., McLeland, C.B., Dobrovolskaia, M.A. and McNeil, S.E., 2009. Nanoparticle interaction with plasma proteins as it relates to particle biodistribution, biocompatibility and therapeutic efficacy. *Advanced drug delivery reviews*, *61*(6), pp.428-437.

Alonso, M.J., 2004. Nanomedicines for overcoming biological barriers. *Biomedicine & Pharmacotherapy*, *58*(3), pp.168-172.

Awaad, A., Nakamura, M. and Ishimura, K., 2012. Imaging of size-dependent uptake and identification of novel pathways in mouse Peyer's patches using fluorescent organosilica particles. *Nanomedicine: Nanotechnology, Biology and Medicine*, *8*(5), pp.627-636.

Bareford, L.M. and Swaan, P.W., 2007. Endocytic mechanisms for targeted drug delivery. *Advanced drug delivery reviews*, *59*(8), pp.748-758.

Baroli, B., Ennas, M.G., Loffredo, F., Isola, M., Pinna, R. and López-Quintela, M.A., 2007. Penetration of metallic nanoparticles in human full-thickness skin. *Journal of Investigative Dermatology*, *127*(7), pp.1701-1712.

Barua, S. and Rege, K., 2009. Cancer-Cell-Phenotype-Dependent Differential Intracellular Trafficking of Unconjugated Quantum Dots. *Small*, *5*(3), pp.370-376.

Bertrand, N. and Leroux, J.C., 2012. The journey of a drug-carrier in the body: an anatomo-physiological perspective. *Journal of Controlled Release*, *161*(2), pp.152-163.

Bornsel, M., Prydz, K., Parton, R.G., Gruenberg, J. and Simons, K., 1989. Endocytosis in filter-grown Madin-Darby canine kidney cells. *The Journal of cell biology*, *109*(6 Pt 2), pp.3243-3258.

Brandenberger, C., Rothen-Rutishauser, B., Mühlfeld, C., Schmid, O., Ferron, G.A., Maier, K.L., Gehr, P. and Lenz, A.G., 2010. Effects and uptake of gold nanoparticles deposited at the air–liquid interface of a human epithelial airway model. *Toxicology and applied pharmacology*, *242*(1), pp.56-65.

Brannon-Peppas, L. and Blanchette, J.O., 2012. Nanoparticle and targeted systems for cancer therapy. *Advanced drug delivery reviews*, *64*, pp.206-212.

Brigger, I., Dubernet, C. and Couvreur, P., 2002. Nanoparticles in cancer therapy and diagnosis. *Advanced drug delivery reviews*, *54*(5), pp.631-651.

Brzoska, M., Langer, K., Coester, C., Loitsch, S., Wagner, T.O.F. and Mallinckrodt, C.V., 2004. Incorporation of biodegradable nanoparticles into human airway epithelium cells—in vitro study of the suitability as a vehicle for drug or gene delivery in pulmonary diseases. *Biochemical and biophysical research communications*, *318*(2), pp.562-570.

Champion, J.A. and Mitragotri, S., 2006. Role of target geometry in phagocytosis. *Proceedings of the National Academy of Sciences of the United States of America*, *103*(13), pp.4930-4934.

Champion, J.A., Katare, Y.K. and Mitragotri, S., 2007. Making polymeric micro-and nanoparticles of complex shapes. *Proceedings of the National Academy of Sciences*, *104*(29), pp.11901-11904.

Chen, J., Wu, C. and Oupicky, D., 2009. Bioreducible hyperbranched poly (amido amine) s for gene delivery. *Biomacromolecules*, *10*(10), pp.2921-2927.

Chen-yu, G., Chun-fen, Y., Qi-lu, L., Qi, T., Yan-wei, X., Wei-na, L. and Guang-xi, Z., 2012. Development of a quercetin-loaded nanostructured lipid carrier formulation for topical delivery. *International journal of pharmaceutics*, *430*(1), pp.292-298.

Chithrani, B.D., Ghazani, A.A. and Chan, W.C., 2006. Determining the size and shape dependence of gold nanoparticle uptake into mammalian cells. *Nano letters*, *6*(4), pp.662-668.

Chiu, Y.L., Ho, Y.C., Chen, Y.M., Peng, S.F., Ke, C.J., Chen, K.J., Mi, F.L. and Sung, H.W., 2010. The characteristics, cellular uptake and intracellular trafficking of nanoparticles made of hydrophobically-modified chitosan. *Journal of Controlled Release*, *146*(1), pp.152-159.

Christensen, E.I., Verroust, P.J. and Nielsen, R., 2009. Receptor-mediated endocytosis in renal proximal tubule. *Pflügers Archiv-European Journal of Physiology*, *458*(6), pp.1039-1048.

Coco, R., Plapied, L., Pourcelle, V., Jérôme, C., Brayden, D.J., Schneider, Y.J. and Préat, V., 2013. Drug delivery to inflamed colon by nanoparticles: comparison of different strategies. *International journal of pharmaceutics*, *440*(1), pp.3-12.

Costantino, L. and Boraschi, D., 2012. Is there a clinical future for polymeric nanoparticles as brain-targeting drug delivery agents?. *Drug discovery today*, *17*(7), pp.367-378.

Das, M., Patil, S., Bhargava, N., Kang, J.F., Riedel, L.M., Seal, S. and Hickman, J.J., 2007. Auto-catalytic ceria nanoparticles offer neuroprotection to adult rat spinal cord neurons. *Biomaterials*, *28*(10), pp.1918-1925.

de la Fuente, M., Raviña, M., Paolicelli, P., Sanchez, A., Seijo, B. and Alonso, M.J., 2010. Chitosan-based nanostructures: a delivery platform for ocular therapeutics. *Advanced drug delivery reviews*, *62*(1), pp.100-117.

Decuzzi, P., Godin, B., Tanaka, T., Lee, S.Y., Chiappini, C., Liu, X. and Ferrari, M., 2010. Size and shape effects in the biodistribution of intravascularly injected particles. *Journal of Controlled Release*, *141*(3), pp.320-327.

des Rieux, A., Fievez, V., Garinot, M., Schneider, Y.J. and Préat, V., 2006. Nanoparticles as potential oral delivery systems of proteins and vaccines: a mechanistic approach. *Journal of controlled release*, *116*(1), pp.1-27.

des Rieux, A., Ragnarsson, E.G., Gullberg, E., Préat, V., Schneider, Y.J. and Artursson, P., 2005. Transport of nanoparticles across an in vitro model of the human intestinal follicle associated epithelium. *European Journal of Pharmaceutical Sciences*, *25*(4), pp.455-465.

Devarajan, P.V., Jindal, A.B., Patil, R.R., Mulla, F., Gaikwad, R.V. and Samad, A., 2010. Particle shape: a new design parameter for passive targeting in splenotropic drug delivery. *Journal of pharmaceutical sciences*, *99*(6), pp.2576-2581.

Dhanikula, R.S., Argaw, A., Bouchard, J.F. and Hildgen, P., 2008. Methotrexate loaded polyether-copolyester dendrimers for the treatment of gliomas: enhanced efficacy and intratumoral transport capability. *Molecular Pharmaceutics*, *5*(1), pp.105-116.

Dobrovolskaia, M.A. and McNeil, S.E., 2007. Immunological properties of engineered nanomaterials. *Nature nanotechnology*, *2*(8), pp.469-478.

Doshi, N. and Mitragotri, S., 2010. Macrophages recognize size and shape of their targets. *PloS one*, *5*(4), p.e10051.

Ferrari, M., 2010. Frontiers in cancer nanomedicine: directing mass transport through biological barriers. *Trends in biotechnology*, *28*(4), pp.181-188.

Ferrati, S., McConnell, K.I., Mack, A.C., Sirisaengtaksin, N., Diaz, R., Bean, A.J., Ferrari, M. and Serda, R.E., 2014. Cellular communication via nanoparticle-transporting biovesicles. *Nanomedicine*, *9*(5), pp.581-592.

Fortier, C., Durocher, Y. and De Crescenzo, G., 2014. Surface modification of nonviral nanocarriers for enhanced gene delivery. *Nanomedicine*, *9*(1), pp.135-151.

Freddo, T.F., 2013. A contemporary concept of the blood–aqueous barrier. *Progress in retinal and eye research*, *32*, pp.181-195.

Garcia-Garcia, E., Andrieux, K., Gil, S., Kim, H.R., Le Doan, T., Desmaële, D., d'Angelo, J., Taran, F., Georgin, D. and Couvreur, P., 2005. A methodology to study intracellular distribution of nanoparticles in brain endothelial cells. *International journal of pharmaceutics*, *298*(2), pp.310-314.

Geng, Y.A.N., Dalhaimer, P., Cai, S., Tsai, R., Tewari, M., Minko, T. and Discher, D.E., 2007. Shape effects of filaments versus spherical particles in flow and drug delivery. *Nature nanotechnology*, *2*(4), pp.249-255.

Gomes-da-Silva, L.C., Fernández, Y., Abasolo, I., Schwartz Jr, S., Ramalho, J.S., Pedroso de Lima, M.C., Simões, S. and Moreira, J.N., 2013. Efficient intracellular delivery of siRNA with a safe multitargeted lipid-based nanoplatform. *Nanomedicine*, *8*(9), pp.1397-1413.

Gonzalez-Mariscal, L., Hernández, S. and Vega, J., 2008. Inventions designed to enhance drug delivery across epithelial and endothelial cells through the paracellular pathway. *Recent patents on drug delivery & formulation*, *2*(2), pp.145-176.

Gratton, S.E., Napier, M.E., Ropp, P.A., Tian, S. and DeSimone, J.M., 2008a. Microfabricated particles for engineered drug therapies: elucidation into the mechanisms of cellular internalization of PRINT particles. *Pharmaceutical research*, *25*(12), pp.2845-2852.

Gratton, S.E., Ropp, P.A., Pohlhaus, P.D., Luft, J.C., Madden, V.J., Napier, M.E. and DeSimone, J.M., 2008b. The effect of particle design on cellular internalization pathways. *Proceedings of the National Academy of Sciences*, *105*(33), pp.11613-11618.

Groves, E., Dart, A.E., Covarelli, V. and Caron, E., 2008. Molecular mechanisms of phagocytic uptake in mammalian cells. *Cellular and molecular life sciences*, *65*(13), pp.1957-1976.

Guinedi, A.S., Mortada, N.D., Mansour, S. and Hathout, R.M., 2005. Preparation and evaluation of reverse-phase evaporation and multilamellar niosomes as ophthalmic carriers of acetazolamide. *International Journal of Pharmaceutics*, *306*(1), pp.71-82.

Gunaseelan, S., Gunaseelan, K., Deshmukh, M., Zhang, X. and Sinko, P.J., 2010. Surface modifications of nanocarriers for effective intracellular delivery of anti-HIV drugs. *Advanced drug delivery reviews*, *62*(4), pp.518-531.

Gupta, H., Aqil, M., Khar, R.K., Ali, A., Bhatnagar, A. and Mittal, G., 2010. Sparfloxacin-loaded PLGA nanoparticles for sustained ocular drug delivery. *Nanomedicine: nanotechnology, biology and medicine*, *6*(2), pp.324-333.

Han, Y., Alsayed, A.M., Nobili, M., Zhang, J., Lubensky, T.C. and Yodh, A.G., 2006. Brownian motion of an ellipsoid. *Science*, *314*(5799), pp.626-630.

Hao, N., Li, L., Zhang, Q., Huang, X., Meng, X., Zhang, Y., Chen, D., Tang, F. and Li, L., 2012. The shape effect of PEGylated mesoporous silica nanoparticles on cellular uptake pathway in Hela cells. *Microporous and Mesoporous Materials*, *162*, pp.14-23.

Haraldsson, B., Nyström, J. and Deen, W.M., 2008. Properties of the glomerular barrier and mechanisms of proteinuria. *Physiological reviews*, *88*(2), pp.451-487.

Harush-Frenkel, O., Rozentur, E., Benita, S. and Altschuler, Y., 2008. Surface charge of nanoparticles determines their endocytic and transcytotic pathway in polarized MDCK cells. *Biomacromolecules*, *9*(2), pp.435-443.

Hayashi, M., Tomita, M. and Awazu, S., 1997. Transcellular and paracellular contribution to transport processes in the colorectal route. *Advanced drug delivery reviews*, *28*(2), pp.191-204.

He, B., Jia, Z., Du, W., Yu, C., Fan, Y., Dai, W., Yuan, L., Zhang, H., Wang, X., Wang, J. and Zhang, X., 2013. The transport pathways of polymer nanoparticles in MDCK epithelial cells. *Biomaterials*, *34*(17), pp.4309-4326.

Hillaireau, H. and Couvreur, P., 2009. Nanocarriers' entry into the cell: relevance to drug delivery. *Cellular and Molecular Life Sciences*, *66*(17), pp.2873-2896.

Howard, K.A. and Peer, D., 2013. Providing the full picture: a mandate for standardizing nanoparticle-based drug delivery. *Nanomedicine*, *8*(7), pp.1031-1033.

Huang, X., Peng, X., Wang, Y., Wang, Y., Shin, D.M., El-Sayed, M.A. and Nie, S., 2010. A reexamination of active and passive tumor targeting by using rod-shaped gold nanocrystals and covalently conjugated peptide ligands. *ACS nano*, *4*(10), pp.5887-5896.

Hynynen, K., 2008. Ultrasound for drug and gene delivery to the brain. *Advanced drug delivery reviews*, *60*(10), pp.1209-1217.

Ilina, P., Hyvonen, Z., Saura, M., Sandvig, K., Yliperttula, M. and Ruponen, M., 2012. Genetic blockage of endocytic pathways reveals differences in the intracellular processing of non-viral gene delivery systems. *Journal of controlled release*, *163*(3), pp.385-395.

Jacobs, F., Wisse, E. and De Geest, B., 2010. The role of liver sinusoidal cells in hepatocyte-directed gene transfer. *The American journal of pathology*, *176*(1), pp.14-21.

Jallouli, Y., Paillard, A., Chang, J., Sevin, E. and Betbeder, D., 2007. Influence of surface charge and inner composition of porous nanoparticles to cross blood–brain barrier in vitro. *International journal of pharmaceutics*, *344*(1), pp.103-109.

Jin, H., Heller, D.A., Sharma, R. and Strano, M.S., 2009. Size-dependent cellular uptake and expulsion of single-walled carbon nanotubes: single particle tracking and a generic uptake model for nanoparticles. *Acs Nano*, *3*(1), pp.149-158.

Johnston, H.J., Semmler-Behnke, M., Brown, D.M., Kreyling, W., Tran, L. and Stone, V., 2010. Evaluating the uptake and intracellular fate of polystyrene nanoparticles by primary and hepatocyte cell lines in vitro. *Toxicology and applied pharmacology*, *242*(1), pp.66-78.

Jones, A.T., 2008. Gateways and tools for drug delivery: endocytic pathways and the cellular dynamics of cell penetrating peptides. *International journal of pharmaceutics*, *354*(1), pp.34-38.

Karlsson, J., Ungell, A.L., Gråsjö, J. and Artursson, P., 1999. Paracellular drug transport across intestinal epithelia: influence of charge and induced water flux. *European journal of pharmaceutical sciences*, *9*(1), pp.47-56.

Kerr, M.C. and Teasdale, R.D., 2009. Defining macropinocytosis. *Traffic*, *10*(4), pp.364-371.

Kim, T.H., Park, I.K., Nah, J.W., Choi, Y.J. and Cho, C.S., 2004. Galactosylated chitosan/DNA nanoparticles prepared using water-soluble chitosan as a gene carrier. *Biomaterials*, *25*(17), pp.3783-3792.

Kocbek, P., Obermajer, N., Cegnar, M., Kos, J. and Kristl, J., 2007. Targeting cancer cells using PLGA nanoparticles surface modified with monoclonal antibody. *Journal of Controlled Release*, *120*(1), pp.18-26.

Kochut, A. and Dersch, P., 2013. Bacterial invasion factors: Tools for crossing biological barriers and drug delivery?. *European Journal of Pharmaceutics and Biopharmaceutics*, *84*(2), pp.242-250.

Kodaira, H., Tsutsumi, Y., Yoshioka, Y., Kamada, H., Kaneda, Y., Yamamoto, Y., Tsunoda, S.I., Okamoto, T., Mukai, Y., Shibata, H. and Nakagawa, S., 2004. The targeting of anionized polyvinylpyrrolidone to the renal system. *Biomaterials*, *25*(18), pp.4309-4315.

Kumari, A., Yadav, S.K. and Yadav, S.C., 2010a. Biodegradable polymeric nanoparticles based drug delivery systems. *Colloids and Surfaces B: Biointerfaces*, *75*(1), pp.1-18.

Kumari, S., Swetha, M.G. and Mayor, S., 2010b. Endocytosis unplugged: multiple ways to enter the cell. *Cell research*, *20*(3), pp.256-275.

Kuo, T.R., Wu, C.L., Hsu, C.T., Lo, W., Chiang, S.J., Lin, S.J., Dong, C.Y. and Chen, C.C., 2009. Chemical enhancer induced changes in the mechanisms of transdermal delivery of zinc oxide nanoparticles. *Biomaterials*, *30*(16), pp.3002-3008.

Kuo, Y.C. and Lee, C.L., 2012. Methylmethacrylate–sulfopropylmethacrylate nanoparticles with surface RMP-7 for targeting delivery of antiretroviral drugs across the blood–brain barrier. *Colloids and Surfaces B: Biointerfaces*, *90*, pp.75-82.

Lai, S.K., Wang, Y.Y. and Hanes, J., 2009. Mucus-penetrating nanoparticles for drug and gene delivery to mucosal tissues. *Advanced drug delivery reviews*, *61*(2), pp.158-171.

Lin, A., Liu, Y., Huang, Y., Sun, J., Wu, Z., Zhang, X. and Ping, Q., 2008. Glycyrrhizin surface-modified chitosan nanoparticles for hepatocyte-targeted delivery. *International journal of pharmaceutics*, *359*(1), pp.247-253.

Lin, I.C., Liang, M., Liu, T.Y., Monteiro, M.J. and Toth, I., 2012. Cellular transport pathways of polymer coated gold nanoparticles. *Nanomedicine: Nanotechnology, Biology and Medicine*, *8*(1), pp.8-11.

Lin, T.Y., Li, Y.P., Zhang, H., Luo, J., Goodwin, N., Gao, T., de Vere White, R., Lam, K.S. and Pan, C.X., 2013. Tumor-targeting multifunctional micelles for imaging and chemotherapy of advanced bladder cancer. *Nanomedicine*, *8*(8), pp.1239-1251.

Liu, J., Kopečková, P., Bühler, P., Wolf, P., Pan, H., Bauer, H., Elsässer-Beile, U. and Kopecek, J., 2009. Biorecognition and Subcellular Trafficking of HPMA Copolymer−Anti-PSMA Antibody Conjugates by Prostate Cancer Cells. *Molecular pharmaceutics*, *6*(3), pp.959-970.

Liu, Y., Shipton, M.K., Ryan, J., Kaufman, E.D., Franzen, S. and Feldheim, D.L., 2007. Synthesis, stability, and cellular internalization of gold nanoparticles containing mixed

peptide− poly (ethylene glycol) monolayers. *Analytical chemistry*, *79*(6), pp.2221-2229.

Loh, J.W., Saunders, M. and Lim, L.Y., 2012. Cytotoxicity of monodispersed chitosan nanoparticles against the Caco-2 cells. *Toxicology and applied pharmacology*, *262*(3), pp.273-282.

Loureiro, J.A., Gomes, B., Coelho, M.A., Carmo Pereira, M.D. and Rocha, S., 2014. Targeting nanoparticles across the blood–brain barrier with monoclonal antibodies. *Nanomedicine*, *9*(5), pp.709-722.

Lu, W., Xiong, C., Zhang, R., Shi, L., Huang, M., Zhang, G., Song, S., Huang, Q., Liu, G.Y. and Li, C., 2012. Receptor-mediated transcytosis: a mechanism for active extravascular transport of nanoparticles in solid tumors. *Journal of controlled release*, *161*(3), pp.959-966.

Luk, B.T., Hu, C.M.J., Fang, R.H., Dehaini, D., Carpenter, C., Gao, W. and Zhang, L., 2014. Interfacial interactions between natural RBC membranes and synthetic polymeric nanoparticles. *Nanoscale*, *6*(5), pp.2730-2737.

Luo, Y., Chen, D., Ren, L., Zhao, X. and Qin, J., 2006. Solid lipid nanoparticles for enhancing vinpocetine's oral bioavailability. *Journal of controlled release*, *114*(1), pp.53-59.

Madhav, N.S., Shakya, A.K., Shakya, P. and Singh, K., 2009. Orotransmucosal drug delivery systems: a review. *Journal of controlled release*, *140*(1), pp.2-11.

Martins, S., Tho, I., Reimold, I., Fricker, G., Souto, E., Ferreira, D. and Brandl, M., 2012. Brain delivery of camptothecin by means of solid lipid nanoparticles: formulation design, in vitro and in vivo studies. *International journal of pharmaceutics*, *439*(1), pp.49-62.

Masaoka, Y., Tanaka, Y., Kataoka, M., Sakuma, S. and Yamashita, S., 2006. Site of drug absorption after oral administration: assessment of membrane permeability and luminal concentration of drugs in each segment of gastrointestinal tract. *European journal of pharmaceutical sciences*, *29*(3), pp.240-250.

Mautes, A.E., Weinzierl, M.R., Donovan, F. and Noble, L.J., 2000. Vascular events after spinal cord injury: contribution to secondary pathogenesis. *Physical therapy*, *80*(7), p.673.

Mistry, A., Stolnik, S. and Illum, L., 2009. Nanoparticles for direct nose-to-brain delivery of drugs. *International journal of pharmaceutics*, *379*(1), pp.146-157.

Moghimi, S.M., Hunter, A.C. and Andresen, T.L., 2012. Factors controlling nanoparticle pharmacokinetics: an integrated analysis and perspective. *Annual review of pharmacology and toxicology*, *52*, pp.481-503.

Mohanraj, V.J. and Chen, Y., 2006. Nanoparticles - A Review. *Tropical Journal of Pharmaceutical Research*, 5(1), PP. 561-573.

Mostov, K.E., 1994. Transepithelial transport of immunoglobulins. *Annual review of immunology*, *12*(1), pp.63-84.

Mousavi, S.A., Malerød, L., Trond, B.E.R.G. and Kjeken, R., 2004. Clathrin-dependent endocytosis. *Biochemical Journal*, *377*(1), pp.1-16.

Muthu, M.S. and Singh, S., 2008. Studies on biodegradable polymeric nanoparticles of risperidone: in vitro and in vivo evaluation. *Nanomedicine*, *3*(3), pp.305-319.

Naahidi, S., Jafari, M., Edalat, F., Raymond, K., Khademhosseini, A. and Chen, P., 2013. Biocompatibility of engineered nanoparticles for drug delivery. *Journal of controlled release*, *166*(2), pp.182-194.

Nan, A., Bai, X., Son, S.J., Lee, S.B. and Ghandehari, H., 2008. Cellular uptake and cytotoxicity of silica nanotubes. *Nano letters*, *8*(8), pp.2150-2154.

Narayanan, K., Yen, S.K., Dou, Q., Padmanabhan, P., Sudhaharan, T., Ahmed, S., Ying, J.Y. and Selvan, S.T., 2013. Mimicking cellular transport mechanism in stem cells through endosomal escape of new peptide-coated quantum dots. *Scientific reports*, *3*, p.2184.

Nicolete, R., dos Santos, D.F. and Faccioli, L.H., 2011. The uptake of PLGA micro or nanoparticles by macrophages provokes distinct in vitro inflammatory response. *International immunopharmacology*, *11*(10), pp.1557-1563.

O'Neill, M.J., Guo, J., Byrne, C., Darcy, R. and O'Driscoll, C.M., 2011. Mechanistic studies on the uptake and intracellular trafficking of novel cyclodextrin transfection complexes by intestinal epithelial cells. *International journal of pharmaceutics*, *413*(1), pp.174-183.

Oba, M., Aoyagi, K., Miyata, K., Matsumoto, Y., Itaka, K., Nishiyama, N., Yamasaki, Y., Koyama, H. and Kataoka, K., 2008. Polyplex micelles with cyclic RGD peptide ligands and disulfide cross-links directing to the enhanced transfection via controlled intracellular trafficking. *Molecular pharmaceutics*, *5*(6), pp.1080-1092.

Oh, P., Borgström, P., Witkiewicz, H., Li, Y., Borgström, B.J., Chrastina, A., Iwata, K., Zinn, K.R., Baldwin, R., Testa, J.E. and Schnitzer, J.E., 2007. Live dynamic imaging of caveolae pumping targeted antibody rapidly and specifically across endothelium in the lung. *Nature biotechnology*, *25*(3), pp.327-337.

Owens, D.E. and Peppas, N.A., 2006. Opsonization, biodistribution, and pharmacokinetics of polymeric nanoparticles. *International journal of pharmaceutics*, *307*(1), pp.93-102.

Pang, Z., Gao, H., Yu, Y., Chen, J., Guo, L., Ren, J., Wen, Z., Su, J. and Jiang, X., 2011. Brain delivery and cellular internalization mechanisms for transferrin conjugated biodegradable polymersomes. *International journal of pharmaceutics*, *415*(1), pp.284-292.

Park, H. and Cox, D., 2009. Cdc42 regulates Fcγ receptor-mediated phagocytosis through the activation and phosphorylation of Wiskott-Aldrich syndrome protein (WASP) and neural-WASP. *Molecular biology of the cell*, *20*(21), pp.4500-4508.

Park, J.H., von Maltzahn, G., Zhang, L., Derfus, A.M., Simberg, D., Harris, T.J., Ruoslahti, E., Bhatia, S.N. and Sailor, M.J., 2009. Systematic surface engineering of magnetic nanoworms for in vivo tumor targeting. *small*, *5*(6), pp.694-700.

Parveen, S., Misra, R. and Sahoo, S.K., 2012. Nanoparticles: a boon to drug delivery, therapeutics, diagnostics and imaging. *Nanomedicine: Nanotechnology, Biology and Medicine*, *8*(2), pp.147-166.

Patel, L.N., Zaro, J.L. and Shen, W.C., 2007. Cell penetrating peptides: intracellular pathways and pharmaceutical perspectives. *Pharmaceutical research*, *24*(11), pp.1977-1992.

Patel, N.R., Damann, K., Leonardi, C. and Sabliov, C.M., 2011. Size dependency of PLGA-nanoparticle uptake and antifungal activity against Aspergillus flavus. *Nanomedicine*, *6*(8), pp.1381-1395.

Patel, P.C., Giljohann, D.A., Daniel, W.L., Zheng, D., Prigodich, A.E. and Mirkin, C.A., 2010. Scavenger receptors mediate cellular uptake of polyvalent oligonucleotide-functionalized gold nanoparticles. *Bioconjugate chemistry*, *21*(12), pp.2250-2256.

Pelkmans, L., Püntener, D. and Helenius, A., 2002. Local actin polymerization and dynamin recruitment in SV40-induced internalization of caveolae. *Science*, *296*(5567), pp.535-539.

Pujals, S. and Giralt, E., 2008. Proline-rich, amphipathic cell-penetrating peptides. *Advanced drug delivery reviews*, *60*(4), pp.473-484.

Rand, R.P., 1981. Interacting phospholipid bilayers: measured forces and induced structural changes. *Annual review of biophysics and bioengineering*, *10*(1), pp.277-314.

Reddy, S.T., Berk, D.A., Jain, R.K. and Swartz, M.A., 2006. A sensitive in vivo model for quantifying interstitial convective transport of injected macromolecules and nanoparticles. *Journal of applied physiology*, *101*(4), pp.1162-1169.

Reid, D.M., Perry, V.H., Andersson, P.B. and Gordon, S., 1993. Mitosis and apoptosis of microgliain vivo induced by an anti-CR3 antibody which crosses the blood-brain barrier. *Neuroscience*, *56*(3), pp.529-533.

Roger, E., Lagarce, F., Garcion, E. and Benoit, J.P., 2009. Lipid nanocarriers improve paclitaxel transport throughout human intestinal epithelial cells by using vesicle-mediated transcytosis. *Journal of Controlled Release*, *140*(2), pp.174-181.

Rotoli, B.M., Bussolati, O., Bianchi, M.G., Barilli, A., Balasubramanian, C., Bellucci, S. and Bergamaschi, E., 2008. Non-functionalized multi-walled carbon nanotubes alter the paracellular permeability of human airway epithelial cells. *Toxicology letters*, *178*(2), pp.95-102.

Ryman-Rasmussen, J.P., Riviere, J.E. and Monteiro-Riviere, N.A., 2006. Penetration of intact skin by quantum dots with diverse physicochemical properties. *Toxicological Sciences*, *91*(1), pp.159-165.

Sadeghi, B., Garmaroudi, F.S., Hashemi, M., Nezhad, H.R., Nasrollahi, A., Ardalan, S. and Ardalan, S., 2012. Comparison of the anti-bacterial activity on the nanosilver shapes: nanoparticles, nanorods and nanoplates. *Advanced Powder Technology*, *23*(1), pp.22-26.

Sahay, G., Alakhova, D.Y. and Kabanov, A.V., 2010. Endocytosis of nanomedicines. *Journal of controlled release*, *145*(3), pp.182-195.

Sahoo, S.K., Ma, W. and Labhasetwar, V., 2004. Efficacy of transferrin-conjugated paclitaxel-loaded nanoparticles in a murine model of prostate cancer. *International journal of cancer*, *112*(2), pp.335-340.

Salamat-Miller, N. and Johnston, T.P., 2005. Current strategies used to enhance the paracellular transport of therapeutic polypeptides across the intestinal epithelium. *International journal of pharmaceutics*, *294*(1), pp.201-216.

Sambruy, Y., Ferruzza, S., Ranaldi, G., De Angelis, I., 2001. Intestinal Cell Culture Models. *Cell Biology and Toxicol*ogy, 21, pp.1–26.

Shim, J., Kang, H.S., Park, W.S., Han, S.H., Kim, J. and Chang, I.S., 2004. Transdermal delivery of mixnoxidil with block copolymer nanoparticles. *Journal of Controlled Release*, *97*(3), pp.477-484.

Snijder, B., Sacher, R., Rämö, P., Damm, E.M., Liberali, P. and Pelkmans, L., 2009. Population context determines cell-to-cell variability in endocytosis and virus infection. *Nature*, *461*(7263), pp.520-523.

Sonaje, K., Lin, K.J., Tseng, M.T., Wey, S.P., Su, F.Y., Chuang, E.Y., Hsu, C.W., Chen, C.T. and Sung, H.W., 2011. Effects of chitosan-nanoparticle-mediated tight junction opening on the oral absorption of endotoxins. *Biomaterials*, *32*(33), pp.8712-8721.

Stam, R., 2010. Electromagnetic fields and the blood–brain barrier. *Brain research reviews*, *65*(1), pp.80-97.

Temsamani, J. and Vidal, P., 2004. The use of cell-penetrating peptides for drug delivery. *Drug discovery today*, *9*(23), pp.1012-1019.

Teubl, B.J., Absenger, M., Fröhlich, E., Leitinger, G., Zimmer, A. and Roblegg, E., 2013. The oral cavity as a biological barrier system: design of an advanced buccal in vitro permeability model. *European Journal of Pharmaceutics and Biopharmaceutics*, *84*(2), pp.386-393.

Thorne, R.G. and Nicholson, C., 2006. In vivo diffusion analysis with quantum dots and dextrans predicts the width of brain extracellular space. *Proceedings of the National Academy of Sciences*, *103*(14), pp.5567-5572.

Ting, S.S., Whitelock, J.M., Tomic, R., Gunawan, C., Teoh, W.Y., Amal, R. and Lord, M.S., 2013. Cellular uptake and activity of heparin functionalised cerium oxide nanoparticles in monocytes. *Biomaterials*, *34*(17), pp.4377-4386.

Tkachenko, A.G., Xie, H., Coleman, D., Glomm, W., Ryan, J., Anderson, M.F., Franzen, S. and Feldheim, D.L., 2003. Multifunctional gold nanoparticle− peptide complexes for nuclear targeting. *Journal of the American Chemical Society*, *125*(16), pp.4700-4701.

Torchilin, V.P., 2006. Recent approaches to intracellular delivery of drugs and DNA and organelle targeting. *Annu. Rev. Biomed. Eng.*, *8*, pp.343-375.

Torrano, A.A., Blechinger, J., Osseforth, C., Argyo, C., Reller, A., Bein, T., Michaelis, J. and Bräuchle, C., 2013. A fast analysis method to quantify nanoparticle uptake on a single cell level. *Nanomedicine*, *8*(11), pp.1815-1828.

Vllasaliu, D., Alexander, C., Garnett, M., Eaton, M. and Stolnik, S., 2012. Fc-mediated transport of nanoparticles across airway epithelial cell layers. *Journal of controlled release*, *158*(3), pp.479-486.

Vllasaliu, D., Fowler, R., Garnett, M., Eaton, M. and Stolnik, S., 2011. Barrier characteristics of epithelial cultures modelling the airway and intestinal mucosa: a comparison. *Biochemical and biophysical research communications*, *415*(4), pp.579-585.

Wanakule, P., Liu, G.W., Fleury, A.T. and Roy, K., 2012. Nano-inside-micro: disease-responsive microgels with encapsulated nanoparticles for intracellular drug delivery to the deep lung. *Journal of controlled release*, *162*(2), pp.429-437.

Wang, J., Chen, J., Ye, N., Luo, Z., Lai, W., Cai, X. and Lin, Y., 2012. Absorption, pharmacokinetics and disposition properties of solid lipid nanoparticles (SLNs). *Current drug metabolism*, *13*(4), pp.447-456.

Wang, Z., Tiruppathi, C., Minshall, R.D. and Malik, A.B., 2009. Size and dynamics of caveolae studied using nanoparticles in living endothelial cells. *ACS nano*, *3*(12), pp.4110-4116.

Wen, C.J., Yen, T.C., Al-Suwayeh, S.A., Chang, H.W. and Fang, J.Y., 2011. In vivo real-time fluorescence visualization and brain-targeting mechanisms of lipid nanocarriers with different fatty ester: oil ratios. *Nanomedicine*, *6*(9), pp.1545-1559.

Xiang, S., Tong, H., Shi, Q., Fernandes, J.C., Jin, T., Dai, K. and Zhang, X., 2012. Uptake mechanisms of non-viral gene delivery. *Journal of controlled release*, *158*(3), pp.371-378.

Xu, S., Olenyuk, B.Z., Okamoto, C.T. and Hamm-Alvarez, S.F., 2013. Targeting receptor-mediated endocytotic pathways with nanoparticles: rationale and advances. *Advanced drug delivery reviews*, *65*(1), pp.121-138.

Yamamoto, Y., Tsutsumi, Y., Yoshioka, Y., Kamada, H., Sato-Kamada, K., Okamoto, T., Mukai, Y., Shibata, H., Nakagawa, S. and Mayumi, T., 2004. Poly (vinylpyrrolidone-co-dimethyl maleic acid) as a novel renal targeting carrier. *Journal of controlled release*, *95*(2), pp.229-237.

Yang, K. and Ma, Y.Q., 2010. Computer simulation of the translocation of nanoparticles with different shapes across a lipid bilayer. *Nature Nanotechnology*, *5*(8), pp.579-583.

Yang, M., Lai, S.K., Wang, Y.Y., Zhong, W., Happe, C., Zhang, M., Fu, J. and Hanes, J., 2011. Biodegradable nanoparticles composed entirely of safe materials that rapidly penetrate human mucus. *Angewandte Chemie International Edition*, *50*(11), pp.2597-2600.

Yuan, Z.X., Zhang, Z.R., Zhu, D., Sun, X., Gong, T., Liu, J. and Luan, C.T., 2008. Specific renal uptake of randomly 50% N-acetylated low molecular weight chitosan. *Molecular pharmaceutics*, *6*(1), pp.305-314.

Zhang, L.W. and Monteiro-Riviere, N.A., 2009. Mechanisms of quantum dot nanoparticle cellular uptake. *Toxicological Sciences*, *110*(1), pp.138-155.

Zhang, X., Chen, G., Wen, L., Yang, F., Shao, A.L., Li, X., Long, W. and Mu, L., 2013. Novel multiple agents loaded PLGA nanoparticles for brain delivery via inner ear administration: in vitro and in vivo evaluation. *European Journal of Pharmaceutical Sciences*, *48*(4), pp.595-603.

# CHAPTER 3

# NEO-GEOMETRIC COPPER NANOCRYSTALS BY COMPETITIVE, DUAL SURFACTANT-MEDIATED FACET ADSORPTION CONTROLLING SKIN PERMEATION

## 3.1. Introduction

Copper nanoparticles (CuNPs) have gained considerable research interest in the recent years for investigation in the biomedical and pharmaceutical sciences. The versatility of CuNPs facilitates its biomedical applications as a cytotoxic agent via oxidative stress (Galhardi *et al*., 2004; Laha *et al*., 2014), an antibacterial agent (Wu *et al*., 2010), an *in vivo* agent for imaging (Wegner *et al*., 2010) as well as for advanced drug delivery applications (Courant *et al*., 2009). In the last decade, researchers have proven that by manipulating the physicochemical, physicomechanical and morphological properties of CuNPs its industrial application expands and its extent of use. In particular, the geometrical shape and size of CuNPs has gained much interest (Zeng *et al*., 2004). Variation in the shape of CuNPs can be controlled via modification of synthesis processes and methods such as microemulsion (Solanki *et al*., 2010), reverse micelle method (Nomura *et al*., 2009), chemical reduction (Zhang *et al*., 2010), electrochemical reduction (Cioffi *et al*., 2005), metal vaporization (Lo *et al*., 2005), sonochemical processing (Dhas *et al*., 1998), solution plasma methods (Saito *et al*., 2011) and microwave-assisted synthesis (Ranu *et al*., 2007).

However, utilizing these methods does not ensure specificity in controlling the shape of CuNPs. In the bottom-up synthesis of shape controlled inorganic nanocrystals, studies have proven that colloidal solutions and key parameters such as temperature fluctuation, concentration of polymers and stabilizers, reducing agents, copper salt type and concentration, inert or ambient conditions, reaction time and water content are efficient for the minimal organization of particle shape. The self-assembly control process is able to maintain the nano-shape within the colloidal dispersion by minimal chemical, physical or mechanical modification during synthesis. Despite these advances, it is still highly complex to optimize the shape of CuNPs.

A few studies have confirmed the novel synthesis parameters of metal nanoparticles through the formation of shape-controlled nanoparticle fabrication. For instance, Sadjadi and co-workers (2008) investigated the effect of temperature and reaction time on the morphology

and aspect ratios of silver nano-rods. Pileni and co-workers (1997) demonstrated the effect of water volume on the morphology of CuNPs. In order of low to high water content, spherical and cylindrical nanoparticles and planar-type lamellar were formed. Another group of researchers, Nomura and co-workers (2009), varied the raw ion concentration and addition of ethanol in the synthesis of self-assembled barium chromate nano-wires, nanodots and nanorods. Spherical CuNPs and nanorods were achieved by De and Mandal (2013) when altering the surfactant concentration.

Despite the significant studies on metallic nanoparticle shape, these have been limited to two or three self-assemblies per formulation synthesis, partial synthesis of microparticles or formulations not displaying complete shape homogeneity due to the high chemical reactivity of the surface of the copper metal. Therefore, this chapter focuses on the exploits of the surfactants to partially reduce and cap CuNPs to stabilize and simultaneously dictate nanoparticle shape to produce samples of homogenous geometries. The study aimed to synthesize CuNPs of distinct shapes by manipulating two surfactant concentrations with homogeneity throughout each colloidal solution. This research also reports on the successful thermo-chemical reduction in the organised synthesis of neo-geometrical CuNPs and epidermal skin permeation kinetics based on nano-geometry.

### 3.2. Materials and Methods

Copper II sulphate pentahydrate ($CuSO_4 \cdot 5H_2O$) was purchased from Merck (Darmstadt, Germany); hexadecetyl trimethylammonium bromide (CTAB) and sodium dodecyl sulphate (SDS) were purchased from Sigma-Aldrich Co. (Aldrich, Steinheim, Germany); L-ascorbic acid (98%) was purchased from Roche (Johannesburg, South Africa); and trypsin/EDTA was purchased from Lonza (Walkersville, MD, USA). All water used for the synthesis was deionized. All chemicals were analytical grade and used without further purification.

#### 3.2.1. Synthesis of copper nanostructures

The thermal-reduction method of synthesizing nanocrystals included a standard $CuSO_4 \cdot 5H_2O$ solution added to varied molar concentrations of aliquot CTAB and SDS solutions heated at 50 °C. Solution was further heated between 85 and 90°C and a standard ascorbic acid solution was added as the reducing agent in a drop-wise manner to allow for spontaneous copper formation without a reducing agent overload. The temperature was then maintained at 80 °C using a mercury thermometer (Brannon Thermometers, Cumbria, UK).

### 3.2.2. Determination of the effect of surfactant concentration on particle morphology

TEM (FEI T12 Spirit Transmission Electron Microscope (120 kV), Hillsborough, CA, USA) and HR-TEM (JEOL JEM 2100F (200 kV), Tokyo, Japan) confirmed the synthesis of self-assembled neo-geometrical nanoparticles. Samples were also subjected to TEM-Energy Dispersive Spectroscopy (EDS) for high-speed elemental analysis.

### 3.2.3. Crystallinity and composition characterization of synthesized copper

A powder X-Ray Diffractometer (XRD) (MiniFlex 600, Tokyo, Japan) was used to monitor diffraction patterns of the CuNP samples to validate the synthesis of crystalline copper. A continuous scan rate of 0.1°/min from 0 to 90° was used with copper Kα radiation (λ = 1.54 Å).

### 3.2.4. Determination of the stability of the copper nanoparticles

The zeta potential measured the surface charge of the CuNPs, thus indicating the stability and aggregation potential of the nanoparticles. Each suspension was diluted 1:15 in distilled water, filtered through a 0.22µm Millipore filter, transferred into a capillary cell and was analyzed by a Zeta sizer (DTS (nano), Malvern instruments Ltd., Worcestershire, UK).

### 3.2.5. Molecular and structural transitional analysis of the surfactant-coated copper nanoparticles

Fourier-Transform Infrared (FTIR) analysis of ascorbic acid, CTAB, SDS and synthesized surfactant-coated CuNPs was undertaken to evaluate and compare vibrational characteristics of the chemical functional groups in response to infrared light interactions. FTIR spectra were recorded on a Perkin Elmer Spectrum 2000 FTIR spectrometer with a MIRTGS detector (PerkinElmer Spectrum 100, Wales, UK) at a wavenumber range of 650–4000cm$^{-1}$ with a resolution of 4cm$^{-1}$ and 10 scans per spectrum.

### 3.2.6. Determination of nanoparticle yield

Yield studies were conducted to elucidate the effect of surfactants in the investigation of copper reduction. The yield of the CuNPs was determined by weighing the dried CuNP samples using an electronic balance (Mettler, Model AE 240, Greifensee, Switzerland) with readings recorded to 2 decimal places. Percentage yield was calculated using Equations (3.1-3.3).

$$\text{Number of moles} = C \times V \tag{3.1}$$

Reacting mass of copper (theoretical yield) = $n \times M$ (3.2)

$$\% \text{ Yield} = \frac{\text{actual yield}}{\text{theoretical yield}} \times 100 \quad (3.3)$$

### 3.2.7. Thermal degradation analysis of the surface surfactant-coating of the copper nanoparticles

Thermogravimetric Analysis (TGA) using a 4000 TGA (PerkinElmer Inc., Waltham, MA, USA) was conducted to evaluate the surfactant-coating of the CuNP samples as the function of temperature in nitrogen atmosphere under a flow of 40ml/min and heating rate of 10°C/min from 30 to 900°C. The Pyris 6 software (PerkinElmer Inc., Waltham, MA, USA) was used to perform the thermal analysis. Each test consisted of a powder weighing approximately 10–20mg and produced similar results among all samples.

### 3.2.8. *Ex vivo* permeation evaluation of five distinct nano-shapes

*Ex vivo* studies were conducted to determine the skin permeation efficiency of five nanosystems with the most constructive structures. The study served to identify the nano-shape with the highest potential of crossing the stratum corneum barrier and entering the epidermal layer of BALB/c mice skin samples. The hair from the dorsal aspect of the mice was shaved and the skin was thereafter excised. The skin was washed and incubated in trypsin/EDTA at 37°C for 2 hours in an incubator controlled in a 5% $CO_2$ environment allowing for the detachment of the dermal layer thereafter. Skin integrity testing was conducted before and after permeation studies using a Seven Multi S40 pH/electrical conductivity meter (Mettler-Toledo, Zurich, Switzerland). The permeation studies were carried out utilizing a Franz Diffusion Cell (FDC) apparatus (PermeGear Inc., Bethlehem, PA, USA) equipped with a 12ml receptor compartment, clamp, stirrer-bar and a thermostat controlled water jacket. Epidermal BALB/c mice skin samples were placed between the donor and receptor compartments of the FDC. Samples of simulated plasma (100µL) in the receptor compartment (PBS; 12ml; pH 7.4; 37°C) were withdrawn at suitable time intervals over 24 hours. Post permeation studies, the skins were digested with nitric acid at 70°C for analysis to determine copper content retained by the dermal skin tissue. Receptor samples and skin samples were analyzed by Inductively Coupled Plasma-Optical Emission Spectroscopy (Activa S) (Horiba Scientific, Munich, Germany).

### 3.2.9. Data analysis and confirmation of statistical significance of all assays performed

All synthesis and characterization studies including TEM analysis, nanoparticle counting, XRD, zeta potential, yield, TGA and *ex vivo* permeation studies were carried out in 3

independent experiments in duplicates for each evaluation. Data were expressed as mean (±standard error (SE)) and analyzed by 1-way analysis of variance (ANOVA). *p* values less than 0.05 was considered statistically significant.

### 3.3. Results and Discussion

CuNP synthesis involves the reduction of a copper precursor, Cu(II) species, by ascorbic acid in solution leading to the nucleation and growth of metal nanoparticles. In addition to its use as a reducing agent, ascorbic acid also functions as a capping agent (Mushran *et al*., 1974; Xiong *et al*., 2011).

#### 3.3.1. Influence of variation in surfactant concentration on copper nanoparticles shape

The scope for change and sensitivity to an external parameter was ascertained to determine the geometries that could be derived from the crystalline cubic structure of nanocrystals and to assist with the synthesis of uniform neo-geometric CuNPs. After the nucleation of the copper crystal, the growth of the nanocrystal facets is controlled to synthesize the various shapes. In this study, the major influence involved in the dictation of nanoparticle shape is the organization of the surfactant molecules on specific faces to preferentially grow facets of certain dimensions and the induction of truncation of the CuNPs. The surfactants adsorb on the solid-liquid interface of particular nanocrystal facets imparting various energies on the different facets and the controlled, elevated reaction temperature allow for the deviation from the shape formation during synthesis using standard reaction parameters (Xia *et al*., 2009; Personick and Mirkin, 2013). Previous research studies show that CTAB can act as a soft template, this study proves that the simultaneous use of various concentrations of CTAB and SDS in the presence of heat can dictate and control the shape of seeded CuNPs. The varied surfactant molar concentrations used to synthesize neo-geometrical CuNPs are listed in Table 3.1.

**Table 3.1:** Surfactant variations corresponding to physicochemical characteristics of synthesized CuNPs. Data presented are mean ± SE of three experiments performed in duplicate. *$p \leq 0.05$.

| Formulation | [CTAB] (M) | [SDS] (M) | Yield (%) | Geometrical Structures | Size of Nanostructures (nm) | Figure |
|---|---|---|---|---|---|---|
| S1 [a] | 0.00 | 0.000 | 81.0 | Spheres | 90 ± 9 | 3.1a |
| S2 [b] | 0.01 | 0.087 | 83.6 | Combination | Shape dependent | 3.1b |
| S3 [b] | 0.01 | 0.100 | 85.0 | Spheres and rods | Shape dependent | 3.1c |
| S4 [a] | 0.02 | 0.000 | 86.0 | Rods | 150 × 20 | 3.1d |

| | | | | | | |
|---|---|---|---|---|---|---|
| S5 [a] | 0.02 | 0.087 | 89.8 | Cubes | 200 × 200 ± 13 | 3.1e |
| S6 [a] | 0.02 | 0.100 | 90.5 | Pyramids | 100 ± 12 | 3.1f |
| S7 [b] | 0.03 | 0.000 | 87.0 | Irregular spheres | 300 ± 11 | 3.1g |
| S8 [b] | 0.03 | 0.087 | 92.2 | Combination | Shape dependent | 3.1h |
| S9 [b] | 0.03 | 0.100 | 96.2 | Combination | Shape dependent | 3.1i |
| S10 [b] | 0.04 | 0.000 | 89.7 | Irregular spheres | 500 ± 8 | 3.1j |
| S11 [b] | 0.04 | 0.087 | 96.8 | Irregular spheres | 200–250 ± 10 | 3.1k |
| S12 [a] | 0.04 | 0.100 | 97.1 | Spheres | 5 ± 3 | 3.1l |

[a] Sample with ideal, homogenous nano-geometries*;* [b] Sample with irregular or combination geometries.

As the copper nanocrystals nucleate in aqueous solution, surfactant molecules adsorb onto the surface of facets dictating the shape formation by inhibiting or stimulating facet growth. It is suggested that shape of a Face-Centred Cubic (FCC) nanocrystal can be influenced by the ratio of the growth rates along the (100) and (111) directions (Borchardt-Ott, 1993; Kim *et al*., 2004). According to Personick and co-workers (2011), CTAB is a cationic surfactant which displays preferential facet adsorption altering growth rates along crystallographic planes. In water, the critical micelle concentration of CTAB is $9 \times 10^{-4}$mmol/L and SDS is $8 \times 10^{-3}$M, rendering the number of surfactant molecules sufficient to provide a micellar environment for the newly synthesized CuNPs forming an adsorption layer around the nanoparticles (Li *et al*., 2006). Table 3.1 and Figure 3.1 particularly demonstrate the dependence of surfactant concentration on nanoparticle shape formation. The relative percentage co-existence of the shapes in the poly disperse samples are obtained from a population of 100 nanoparticles as per Anova analysis.

Whilst maintaining a constant concentration of CTAB, the difference in morphology using 0.02M CTAB is far more sensitive than the samples using 0.01M CTAB as shown in Figure 3.2. Homogenous samples of geometries with varying aspects from rods to cubes and pyramids can be attributed to the variation in SDS concentration. Upon addition of SDS whilst maintaining 0.02M CTAB, the aspect ratio of the nanoparticles showed a fundamental decrease in aspect ratio of the nano-rods and nano-cubes. Further increasing the SDS concentration reduced the number of geometric aspects resulting in a change from a four-aspect structure to a three-aspect structure and additionally reducing the size dimensions of the nanoparticles. The number of sharp aspects increases and decreases spontaneously, showing responsiveness to increasing SDS in the presence of 0.02M CTAB.

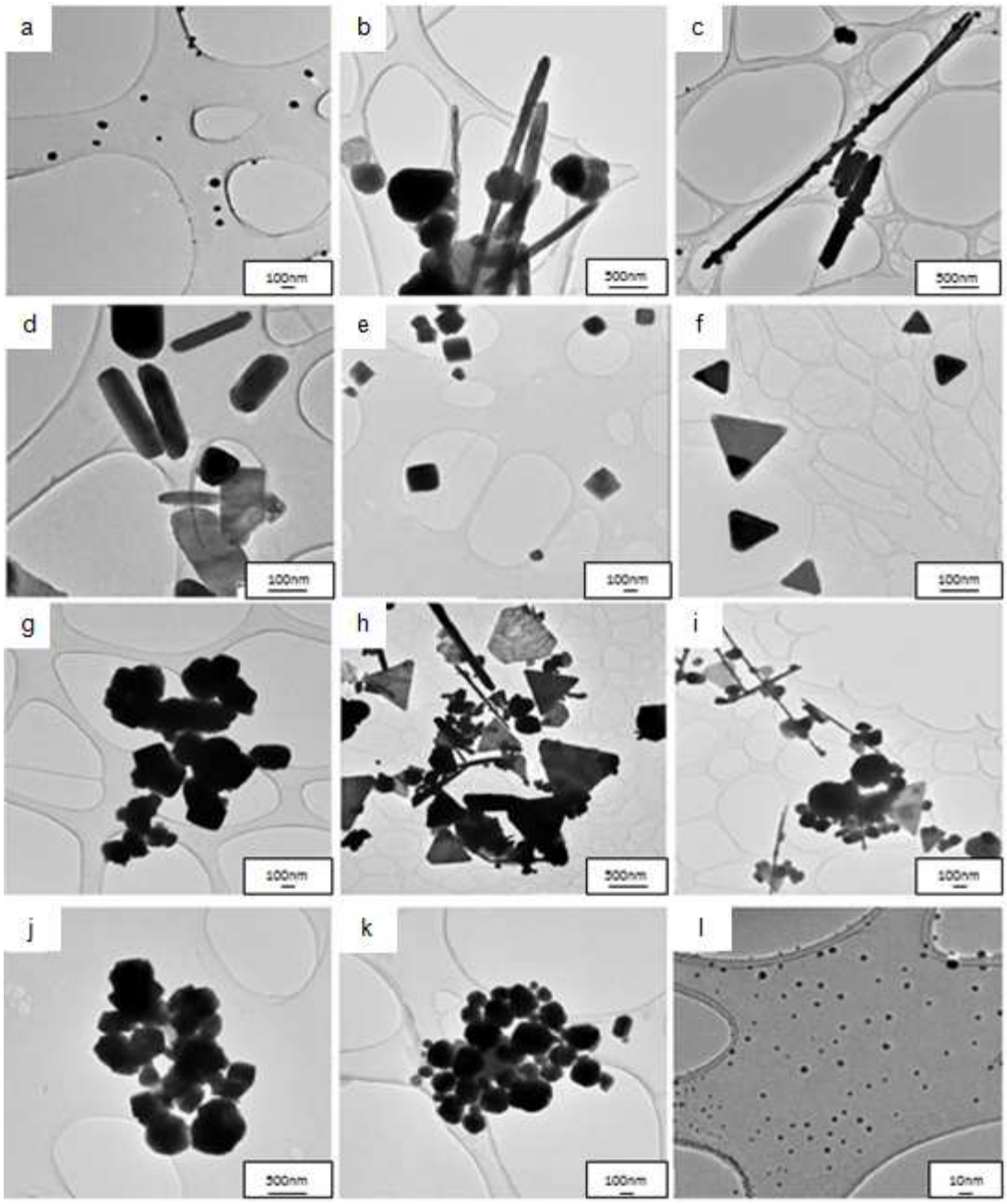


**Figure 3.1:** a) sample S1, spherical nanoparticles (90nm); b) sample S2, combination of spheres and rods; c) sample S3, combination spheres and rods with predominant rods; d) sample S4, rod-like nanoparticles; e) sample S5, cubic-shaped nanoparticles; f) sample S6, pyramidal nanoparticles; g) sample S7, irregular spherical particles; h) sample S8, combination of neo-geometrical nanoparticles; i) sample S9, combination of neo-geometrical nanoparticles at reduced size range; j) sample S10, irregular nanospheres; k) sample S11, spherical nanoparticles (250–300nm); l) sample S12, spherical nanoparticles (5nm).

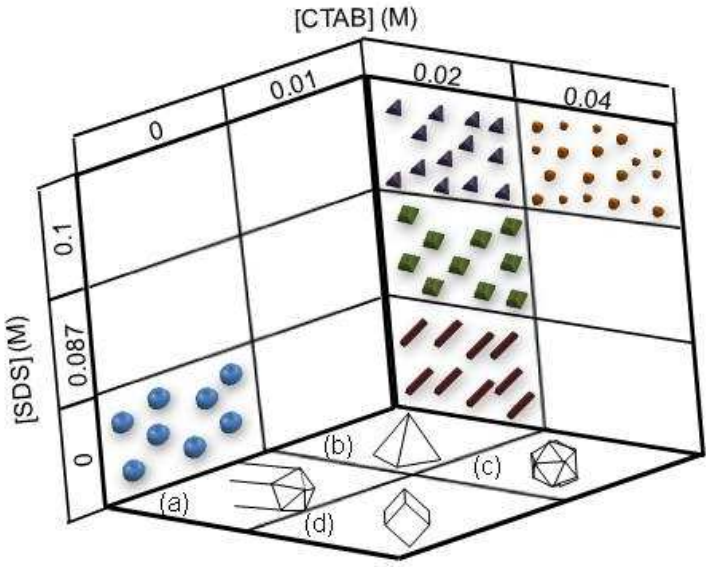


**Figure 3.2:** Schematic of growth of homogenous shapes according to surfactant variation: a) growth of a rod structure from the decahedral precursor; b) tetrahedral precursor geometry; c) polyhedral precursor geometry; d) cuboctahedral precursor geometry growing from the (100) and (111) planes.

The morphology difference between different CuNP samples in the current study is a result of the interaction achieved by the coordination bonds between copper ions, CTAB and SDS. Prior to nucleation of Cu, the $CuSO_4 \cdot 5H_2O$ salt interacts with CTAB and SDS molecules at concentrations above the critical micelle concentration which then surrounds the copper ions. The chemically adsorbed surfactant molecules and ions mediate the morphological changes of the CuNPs as well as act as stabilising agents by coating the nanocrystals and prevent oxidation of the metal copper under ambient conditions (Pileni, 2003). The adsorption of surfactant promotes facet growth and, as shown in Table 3.1, facet growth is dependent on surfactant concentration. Considering this concept, copper nuclei are most stable in the cuboctahedral, decahedral and tetrahedral and polyhedral precursor nuclei and assume these geometries during synthesis (Salzemann *et al*., 2004a).

The structure of the rod-shaped nanoparticle grows from a decahedron and exists with a five-fold symmetry (Salzemann *et al*., 2004a). The induction of the decahedron formation is mediated by the truncation of the five subunit edges of the decahedra nucleus in the (111) planes and additional intermediate faces in the (100) planes as shown in Figure 3.2a. Growth along the facet of the {100} surface results in an elongated structure with two 5-fold symmetry points on either end. The stable tetrahedral geometry with a threefold axis acts as the precursor nucleus in the formation of the pyramidal-shaped nanoparticles (Salzemann *et al*., 2004a) as shown in Figure 3.2b. The facets are dominated by {111} suggesting that the growth of the tetrahedral geometry is directed by this facet unlike the decahedron and

cuboctahedron geometries. It can be assumed that the spherical nanoparticles are formed from the truncated polyhedral precursor nuclei and are composed of several {100} and {111} facets as shown in Figure 3.2c. The cuboctahedral precursor is defined by its {100} and {111} facets as shown in Figure 3.2d. Cubic nanoparticle geometry arises from the selective growth of the {111} facet of the cuboctahedral nucleus. The selective growth of this facet suggests that it has a particularly higher surface energy than the {100} facet. Selective adsorption of surfactant on {100} retards its growth, allowing for the exaggerated growth of this slow growing surface resulting in a cubic geometry (Salzemann *et al*., 2004a). Slow growth of (100) results in this dominant facet producing cube shaped nanoparticles.

In the absence of CTAB and SDS, spherical nanoparticles are formed. It can be assumed that polyhedrons (Figure 3.2c) as the initial stable precursor nuclei with equal dimensions are formed. Thereafter, upon the addition of surfactant, there is preferential facet growth due to surface energy and surface adsorption. It is evident from other research (Biçer and Şişman, 2010) and these results that the surface energy varies between the different facets and displays competitive and selective adsorption of ions and molecules. The molecular and ionic affinity to certain facets could also be used to rationalise the geometry of nanocrystals. Due to the presence of the surfactants in the solution before, during and after the seeding process, the precursor nuclei geometries are uniform and can be controlled. After the seeding of the nuclei, the formation of the precursor nuclei is dictated by the type of surfactant molecules and ions and its concentration. Thereafter, its growth is also mediated by surface adsorption onto specific facets. In the study conducted by Pileni and co-workers (1997), the research team suggested the reverse micelle synthesis of shaped CuNPs involves the initial formation of decahedral, cuboctohedral or tetrahedral precursor shape followed by the favoured adsorption of surfactants on the facets of the nanocrystals to stimulate facet growth of certain dimensions. Thus, the growth rates of specific nanoparticle facets can be controlled during synthesis to direct the required nano-shape.

The {111} planes are more energetically favourable when directing tetrahedral growth compared to the decahedron and cuboctahedron which have high-energy facets specific to each geometry (Kim *et al*., 2004). The results indicate that directing tetrahedral, decahedral or cuboctahedral growth can be achieved by the ionic and molecular adsorption on (100), (110) and (111) planes while spherical CuNPs are directed by polyhedral structures. The affinity of these ions and molecules to certain planes plays the key role in geometry dictation. Surfactant adsorption on a facet reduces the growth of the facet and the remaining facets grow steadily becoming the least dominant facet (Borchardt-Ott, 1993).

During the synthesis of blank copper nanocrystals (Sample S1), polyhedral precursor nuclei are directed. Excess ascorbic acid and its degradative products promote the growth of this crystal nucleus. When CTAB at 0.01M and SDS at 0.087M are introduced into solution, decahedral and polyhedral precursor nuclei are grown. This is a clear indication that competitive inhibition of facet adsorption occurs by CTAB and SDS. When CTAB is increased to 0.03M at SDS 0.087M, a sample consisting of combinatorial geometries are synthesized. It can be assumed that the increased CTAB reduces the growth of (111) to promote the tetrahedral structure, as well as the polyhedral structure. According to the results, when CTAB is used at 0.02M, the geometry of the nanocrystals is the most responsive to surfactant concentration, hence, highly controlled. When CTAB at 0.01M is reacted with SDS at maximum concentration (0.1M), rod and spherical nanocrystals are formed. When compared to the sample synthesis of SDS at 0.087M (42% rods, 58% spheres), the composition of rods and spheres are now significantly different (78% rods, 22% spheres) implying that the excess SDS competes for adsorption on the {100} facet when used simultaneously with CTAB since the rod:spherical nanocrystal ratio has increased.

Regarding the neo-geometrical CuNP synthesis, it is suggested that at 0.02M the aqueous CTAB surfactant environment is ideal for the generation of single-shaped geometrical precursor ions (Figure 3.2). Specific to 0.02M CTAB, monodisperse rods, cubes and pyramids were formed in solution when compared to samples of other CTAB concentrations. The rod-shaped nanoparticles indicate CTAB adsorption on the (100) plane which can be accurately presumed due to CTAB being the independent surfactant during nano-rod synthesis. Adsorption on (100) prolongs the growth of the facet allowing for the elongation of the decahedron as shown in Figure 3.3.1a. In the absence of SDS, the formation of the decahedral precursor structure is clearly dominant. Upon introducing 0.087M SDS to 0.02M CTAB the cuboctahedral precursor nuclei is directed and the effect of selective CTAB adsorption on (100) is maintained resulting in cube shaped nanocrystals. As shown by the results, when SDS is used at 0.1M there is competitive inhibition of CTAB adsorbing onto the (100) facet. The SDS at 0.1M when used simultaneously with 0.02M CTAB promotes the synthesis of the tetrahedral precursor stimulating the synthesis of pyramidal nanocrystals, adsorbing on the (111) facet.

When CTAB is used at 0.03M in the absence of SDS, the formation of irregular polyhedrons is evident as shown in Figure 3.1j. This is shows the non-selective surfactant adsorption in this concentration range. Similar to the sample S10 where CTAB is used independently at 0.04M, the higher concentration can be rewarded of its excess by producing more regular

surface adsorption and also reducing the crystal size by 100nm. CTAB at 0.03M and SDS at 0.087 and 0.1M both produce samples various geometries showing non-selective precursor nuclei and facet growth. The increased SDS, however, is able to control the size of all geometries indefinitely. The tetrahedral size reduction is 400nm, rods by an aspect ratio of 7 and spheres by 50nm in diameter.

At the specific CTAB concentration of 0.04M, the growth of polyhedrons is constant. The excess CTAB adsorbs on all faces unselectively resulting in a geometrical structure with several facets. The addition of SDS at 0.087M partially assists with the control of CTAB adsorption equally on facets resulting in polyhedral nanostructures that are slightly more regular than spheres. At 0.04M CTAB, 0.087M SDS also affects the size of the nanocrystal, reducing the polyhedron diameter by 200nm affirming the use of SDS as a size controlling agent in the synthesis of nanocrystals (De and Mandal, 2013). When SDS is used in an excess of 0.1M at CTAB 0.04M, the polyhedral structure is at its most stable spherical structure. The SDS enhances equal adsorption of CTAB while reducing the nanocrystal size significantly by 90nm.

### 3.3.2. Nanocrystal lattice spacing

Individual nanoparticle geometry and crystallinity was analyzed to determine the lattice fringe spacing. A single rod nanocrystal (Figure 3.3.1a) consists of lattice fringes along (111) with a spacing of 2.09Å and (100) with 1.81Å as shown in Figure 3.3.1b indicating the copper nanocrystals are of FCC structure. The inset in Figure 3.3.1a clearly shows the 5-fold centre of the rod tip with the rod orientated to display its {111} facet. Figure 3.3.2a shows a single cube-shaped nanocrystal consisting of an inter-fringe distance of 1.81Å which is attributed to the lattice space along (100) (Figure 3.3.2b). The pyramidal-shaped nanoparticle (Figure 3.3.3a) shows a monodisperse 2.09Å (111) lattice fringe (Figure 3.3.3b). Spherical nanocrystals 3.3.4a) have lattice fringes along (111) with a spacing of 2.09Å and (100) with 1.81Å as shown in Figure 3.3.4b. Selected Area Electron Diffraction (SAED) patterns of the single nanocrystal illustrate ordered diffraction spots indicating high crystalline features of the capped CuNPs (Figure 3.3 (1c, 2c, 3c, 4c)).

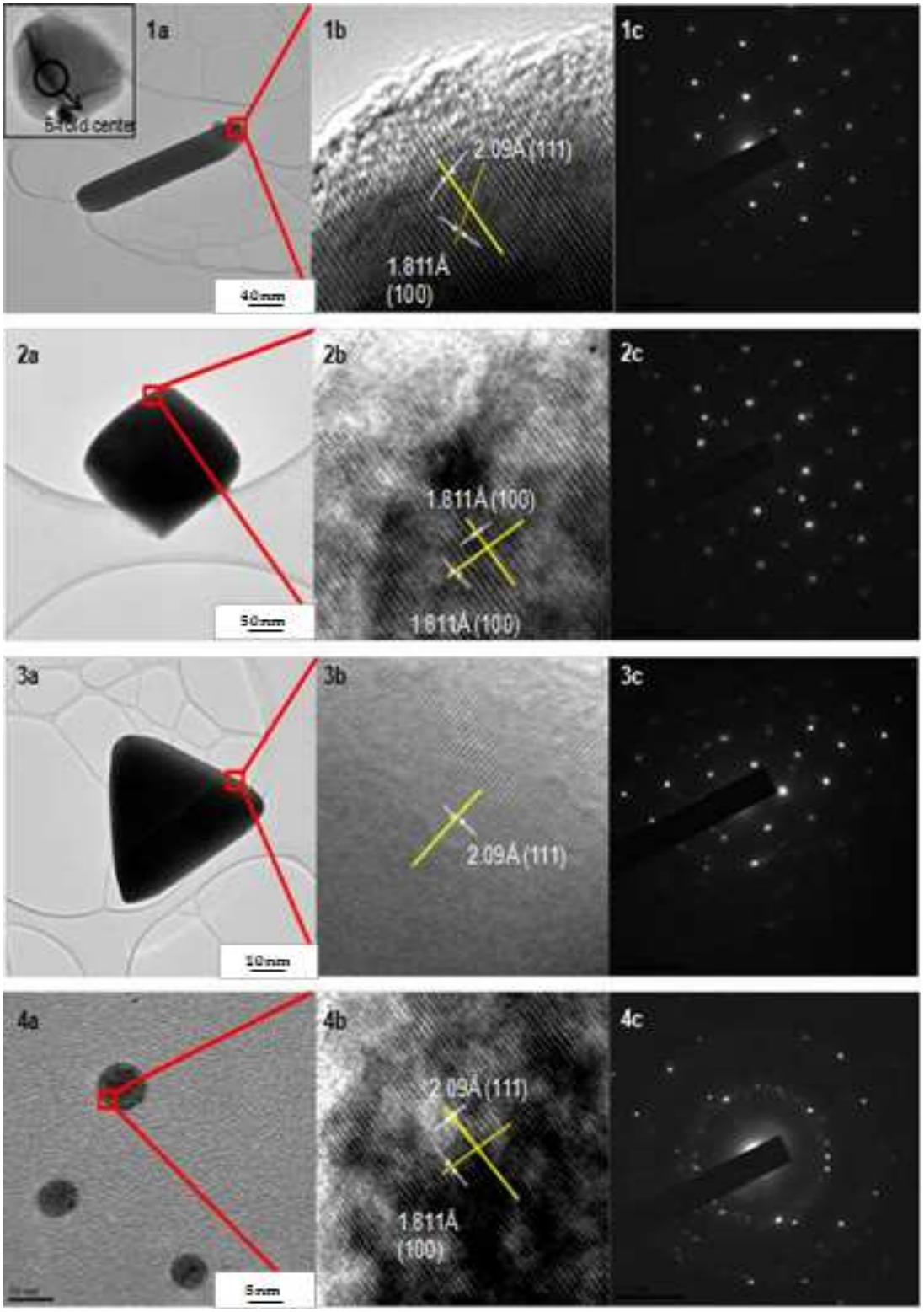


**Figure 3.3:** 1a) rod-shaped nanoparticle and inset showing 5-fold center of the decahedral geometry at (111); 1b) lattice fringes and spacing of rod-shaped nanoparticle; 1c) uniform SAED patterns; 2a) Cube-shaped nanoparticle; 2b) lattice fringes and spacing of cube-shaped nanoparticle; 2c) uniform SAED patterns; 3a) Pyramid-shaped nanoparticle; 3b) lattice fringes and spacing of pyramid-shaped nanoparticle; 3c) uniform SAED patterns; 4a) Spherically-shaped nanoparticles; 4b) lattice fringes and spacing of spherical nanoparticles; 4c) uniform SAED patterns.

### 3.3.3. X-ray and electron diffraction analysis

The powder X-Ray diffraction patterns of the CuNPs as shown in Figure 3.4a are indicative of highly oriented crystalline CuNPs and are similar amongst all samples. It corresponds to phase-pure copper according to the literature pattern (JCPDS, File No. 04-0836) with strong, prominent peaks at 43.1°, 50.3° and 74° correlating to (111), (200) and (220) planes of copper crystals, respectively. The 100% pure-crystalline copper characteristic peaks are indexed to a FCC crystal structure. A small proportion of impurity, copper oxide, was detected at 35.5° (002) and is owing to formation of copper oxide following interactions with air during the XRD analysis.

As indicated by enlarged views, rods (Figure 3.3.1a), cubes (Figure 3.3.2a), pyramids (Figure 3.3.3a) and spheres (Figure 3.3.4a) have well-defined edges and aspects. The lattice fringes and SAED patterns corresponding to Figure 3.3.1a–3.3.4c indicate FCC copper and differ according to their individual orientation. According to the Bragg equation (Equation 3.4),

$$n\lambda = 2d\sin(\theta) \tag{3.4}$$

can be rearranged to determine the spacing, *d*, between corresponding lattices (Equation 3.5),

$$d = n \times \frac{wavelength}{2sin(\theta)} \tag{3.5}$$

Using θ from the crystalline peaks arising from the X-ray diffraction data (Figure 3a), the lattice distance can be calculated from the (111), (200), (220) and (311) planes as 2.09Å (0.209nm), 1.81Å (0.181nm), 1.27Å (0.127nm) and 1.09Å (0.109nm) respectively. These values correspond ideally with the figures associated to the lattice fringe spaces giving a clear indication that copper of the correct domains were formed.

The EDS plots of CuNPs (Figure 3.4b) exclusively exhibits the characteristic peaks of ideal elemental copper. Strong signals of copper atoms show at a dominant $K\alpha_1$ peak at 8.0477keV followed by a smaller $K\beta_1$ peak 8.0905keV. The peak at 0.9498keV demonstrates the $L\beta_1$ peak for electrons in the L-shell. The EDS plots for all CuNPs samples resulted in similar spectra. Thus, both metal characterization analysis indicate the synthesis of pure copper. The strong FCC copper peaks from XRD and elemental copper peaks from EDS (Figure 3.4b) demonstrates that the thermal-chemical reduction method used in conjunction with ascorbic acid serving the dual function of reducing agent and capping agent; and two

surfactants coating the CuNPs in the aim of preventing oxidation results in the synthesis of pure copper nanocrystals without additional impure phases.

a

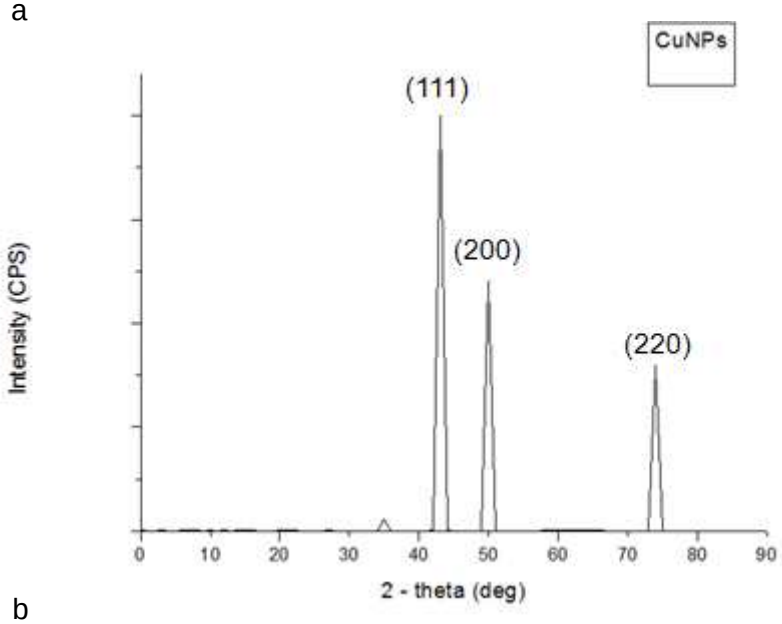


b

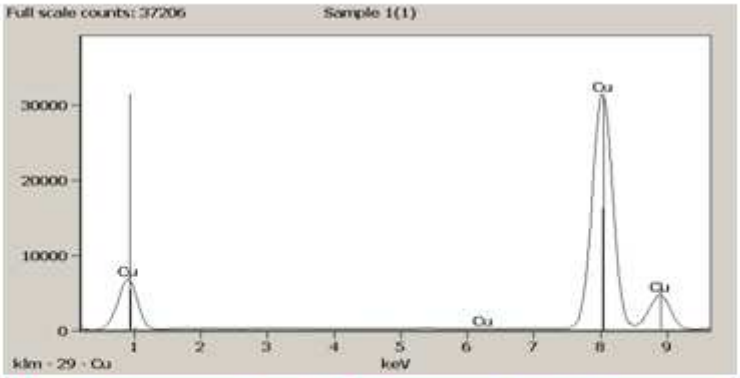


| Element Line | Weight % | Weight % Error |
|---|---|---|
| Cu K | 100.00 | ±0.40 |
| Cu L | --- | --- |
| Total | 100.00 | |

**Figure 3.4:** a) powder X-Ray diffraction patterns of synthesized copper nanocrystals; b) energy dispersive spectra showing pure elemental copper.

### 3.3.4. Surface charge analysis

Zeta potential, as an indicator of surface charge, gives the probability of stability of the sample. The greater the potential of the CuNPs, the higher the stability and reduced likeliness to aggregate due to the repel of the charged nanoparticles. Ascorbic acid has a negative charge, hence sample S1 has a negative potential (Roy *et al*., 2003). The reducing agent also serves as a stabilising agent by binding to the surface of the synthesized

nanocrystal, preventing aggregation of the nanoparticles (Personick and Mirkin, 2013). The results indicate a change in surface charge with different surfactant types and concentrations. The use of cationic CTAB and anionic SDS manipulates the surface charge from the standard negative charge (sample S1 = −28.3mV) of the CuNPs synthesized without surfactant as shown in Table 3.2. The surface charge of the CuNPs synthesized with CTAB as the independent surfactant (S4, S7 and S10) are fairly stable with positive potentials and the least stable values are due to the high concentrations of both surfactants simultaneously used in CuNP synthesis. Samples S2, S6, S8 and S11 where SDS is used at 0.087 or 0.1M has characteristics of least stabile profiles and may possess the highest aggregation while relatively low concentrations of CTAB (S3, S5 and S9) displayed strongly negative charges as expected. The samples synthesized with one surfactant with a dominant concentration prove to be most stable with potentials less than −25mV or exceeding +25mV.

**Table 3.2:** Zeta potential data collated from all CuNPs samples.

| Formulation | [CTAB] | [SDS] | Zeta Potential (mV) |
|---|---|---|---|
| S1 | 0.00 | 0.000 | −28.3 |
| S2 | 0.01 | 0.087 | −19.9 |
| S3 | 0.01 | 0.100 | −25.7 |
| S4 | 0.02 | 0.000 | 26.9 |
| S5 | 0.02 | 0.087 | −30.3 |
| S6 | 0.02 | 0.100 | −21.3 |
| S7 | 0.03 | 0.000 | 27.1 |
| S8 | 0.03 | 0.087 | −6.75 |
| S9 | 0.03 | 0.100 | −34.5 |
| S10 | 0.04 | 0.000 | 33.1 |
| S11 | 0.04 | 0.087 | −18.4 |
| S12 | 0.04 | 0.100 | 16.7 |

### 3.3.5. Yield analysis

Yield analysis was conducted on the CuNPs samples with differing results as shown in Table 3.1. An additional aspect of interest noted in this study regarded the variation in yield between the samples. The percentage of CuNPs synthesized is influenced by the surfactants and possibly potentiates the synthesis of the copper nanocrystals and enhances the capping effect. Typically, CTAB has been shown to increase the number of nanocrystals formed during reduction while using an independent reducing agent (Salzemann *et al*., 2004b). This confirms the use of CTAB as a catalyst reducing agent. CTAB samples prepared without ascorbic acid did not produce CuNPs reiterating that CTAB is not an independent reducing agent; however, samples that contained higher CTAB increased the CuNP yield. CuNP samples that contained a constant CTAB concentration varied in yield when the SDS concentration differed. The results show that SDS may have also functioned

as a catalyst and the samples increased in yield with an increase in SDS concentration. Additionally, an increase in yield seen with SDS may be due to the surfactant adsorption on the crystal facets and coating of the nanoparticle surface.

### 3.3.6. Evaluation of chemical and structural changes of the surfactant-coated copper nanoparticles

FTIR analysis was conducted on the reducing agent, surfactants and coated CuNPs to determine the adsorption of the excess ascorbic acid, CTAB and SDS on the CuNPs (Figure 3.5). The capping effect of the surfactants also promotes stability towards aggregation allowing for the optimal function of the nanoparticles. Similar characteristic peaks found between ascorbic acid (Figure 3.5a) and sample S1 (Figure 3.5b) and between CTAB (Figure 3.5c), SDS (Figure 3.5d), sample S4 (Figure 3.5e) and S5 (Figure 3.5f) give an indication of the adsorption on the CuNPs. Common peaks found on the ascorbic acid and sample S1 spectra include CH stretching at 2943cm$^{-1}$, carbonyl groups at 1711cm$^{-1}$, aromatic rings at 1408cm$^{-1}$, ether groups at 1137 and 1177cm$^{-1}$. The FTIR spectrum of sample S4 (Figure 3.5e) and selective peaks of sample S5 (Figure 3.5f) can be attributed to the adsorption of CTAB (Figure 3.5c) on the surface of the CuNPs.

Both spectra exhibited CTAB characteristic peaks of CH bending in the 1400–1500cm$^{-1}$ region, stretching vibrations of C–CH2 in the methylene chains at 2848cm$^{-1}$ (Riccardi *et al*., 2009) and 2916cm$^{-1}$ (Campbell *et al*., 2004). Sample S5 displays a peak at 3018cm$^{-1}$ assigned to the antisymmetric stretching modes of the trimethylammonium headgroup of CTAB (Campbell *et al*., 2004) indicating facet adsorption of CTAB. When comparing the spectrum of sample S5 (Figure 3.5f) with the SDS (Figure 3.5d) spectra, several corresponding peaks are definite indicating the presence of the surfactant in the CuNP sample. The bands on spectrum Figure 3.5f correspond to the $OSO_3^-$ bands at 1215 and 1247cm$^{-1}$ (Yada *et al*., 1996) and peaks at 2918 and 2954cm$^{-1}$ assigned to the $CH_2$ group on the SDS spectrum (Sperline *et al*., 1992). The FTIR data are indicative of reducing agent and surfactant adsorption on the CuNPs and is further corroborated by the following TGA data.

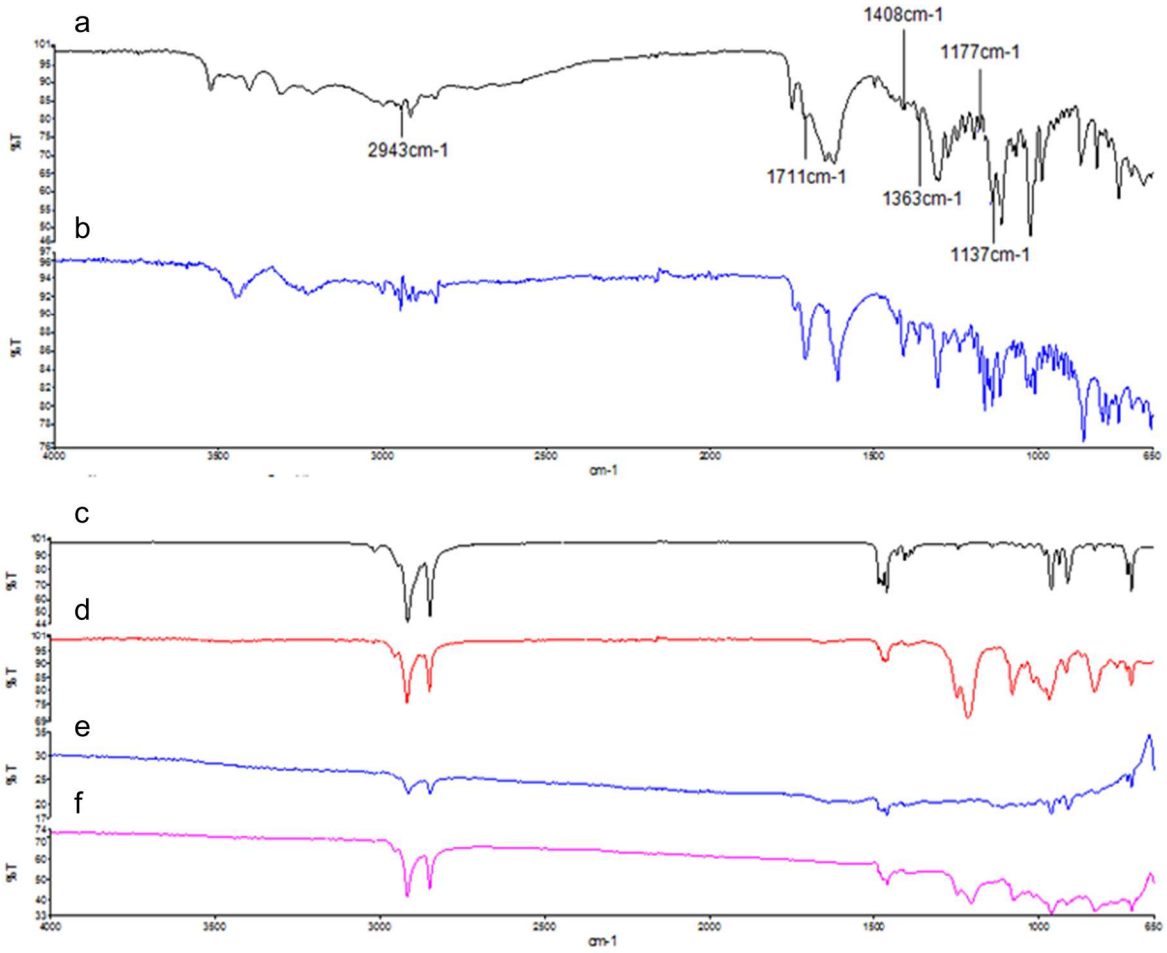


**Figure 3.5:** FTIR spectra of: a) ascorbic acid; b) sample S1; c) CTAB; d) SDS; e) sample S4; f) sample S5.

### 3.3.7. Thermal degradation analysis of surfactant-coated copper nanoparticles

TGA was used to assess the relative composition of the capping agents on the CuNPs. Figure 3.6a and b shows the representative TGA curves obtained for samples S1 and S2 which were heated from 30 to 900°C in the presence of nitrogen gas. The curve in Figure 3.6a shows one key degradation point between 110 and 320°C, which can be related to the decomposition of the ascorbic acid on the surface of the CuNPs. Sample S2 (Figure 3.6b), capped with ascorbic acid, CTAB and SDS, displays two key degradation steps. The first weight loss step in Figure 3.6b curve occurs between 110 and 240°C indicating the degradation of ascorbic acid as the capping agent and between 300 and 410°C, which is attributed to the degradation of the adsorbed surfactants. All remaining samples have TGA profiles similar to Figure 3.6b.

The degradation of the ascorbic acid in sample S1 occurs at temperatures between 100 and 320°C and between 110 and 240°C in sample S2. This data indicates the capping effect of the ascorbic acid and the intramolecular interactions between ascorbic acid and the

surfactants resulting in a slightly raised degradation temperature in sample S2. After analysis at the end temperature of 900°C, an average of 95.7% of sample remains. Copper degrades at temperatures higher than 900°C indicating that the degradation that occurred is attributed to the supporting surfactants in the samples and that the synthesized CuNPs are thermally stable. The change in mass can be translated to the ratio of capping agents to CuNPs. A shell of about 2% ascorbic acid and 6% surfactant adsorption was determined from thermogravimetric analysis, resulting in 93%–96.4% of the mass due to the copper.

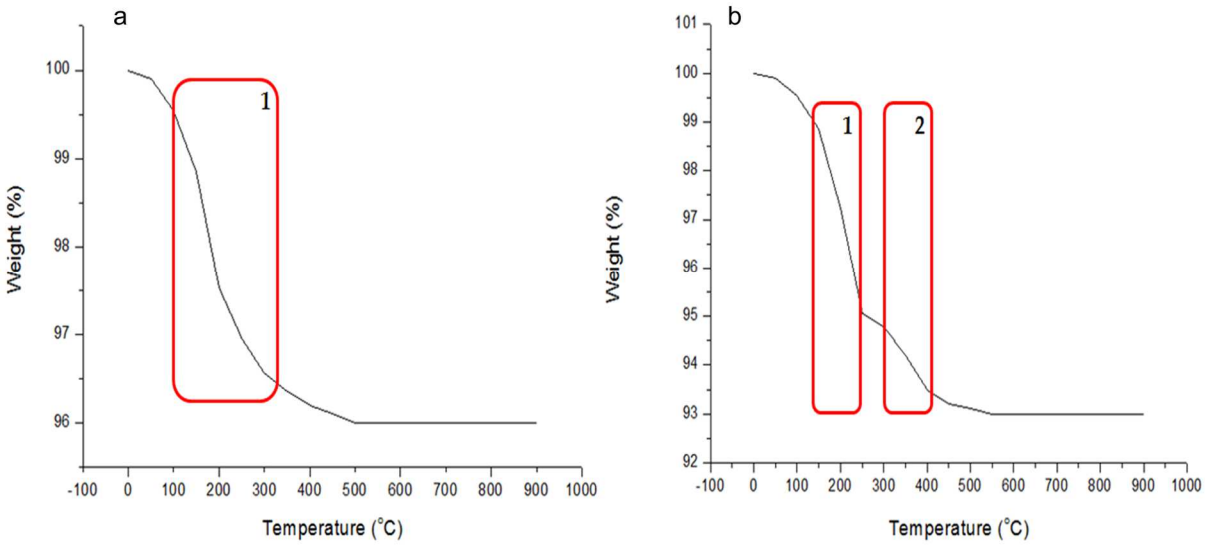


**Figure 3.6:** TGA curves of: a) sample S1 showing degradation of reducing agent; b) sample S2 showing degradation of surfactants on the nanoparticle surface.

### 3.3.8. Effect of nano-shape on skin permeation through excised mice skin

Permeation studies were conducted to determine the effect of nanoparticle geometry on transcellular drug delivery. Pre- and post-*ex vivo* characterization, conductivity analyses confirmed maintenance of skin integrity of the mice skin tissue samples. Analyses of the *ex vivo* permeation results (Figure 3.7) within the first 2 hours show the CuNPs reaching a state of equilibrium in the epidermal tissue. No CuNPs permeation is detected in the first hour and a mere 0.0149mg·cm$^{-2}$ CuNPs is detected in the rod nanoparticle sample, 0.05mg·cm$^{-2}$ of the pyramid nanoparticle sample and 0.17mg·cm$^{-2}$ of the 5nm sphere nanoparticle sample at 2 hours. The first CuNP detection of the 90nm spheres and cubes occurs at 4 hours at 0.122 and 0.254mg·cm$^{-2}$, respectively. The permeation lag can be explained by the CuNPs reaching a state of concentration equilibrium in the epidermal tissue and thereafter permeating into the receptor compartment. Interestingly, the skin permeation and transcellular transport due to shape kinetics of the spheres are higher than the other geometrical nanoparticles. The 90nm spheres have the highest cumulative diffusion per unit area (0.78mg·cm$^{-2}$) (Figure 3.7) but have a lower nanoparticle flux (4.20 x10$^{-2}$mg·cm$^{-2}$·hr$^{-1}$),

as shown in Table 3.3, compared to the 5nm spheres which have a lower cumulative diffusion per unit area (0.73mg·cm$^{-2}$) with a higher nanoparticle flux (5.88 x10$^{-2}$mg·cm$^{-2}$·hr$^{-1}$). The initial CuNP permeation of the 5nm spheres supersedes the 90nm spheres and eventually stabilizes at a concentration below the 90nm spheres while the rods have an initial lower flux than the pyramids and cubes but steadily increase with all geometries reaching system equilibrium after 14–16 hours. The 5nm spheres show a long burst release permeation as opposed to the rods, pyramids and cubes which is followed by the 90nm spheres. Interestingly, the pyramids show a short burst release until 6 hours, thereafter reaching a stable flux.

Figure 3.7 confirms the hypothesis of the nano-shape effects on cellular permeation where the geometrical structure of the nanoparticle affects cellular and transdermal permeation. Cellular internalization and epidermal tissue localization of the CuNPs also show nano-shape to be a dictating factor when considering this drug delivery system for specific transdermal or dermal use. Table 3.3 lists the concentration of neo-geometric CuNPs retained by the epidermal tissue post-internalization after analysis using Inductively Coupled Plasma Optical Emission Spectrometry (ICP-OES). The cube-shaped CuNPs shows the highest retained concentration at 0.34mg with 90nm spheres being the lowest at 0.09mg. Having the highest retention potential, cubes also have the lowest permeation potential with an average flux indicating a system application for epidermal drug delivery. The 90nm spheres retain the least amount of CuNPs but have the highest permeation with an above average flux when compared with other neo-geometric CuNPs giving the probability of its use as a transdermal drug delivery system. The alternative nano-shapes can be dually used as systems requiring dermal and transdermal drug delivery depending on application specificities as can be extrapolated from Figure 3.7 and Table 3.3. The results of the CuNPs retained correlate with the CuNPs diffusion through the epidermal skin tissue. The high permeation of the CuNPs accounts for the low concentration of CuNPs retained and vice versa. The results do not indicate a superior system for drug delivery but rather results based application of the neo-geometric CuNPs. Previous studies identified hollow copper-sulphide nanoparticles as a skin disruption mechanism to enhance transdermal drug delivery of human growth hormone upon application of a near-infrared laser (Ramadan *et al*., 2012). In addition, Ahamed and associates (2014) recently studied the antibacterial effects of CuNPs which can be included in medical devices similar to the study conducted by Sankar and co-workers (2015) who investigated the antibacterial effects of CuNPs on wound healing. Having the benefit of inhibiting pathogenic bacterial growth, the future goals of this study will also focus on the toxic properties of CuNPs in transdermal drug delivery.

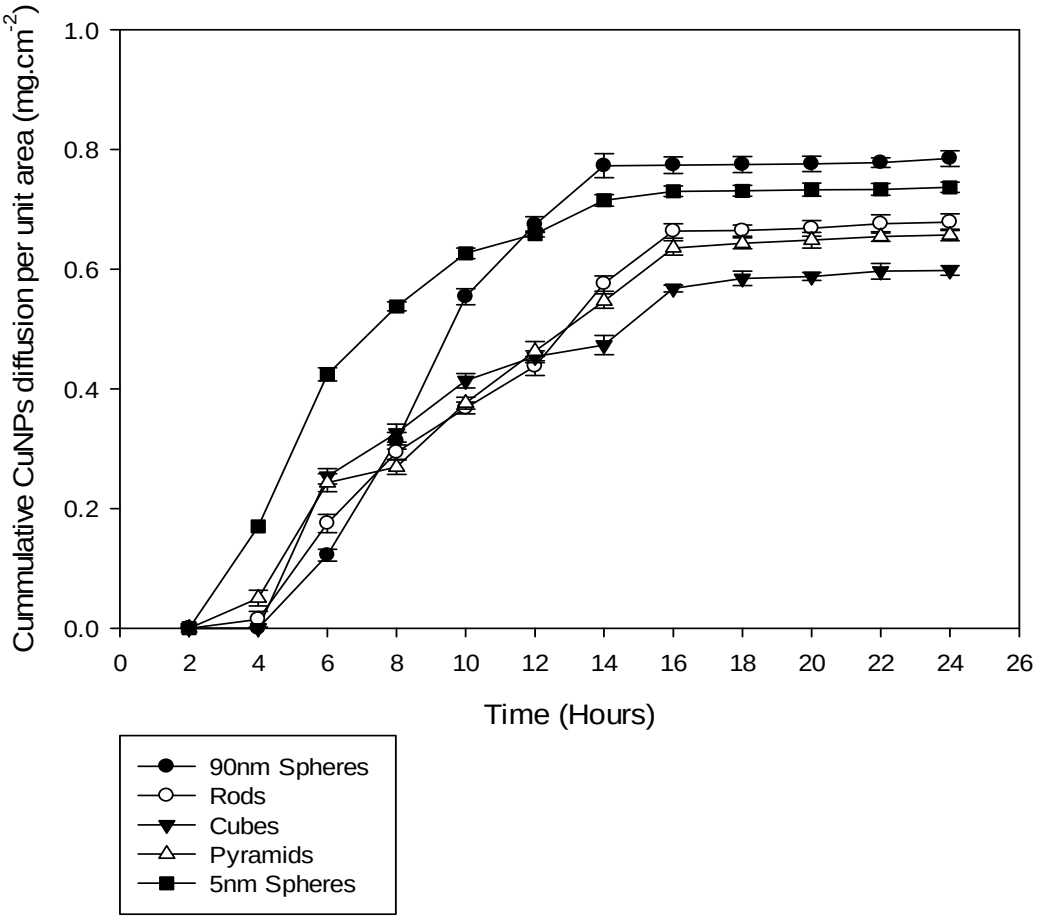


**Figure 3.7:** *Ex vivo* permeation profiles of geometric copper nanoparticles through excised BALB/c mice dermal tissue. Data presented are mean ± SE of three experiments performed in duplicate. *$p \leq 0.05$.

**Table 3.3:** Copper nanoparticle flux and associated permeability coefficients for the geometric copper nanoparticles through excised BALB/c mice dermal tissue. Data presented are mean ± SE of three experiments performed in duplicate. *$p \leq 0.05$.

| Formulation | Geometrical Structure | Flux, $J_S$, ($mg \cdot cm^{-2} \cdot hr^{-1}$) | CuNPs Retained in Dermal Tissue (mg) |
|---|---|---|---|
| S1 | Spheres (90 nm) | $4.20 \times 10^{-2}$ | 0.09 |
| S4 | Rods | $3.61 \times 10^{-2}$ | 0.14 |
| S5 | Cubes | $3.75 \times 10^{-2}$ | 0.34 |
| S6 | Pyramids | $2.66 \times 10^{-2}$ | 0.28 |
| S12 | Spheres (5 nm) | $5.88 \times 10^{-2}$ | 0.11 |

### 3.4. Concluding Remarks

The fabrication of non-agglomerated, monodispersed and exquisite geometrically organised CuNPs has been successfully demonstrated by reducing a copper salt using ascorbic acid in the presence of two key surfactants. Homogenous samples of cubes, pyramids, rods and spheres were synthesized proving shape control of the method. Particle morphologies could be controlled by manipulating the surfactant concentration, as well as by utilizing the degradation products of ascorbic acid to assist with capping and shape dictation of the

nanoparticles. It can be concluded that CTAB at 0.02 and 0.04M are most stable when synthesizing homogenous geometries in one pot. The SDS variation thereafter plays the key role in inhibiting or stimulating the adsorption of CTAB by its own adsorption. The function of the SDS can be assumed to be a vital one as an additional geometry and size dictator. The shape organization of the CuNPs is remarkable despite the small increase in surfactant concentration between the samples. The epidermal permeation, flux and tissue-retained CuNPs clearly show a shape-dominated trend and the drug delivery uses of the CuNPs thereof prove to be varied. This approach in the synthesis of neo-geometric copper nanocrystals offers the controlled shape formation of copper nanocrystals and reproducibility of heterogeneous and homogenous shape-formation based on the surfactant concentration. In addition to nano-shape, the surface chemistry of the CuNPs also affects *ex vivo* kinetics related to drug delivery and will be considered for functionalization. The CuNPs will be further applied in drug delivery as a function of its shape and toxicity. Considering the CuNPs retaining potential or transbarrier transport, the nanosystems will be applied to human keratinocytes in the determination of ideal nano-shape for enhanced cell uptake.

### 3.5. References


Ahamed, M., Alhadlaq, H.A., Khan, M.A., Karuppiah, P. and Al-Dhabi, N.A., 2014. Synthesis, characterization, and antimicrobial activity of copper oxide nanoparticles. *Journal of Nanomaterials*, *2014*, p.17.

Biçer, M. and Şişman, İ., 2010. Controlled synthesis of copper nano/microstructures using ascorbic acid in aqueous CTAB solution. *Powder Technology*, *198*(2), pp.279-284.

Borchardt-Ott, W., 1993. *Crystallography*. Springer Science & Business Media.

Campbell, R.A., Parker, S.R., Day, J.P. and Bain, C.D., 2004. External reflection FTIR spectroscopy of the cationic surfactant hexadecyltrimethylammonium bromide (CTAB) on an overflowing cylinder. *Langmuir*, *20*(20), pp.8740-8753.

Cioffi, N., Torsi, L., Ditaranto, N., Tantillo, G., Ghibelli, L., Sabbatini, L., Bleve-Zacheo, T., D'Alessio, M., Zambonin, P.G. and Traversa, E., 2005. Copper nanoparticle/polymer composites with antifungal and bacteriostatic properties. *Chemistry of Materials*, *17*(21), pp.5255-5262.

Courant, T., Roullin, V.G., Cadiou, C., Delavoie, F., Molinari, M., Andry, M.C. and Chuburu, F., 2009. Development and physicochemical characterization of copper complexes-loaded PLGA nanoparticles. *International journal of pharmaceutics*, *379*(2), pp.226-234.

De, S. and Mandal, S., 2013. Surfactant-assisted shape control of copper nanostructures. *Colloids and Surfaces A: Physicochemical and Engineering Aspects*, *421*, pp.72-83.

Dhas, N.A., Raj, C.P. and Gedanken, A., 1998. Synthesis, characterization, and properties of metallic copper nanoparticles. *Chemistry of materials*, *10*(5), pp.1446-1452.

Galhardi, C.M., Diniz, Y.S., Faine, L.A., Rodrigues, H.G., Burneiko, R.C., Ribas, B.O. and Novelli, E.L., 2004. Toxicity of copper intake: lipid profile, oxidative stress and susceptibility to renal dysfunction. *Food and chemical toxicology*, *42*(12), pp.2053-2060.

Kim, F., Connor, S., Song, H., Kuykendall, T. and Yang, P., 2004. Cover Picture: Platonic Gold Nanocrystals (Angew. Chem. Int. Ed. 28/2004). *Angewandte Chemie International Edition*, *43*(28), pp.3615-3615.

Laha, D., Pramanik, A., Maity, J., Mukherjee, A., Pramanik, P., Laskar, A. and Karmakar, P., 2014. Interplay between autophagy and apoptosis mediated by copper oxide nanoparticles in human breast cancer cells MCF7. *Biochimica et Biophysica Acta (BBA)-General Subjects*, *1840*(1), pp.1-9.

Li, W., Zhang, M., Zhang, J. and Han, Y., 2006. Self-assembly of cetyl trimethylammonium bromide in ethanol-water mixtures. *Frontiers of Chemistry in China*, *1*(4), pp.438-442.

Lo, C.H., Tsung, T.T. and Chen, L.C., 2005. Shape-controlled synthesis of Cu-based nanofluid using submerged arc nanoparticle synthesis system (SANSS). *Journal of Crystal Growth*, *277*(1), pp.636-642.

Mushran, S.P., Agrawal, M.C., Mehrotra, R.M. and Sanehi, R., 1974. Kinetics and mechanism of reduction of silver (I) by ascorbic acid. *Journal of the Chemical Society, Dalton Transactions*, (14), pp.1460-1462.

Nomura, T., Mori, T., Arima, H. and Konishi, Y., 2009. Shape and size control of barium chromate nanoparticles using reverse micelle. *Advanced Powder Technology*, *20*(1), pp.101-105.

Personick, M.L. and Mirkin, C.A., 2013. Making sense of the mayhem behind shape control in the synthesis of gold nanoparticles. *Journal of the American Chemical Society*, *135*(49), pp.18238-18247.

Personick, M.L., Langille, M.R., Zhang, J., Harris, N., Schatz, G.C. and Mirkin, C.A., 2011. Synthesis and isolation of {110}-faceted gold bipyramids and rhombic dodecahedra. *Journal of the American Chemical Society*, *133*(16), pp.6170-6173.

Pileni, M.P., 2003. Nanocrystals: Fabrication, organization and collective properties. *Comptes Rendus Chimie*, *6*(8), pp.965-978.

Pileni, M.P., Tanori, J. and Filankembo, A., 1997. Biomimetic strategies for the control of size, shape and self-organization of nanoparticles. *Colloids and Surfaces A: Physicochemical and Engineering Aspects*, *123*, pp.561-573.

Ramadan, S., Guo, L., Li, Y., Yan, B. and Lu, W., 2012. Hollow Copper Sulfide Nanoparticle-Mediated Transdermal Drug Delivery. *Small*, *8*(20), pp.3143-3150.

Ranu, B.C., Saha, A. and Jana, R., 2007. Microwave-Assisted Simple and Efficient Ligand Free Copper Nanoparticle Catalyzed Aryl-Sulfur Bond Formation. *Advanced synthesis & catalysis*, *349*(17-18), pp.2690-2696.

Riccardi, C.S., Lima, R.C., Dos Santos, M.L., Bueno, P.R., Varela, J.A. and Longo, E., 2009. Preparation of CeO 2 by a simple microwave–hydrothermal method. *Solid State Ionics*, *180*(2), pp.288-291.

Roy, P.R., Okajima, T. and Ohsaka, T., 2003. Simultaneous electroanalysis of dopamine and ascorbic acid using poly (N, N-dimethylaniline)-modified electrodes. *Bioelectrochemistry*, *59*(1), pp.11-19.

Sadjadi, M.A.S., Sadeghi, B., Meskinfam, M., Zare, K. and Azizian, J., 2008. Synthesis and characterization of Ag/PVA nanorods by chemical reduction method. *Physica E: Low-dimensional Systems and Nanostructures*, *40*(10), pp.3183-3186.

Saito, G., Hosokai, S., Tsubota, M. and Akiyama, T., 2011. Synthesis of copper/copper oxide nanoparticles by solution plasma. *Journal of applied physics*, *110*(2), p.023302.

Salzemann, C., Lisiecki, I., Brioude, A., Urban, J. and Pileni, M.P., 2004b. Collections of copper nanocrystals characterized by different sizes and shapes: optical response of these nanoobjects. *The Journal of Physical Chemistry B*, *108*(35), pp.13242-13248.

Salzemann, C., Lisiecki, I., Urban, J. and Pileni, M.P., 2004a. Anisotropic copper nanocrystals synthesized in a supersaturated medium: Nanocrystal growth. *Langmuir*, *20*(26), pp.11772-11777.

Sankar, R., Baskaran, A., Shivashangari, K.S. and Ravikumar, V., 2015. Inhibition of pathogenic bacterial growth on excision wound by green synthesized copper oxide nanoparticles leads to accelerated wound healing activity in Wistar Albino rats. *Journal of Materials Science: Materials in Medicine*, *26*(7), pp.1-7.

Solanki, J.N., Sengupta, R. and Murthy, Z.V.P., 2010. Synthesis of copper sulphide and copper nanoparticles with microemulsion method. *Solid State Sciences*, *12*(9), pp.1560-1566.

Sperline, R.P., Song, Y. and Freiser, H., 1992. Fourier transform infrared attenuated total reflection spectroscopy linear dichroism study of sodium dodecyl sulfate adsorption at the alumina/water interface using alumina-coated optics. *Langmuir*, *8*(9), pp.2183-2191.

Wegner, S.V., Arslan, H., Sunbul, M., Yin, J. and He, C., 2010. Dynamic copper (I) imaging in mammalian cells with a genetically encoded fluorescent copper (I) sensor. *Journal of the American Chemical Society*, *132*(8), pp.2567-2569.

Wu, B., Huang, R., Sahu, M., Feng, X., Biswas, P. and Tang, Y.J., 2010. Bacterial responses to Cu-doped TiO 2 nanoparticles. *Science of the Total Environment*, *408*(7), pp.1755-1758.

Xia, Y., Xiong, Y., Lim, B. and Skrabalak, S.E., 2009. Shape-Controlled synthesis of metal nanocrystals: simple chemistry meets complex physics?. *Angewandte Chemie International Edition*, *48*(1), pp.60-103.

Xiong, J., Wang, Y., Xue, Q. and Wu, X., 2011. Synthesis of highly stable dispersions of nanosized copper particles using L-ascorbic acid. *Green Chemistry*, *13*(4), pp.900-904.

Yada, M., Machida, M. and Kijima, T., 1996. Synthesis and deorganization of an aluminium–based dodecyl sulfate mesophase with a hexagonal structure. *Chemical Communications*, (6), pp.769-770.

Zeng, H., Rice, P.M., Wang, S.X. and Sun, S., 2004. Shape-controlled synthesis and shape-induced texture of MnFe2O4 nanoparticles. *Journal of the American Chemical Society*, *126*(37), pp.11458-11459.

Zhang, Q.L., Yang, Z.M., Ding, B.J., Lan, X.Z. and Guo, Y.J., 2010. Preparation of copper nanoparticles by chemical reduction method using potassium borohydride. *Transactions of Nonferrous Metals Society of China*, *20*, pp.s240-s244.

# CHAPTER 4

# CELLULAR INTERNALIZATION KINETICS AND CYTOTOXIC PROPERTIES OF STATISTICALLY DESIGNED AND OPTIMIZED NEO-GEOMETRIC COPPER NANOCRYSTALS

## 4.1. Introduction

Surface engineering of nanotherapeutics is considered as the frontrunner in biomedical applications and drug delivery as a smart means of delivering drugs and dictating their fate. Nanoparticles as a drug carrier have been exploited in the delivery of biomedical agents owing to their nano-size allowing for drugs to be delivered at a cellular level thereby increasing drug deposition intracellularly, reducing the amount of drug required and more importantly, reducing the side effects of drugs by targeting nanoparticles to diseased cells. With this emerged field of research gaining significant momentum since its inception, the pathway has been paved for improvements on the original concept of nanoparticles as a drug delivery system.

With recent advances in nanotechnology, studies show that manipulating the physicochemical and physicomechanical parameters of nanoparticles have an effect on the cellular internalization (Zhao *et al*., 2011; Sami *et al*., 2012). Modifying the characteristics of nanoparticles assist with the enhanced internalization and improving therapeutic time. Engineering nano features such as size, shape, surface charge, chemical chemistry, hydrophobicity and ligand attachments are a few parameters of nanoconstructs that can be manipulated (Sahay *et al*., 2010; Venkataraman *et al*., 2011). If focused on during synthesis, these characteristics may be the dictating factor in improving nanoparticle internalization kinetics, thus, positively affecting intracellular drug delivery.

Amongst these possible nanoparticle modifications, nanoparticles with engineered geometries seem to be an interesting one with varying rates of internalization based on the interactions between the scaffold design and cell membrane. Nano-shape and geometry-related parameters form factors inclusive of aspect ratios or edges that affect nanoparticle internalization kinetics and influence cell-particle interactions (Champion *et al*., 2007; Yang and Ma, 2010). By varying the shape of nanoparticles having the same volume, or varying the volume of particles of the same shape, it can be studied that nanoparticles with different shapes penetrate the lipid bilayer of the cell membrane differently and geometric

internalization may even vary between different cell types (Yang and Ma, 2010). Nano-vector design as a function of its shape has been proven to have diverging effects on cell uptake which also ranges from active and passive translocation mechanisms such as phagocytosis, macropinocytosis, clathrin-mediated endocytosis, caveolae-mediated endocytosis, and clathrin- and caveolae-independent endocytosis (Venkataraman *et al*., 2011).

Hence, the aim of the study was to engineer neo-geometric CuNPs in the investigation of nano-shape in drug delivery application. As for any formulation, design criteria including material selection and network fabrication are crucial for drug delivery. In this study, these criteria are essential in governing the outcome of the geometrical structure and charge stability of the CuNPs. Prior to the synthesis of the CuNPs, these criteria have to be evaluated based on the two independent variables. In order to achieve the aim of formulating homogenous, stable CuNPs, extensive shape elucidating characterization and zeta potential analyses were conducted. The use of the two key surfactants offered shape dictation and varying surface charge of the formulations in the statistical design for its use in further studies to investigate the effect of shape on cell uptake, simultaneously improving drug delivery. As a result, in this investigation a new strategy for the preparation of novel geometric CuNPs, with optimization through a full factorial experimental design is reported on.

Based on the concept of nano-geometry influencing cell uptake, after optimization of the nano-systems, this study investigated the internalization kinetics of neo-geometric CuNPs in normal human epidermal keratinocytes (NHEK) and cytotoxic analyses using NHEK and HeLa cells. The successful optimization of the bottom-up synthesis of geometric CuNPs synthesized by selective surfactant-mediated surface adsorption on preferential crystal facets serves as the geometric nano-vector.

### 4.2. Materials and Methods

Copper II sulphate pentahydrate ($CuSO_4.5H_2O$) was purchased from Merck (Darmstadt, Germany), CTAB, SDS and MTT, LDA, GSH and MDA assays were purchased from Sigma-Aldrich Co. (Aldrich, Steinheim, Germany) and L-ascorbic acid (98%) was purchased from Roche (Johannesburg, South Africa). NHEK cells, keratinocyte basal medium, growth factors and supplements including bovine pituitary extract, human epidermal growth factor, insulin, hydrocortisone, epinephrine, gentamicin, amphotericin B, transferrin, trypsin/EDTA were all purchased from Whitehead Scientific (Cape Town, South Africa). HeLa cells and

Dulbeccos Modified Eagles Medium (DMEM) were purchased from Separations (Johannesburg, South Africa). All chemicals and assay kits were analytical grade and used without further purification.

### 4.2.1. Synthesis of geometric copper nanocrystals

The thermal-reduction method of synthesizing nanocrystals included a standard $CuSO_4.5H_2O$ solution added to varied molar concentrations of aliquot CTAB and SDS solutions heated at 50°C. Solution was further heated between 85-90°C and a standard ascorbic acid solution was added as the reducing agent in a drop-wise manner to allow for spontaneous copper formation without a reducing agent overload. The temperature was then maintained at 80°C using a mercury thermometer (Brannon Thermometers, Cumbria, England).

### 4.2.2. Experimental design and constraint optimization of neo-geometric copper nanoparticles

A full factorial design was used to optimize the neo-geometric nanoparticles. Optimization using the two variable design model was employed to ascertain the ideal combination of dual surfactants (CTAB and SDS) as the independent variables to achieve optimal homogenous geometries and zeta potential to ensure stable nanosystems. For each of the two parameters selected, two factors were fixed, an upper and a lower level as summarized in Table 4.1 and these values were obtained from preliminary studies undertaken with 4 levels for CTAB and 3 levels for SDS. Also shown in Table 4.1 are the responses and the optimization constraints for each variable. The design was both generated and analyzed using Minitab V15 software (Minitab® Inc, PA, USA) and for the design 12 experimental formulations were obtained as summarized in Table 4.2.

**Table 4.1:** Formulation variables and responses applied in the Full Factorial design.

| | Levels | | Objective |
|---|---|---|---|
| | **Upper** | **Lower** | |
| **Parameters** | | | |
| CTAB (M) | 0.040 | 0.000 | |
| SDS (M) | 0.100 | 0.000 | |
| **Responses** | | | |
| Shape uniformity | | | Maximise |
| Surface charge | | | ≤25≥ |

**Table 4.2:** Statistically generated formulations obtained from a Full Factorial Design of optimization.

| Formulation | Variable 1 [CTAB] (M) | Variable 2 [SDS] (M) |
|---|---|---|
| 1 | 0.04 | 0.000 |
| 2 | 0.00 | 0.087 |
| 3 | 0.02 | 0.000 |
| 4 | 0.04 | 0.100 |
| 5 | 0.00 | 0.100 |
| 6 | 0.00 | 0.000 |
| 7 | 0.02 | 0.100 |
| 8 | 0.04 | 0.087 |
| 9 | 0.02 | 0.087 |
| 10 | 0.03 | 0.000 |
| 11 | 0.03 | 0.087 |
| 12 | 0.03 | 0.100 |

### 4.2.3. Geometric and morphological characterization of the copper nanoparticles

TEM (FEI T12 Spirit TEM (120kV), Hillsborough, USA) and HR-TEM (JEOL JEM 2100F (200kV), Oregan, USA) were conducted to confirm the synthesis of self-assembled neo-geometrical nanoparticles. CuNPs were dispersed on a copper grid coated with Formvar/carbon (200 mesh, BAL-TEC, EMTechnology and Application, Witten, Germany). Excess sample was removed by solvent evaporation under ambient conditions. Samples were also subjected to TEM-EDS for high-speed elemental analysis.

### 4.2.4. Zeta potential and stability analyses of copper nanoparticles

The zeta potential measured the surface charge of the CuNPs, thus indicating the stability and aggregation potential of the nanoparticles. Each suspension was diluted 1:15 in distilled water, filtered through a 0.22µm Millipore filter, transferred into a capillary cell and was analyzed by a Zeta sizer (DTS (nano), Malvern instruments ltd, Worcestershire, UK).

### 4.2.5. Crystal and elemental analysis of the optimized copper nanoparticles

A powder X-Ray diffractometer (MiniFlex 600, Tokyo, Japan) was used to monitor diffraction patterns of the CuNP samples to validate the synthesis of crystalline copper. A continuous scan rate of 0.1°/min from 0-90° was used with copper Kα radiation (λ=1.54Å). Percent crystallinity of distinctive peaks was computed employing PDXL software (Rigaku, Tokyo, Japan). Concurrent characterization was carried out using an Oxford INCA EDS system coupled to a TEM which monitored diffraction patterns to determine the elemental composition of the CuNP samples.

### 4.2.6. Thermal degradation analysis of the surface surfactant-coating of the copper nanoparticles

TGA using a 4000 thermogravimetric analyzer (PerkinElmer Inc., Massachusetts, USA) evaluated the surfactant-coating of the CuNP samples as the function of temperature in nitrogen atmosphere under a flow of 40ml/min and heating rate of 10°C/min from 30-900°C. The Pyris 6 software (PerkinElmer Inc., Massachusetts, USA) was used to perform the thermal analysis. Each test consisted of a powder weighing approximately 10-20mg and produced similar results among all samples.

### 4.2.7. Optimization of the neo-geometric copper nanoparticles

Following generation of the polynomial equations relating to the dependent and independent variables, the formulation process was optimized under constrained conditions for the measured responses of shape uniformity and surface charge. Response surface analysis of various response variables was carried out employing Minitab® statistical software (V15, Minitab Inc., PA, USA). The results were demonstrated using residual plots, interaction plots and response surface plots derived for the measured responses

### 4.2.8. Cell culturing and copper nanoparticle-cell incubation

Primary NHEK cells were sub-cultured until passage 6 and used for all internalization and cell viability assays. HeLa cells were used as a comparison for the cytotoxicity evaluation giving a perspective on the toxicity of the CuNPs on a cancer line. The NHEK cells were cultured in keratinocyte basal medium and supplemented with bovine pituitary extract, recombinant human epidermal growth factor, insulin, hydrocortisone, epinephrine, transferrin, gentamicin and amphotericin B. The HeLa cells were cultured using DMEM and 5% Foetal Bovine Serum (FBS) solution with both cell lines incubated in a humidified 37°C environment controlled at 5% CO2. At 80% confluence, the cells were harvested using trypsin/EDTA and were subcultured into 75cm$^2$ flasks, 12-well plates on circular glass cover-slides for internalization studies, and 96-well plates for the toxicity assays. The cells were allowed to attach to the surface for 48 hours prior to treatment.

### 4.2.9. Qualitative and quantitative cellular internalization studies

NHEK cells were cultured on circular glass cover slips in 12-well plates at 1x10$^3$ cells per well. After 48 hours of seeding, the cells were exposed to the geometric CuNPs (12.5µg/ml) for 12 hours. At suitable time intervals, the samples were dehydrated using 50%, 60%, 70%, 80% and 90% ethanol solution for 10 minutes each, consecutively and finally 100% ethanol. Once dehydrated, the glass cover slips were mounted on cover slides and analyzed for

CuNPs internalization imaging using a BX63 light microscope (Olympus, Tokyo, Japan) equipped with a DP 80 camera (Olympus, Tokyo, Japan). In addition, quantitative analysis of internalized CuNPs was conducted to quantify internalization of the geometric nanoparticles at set time-points. $1x10^3$ cells/well were seeded in 96-well plates and exposed to the CuNPs for 1, 2, 4, 8 and 24 hours. At the end of the respective exposure periods, cells were detached from the wells using trypsin/EDTA, centrifuged, rinsed to remove non-internalized CuNPs and collected for Inductively-Coupled Plasma Optical Emission Spectroscopy (Activa S) (Horiba Scientific, Munich, Germany) analysis to determine the amount of copper internalized**.**

#### 4.2.10. Geometric dependency of copper nanoparticles on cell viability

A MTT assay was conducted on the cells exposed to various geometric CuNPs to determine the effect of concentration, geometry and cell type on cellular viability and mitochondrial function. $1x10^3$ cells/well were seeded in 96-well plates and exposed to different concentrations (6.25, 12.5, 25, and 50µg/ml) of CuNPs for 24 hours. At the end of exposure, 10µL of MTT dye (3-(4,5-Dimethylthiazol-2-Yl)-2,5-Diphenyltetrazolium Bromide) (5mg/ml) was added to each well and incubated for 3 hours at 37°C. As a result, formazan crystals were formed and then dissolved using MTT solubilising solution. The plates were further incubated for 30 minutes and then analyzed at 570nm using a Powerwave XS multiplate spectrophotometer (BioTek, Vermont, USA). Untreated cells were run under identical conditions and served as controls.

#### 4.2.11. Lactate dehydrogenase activity

Lactate dehydrogenase (LDH) activity was determined using an assay kit which measured the levels of LDH production and subsequent cell damage. NHEK cells were seeded in 96-well plates for 48 hours ($6x10^6$ cells/well) and thereafter exposed to geometric CuNPs for 24 hours at different concentrations (6.25, 12.5, 25, and 50µg/ml). After exposure, cells were homogenized and 50µL samples were collected for analysis. LDH activity was assayed using LDH substrate mix and assay buffer and its absorbance read at 450nm with 5 readings at 3 minute intervals using a Powerwave XS multiplate spectrophotometer.

#### 4.2.12. Glutathione assay

As a marker of oxidative stress, reduced glutathione (GSH) was measured to determine intracellular free-radical damage. NHEK cells were seeded in 96-well plates for 48 hours ($6x10^6$ cells/well) and thereafter exposed to geometric CuNPs for 24 hours at different concentrations (6.25, 12.5, 25, 50µg/ml). After exposure, cells were centrifuged and

collected in a pellet. To the pellet, three times the volume of 5% sulfosalicylic acid was added and vortexed. The cell suspension was frozen in liquid nitrogen and thawed in a 37°C water bath twice before temporary storage at 2-8°C. The sample was then centrifuged and the supernatant collected. To 10µL of supernatant, 150µL of assay buffer and 5,5-dithio-bis-(2-nitrobenzoic acid (DTNB) solution was added. After 5 minutes of incubation, 50µL of nicotinamide adenine dinucleotide phosphate (NADPH) was added to each well and the absorbance was read at 412nm for 5 minutes at 1 minute intervals using a Powerwave XS multiplate spectrophotometer.

#### 4.2.13. Lipid peroxidation activity

Lipid peroxidation activity (LPO) was determined by measuring the formation of malondialdehyde (MDA) which is a product of membrane LPO. NHEK cells were seeded in 96-well plates for 48 hours ($6x10^8$ cells/well) and thereafter exposed to geometric CuNPs for 24 hours at different concentrations (6.25, 12.5, 25, 50µg/ml). After exposure, cells were centrifuged, collected in a pellet and lysed. The resultant supernatant was used for analysis. Thiobarbituric acid (TBA) was added to the supernatant to form a MDA-TBA adduct, thereafter incubated for 60 minutes at 95°C and its absorbance read at 532nm using a Powerwave XS multiplate spectrophotometer.

#### 4.2.14. Data analysis and confirmation of statistical significance of all assays performed

The 4 assays were carried out in 3 independent experiments in duplicates for each evaluation. Data were expressed as mean (±SE) and analyzed by 1-way Anova. *p* values less than 0.05 was considered statistically significant.

### 4.3. Results and Discussion

#### 4.3.1. Geometric analyses of copper nanocrystals

It is ascertained that parameters of nanoparticles can be controlled to achieve desirable characters. As is with this study, the novelty of using two surfactants during the synthesis of CuNPs yielded nanoparticles of various geometric structures (Table 4.3). The aim of the design, however, focused on streamlining the synthesis parameters to produce nano-systems of homogenous shapes. The CuNPs were synthesized using a thermal-chemical reduction method as per Table 4.2 and characterized to confirm nano-shape fabrication. Figure 4.1 includes TEM images of all 12 experimental formulations in the design and

compares the variable surfactant concentration to establish the optimal responses according to the surfactant concentrations employed in the study.

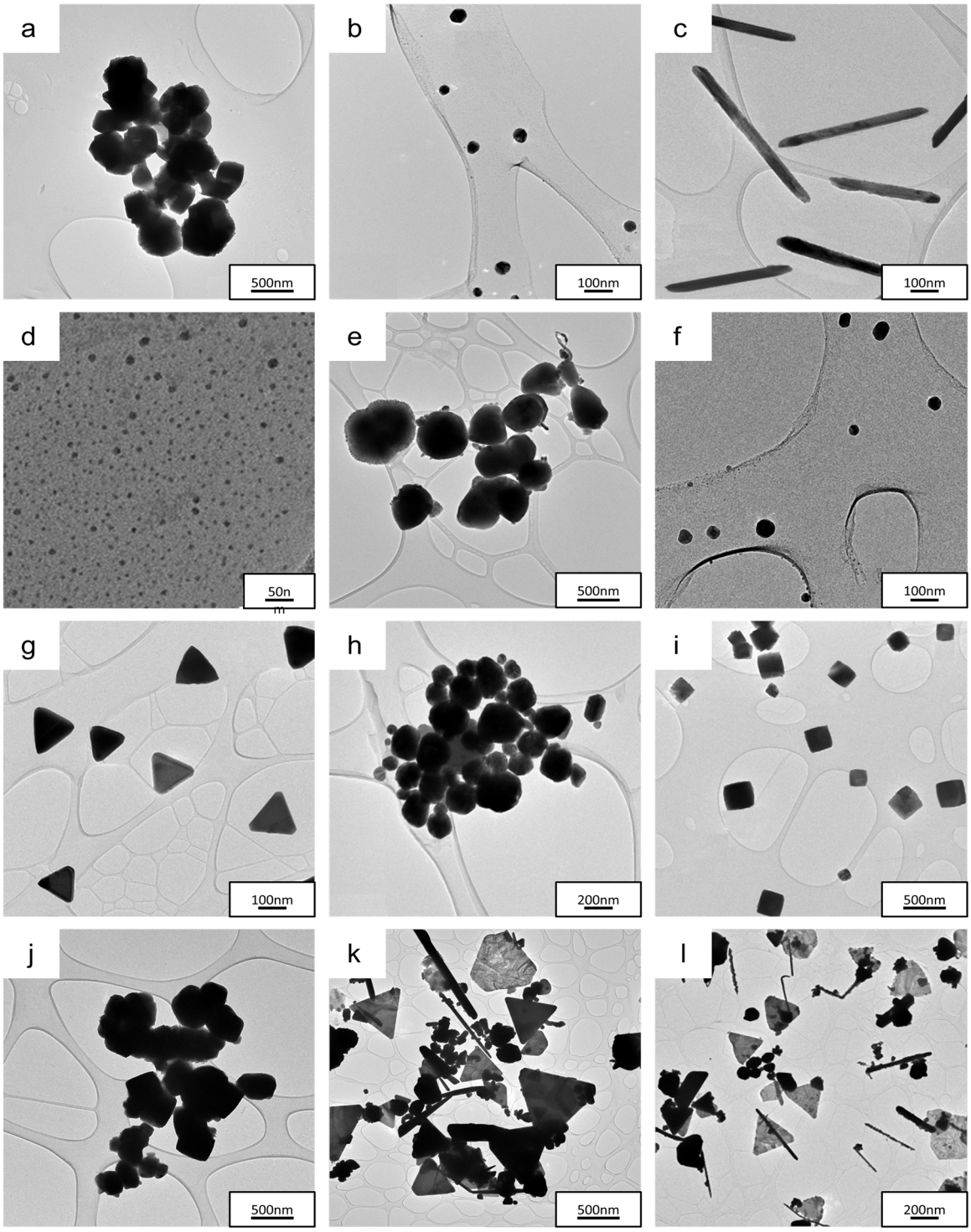


**Figure 4.1:** TEM images of the nanoparticles synthesized from 12 formulations as per the Full Factorial Design.

Surfactant-driven growth of geometric nanoparticles has been successfully conducted by exploiting its surface-adsorbing nature. Adapting Tah and associates (2011) theory of

cationic complex formation, the surfactants form aggregates in specific ratios baring specific energy profiles. It can be assumed that these cationic complexes have preferential adsorption based on its energy and affinity for certain charged facets of the nanocrystal and its own energy profile. The dual surfactants used compete preferentially for the various faces of the nanocrystals during synthesis after nucleation controlled facet-growth and consequent shape formation. Slight surfactant concentration variation significantly affects nano-shape of crystals as shown in this design and may be attributed to the anisotropy of the cationic complex adsorption on preferential crystal facets. Evolving nanoparticle morphology is clearly evident in the comparison of the experimental formulations. As a result of manipulating CTAB and SDS ratios, the surface energy of the nanocrystals, adsorption energy of the surfactants and interaction sites provided by the dominant molecules in solution consequently give way to the growth of neo-geometric nanoparticles.

According to distinguished mathematical physicist J. Willard Gibbs, matter will attain a shape in which the total surface energy is minimal (Gibbs, 1878). The general shape of a nanocrystal will therefore assume polyhedron geometry (Figure 4.2c) when the CuNPs were synthesized deficient of either surfactant to interfere with facet growth or energy alteration within the system. There were no additional factors to deviate the standard growth of the nanocrystals. Gibbs adsorption equation based on the conditions of equilibrium in a system is given as:

$$d\sigma + \Gamma . d\mu = 0 \qquad \text{(Equation 4.1)}$$

Where d is range of intermolecular force, σ is surface tension, $\Gamma$ is adsorption and $\mu$ is chemical potential, supplements the theory of minimising surface energy of a crystal. It can then be supposed that faces with a relatively low surface energy will dominate the equilibrium shape (Barmparis *et al*., 2015) and addition of surfactant subsequently obstructs the stable geometry and influences surface energy variation on the crystals facets. In addition, theoretical simulations and considerations based on the Wulff theorem classify characteristic nanocrystal shapes according to surface energies (Barmparis *et al*., 2015). The concept of this theory allows for the analysis and includes the application of surfactants tailoring nano-shape. With regards to Wulff's theory, the equation:

$$\gamma hkl = \gamma hkl + \theta \frac{Eads}{Aat} \qquad \text{(Equation 4.2)}$$

where γ(*hkl*) refers to the interface tension between the *hkl* facets, Eads is the adsorption energy, θ is the surface coverage and Aat is the area per surface atom, interactions between the adsorbing agents are crystal are crucial (Barmparis *et al*., 2015). Thus, preferential adsorption of surfactant molecules reduces the surface energy of particular facets and typically adopts a state of equilibrium supporting the growth of neo-geometric CuNPs (Figure 4.1). The CTAB and SDS complex evidently compete for adsorption on the crystal facets based on energy profiles and varying molar concentrations assist with providing a principal adsorbent. In the synthesis of nanocrystals, the high-energy facet grows at a higher rate than low-energy facets concluding in the fast growing faces disappearing resulting in a nanocrystal with low-energy facets (Liao *et al*., 2014) which supports the equilibrium theory as per Gibbs.

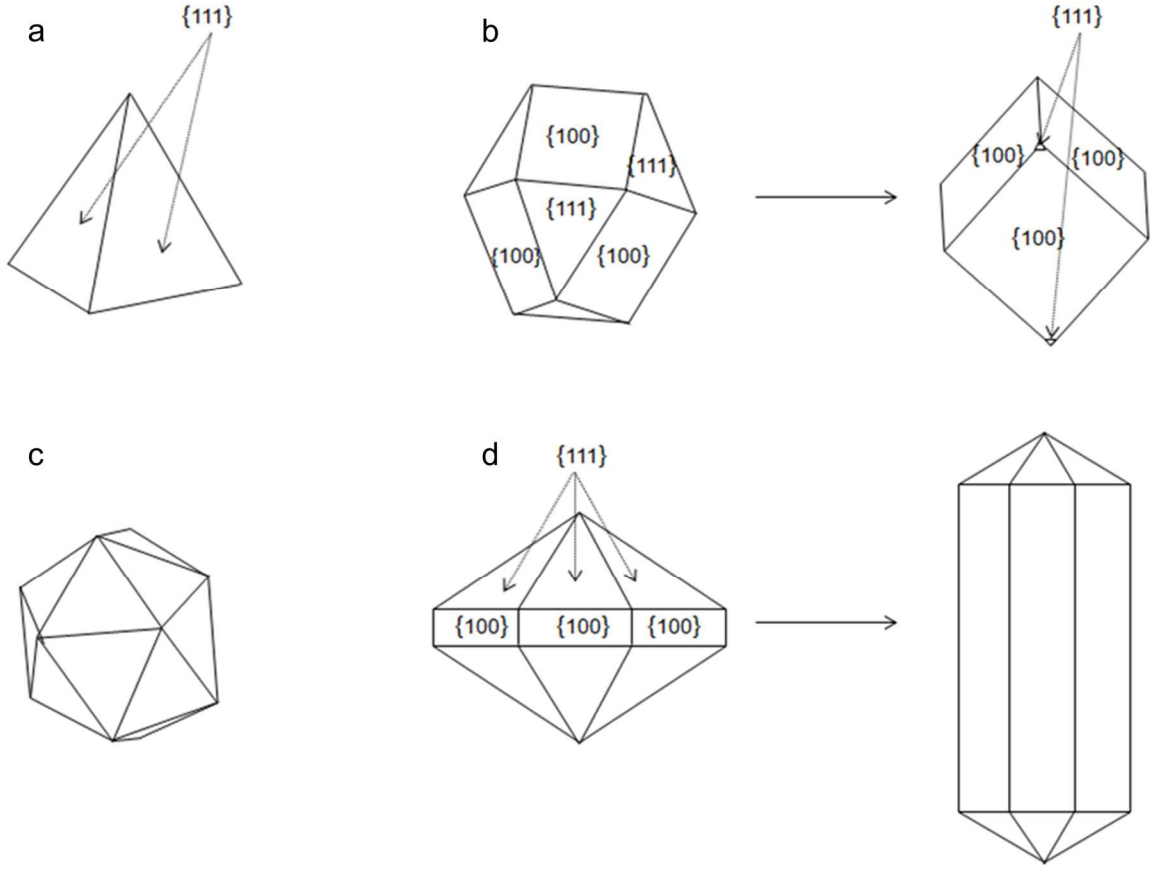


**Figure 4.2:** Precursor nuclei and geometric structures from which nanocrystals arise.

In this study, the growth of the neo-geometric CuNPs is in congruence with the adsorption of dual surfactants competing for preferential facets, adsorption on certain facets causing a reduction of surface energy, hence, directing geometric growth of the nanocrystals. Formulations 1 (Figure 4.1a), 5 (Figure 4.1e), 8 (Figure 4.1h) and 10 (Figure 4.1j) produced irregular spherical nanoparticles arising from the polyhedron nucleus (Figure 4.2c). The difference in irregularity can be explained by the unequal adsorption of the surfactants and

due to the variant concentrations, the degrees of irregularities are obvious. CTAB or SDS adsorb onto preferential faces causing certain faces to appear larger than others. Formulations 2 (Figure 4.1b), 4 (Figure 4.1d) and 6 (Figure 4.1f) are also initiated from the polyhedron, however, the ratios of the different surfactants are equal resulting in perfect spherically shaped nanocrystals. The size discrepancy is due to the different surfactant concentrations used and its rate of adsorption. Observation of the shape formation between Formulation 2 and 6 also clearly indicates the size reduction of the spheres upon the addition of SDS corroborating the use of SDS in controlling nano-size (De and Mandal, 2013).

Formulations 3 (Figure 4.1c), 7 (Figure 4.1g) and 9 (Figure 4.1i) are all homogenous samples of idealistic geometries with varying aspects from rods to cubes and pyramids due to the variation in SDS concentration. Upon addition of SDS whilst maintaining 0.02M CTAB, the aspect ratio of the nanoparticles showed a fundamental decrease in aspect ratio between the nano-rods and nano-cubes. Further increasing the SDS concentration reduced the number of geometric aspects resulting in a change from a four-aspect structure to a three-aspect structure and additionally reducing the size dimensions of the nanoparticles. The numbers of sharp aspects increase and decrease spontaneously, showing responsiveness to increasing SDS in the presence of 0.02M CTAB.
The elongated decahedron (Figure 4.2c) which forms the rod-shaped nanoparticle (Figure 4.1c) is obtained by lowering the {100} surface energy (Ringe *et al*., 2013). From this, it can be deduced and applied that lowering the surface energy of a facet will potentiate its ability to become the dominating facet, hence, eventually acquiring properties of distinguished geometries. This theory allows for the dictation of shape through surface energy, tension and selective adsorption of surfactants. The pyramidal nanocrystals (Figure 4.1g) grow from the tetrahedral nucleus (Figure 4.2a) by competitive adsorption on the {111} facets creating the dominant faces of the crystal. Upon the addition of SDS to the stable 0.02M CTAB, cube-shaped nanocrystals are fabricated from the cuboctahedron precursor nucleus (Figure 4.2b) and are characterized by the selective adsorption onto the {100} face causing the {111} face to grow rapidly and eventually disappear due to maintaining its high surface energy. The homogenous geometries synthesized at 0.02M CTAB is an indication of complete adsorption control and surface energy direction when synthesizing geometric CuNPs.

Formulations 11 (Figure 4.1k) and 12 (Figure 4.1l) consist of heterogeneous geometrical CuNPs when 0.03M CTAB is used with varying SDS concentrations and differ in size which can be correlated to the size-controlling factors of SDS. The heterogeneous sample is described as such owing to the possible erratic adsorption of surfactant when used at that

particular CTAB concentration. Concentration variation of the dual surfactants gives eccentric formulations based on surface energy which has been exploited in this design.

### 4.3.2. Analyses of the stability and aggregation potential of copper nanoparticles

Zeta potential, as an indicator of surface charge, gives the probability of stability of the sample. A potential greater than +25mV or lower than -25mV indicates a higher stability and reduced likeliness to aggregate due to the repel of the charged nanoparticles. Ascorbic acid has a negative charge, hence formulation 6 (Table 4.3) synthesized devoid of surfactant has a negative potential (Roy *et al*., 2003). The reducing agent also serves as a stabilising agent by binding to the surface of the synthesized nanocrystal, preventing aggregation of the nanoparticles. The results indicate a change in surface charge with surfactant additions and concentrations. The use of cationic CTAB and anionic SDS manipulates the surface charge from the standard negative charge of the CuNPs synthesized without surfactant as shown in Table 4.3. The surface charge of the CuNPs synthesized with CTAB as the independent surfactant are fairly stable with positive potentials and the least stable values are due to the high concentrations of both surfactants simultaneously used in CuNP synthesis. Formulations with outlying potential values have CTAB and SDS concentrations cancelling a strong positive or negative value resulting in surface charge readings that are minimally unstable.

**Table 4.3:** Measured responses as per a Full Factorial Design.

| Formulation | [CTAB] (M) | [SDS] (M) | Geometrical structures | Size of nanostructures (nm) | Zeta potential (mV) | Figure |
|---|---|---|---|---|---|---|
| 1 | 0.04 | 0.000 | Irregular spheres | 500 ±30 | 33.5 | 4.1a |
| 2 | 0.00 | 0.087 | Spheres | 60 | -32.8 | 4.1b |
| 3 | 0.02 | 0.000 | Rods | 500 x 40 | 27.0 | 4.1c |
| 4 | 0.04 | 0.100 | Spheres | 5 ±3 | 16.9 | 4,1d |
| 5 | 0.00 | 0.100 | Irregular spheres | 500±60 | -36.1 | 4.1e |
| 6 | 0.00 | 0.000 | Spheres | 100 ±9 | -28.6 | 4.1f |
| 7 | 0.02 | 0.100 | Pyramids | 150 ±12 | -21.2 | 4.1g |
| 8 | 0.04 | 0.087 | Irregular spheres | 200±10 | -18.4 | 4.1h |
| 9 | 0.02 | 0.087 | Cubes | 200 ±13 | -30.6 | 4.1i |
| 10 | 0.03 | 0.000 | Irregular spheres | 300 ±11 | 27.1 | 4.1j |
| 11 | 0.03 | 0.087 | Combination | Shape dependent | -6.72 | 4.1k |
| 12 | 0.03 | 0.100 | Combination | Shape dependent | -34.4 | 4.1l |

### 4.3.3. Evaluation of copper nanoparticle crystallinity and elemental composition of copper nanoparticles

The powder XRD patterns of the CuNPs (Figure 4.3a) correlate with highly oriented crystalline CuNPs. Patterns across all 12 formulations share the same peaks of similar intensity and conclude that crystallinity is maintained in all samples. All spectra correspond to phase-pure copper according to the literature pattern (JCPDS, File No 04-0836) with strong, prominent peaks at 43.1°, 50.3° and 74° related to the (111), (200) and (220) planes

of copper crystals, respectively. The results confirm the crystalline copper peaks are indexed to an FCC crystal structure which is congruent with the native crystal structure and orientation. At 35.5° (002) a small proportion of copper oxide is detected across all samples and is accounted for by minimal interaction with oxygen. The CuNPs composition uniformity is maintained and the low oxide presence does not significantly affect the function of the CuNPs as a drug delivery system. Essentially, the synthesis of the nanocrystals yields highly crystalline nanostructures and the surfactant adsorption maintains crystallinity by preventing oxidation by the environment.

The CuNPs were also analyzed for elemental composition via EDS plots as shown in Figure 4.3b. The plots exclusively display the characteristic peaks of elemental copper and complement the XRD spectra with composition and crystallinity analyses. A dominant $K\alpha_1$ peak at 8.0477keV followed by a smaller $K\beta_1$ peak 8.0905keV show strong signals of copper atoms confirming pure copper formation. The peak at 0.9498keV demonstrates the $L\beta_1$ peak for electrons in the L-shell. As expected, EDS plots for all CuNPs samples resulted in similar spectra of prominent copper peaks. Thus, both XRD and EDS metal characterization indicate the synthesis of pure copper. The strong FCC copper peaks from XRD and elemental copper peaks EDS (Figure 4.3) demonstrates that the thermal-chemical reduction method used in conjunction with ascorbic acid serving the dual function of reducing agent and capping agent and two surfactants results in the synthesis of pure copper nanocrystals without additional impure phases.

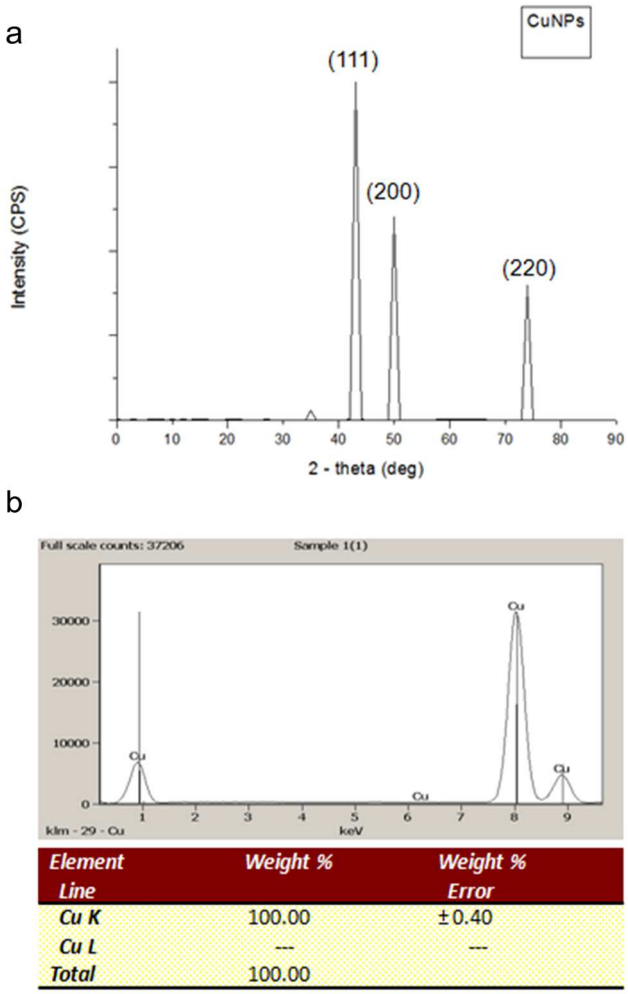


| Element Line | Weight % | Weight % Error |
|---|---|---|
| Cu K | 100.00 | ±0.40 |
| Cu L | --- | --- |
| Total | 100.00 | |

**Figure 4.3:** a) XRD patterns of the neo-geometric nanosystems; b) energy dispersive spectra indicating elemental analysis.

### 4.3.4. Investigation of surface surfactant-coating due by thermal degradation of copper nanoparticles

TGA assessed the relative composition of the ascorbic acid, CTAB and SDS as capping agents on the CuNPs. Representative TGA curves obtained for formulations 6 (Figure 4.4a) and 9 (Figure 4.4b) indicate the degradation of the respective capping agents. These curves were selected for representation as formulation 6 was synthesized devoid of surfactant and formulation 9 depicts an average surfactant concentration. Figure 4.4a shows one key degradation point between 100-340°C which can be related to the decomposition of the ascorbic acid on the surface of the CuNPs. Formulation 9 (Figure 4.4b), capped with ascorbic acid, CTAB and SDS, displays two key degradation steps. The first weight loss step in Figure 4.4b occurs between 150-230°C indicating the degradation of ascorbic acid as the capping agent and between 300-410°C which is attributed to the degradation of the adsorbed surfactants. All formulations synthesized with surfactant have TGA profiles similar to Figure 4.4b.

The degradation of the ascorbic acid in formulation 6 occurs at temperatures between 100-340°C and between 150-230°C in formulation 9. This data indicates the capping effect of the ascorbic acid and the intramolecular interactions between ascorbic acid and the surfactants resulting in a slightly raised degradation temperature in formulation 9. At the end temperature of 900°C, an average of 95.7 - 97% of sample remains. Copper degrades at temperatures higher than 900°C indicating that the degradation that occurred is attributed to the supporting surfactants in the samples and that the synthesized CuNPs are thermally stable. The change in mass can be translated to the ratio of capping agents to CuNPs. A shell of about 3% of ascorbic acid and 5% of surfactant adsorption was determined from thermogravimetric analysis, resulting in a remaining 95-97% of the mass due to the copper.

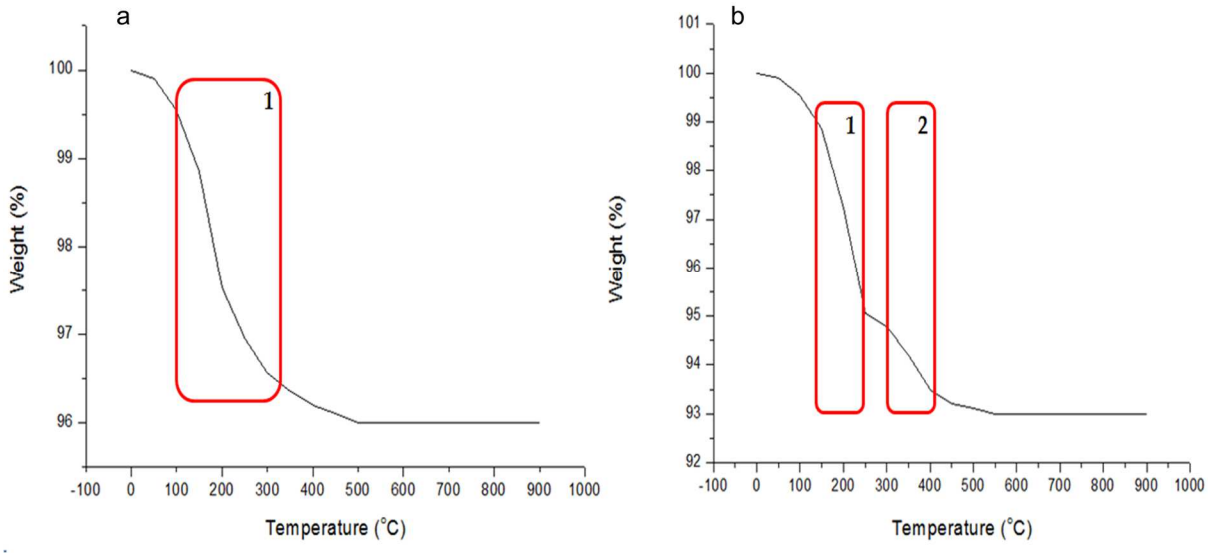


**Figure 4.4:** TGA analysis confirming the surfactant adsorption on the CuNPs.

### 4.3.5. Analysis of a full factorial response surface design

The nanoparticle geometry and zeta potential for the experimentally synthesised formulations were included in the statistical design for identification of formulations with a homogenous, distinctive nano-shape and a stable surface charge. Residual analysis (run order, predicted values) for the nanoparticle geometry and zeta potential data (Figure 4.5) generally showed random scatter i.e. no trends, indicating none of the underlying assumptions of the multiple regression analysis were grossly violated; however a drastic discrepancy was noted in the histogram of the residuals (Figure 4.5a) indicative of a degree of non-constant variance. This, however, was expected due to the nanoparticle shape formation being independent of ordered surfactant addition. The normal probability plots of the residuals fell on a straight line indicating the data to be normally distributed with no evidence of unidentified variables.

a

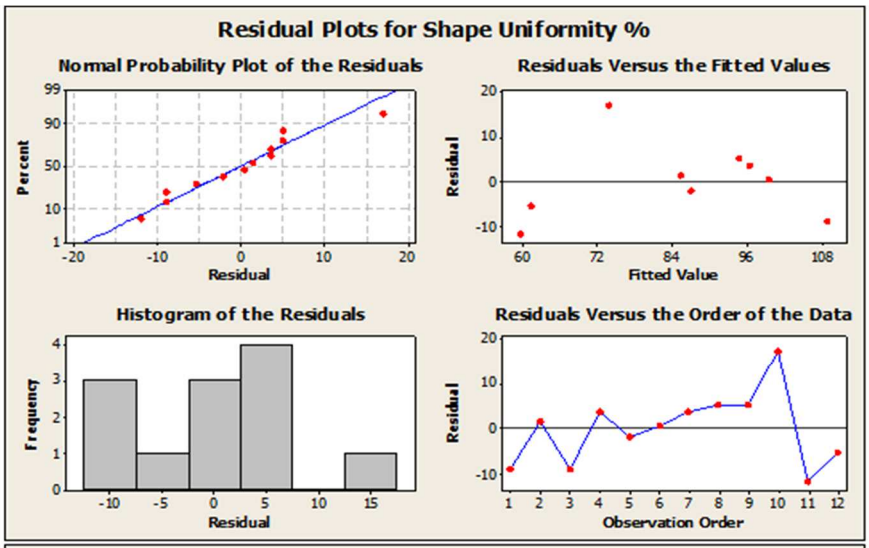


b

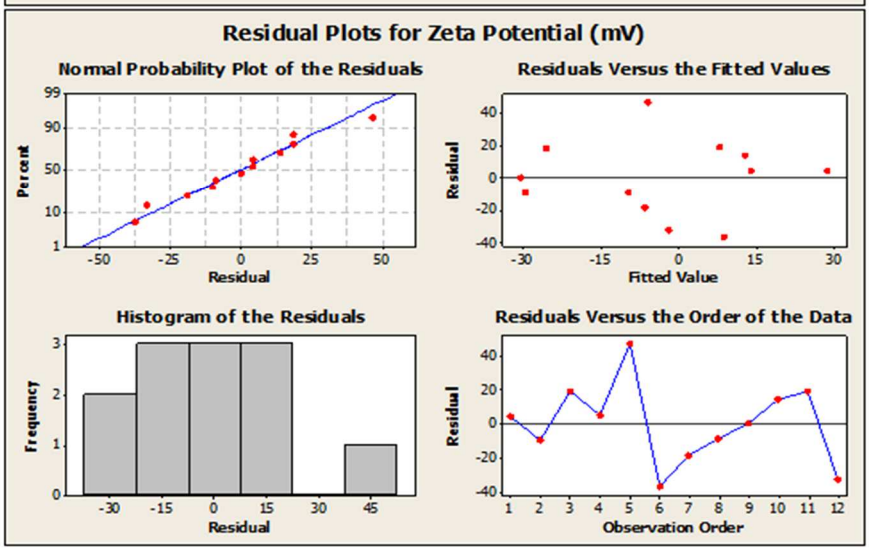


**Figure 4.5:** Residual plots: a) shape uniformity per sample; b) zeta potential.

### 4.3.6. Response surface analysis

Main effects, interaction and response surface plots were obtained for the measured responses (shape uniformity and zeta potential) based on the experimental model. The relationship between the independent variables and the responses can be further explained through graphical illustration of the effect of the independent variables and their interactions. The interaction effects are estimated by subtracting the mean positive response values from the mean negative response values and the estimated interaction effects of the responses studied are shown in Figures 4.6b and 4.7b. The main effects plots (Figures 4.6a and 4.7a) determine the relative significance of the effects across factors and the surface plots generated (Figure 4.8) represent the functional relationship between the response and the experimental factors (du Toit *et al*., 2008).

#### 4.3.6.1. Main effects and interaction effects plots on the formulation responses

Interaction effects represent the combined effects of factors on the dependent measure where the impact of one factor depends on the level of the other factor when an interaction effect is present. The plot displays both the levels and mean of each level of one variable on the X axis, ultimately testing the moderation. A “main effect” is the effect of one the independent variables on the dependent variable, ignoring the effects of all other independent variables (Dawson, 2014).

The main effects plots (Figures 4.6a and 4.7a) depict a horizontal line drawn at the overall mean. The effects of the variables on the formulation are represented by the differences between the mean and the reference line. Both CTAB and SDS have a definite effect on the geometry control and surface charge of the nanosystems (Figures 4.6a and 4.7a). The main effects for shape uniformity (Figure 4.6a) did not drift significantly from the overall mean at CTAB concentrations of 0M, 0.02M and 0.04M much unlike the shape uniformity behaviour when using CTAB at 0.03M. This substantiates the heterogeneous growth of geometric CuNPs indicating minimal shape controlling activity. With SDS, however, all 3 concentrations used lie near the mean showing stability with regards to crystallizing homogenous geometries. SDS undoubtedly has an effect on CuNPs geometric organization but this is nominal in comparison with CTAB. The main effects for zeta potential analysis (Figure 4.7a) show the difference in effect that SDS has with CTAB. Anionic SDS has a major effect on zeta potential but is highly influenced by the presence of CTAB and variation in effect occurs due to surfactant concentration differentiation. CTAB has fairly more stable effect than SDS having the main effects plot points close to the zeta potential mean.

In all interaction plots disordinal interactions were observed indicating that the interaction effect between the variables is significant. The greater deviations imply higher degrees of interaction as can be seen especially with varying CTAB concentration. In the concurrent use of CTAB and SDS as can be seen in Figure 4.6a when CTAB is used at 0.02M and 0.04M, irrespective of SDS concentration, the shape uniformity maintains 100% shape uniformity verifying the competence of the high shape controlling activity of CTAB at these concentrations. The interaction plot for zeta potential shows much higher interactions between the different design formulations compared to the surfactant interaction plots for shape uniformity. CTAB and SDS have a strong cationic and ionic charge, respectively, and the fluctuation of the surface charge is noteworthy. The sharp increase of zeta potential when using 0.087-0.1M SDS shows the effect of this surfactant, especially in the absence of CTAB. In the presence of 0.02M CTAB, the effect is not as significant confirming the equalising effect of the surfactants when used concurrently.

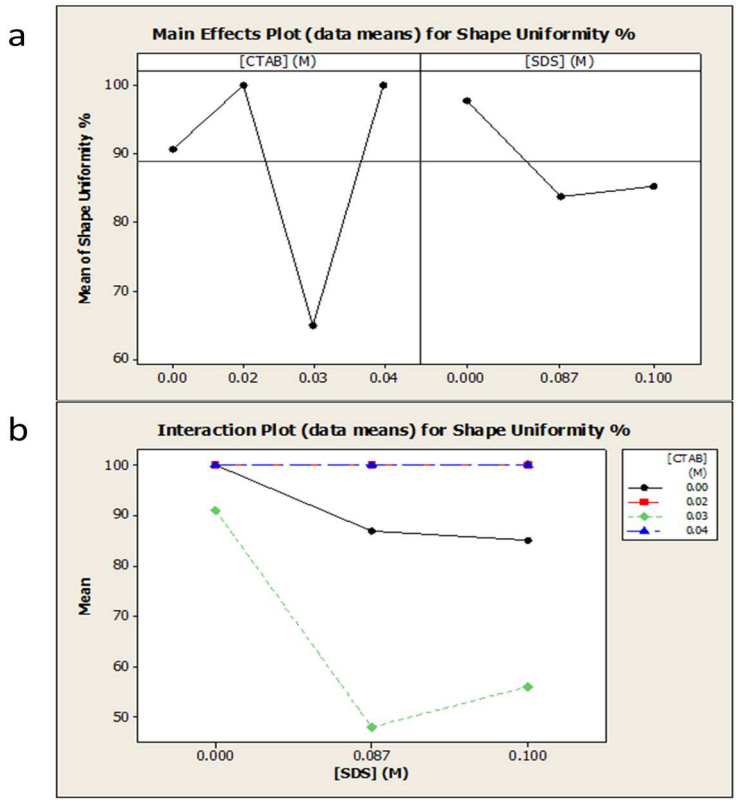


**Figure 4.6:** a) main effects; b) interaction plots for shape uniformity.

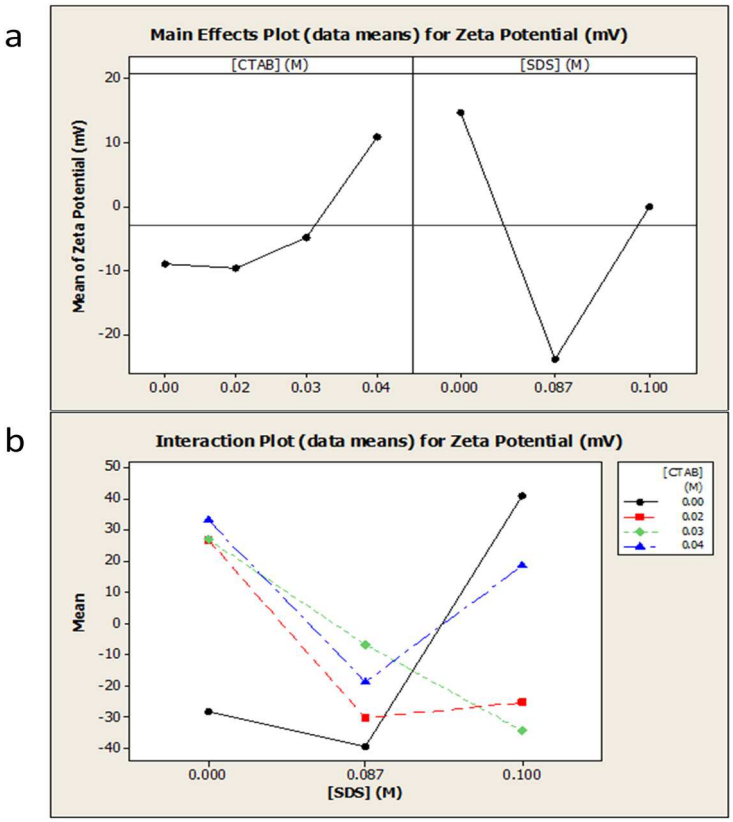


**Figure 4.7:** a) main effects; b) interaction plots for zeta potential.

#### 4.3.6.2. Response surface and contour plots on the formulation responses

Contour plots were used to represent the functional relationship between the experimental variables and the responses achieved. The effects of CTAB and SDS on shape uniformity are depicted in Figure 4.8a. It is obvious that CTAB plays the crucial deciding role in shape formation and shape uniformity. The highest control of shape uniformity is seen at CTAB concentrations 0-0.02M which is also where the most distinctive nano-geometries are formed. Increased concentrations of CTAB (>0.02M) and SDS (>0.02M) resulted in the least ideal formulations consisting of heterogeneous samples. Reducing the concentration of SDS while maintaining a high CTAB concentration show to yield homogenous samples of CuNPs. A striking characteristic is the inability of forming uniform shapes throughout one CuNP formulation at SDS concentrations of 0.04-0.1M which may indicate a higher ability of SDS to competitively dislocate the adsorption of CTAB from certain facets or SDS providing an unstable energy in the system. The 100% shape uniformity at CTAB <0.02M is slightly reduced upon the addition of SDS and the reduction increases with an increase in SDS. It is apparent that SDS has the energy to displace CTAB from its adsorption sites resulting in formulations of low homogeneity, however, at different CTAB concentrations SDS may play the key role in shape dictation and uniformity.

Contour and response surface plots for zeta potential (Figure 4.8b) is highly dependent on both surfactants. It has a very large characteristic region showing anionic SDS responsible for low zeta potential values (≤25mV) and 2 smaller regions showing cationic CTAB responsible for the higher zeta potential values (≥25mV). As seen in the plots, SDS maintains the stability of the CuNPs but the potential fluctuates upon the addition of CTAB. In the presence of SDS, as CTAB concentrations increase, the stability reduces. However, a notable occurrence in the zeta potential occurs when CTAB is introduced into the system at low SDS concentrations of ≤0.02M where stability is maintained. Potential values are seen to fall most out of the stable range when CTAB is 0.02-0.035M in the presence of SDS at 0.02-0.06M and increases in stability upon reducing SDS. With opposing charges, both surfactants used simultaneously may neutralise the system and contribute to the aggregation of the CuNPs. The pattern is observed again when SDS concentrations are ≥0.09M and it can be presumed that the stability will continue to fluctuate when CTAB is used at 0.02-0.035M at higher concentrations of SDS to neutralise the charge effect and reduce stability. At CTAB ≥0.04M, the cationic charge is sufficient enough to overcome the anionic charge of SDS and resume stability of the CuNPs nanosystem.

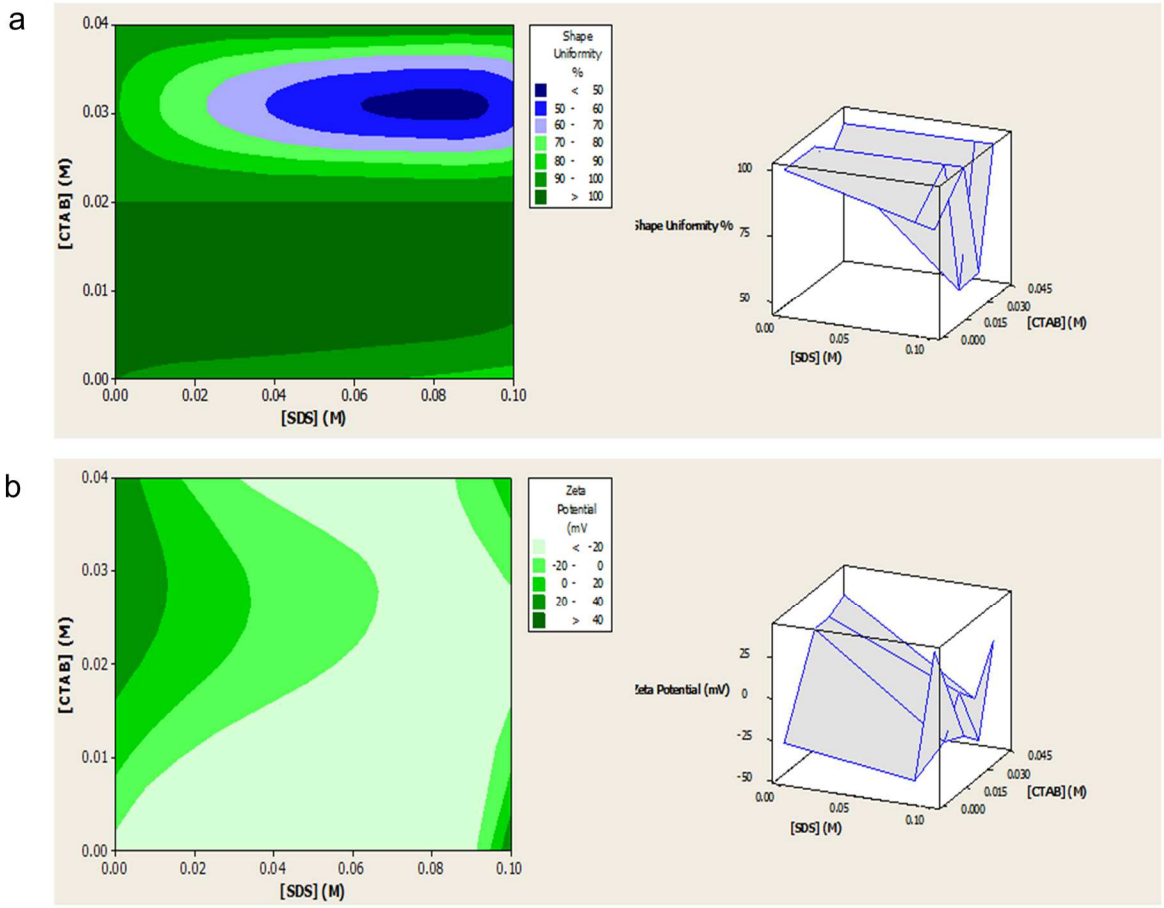


**Figure 4.8:** Contour plot and response surface plots. a) shape uniformity per sample; b) zeta potential.

### 4.3.7. Response optimization of the neo-geometric copper nanoparticles

A response optimization procedure was used to obtain the preferred levels of the selected formulation components to yield specific shapes. Optimal formulations were developed following simultaneous constrained optimization of geometric shape uniformity and zeta potential. Maximization of shape uniformity and targeting of zeta potential values based on the specific shapes required were used for response optimization. The optimized levels of the independent variables and their predicted responses were then determined. Optimal levels of the independent variables and constraint settings were utilized as well as goals for the response that would achieve the desired characteristics are listed in Table 4.1. Based on the analysis and aims of the study to generate homogenous samples of CuNPs using the necessary parameters (Table 4.1), the optimized formulations are listed in Table 4.4.

**Table 4.4:** Optimized formulations or representing homogenous samples of stable neo-geometric CuNPs.

| Formulation | [CTAB] (M) | [SDS] (M) | Shape Uniformity (%) | Zeta potential (mV) | Surface area per nanoparticle ($nm^2$) | Volume per nanoparticle ($nm^3$) | TEM Images |
|---|---|---|---|---|---|---|---|
| 3 | 0.02 | 0.000 | 100% Rods | 27.0 | 62831.85 | 611 563.37 | 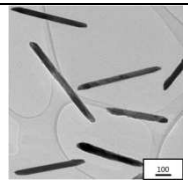 |
| 4 | 0.04 | 0.100 | 100% 5nm Spheres | 16.9 | 78.54 | 65.45 | 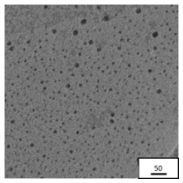 |
| 6 | 0.00 | 0.000 | 100% 90nm Spheres | -28.6 | 31415.93 | 523 598.78 | 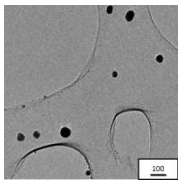 |
| 7 | 0.02 | 0.100 | 100% Pyramids | -21.2 | 38712.00 | 421 875.80 | 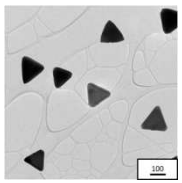 |
| 9 | 0.02 | 0.087 | 100% Cubes | -30.6 | 240000.00 | 8 000 000.00 | 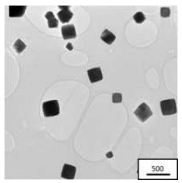 |

The formulation parameters were finalised based on the shape uniformity behaviour and stability of the systems. In varying the surfactant concentrations, heterogeneous and irregular samples were also achieved. Samples providing stable CuNPs of homogenous geometries were the idealistic characteristics as per the aim of the study. The required zeta potential values were primarily based on nano-shape but as an important parameter, the surface charge needed to correlate with stability.

### 4.3.8. Qualitative and quantitative analyses of cellular internalization studies based on nano-geometry

Cell uptake was conducted by incubating the optimized geometrical CuNPs with NHEK cells over a 24 hour period to elucidate the effect of nano-shape on endocytosis rates. Qualitative (Figure 4.9) and quantitative characterization (Figure 4.10) depicts the variation in internalization kinetics in the determination of nano-shape with the highest cellular internalization for use as an optimized drug delivery carrier with elevated uptake over the shortest time period.

Within the first hour of CuNPs incubation with the keratinocytes, it was noted that the nanoparticles began the endocytosis process by adhering to the cell membrane. Interactions between the nanoparticles to be endocytosed and receptors in the cell membrane assist in triggering recognition and uptake of the nanoparticles which consists of two processes, adherence to the outer cell membrane and actual internalization (Lesniak *et al*., 2013). CuNPs detected via ICP-OES analysis within the first hour (Figure 4.10) can be attributed to CuNPs that have started the adhesion process and attached to the cell membranes.

Within the second hour, the process of adherence and attachment to the cell membrane increased and by the end of the fourth hour of cell-nanoparticle incubation, the CuNPs had internalized. The initiation of CuNP endocytosis steadily resulted in the complete uptake of the nanocrystals with small yet distinctive differences in rates of cell uptake and can be accounted for in conjunction with qualitative data. Internalization kinetics differs slightly with the cubic CuNPs persisting with the highest uptake throughout each period in the 24 hours of incubation. The rate of uptake of the 5nm spherical CuNPs remained steadily behind the 200x200nm cubes; with the pyramids, 90nm spheres and rods following, respectively (Figures 4.9 and 4.10). Time-dependent internalization is clearly indicated by the results showing more particle-cell associations with longer incubation time (Zhao *et al*., 2013). The uptake kinetics display a slight initial transient uptake followed by steady uptake at 4 hours after initial attachment, thereafter pursuing a linear uptake pattern. The cube-shaped CuNPs

having higher copper concentrations post analysis also shows the higher capability of cell membrane adhesion as compared to the other nano-shapes.

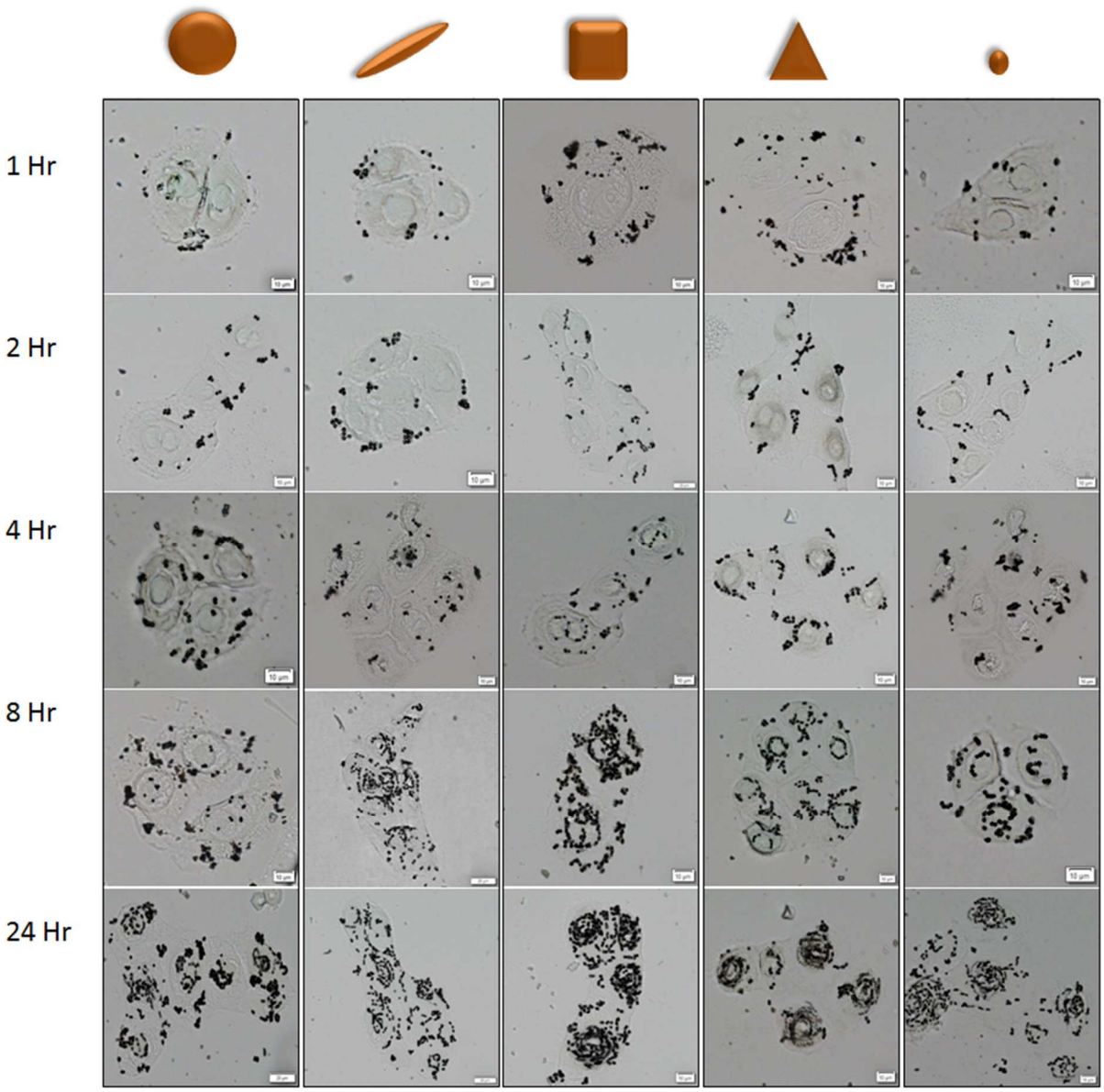


**Figure 4.9:** Phase contrast images of geometric CuNP internalization over a 24 hour incubation period.

The mechanism of physical penetration into the cell differs between the various geometries due to the actual structures of the different nanoparticles. Pertaining to the spheres where there is no sharp end or aspect ratio, endocytosis occurs regardless of any internalization mechanism. However, with rods, cubes and pyramids it is dependent on the number of faces for attachment, the aspect ratio of the shape and the angle of orientation. This study on the geometric effect of nanoparticles investigated and challenged the claim by Némethová and associates (2017) that size is the primary determinant factor for cell uptake.

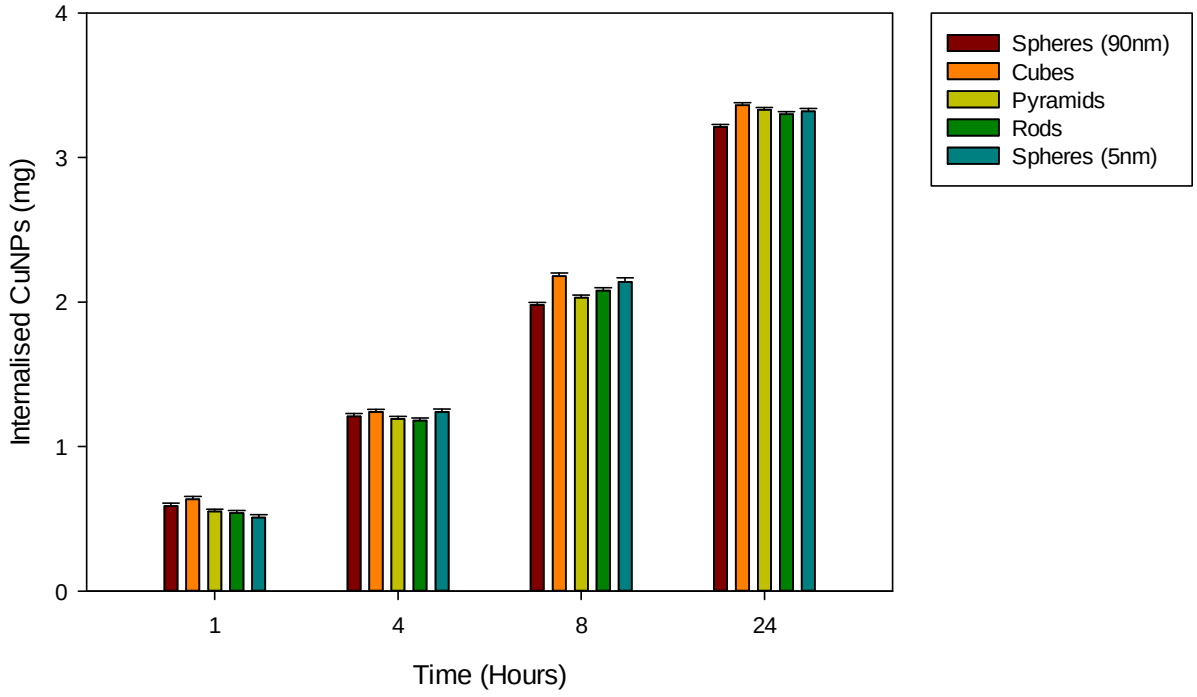


**Figure 4.10:** Quantitative analysis of cell internalized CuNPs over 1, 4, 8 and 24 hours. Data presented are mean ± SE of three experiments performed in duplicate. *$p \leq 0.05$.

The increase in volume of the geometric nanoparticles (Table 4.4) consequently requires more energy for the internalization to occur as the surface area between the nanoparticle and the cell membrane increases. However, the effect of the orientation and aspect of the shape on its attachment to the cell membrane also shows to have a key role. After the nanoparticle has attached to the surface of the membrane, according to Yang and Ma (2010), under the influence of the elastic deformation of the bilayer, the long axis of the nanoparticle is compelled to be as perpendicular as possible to the cell membrane plane. This occurrence will increase the contact area between the nanoparticle and membrane to allow for quicker uptake and will then only require the minimum amount of energy for the endocytosis with respect to the different nano-geometries and volumes involved. Agreeing with increasing contact area for quicker uptake, Venkataraman and co-workers (2011) showed that a larger surface area allows for more multivalent ionic interactions with the cell membranes to undergo clathrin- and caveolae-mediated endocytosis as well as to a lesser extent, macropinocytosis. This was also supported by Munoz and associates (2013) who stated that an increased contact area with the cell surface provides potentially more sites for interaction and has been previously identified as an important contributor to enhance nanoparticle targeting effects. In support of this theory, several researchers (Venkataraman

*et al*., 2011; Hao *et al*., 2012; Kolhar *et al*., 2013; He and Park, 2016; Wang *et al*., 2016) proved that higher aspect ratios resulted in higher internalization rates.

Taking the results into consideration, it may be argued that the nanoparticle volume does not play a significant role when compared to the geometry and effect of particle surface structure on cell uptake. The geometry of the nanoparticles is an independent factor and the endocytosis process may be dependent on this completely. In addition, the shape anisotropy and initial orientation of the particle are crucial to the nature of the interaction between the particle and lipid bilayer. The endocytic potential of nanoparticles across a lipid bilayer is also determined by its contact area, local curvature of the particle at the contact point, nanoparticle volume affecting translocation indirectly and nanoparticle rotation which can complicate the penetration process (Yang and Ma, 2010). Li and co-workers (2012) indicated that nano-shape affects the kinetics of endocytosis, also reiterating that nanoparticle rotation regulates the competition of receptor binding and membrane deformation. The internalization process comprises membrane invagination and nanoparticle wrapping where the strong binding energy results in the rotation of nanoparticles to maximise contact area with the membrane during the invagination stage (Li *et al*., 2012). Rotation of the nanoparticle after attachment leads to an arrested internalization state explaining the delayed uptake of the rods as compared to the cubes and pyramids due to the rods having a higher rotation because of its high aspect ratio, also dependent on its orientation to the cell membrane. The wrapping stage is doctored by the largest local mean curvature of the part of the nanoparticle bound to the membrane, hence, the varying uptake rates of the different nano-shapes with spherical nanoparticle uptake being the exception due to a continuous geometry.

The results from this uptake study oppose the theory of the rods having the highest uptake rates and show rods to have slow uptake in comparison to the other geometric CuNPs used. Cubes have the highest uptake and may be attributed to certain cells preferring sharp edges and recruiting actin filaments to wrap around the nanoparticle (He and Park, 2016). Pyramids and rods also have sharp edges explaining the higher internalization than 90nm spheres. With rod CuNPs, internalization depends on the orientation to the cell membrane as the pyramids are equilateral. After adhesion, the cell membrane maintains attachment and will rotate the nanoparticle during the internalization process therefore affecting uptake rates. Rods take longer to rotate if on an unfavourable axis and with the pyramid, the 120° outer angle takes longer to rotate than the 90° outer angle of the cube if incorrectly orientated. The internalization of the nanoparticle is also based on the curvature energy of lipid-bilayer membrane combined with contact adhesion energy for the particle−membrane interaction. Thus, the total energy is given by:

$\varepsilon_{tot} = \int_S dS[2\kappa H^2 + \sigma] - w \int_{Sad} dS$ (Equation 4.3)

where *S* is the entire membrane area, *Sad* the adhered membrane area, H the mean membrane curvature, κ the bending rigidity, σ the membrane tension, and w the adhesion strength for the interaction between membrane and nanoparticle (Dasgupta *et al*., 2014).

It is noted that the CuNPs with varying zeta potential values do not influence attachment or uptake kinetics whereby in order of highest internalization rates, -30.6mV (cubes), 16.9mV (5nm spheres), -21.2mV (pyramids), -28.6mV (90nm spheres) and 27mV (rods) there is no pattern during analyses. Typically, having a negatively charged cell membrane, it is expected that there would be higher uptake profile for the positively charged CuNPs, 5nm spheres and rods, due to electrostatic interactions with the cell membrane. In addition to surface charge variation, colloidal instability during the biological experiment affects uptake kinetics (Némethová *et al*., 2017) and has been considered. This is especially seen after the CuNPs have been internalized and is predominantly viewed in clusters or aggregates. This finding also assists with confirming the type of uptake pathway. It is most probable that nanoparticles with negative surface charges are likely to have the greatest affinity for caveolae-based uptake. Although surface chemistry and functional groups can influence CuNP-cell interaction, it has been reported that negatively charged nanoparticles can interact with cationic lipid domains in the lipid raft (Adjei *et al*., 2014). Irrespective of researchers confirming the rod shape for highest internalization due to the high aspect ratio, the principle theory of larger nanoparticle surface areas allowing for more attachment on cell membranes is the basis for the results obtained in this study with cubes having the highest surface area as compared to the other nano-geometries. The uptake kinetics is thereafter followed by the volume per CuNP relative to its geometry.

### 4.3.9. MTT assay

To examine the cytotoxicity of the geometric CuNPs, cell viability was analyzed using NHEK and HeLa cell models. The viability data of a normal cell line was compared with a cancer cell line to elucidate the difference in toxicity and the effect of the CuNPs when applied on healthy and cancerous cells for application purposes. The effect of nano-geometry of the CuNPs was analyzed as the primary toxicity factor, as well as at increasing concentrations to determine a toxic dose.

Figures 4.11a and 4.11b shows the clear differences in toxicity after incubation at increasing concentrations, with differences in nanoparticle shape and across both cell lines. Cell viability % reduced steadily in a CuNP dose dependent manner with a noted difference in

toxicity between the geometrically structured nanoparticles and the two cell lines. With an initial CuNP concentration of 6.25µg/ml serially increasing to 50µg/ml, the apparent change in cell viability indicates dose dependent toxicity having an average of 92.56% cell viability at a CuNP concentration of 6.25µg/ml, 73.56% at 12.5 µg/ml, 52.22% at 25 µg/ml and 33.33% cell viability at the highest CuNP concentration on the NHEK cell line. CuNP exposure to the HeLa cell line shows 79.16% cell viability at 6.25µg/ml, 55.18% at 12.5 µg/ml, 37.62% at 25 µg/ml and 26.23% cell viability at 50µg/ml. The median lethal concentration ($LC_{50}$) values of the CuNPs on the two cell lines occur at approximately 12.5µg/ml and 25µg/ml respectively for NHEK and HeLa cells. In general, irrespective of nano-shape and cell line, toxicity increased with an increase in CuNP concentration. The results confirm dose dependent toxicity and can be further considered for biological application.

The obvious variation in cell viability dependent on the geometric nanoparticles give an indication that nano-shape has an effect on cell toxicity. A similar tendency for toxicity based on nano-shape is seen with both cell lines; however, the viability % differs while the viability ratios between the different shapes remain constant. The MTT data in Figure 4.11a and 4.11b indicates slight but notable differences in viability percentage with regards to cube-shaped nanoparticles. A pattern occurs whereby at all concentrations and across both cell lines the cubic CuNP displays the lowest cell viability indicating highest toxicity followed by the 90nm spheres. The rod shaped nanoparticles demonstrate higher cell viability than the cubes and 90nm spheres but are clearly more toxic to both cell lines than the pyramidal and 5nm spherical nanoparticles. The order of $LC_{50}$ for shape-dependent toxicity on cell lines were cubes > 90nm spheres > rods > pyramids > 5nm spheres.

Taking the volume per nanoparticle into consideration (Table 4.4), the number of copper atoms in each geometrically organised nanoparticle would be directly proportional to its total volume. It can then be assumed that the increase in copper atoms would increase the cell toxicity due to the DNA degradation properties of copper as well as the nano-shape with the highest internalization rates. This is congruent with the cubic nanoparticles having the highest rate of internalization and occupying the largest volume compared to the other nano-geometries and displaying the highest toxicity potential. The increase in concentration of CuNPs internalized potentiates the toxicity due to its influence on producing reactive oxygen species (ROS) promoting DNA cleavage and subsequent metabolic inactivity (Jose *et al*., 2011). This principle can also be adapted for the other key shapes and their corresponding volumes irrespective of the number of CuNPs internalized.

Shape has an effect on cell toxicity that is directly related to shape volume. The structure of the nanoparticle forms a vehicle for the volume and will pose a possible medium for the entrapment of drugs in these geometrical nanoparticles assuming a Trojan Horse approach to drug delivery. Distinguishing the impact of the geometric factor on cytotoxicity is based on several other surface chemistry paradigms, therefore, when elucidating nano-shape and cellular toxic effects, it is completely dependent on maintaining many aspects such as the nanoparticle material, shape, surface charge and surface reactivity. Chithrani and associates (2006) and Han and co-workers (2006) both attributed the highest internalization rates to the spherical nanoparticle while Champion and Mitrogotri (2007) owed the nanoparticle orientation on the cell surface to internalization kinetics. Therefore, it can be deduced that several factors dictate cell uptake results unless consistency is maintained. In the instance that nanoparticles are specifically tailored for functional use, the concept is plausible.

The HeLa cells showed a higher susceptibility to toxicity to the copper than the NHEK cell line ranging from 15.55% to 13.36% over the concentration difference. The difference in toxicity across the two cell lines was expected, however, the degree of variation far exceeds the hypothesis. Despite the variation in toxicity between the nano-shapes, the consistent ratio of toxicity between the two cell lines is interesting. Mutational asymmetries between the two DNA strands in a cancer cell (Haradhvala *et al*., 2016) indicate current DNA damage in the HeLa cell line. CuNPs exerts a mechanism of DNA damage by ROS thereby inducing cell death. It can then be postulated that the CuNP-exerted toxicity may be easily potentiated due to the already damaged DNA of the cancer cells as opposed to the healthy DNA strands in the keratinocytes.

Comparatively, in a study conducted by Wang and associates (2015) on alumina nanotubes of varied aspect ratios and their toxic effects on mouse macrophage cells and human breast cancer cells, it was demonstrated that macrophage cells were more sensitive and responsive to the nanotubes showing higher toxicity than the breast cancer cells. Their results also distinctively identify nano-shapes with longer aspect ratios with high toxicity, very much unlike the data acquired in our study which shows the cube of low aspect ratio to be most toxic. Hence, the importance of tailoring nano-characteristics for stream-lined purposes. A recent study by Zong and co-workers (2017) showed a cell proliferation effect of copper-incorporated titanium nanotube arrays in addition to research by Bagchi's research group (2012) who concluded that at concentrations under 100mg/ml, CuNPs adsorbed onto ceramic composites had negligible toxicity in cancer cell lines. This differed to the current study as concentrations below 100mg/ml exhibited significant toxicity. Lin and associates (2016) also confirmed dose dependent toxicity when copper ions were released into an

osteogenic cell line while Zhang and research group (2015) studied titanium-copper alloys on MG63 cells confirming no toxicity or proliferation after incubation.

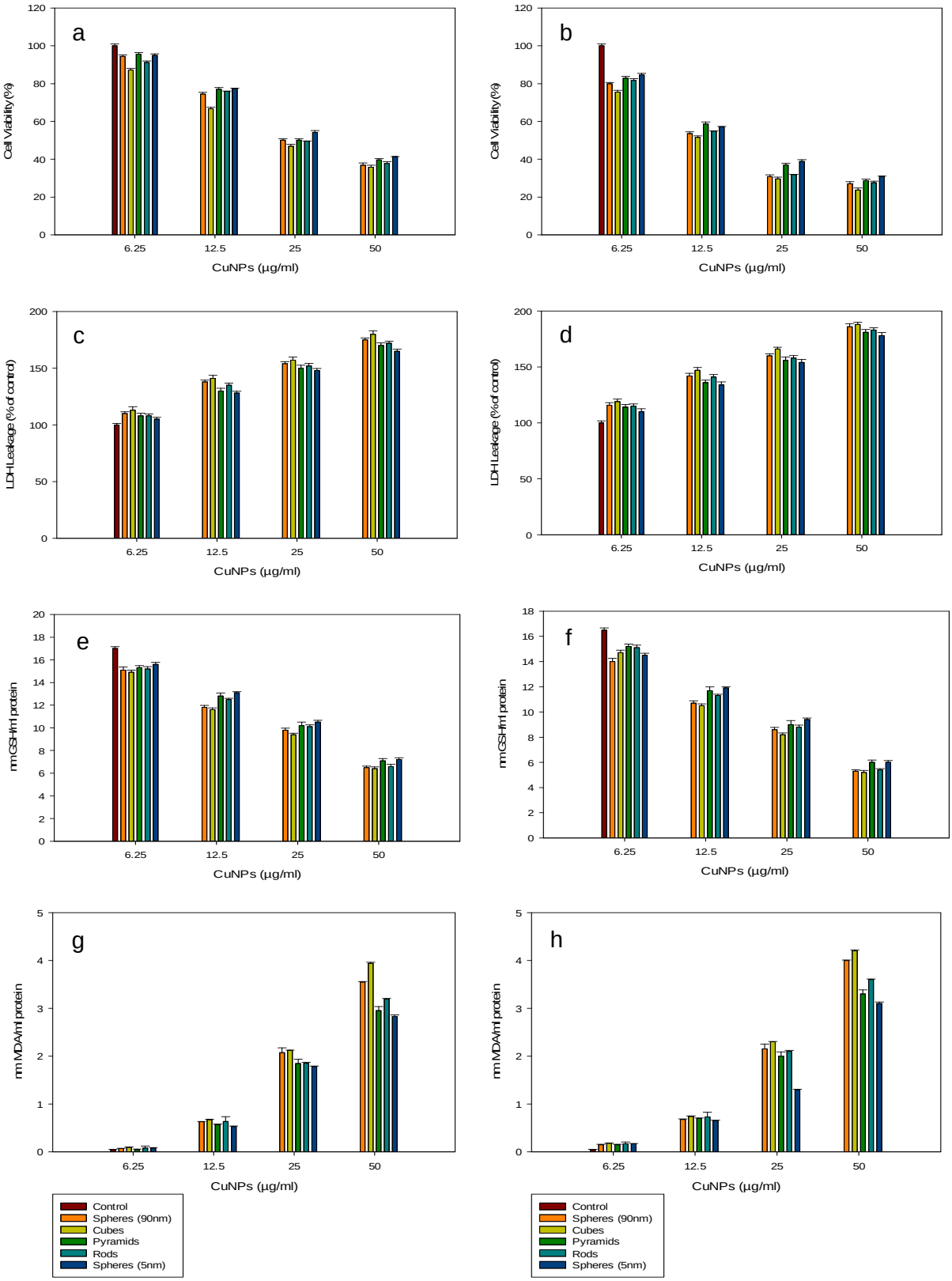


**Figure 4.11:** Cell viability after 24 hour neo-geometric CuNP exposure to a) NHEK cells and b) HeLa cells. Lactate dehydrogenase leakage after 24 hour neo-geometric CuNP exposure

to c) NHEK cells and d) HeLa cells. Glutathione levels after 24 hour neo-geometric CuNP exposure to e) NHEK cells and f) HeLa cells. Malondialdehyde levels after 24 hour neo-geometric CuNP exposure to g) NHEK cells and h) HeLa cells. Data presented are mean ± SE of 3 experiments performed in duplicate. *$p \leq 0.05$ versus control.

### 4.3.10. Lactate dehydrogenase activity

Extracellular LDH levels found in the cell media were measured to determine the extent of cell membrane damage induced by geometric CuNPs on two cell lines. Upon cell membrane damage, intracellular LDH is released into the culture medium and is considered an indicator of irreversible cell death. The geometric CuNPs were assessed for its effect on plasma membrane integrity to elucidate an extension of cell death by DNA damage.

Figures 4.11c and 4.11d outlines the LDH leakage into the cell medium as a correlation to the control. The LDH leakage by the cells exposed to the CuNPs in increasing concentration far exceed the LDH leakage of the control, except for the 6.25µg/ml CuNP concentration which shows LDH release similar to the control. Furthermore, leakage increases as a function of the increase in CuNP concentration. The slightest increase in leakage is due to the low concentration of CuNPs when compared with the controls. We also took note of the geometric effect of cell membrane damage by acknowledging the fluctuation in LDH leakage values between the different shapes. Similarly, the order of damage can be represented by cubes > 90nm spheres > rods > pyramids > 5nm spheres and may be associated with the difference in volume leading to the variation in LDH release. The difference cell membrane damage between the two cell lines can be analyzed by the lower LDH leak for NHEK compared to the HeLa cells. Although not significant, the difference exists and can be exploited when taking the cytotoxic effects of the CuNPs into consideration.

After 24 hours of CuNP-cell incubation, uptake of the CuNPs induces damage by oxidation of the metal. Essentially, based on a reduction-oxidation reaction where the oxidation of Cu(s) to $Cu^{2+}$ which is energetically favourable along with production of $H_2O_2$ from oxygen and protons give the redox equation:

$$Cu_{(s)} + O_2 + 2H^+ = Cu^{2+} + H_2O_2 \qquad \text{(Equation 4.4)}$$

$H_2O_2$ production at the oxygen-rich cell membrane induces the membrane damage signified by the LDH release (Kumar and Müller, 1999) in Figures 4.11c and 4.11d. In a recent study by Alarifi and associates (2013), copper oxide nanoparticles (CuONPs) also displayed LDH release in a dose-dependent manner but with differing leakage of 200% of the control at 30µg/ml whereas the cube CuNPs in this study induce LDH release of a maximum 180% of

the control at 50µg/ml on the NHEK cell line and 188% on the HeLa cell line. The possible difference in dose-dependency may be due to the oxidised copper in their nanoparticles; however, it endorses this study's geometric CuNPs for having a lower toxicity. Li and co-workers (2012) showed the size-dependent membrane damage of silver nanoparticles on human lung fibroblast cells. Interestingly, the nano-size played a role in the difference of necrosis or apoptosis by the measurement of loss of membrane integrity with the 25nm nanoparticles causing more damage than 70nm nanoparticles. Using the same principle, our geometric nanoparticles cause higher LDH release as a function of shape-volume dependency on cell toxicity.

#### 4.3.11. Glutathione activity

Change in glutathione production assisted with supplementary toxicity analysis and breakdown in mechanism of toxicity of the NHEK and HeLa cells. The levels of reduced form of GSH are a measure of oxidative stress occurring intracellularly. Figures 4.11e and 4.11f displays the reduction in GSH following the dose-increasing exposure of the geometric CuNPs. In comparison to the control, GSH levels decrease consistently as the CuNPs concentration increases illustrating dose-dependent intracellular stress. The minor differences in GSH levels using different nano-shapes at constant concentrations indicate the shape effect of CuNPs on oxidative stress highlighting the cube-shaped nanoparticle as inducing the highest degree of oxidative stress when compared to the other shapes. In addition, the GSH levels vary slightly between the NHEK and HeLa cell lines with an average of 1.1% reduction in GSH in the HeLa cells indicating minimal but important difference.

The depletion in GSH due to CuNP exposure suggests oxidative stress as the primary mechanism of toxicity in both cell lines. Post endocytosis and subsequent release of the ionic species into the intracellular compartment leads to spontaneous generation of ROS at the surface of the nanoparticle which promotes the formation of free radicals. In the cellular environment, radicals oxidise and reduce macromolecules such as DNA, lipids and proteins resulting in oxidative damage to the cell, DNA damage and apoptosis (Alarifi *et al*., 2013). High levels of ROS disrupt cellular processes by non-specifically attacking DNA, proteins and lipids. It can be assumed that this mechanism precedes and further leads to the toxicity as identified by the MTT data. Arora and co-workers (2016) recently also confirmed the triggering of ROS leading to induced nuclear damage at 100mg/ml when copper adsorbed chitosan nanoparticles were applied to a human kidney cell line.

Srikanth and co-workers (2016) recently reiterated the toxicity effects of internalized nanoparticles and macromolecule damage due to copper accumulation within the cell. Their MTT toxicity results pertaining to CuONP exposure to cells closely resemble that of the study by Alarifi and associates (2013), however, their GSH levels are unusually lower when compared to Alarifi's and our study. The difference in GSH levels can be repeatedly explained by the difference in cell lines used where Alarifi and associates (2013) used human keratinocytes, Srikanth and co-workers (2016) used Chinook salmon cells while keratinocytes and HeLa cells were used in this study, as well as the geometry difference of the CuNPs.

### 4.3.12. Lipid peroxidation activity

The extent of membrane LPO was measured as an indicator of cellular oxidative stress, supplementary to the analysis of GSH release. The formation of MDA is measured as it a product of membrane LPO, oxidation of cellular lipids. The MDA formation increases in both cell lines as a function of dose-dependency with minimal MDA detection in the 6.25µg/ml concentration, not diverging significantly from the control readings (Figures 4.11g and 4.11h). The shape effect is obvious at 25 and 50µg/ml where the cubes and 90nm spheres induce the most membrane LPO and the 5nm spheres show the least toxicity. The greatest difference in MDA detection is noted at 50µg/ml between cubes and 5nm spheres at 1.1nm MDA/ml protein on both the NHEK and HeLa cell lines. The difference in membrane LPO also exists between the two cell lines where the MDA readings for the HeLa cell line is 0.2nm MDA/ml protein higher than the NHEK cell line indicating more membrane LPO damage exerted on the HeLa cell line. These results indicate that the shape effect on cell toxicity is consistent across all assays and the cervical cancer cell line is more sensitive to the ROS inducing effects of neo-geometric CuNPs.

The geometric CuNPs showing activity of lactate dehydrogenase, GSH release and membrane LPO detection, can assist with deducing the mechanistic approach to cellular toxicity. Induction of ROS by the CuNPs includes the superoxide radical ($O^{2-}$), hydrogen peroxide ($H_2O_2$), and hydroxyl radical ($OH^-$) which promote the intracellular changes observed leading to cell death. The observation of MDA production indicates the lipid oxidative damage caused by the CuNPs in response to its concentration, geometry and change in cell type. Supplementary to GSH release, LPO also confirms oxidative stress exerted on the intracellular components which can further give rise to more free radicals and damage biomolecules such as the cell's DNA, protein, lipids and cell membrane as is indicated by the LDH release, in conjunction with ROS (Alarifi *et al*., 2013).

## 4.4. Concluding Remarks

The ordered synthesis of geometric CuNPs was successfully completed with the determining factors of the study including a completely homogenous sample of one geometry, as well as CuNPs with a stable surface charge. CTAB and SDS significantly affected nano-shape, uniformity and zeta potential. The design aimed to yield stable CuNPs of single geometries per sample in order to serve as drug delivery systems in a study elucidating the ideal nano-shape for enhanced internalization and in effect, determining the cytotoxic properties of the nanosystems as a function of its shape.

Nano-shape has a promising ability in dictating cellular uptake, therefore, the cube-shaped CuNPs will be considered for futher experiments. By combining the shape properties of the CuNPs to internalize at different rates and the cytotoxic activity of the copper, the novel neo-geometric CuNPs nanosystem may prove to be a dual system for enhanced cellular uptake simultaneously using the copper to exert cytotoxic activity on proliferating cells in an inflammatory environment. Future developments in the study include the formulation and statistical design of a SOPN vehicle for the promoted stimulation of the cubic CuNPs across the stratum corneum of the skin.

## 4.5. References


Adjei, I.M., Sharma, B. and Labhasetwar, V., 2014. Nanoparticles: cellular uptake and cytotoxicity. In *Nanomaterial* (pp. 73-91). Springer Netherlands.

Alarifi, S., Ali, D., Verma, A., Alakhtani, S. and Ali, B.A., 2013. Cytotoxicity and genotoxicity of copper oxide nanoparticles in human skin keratinocytes cells. *International journal of toxicology*, *32*(4), pp.296-307.

Arora, D., Dhanwal, V., Nayak, D., Saneja, A., Amin, H., ur Rasool, R., Gupta, P.N. and Goswami, A., 2016. Preparation, characterization and toxicological investigation of copper loaded chitosan nanoparticles in human embryonic kidney HEK-293 cells. *Materials Science and Engineering: C*, *61*, pp.227-234.

Bagchi, B., Dey, S., Bhandary, S., Das, S., Bhattacharya, A., Basu, R. and Nandy, P., 2012. Antimicrobial efficacy and biocompatibility study of copper nanoparticle adsorbed mullite aggregates. *Materials Science and Engineering: C*, *32*(7), pp.1897-1905.

Barmparis, G.D., Lodziana, Z., Lopez, N. and Remediakis, I.N., 2015. Nanoparticle shapes by using Wulff constructions and first-principles calculations. *Beilstein journal of nanotechnology*, *6*(1), pp.361-368.

Champion, J.A., Katare, Y.K. and Mitragotri, S., 2007. Particle shape: a new design parameter for micro-and nanoscale drug delivery carriers. *Journal of Controlled Release*, *121*(1), pp.3-9.

Chithrani, B.D., Ghazani, A.A. and Chan, W.C., 2006. Determining the size and shape dependence of gold nanoparticle uptake into mammalian cells. *Nano letters*, *6*(4), pp.662-668.

Dasgupta, S., Auth, T. and Gompper, G., 2014. Shape and orientation matter for the cellular uptake of nonspherical particles. *Nano letters*, *14*(2), pp.687-693.

Dawson, J.F., 2014. Moderation in management research: What, why, when, and how. *Journal of Business and Psychology*, *29*(1), pp.1-19.

De, S. and Mandal, S., 2013. Surfactant-assisted shape control of copper nanostructures. *Colloids and Surfaces A: Physicochemical and Engineering Aspects*, *421*, pp.72-83.

Du Toit, L.C., Pillay, V., Danckwerts, M.P. and Penny, C., 2008. Formulation and statistical optimization of a novel crosslinked polymeric anti-tuberculosis drug delivery system. *Journal of pharmaceutical sciences*, *97*(6), pp.2176-2207.

Gibbs, J.W., 1878. On the equilibrium of heterogeneous substances. *American Journal of Science*, 96, pp.441-458.

Han, Y., Alsayed, A.M., Nobili, M., Zhang, J., Lubensky, T.C. and Yodh, A.G., 2006. Brownian motion of an ellipsoid. *Science*, *314*(5799), pp.626-630.

Hao, N., Li, L., Zhang, Q., Huang, X., Meng, X., Zhang, Y., Chen, D., Tang, F. and Li, L., 2012. The shape effect of PEGylated mesoporous silica nanoparticles on cellular uptake pathway in Hela cells. *Microporous and Mesoporous Materials*, *162*, pp.14-23.

Haradhvala, N.J., Polak, P., Stojanov, P., Covington, K.R., Shinbrot, E., Hess, J.M., Rheinbay, E., Kim, J., Maruvka, Y.E., Braunstein, L.Z. and Kamburov, A., 2016.

Mutational strand asymmetries in cancer genomes reveal mechanisms of DNA damage and repair. *Cell*, *164*(3), pp.538-549.

He, Y. and Park, K., 2016. Effects of the microparticle shape on cellular uptake. *Molecular pharmaceutics*, *13*(7), pp.2164-2171.

Jose, G.P., Santra, S., Mandal, S.K. and Sengupta, T.K., 2011. Singlet oxygen mediated DNA degradation by copper nanoparticles: potential towards cytotoxic effect on cancer cells. *Journal of nanobiotechnology*, *9*(1), p.9.

Kolhar, P., Anselmo, A.C., Gupta, V., Pant, K., Prabhakarpandian, B., Ruoslahti, E. and Mitragotri, S., 2013. Using shape effects to target antibody-coated nanoparticles to lung and brain endothelium. *Proceedings of the National Academy of Sciences*, *110*(26), pp.10753-10758.

Kumar KC, S. and Müller, K., 1999. Lichen metabolites. 2. Antiproliferative and cytotoxic activity of gyrophoric, usnic, and diffractaic acid on human keratinocyte growth. *Journal of natural products*, *62*(6), pp.821-823.

Lesniak, A., Salvati, A., Santos-Martinez, M.J., Radomski, M.W., Dawson, K.A. and Åberg, C., 2013. Nanoparticle adhesion to the cell membrane and its effect on nanoparticle uptake efficiency. *Journal of the American Chemical Society*, *135*(4), pp.1438-1444.

Li, L., Sun, J., Li, X., Zhang, Y., Wang, Z., Wang, C., Dai, J. and Wang, Q., 2012. Controllable synthesis of monodispersed silver nanoparticles as standards for quantitative assessment of their cytotoxicity. *Biomaterials*, *33*(6), pp.1714-1721.

Li, Y., Yue, T., Yang, K. and Zhang, X., 2012. Molecular modeling of the relationship between nanoparticle shape anisotropy and endocytosis kinetics. *Biomaterials*, *33*(19), pp.4965-4973.

Liao, H.G., Zherebetskyy, D., Xin, H., Czarnik, C., Ercius, P., Elmlund, H., Pan, M., Wang, L.W. and Zheng, H., 2014. Facet development during platinum nanocube growth. *Science*, *345*(6199), pp.916-919.

Lin, Y., Xiao, W., Bal, B.S. and Rahaman, M.N., 2016. Effect of copper-doped silicate 13–93 bioactive glass scaffolds on the response of MC3T3-E1 cells in vitro and on bone regeneration and angiogenesis in rat calvarial defects in vivo. *Materials Science and Engineering: C*, *67*, pp.440-452.

Munoz, E.M., Correa, J., Riguera, R. and Fernandez-Megia, E., 2013. Real-time evaluation of binding mechanisms in multivalent interactions: a surface plasmon resonance kinetic approach. *Journal of the American Chemical Society*, *135*(16), pp.5966-5969.

Némethová, V., Buliaková, B., Mazancová, P., Bábelová, A., Šelc, M., Moravčíková, D., Kleščíková, L., Ursínyová, M., Gábelová, A. and Rázga, F., 2017. Intracellular uptake of magnetite nanoparticles: A focus on physico-chemical characterization and interpretation of in vitro data. *Materials Science and Engineering: C*, *70*, pp.161-168.

Ringe, E., Van Duyne, R.P. and Marks, L.D., 2013. Kinetic and thermodynamic modified wulff constructions for twinned nanoparticles. *The Journal of Physical Chemistry C*, *117*(31), pp.15859-15870.

Roy, P.R., Okajima, T. and Ohsaka, T., 2003. Simultaneous electroanalysis of dopamine and ascorbic acid using poly (N, N-dimethylaniline)-modified electrodes. *Bioelectrochemistry*, *59*(1), pp.11-19.

Sahay, G., Alakhova, D.Y. and Kabanov, A.V., 2010. Endocytosis of nanomedicines. *Journal of controlled release*, *145*(3), pp.182-195.

Sami, H., Maparu, A.K., Kumar, A. and Sivakumar, S., 2012. Generic delivery of payload of nanoparticles intracellularly via hybrid polymer capsules for bioimaging applications. *PLoS One*, *7*(5), p.e36195.

Srikanth, K., Pereira, E., Duarte, A.C. and Rao, J.V., 2016. Evaluation of cytotoxicity, morphological alterations and oxidative stress in Chinook salmon cells exposed to copper oxide nanoparticles. *Protoplasma*, *253*(3), pp.873-884.

Tah, B., Pal, P., Mahato, M. and Talapatra, G.B., 2011. Aggregation behavior of SDS/CTAB catanionic surfactant mixture in aqueous solution and at the air/water interface. *The Journal of Physical Chemistry B*, *115*(26), pp.8493-8499.

Venkataraman, S., Hedrick, J.L., Ong, Z.Y., Yang, C., Ee, P.L.R., Hammond, P.T. and Yang, Y.Y., 2011. The effects of polymeric nanostructure shape on drug delivery. *Advanced drug delivery reviews*, *63*(14), pp.1228-1246.

Wang, X., Li, X., Ito, A., Watanabe, Y. and Tsuji, N.M., 2016. Rod-shaped and fluorine-substituted hydroxyapatite free of molecular immunopotentiators stimulates anti-cancer immunity in vivo. *Chemical Communications*, *52*(44), pp.7078-7081.

Wang, Y., Kaur, G., Zysk, A., Liapis, V., Hay, S., Santos, A., Losic, D. and Evdokiou, A., 2015. Systematic in vitro nanotoxicity study on anodic alumina nanotubes with engineered aspect ratio: Understanding nanotoxicity by a nanomaterial model. *Biomaterials*, *46*, pp.117-130.

Yang, K. and Ma, Y.Q., 2010. Computer simulation of the translocation of nanoparticles with different shapes across a lipid bilayer. *Nature Nanotechnology*, *5*(8), pp.579-583.

Zhang, E., Zheng, L., Liu, J., Bai, B. and Liu, C., 2015. Influence of Cu content on the cell biocompatibility of Ti–Cu sintered alloys. *Materials Science and Engineering: C*, *46*, pp.148-157.

Zhao, F., Zhao, Y., Liu, Y., Chang, X., Chen, C. and Zhao, Y., 2011. Cellular uptake, intracellular trafficking, and cytotoxicity of nanomaterials. *Small*, *7*(10), pp.1322-1337.

Zhao, X., Ng, S., Heng, B.C., Guo, J., Ma, L., Tan, T.T.Y., Ng, K.W. and Loo, S.C.J., 2013. Cytotoxicity of hydroxyapatite nanoparticles is shape and cell dependent. *Archives of toxicology*, *87*(6), pp.1037-1052.

Zong, M., Bai, L., Liu, Y., Wang, X., Zhang, X., Huang, X., Hang, R. and Tang, B., 2017. Antibacterial ability and angiogenic activity of Cu-Ti-O nanotube arrays. *Materials Science and Engineering: C*, *71*, pp.93-99.

# CHAPTER 5

# TRANSPORT OF A NOVEL GEOMETRIC COPPER NANOSYSTEM ACROSS THE SKIN BARRIER EMPLOYING A SELF-OSCILLATING POLYMERIC NETWORK IN THE TOPICAL TREATMENT OF PSORIASIS

## 5.1. Introduction

Psoriasis is a chronic inflammatory disease predominantly affecting the skin and concerns 2-5% of the world's population. Plaque formation and skin scaling is a consequence of the conditions epidermal hyper-proliferation, incomplete cornification and retention of nuclei in the stratum corneum (Perera *et al*., 2012). Histopathological hallmarks are epidermal hyperplasia with keratinocyte differentiation, prominent inflammatory infiltrate, and increased vascularization (Boehncke, 2015). Well defined, erythematous scaly skin lesions severely affects patients quality of life and is possibly triggered by a combination of genetic (family background) and environmental factors (alcohol, tobacco, infections, medications, stress) (Sala *et al*., 2016).

Sala and associates (2016) extensively reviewed polymeric nanotherapeutics in the treatment of psoriasis that has been formulated to increase the percutaneous absorption of active agents without damaging the skin barrier function. Enhancing stability, efficacy and increasing residency time is a prime factor in the chronic disease while maintaining safety and a suitable risk/benefit ratio. This correlates with a recent study surrounding natural curcumin which has been studied based on its anti-inflammatory, antioxidant, chemo-preventive and chemo-therapeutic activity (Kang *et al*., 2016).

Nanoparticle delivery through the stratum corneum of diseased skin has been shown to be modest at best (Gattu and Maibach, 2010) and proposed concepts in overcoming this barrier include low-frequency ultrasound, electroporation by high voltage pulses and microneedle arrays (Vogt *et al*., 2016). These strategies, however, are not as convenient an application to the patient in the aim of increasing nanoparticle permeation. This study therefore focuses on the application of cube-shaped CuNPs by exploiting the nano-shape effects of enhancing cellular internalization rates of nanocarriers and the cytotoxic properties of copper in the inflammatory environment provided by the autoimmune disorder. A mechanism in the form of a self-oscillating gel was formulated and designed to improve the transport of the bio-active

geometric CuNPs across the stratum corneum of the skin by investigating mass transport of nanoparticles in a biological application.

Structural deformation at micro-level may potentiate CuNPs permeation rate through a rate-limiting innate barrier by manipulating chemical changes resulting in a mechanical effect. Automatic transportation of object on the surface of oscillating gels has been studied (Murase *et al*., 2008); in addition to oscillating devices forming components of nanomachines (Ito *et al*., 2006). Utilizing polymers and gels responsive to external stimuli are a field of significant interest in drug delivery research particularly in the control of drug release quantity and alteration of drug release and permeation rates. Stimuli-responsive polymers require an external factor to regulate the action of the system; however, employing a self-oscillating system which functions on a chemical to physical oscillatory change eliminates the reliance on an external trigger. Actuating systems using a self-oscillating mechanism employs a built-in arrangement of energy conversion from the chemical oscillations of the BZ reaction to mechanical oscillations of polymer chains (Hara and Yoshida, 2005).

The self-oscillating phenomenon is ruthenium-catalyzed where the subsequent process is the product of oxidation of an organic substrate in the presence of a metal ion catalyst in acidic conditions (Hara and Yoshida, 2005). The catalyst ion fluctuates between its oxidised and reduced states due to the oxidation process resulting in the chemical oscillatory mechanism. The chemical reaction translates into a mechanical reaction when the catalyst ion is polymerized with a polymer that is responsive to changes in hydrophilicity. Swelling of the polymerized responsive-polymer to the catalyst moiety as a result of hydrophilic changes of the polymeric chain is caused by the $(Ru(bpy)_3)^{2+} \leftrightarrow Ru(bpy)_3^{3+}$ oscillations (Pullela *et al*., 2013). The periodic swelling of the responsive polymer exhibits a peristaltic motion which is the basis of self-oscillating systems.

The geometric CuNPs and SOPN system has not yet been applied to pharma-engineering applications owing to its unknown cytotoxic effects when applied to an *in vivo* bio-form or the mechanical oscillations seizing when the oxidation substrates have been reacted. The system becomes irrelevant after a short period of time and cannot function effectively *in vivo* without continuously replacing the reaction substrates. Therefore, this system serves to oscillate for a longer period than other reported oscillating gels where oscillations last 40 minutes (Ito *et al*., 2003), in addition to the dual functionality of neo-geometric and cytotoxic CuNPs as a bio-active with higher internalization kinetics.

## 5.2. Materials and Methods

Copper II sulphate pentahydrate ($CuSO_4.5H_2O$) was purchased from Merck (Darmstadt, Germany), CTAB, SDS, N-isopropylacrylamide (NIPAAm, $M_w$113.16, 97%), carboxymethyl cellulose (CMC) (sodium salt, $M_w$250,000), tris(2,2'bipyridyl) dichlororuthenium (II) hexahydrate ($Ru(bpy)_3$ monomer), N′-methylenebisacrylamide (MBAAm, ≥99.5%), ammonium persulfate (APS, ≥98%), sodium bromate (≥99%), malonic acid (98%) and MTT assay were all purchased from Sigma-Aldrich Co. (Aldrich, Steinheim, Germany). L-ascorbic acid (98%) was purchased from Roche (Johannesburg, South Africa). NHEK cells, keratinocyte basal medium, growth factors and supplements including bovine pituitary extract, human epidermal growth factor, insulin, hydrocortisone, epinephrine, gentamicin, amphotericin B, transferrin, trypsin/EDTA were all purchased from Whitehead Scientific (Lonza Walkersville facility, USA). All chemicals were analytical grade and used without further purification. BALB/c mice (6 weeks old) were provided by the Central Animal Service (CAS), University of the Witwatersrand, South Africa. The study protocol was evaluated and approved by the Research Animal Ethics Committee.

### 5.2.1. Synthesis of cube-shaped copper nanocrystals

The thermal-reduction method of synthesizing nanocrystals included a standard $CuSO_4.5H_2O$ solution added to 0.02M CTAB and 0.087M SDS solutions heated at 50°C. Solution was further heated between 85-90°C and a standard ascorbic acid solution was added as the reducing agent in a drop-wise manner to allow for spontaneous copper formation without a reducing agent overload. The temperature was then maintained at 80°C using a mercury thermometer (Brannon Thermometers, Cumbria, England).

### 5.2.2. Confirmation of cubic geometric copper nanocrystals

TEM (FEI T12 Spirit Transmission Electron Microscope (120kV), Hillsborough, USA) and HR-TEM (JEOL JEM 2100F (200kV), Oregan, USA) confirmed the synthesis of self-assembled neo-geometric NPs. Samples were also subjected to TEM-EDS for high-speed elemental analysis.

### 5.2.3. Polymerization of self-oscillating cross-linked polymer

2g NIPAAm as the swelling/deswelling polymer, 0.04g $Ru(bpy)_3$, 0.05g MBAAm as a cross-linker and 0.035g APS as an initiator were each prepared by dissolving the powders in distilled water while a 3-necked flask was allowed to come to equilibrium under nitrogen flow conditions at 60°C. The aqueous solutions of NIPAAm, ruthenium salt and MBAAm were added to the flask to reach equilibrium before adding the APS solution. Polymerization of the

NIPAAm and ruthenium salt was conducted over 8 hours in a closed nitrogen system and thereafter dialysed for 2 days against distilled water to remove unreacted monomers. The resulting gel was lyophilized and used as a powder.

### 5.2.4. Synthesis validation and investigation of the structural and molecular vibrations of the self-oscillating cross-linked polymer

FTIR utilizing a Spectrum 100 FTIR Spectrometer (Perkin-Elmer, Beaconsfield, BUCKS,UK) was used to detect the vibration characteristics of chemical functional groups in the oscillating polymer samples. FTIR was performed on the native polymers involved in the system as well as the oscillating polymer formulations as a means of validating the successful synthesis of the poly-N-isopropyl acrylamide from the NIPAM. Samples were placed on a diamond crystal and processed by the universal ATR polarization accessory for the FTIR spectrum series at a resolution of $4cm^{-1}$. Each sample was analyzed at wave numbers ranging from 650 to $4000cm^{-1}$.

### 5.2.5. Fabrication of the polymeric network and incorporation of cube-shaped copper nanoparticles

Reaction substrates, 2.1g malonic acid and 4.22g sodium bromide, were solubilised in 30ml distilled water and added to hydrated CMC. The substrates and gelling polymer served as the initiating force of the oscillating mechanism as well as the delivery vehicle for the self-oscillating cross-linked polymer. The geometric CuNPs were sonicated systematically with the complete SOPN system.

### 5.2.6. Application of a Box–Behnken design for the copper nanoparticle-loaded self-oscillating polymeric network

For designing an optimum formulation, a 3-factor, 3 tiered Box–Behnken experimental design was generated using Minitab®V15 statistical software (Minitab®Inc., PA, USA). The final self-oscillating polymeric network was fabricated using quantities and ratios as per a Box-Behnken experimental design which generated 15 formulations (Table 5.1). The independent variables employed in the experimental design were quantities of the self-oscillating polymer, reaction substrates and CMC. These formulations were evaluated with the aim of acquiring high statistical scientific significance.

**Table 5.1:** 15 Formulations generated by Box–Behnken design.

| Formulation | Oscillating Polymer (mg) | Reaction Substrate (parts) | Gel (parts) |
|---|---|---|---|
| 1 | 17.5 | 0.250 | 0.250 |
| 2 | 5.00 | 0.250 | 0.250 |
| 3 | 30.0 | 1.625 | 1.625 |
| 4 | 30.0 | 0.250 | 0.250 |
| 5 | 5.00 | 1.625 | 0.250 |
| 6 | 30.0 | 1.625 | 1.000 |
| 7 | 5.00 | 1.625 | 1.000 |
| 8 | 5.00 | 3.000 | 0.625 |
| 9 | 17.5 | 1.625 | 0.625 |
| 10 | 17.5 | 1.625 | 0.625 |
| 11 | 17.5 | 3.000 | 0.250 |
| 12 | 17.5 | 3.000 | 1.000 |
| 13 | 17.5 | 1.625 | 0.625 |
| 14 | 17.5 | 0.250 | 1.000 |
| 15 | 30.0 | 3.000 | 0.625 |

### 5.2.7. Response surface analysis as per Box–Behnken design

Response surface analysis of various response variables was carried out employing Minitab®V15 statistical software. The results were demonstrated using response surface and contour plots derived for the measured responses (average oscillation amplitude, duration of oscillations, permeation rate and cytotoxicity) based on the experimental model.

### 5.2.8. Lower critical solution temperature measurements of the self-oscillating cross-linked polymer

Differential scanning calorimetry (DSC) was used to determine the Lower Critical Solution Temperatures (LCST) of the Self-Oscillating Cross-Linked Polymer. DSC (model DSC 2910, TA Instruments, New Castle, DE) experiments were performed on swollen specimens of 15mg by heating from 15 to 60°C at 2°C/min. The temperature-sensitive collapse of the polymer was identified as an endotherm in the thermograms. The onset of the thermogram corresponded to the LCST transition.

### 5.2.9. Determination of the degree of crystallinity of synthesized and native polymers

A powder XRD (MiniFlex 600, Tokyo, Japan) was used to monitor diffraction patterns of the polymer samples to validate the synthesis of the self-oscillating cross-linked polymer and

compare crystallinity with the native PNIPAM and NIPAM. A continuous scan rate of 0.1°/min from 0-90° was used with copper Kα radiation (λ=1.54Å).

### 5.2.10. Measurement of optical vibrations to detect oscillations of the self-oscillating polymeric network

The 15 SOPNs were prepared by dissolving the polymer powder into an aqueous gel solution containing the BZ substrates and CMC gel according to concentrations in Table 5.1. The optical transmittance oscillations for the polymer solutions were measured under a constant temperature of 25°C to mimic skin temperature and a once-off stirring mechanism upon introducing the polymer to the reaction gel and reading the optical vibrations. The time course of transmittance at 570nm (isobestic point) was monitored by a multiplate spectrophotometer (Powerwave XS, BioTek, Vermont, USA) to detect the transmittance changes on the basis of conformational changes of the synthesized polymer signifying mechanical oscillations of the system.

### 5.2.11. *In vitro* studies in the determination of permeation rate controlled by the oscillations of the self-oscillating polymeric network

Permeation studies to determine the effect of the self-oscillating phenomenon promoting delivery of drug through a semi-permeable membrane were performed using FDC (Perme Gear, Amie Systems, USA). 15 SOPN formulations with substrates for the initiation of the oscillations (Table 5.1) were loaded with 1.2mg of geometric CuNPs and mounted in the donor compartment of the FDC. Buffer solution of pH 5 was added to the receptor cell and at time intervals of 1, 2, 4, 8, 24 hours sample was removed for analysis to investigate the amount of CuNPs that permeated the membrane. Fresh buffer solution replaced the volume that was removed to maintain sink conditions in an environment maintained at 25°C to mimic body skin temperature. An ICP-OES (Activa S-Horiba Scientific, Munich, Germany) was used to measure the quantity of copper from the samples taken from the receptor half-cell.

### 5.2.12. *Ex vivo* analyses of the biocompatibility of the self-oscillating polymeric network via cell viability studies

Primary NHEK cells were sub-cultured until passage 6 and used for the cell viability study using a MTT assay. The NHEK cells were cultured in keratinocyte basal medium and supplemented with bovine pituitary extract, recombinant human epidermal growth factor, insulin, hydrocortisone, epinephrine, transferrin, gentamicin and amphotericin B. The cells were incubated in a humidified 37°C environment controlled at 5% CO2. At 80% confluence, the cells were harvested using trypsin/EDTA and were sub-cultured into 75cm$^2$ flasks and 96-well plates for the toxicity assay. 1x10$^3$ cells/well was allowed to attach to the surface for

48 hours prior to treatment. The cells were then incubated with the SOPN formulations for 24 hours after which the MTT dye was added followed by the solubilising solution after 4 hours of incubation and analyzed at 570nm using a multiplate spectrophotometer. Untreated cells were run under identical conditions and served as controls.

### 5.2.13. *In vivo* investigation of the cube-shaped copper nanocrystal-loaded self-oscillating polymeric network in the BALB/c induced-psoriasis model

BALB/c mice arrived at CAS, were weighed, examined by CAS staff, caged individually and acclimatized in CAS labs. All mice were provided with a standard mouse diet and water and weighed weekly so as to indicate their general state of well-being. *In vivo* studies were conducted on 75 mice randomly divided into 5 groups with 15 mice per group. The psoriasis-model was induced by applying imiquimod (Aldara 5%) on the shaved dorsal aspect of the mice daily for 5 days. Post-induction, the 5 groups were sorted as follows and the respective treatments were applied daily:

Group 1 (CuNPs experimental group): Geometric CuNPs-loaded aqueous cream at a concentration of 100µg/ml was topically applied to the inflamed, shaved area of each mouse.

Group 2 (CuNPs control group): This group of animals were administered the topical aqueous cream without CuNPs as the placebo dose on the affected area. Results from this group were used to determine the efficacy of the CuNPs experimental formulation and its comparison to the commercial product.

Group 3 (SOPN experimental group): The geometric CuNPs were loaded into the SOPN gel and topically applied to the psoriatic area of each mouse at 60µg/ml of CuNPs.

Group 4 (SOPN control group): The SOPN gel without CuNPs was administered as the placebo dose. Results from this group were used to determine the efficacy of the CuNPs in the SOPN experimental formulation in addition to the SOPN itself as an active agent, and its comparison to the commercial product.

Group 5 (commercial product evaluation): This group of mice were topically administered with a commercial corticosteroid (0.5% hydrocortisone). This study was undertaken in the determination of the potential of the prepared CuNPs and SOPN formulations in comparison to the topical market formulation, thereby determining the efficacy between these different delivery systems.

Photography and Psoriatic Area and Severity Index (PASI) scoring were conducted at the end of the three phases on days 3, 7 and 14. In addition, on days 3, 7 and 14 of treatment interventions, 5 mice from each group were euthanized for excision of treated skin and blood sampling at the different time points. Histopathology investigations analyzed the effect of the treatments on the psoriatic skin and treated skin and blood samples were collected for ICP-OES analyses to determine the *in vivo* residual CuNPs and fate thereof.

### 5.2.14. Data analysis and confirmation of statistical significance of all assays performed

All quantitative investigations were carried out in 3 independent experiments in duplicates for each evaluation. Data were expressed as mean (±SE) and analyzed by 1-way analysis of variance (Anova). *p* values less than 0.05 was considered statistically significant.

## 5.3. Results and Discussion

Cube-shaped geometric CuNPs for enhanced cellular internalization were synthesized using the thermal reduction method in the presence of two key surfactants to direct the growth of the CuNPs. The copper nanocrystals also play a role in exerting cytotoxic effects on the inflamed cells of the psoriatic area, therefore reducing the plaque thickness. The self-oscillating polymer was synthesized by polymerization of native NIPAM with the incorporation of $Ru(bpy)_3$. The resulting polymer forms the oscillating component of the complete SOPN system when incorporated with the reaction substrates. The polymerization of NIPAM and the catalyst ion results in chemical modification to PNIPAM which encompassed the required properties of the new polymer necessary to satisfy the aim of the SOPN system and incorporation of the geometric CuNPs which completed the bio-active system. The following characterization and design ensured the formulation of an ideal system to enhance CuNPs delivery through the stratum corneum to improve psoriasis treatment.

### 5.3.1. Box-Behnken experimental design and constrained optimization of the copper nanoparticle-loaded self-oscillating polymeric network

Optimization of the CuNP-loaded SOPN is as a result of the specific characterization of the 15 formulations generated by the software (Table 5.1). The design program generated responses from the results of each formulation for determining the greatest correlation with response elements for the optimized formulation. Residuals were used for evaluating differences in observed values and predicted responses, thereby correlating results according to the programs desired outcome (Stewardson and Whitfield, 2004). The ideal

histograms represent bell shaped curves for the responses; how-ever, slight variations are evident in the responses obtained due to the variation in ratios of the polymer, substrates and gel.

Minitab®V15 statistical software was used for producing optimal responses for the amplitude and duration of the wave-like oscillations created by the SOPN, rate of CuNP permeation through a semi-permeable membrane affected by the oscillations and cell toxicity of the system. High, low and optimal factors were generated yielding a desirability value of 1, to produce optimal factor levels for the most desirable response behaviour. The above evaluation yielded responses for the optimized formulation, inputting the oscillation vibrations, duration of oscillations, permeation flux as a direct result of the oscillations and cell toxicity data into the Box–Behnken design, for an optimum formulation of desirability of 94.426%. Figure 5.1 indicates the software specifications with profiles generated for the optimized formulation, taking into consideration the responses which are further discussed in subsequent sections.

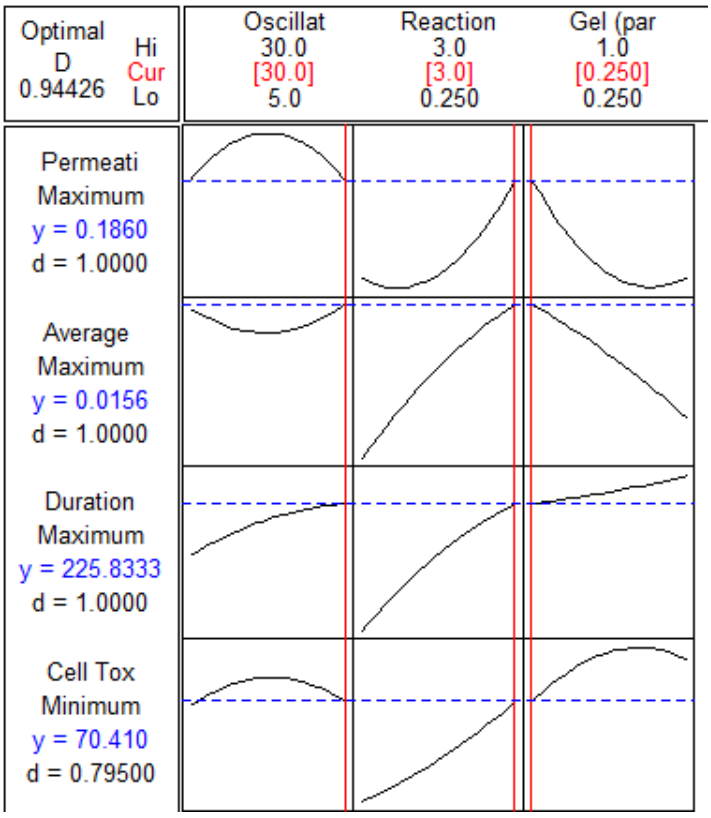


**Figure 5.1:** Optimization plot for the response optimization of the SOPN formulation.

The experimental values of average permeation flux, oscillation wavelengths, duration of oscillations and cell toxicity were 0.186mg.cm$^{-2}$.hr$^{-1}$, 0.0156nm, 225.83 minutes and 70.4%, respectively. The desirability plot describes the influence of each independent variable for formulating the optimized CuNP-loaded SOPN with the desired targeted responses. The optimization approach resulted in a formulation constituting oscillating polymer (30mg), reaction substrates (3 parts) and CMC gel (0.250 parts).

### 5.3.2. Response surface analysis

Response surface and contour plots (Figure 5.2) were derived for the measured responses based on the experimental model. Plots were used to represent the functional relationship between the experimental variables and the responses achieved. The correlating effects of the oscillating polymer, reaction substrates and gel on the responses are shown with respect to the targeted responses. Response surface plots clearly indicate an increase in oscillation amplitude when the oscillation polymer and reaction substrates are at maximum concentrations while an increasing concentration in the gel reduces the oscillation amplitude. Similarly, the duration of the reaction and permeation kinetics is at its desired range when the oscillatory components are maximal but is predominantly reliant on the quantity of reaction substrate to propel the reaction. Considering the use of CMC as the gelling agent to promote a suitable topical delivery system for ideal application, the CMC concentration is inversely proportional to the oscillation amplitude and subsequent permeation kinetics; and may affect oscillation duration based on the concentration of the self-oscillating polymer and reaction substrates. With regards to biocompatibility, in contrast, the increased concentrations of the oscillatory polymer and reaction substrates negatively affect cell viability; however, it gives an indication of the $LD_{50}$ and ideal toxic dose.

Based on a full ANOVA analysis of the measured formulation responses it was determined that the only factors which exhibited significant influence ($p \leq 0.05$) were the duration of oscillation involving the correlation between the reaction substrates and oscillating polymer, and cell toxicity. Despite no statistical significance between the formulation variables and average oscillation amplitude and permeation kinetics ($p \geq 0.05$), response surface plots showed that the relative and definitive effects of the measured responses were reliant on the formulation variables.

The normal probability plots of the residuals (left panel of Figure 5.2) showed clusters of residuals; however these clusters fell on a straight line, signifying the normal distribution of data with no evidence of unidentified variables. Furthermore, a residual plot of the

standardized residuals of the responses show a random distribution of points fluctuating around zero, with no discernible pattern, indicating a non-violation of the assumptions of zero means and constant variance of the regression model despite the presence of outliers in these plots. Evidence of this non-violation was provided by histograms of the residuals of average oscillation amplitude, duration of oscillations, permeation rate and cell toxicity. The residuals versus the order of data showed a random distribution, with rapid changes in signs (+/-) between consecutive residuals for all responses (Figure 5.2). The right panels of Figure 5.2 give an indication ofeach of the limits of the variables with regards to the effect on the responses.

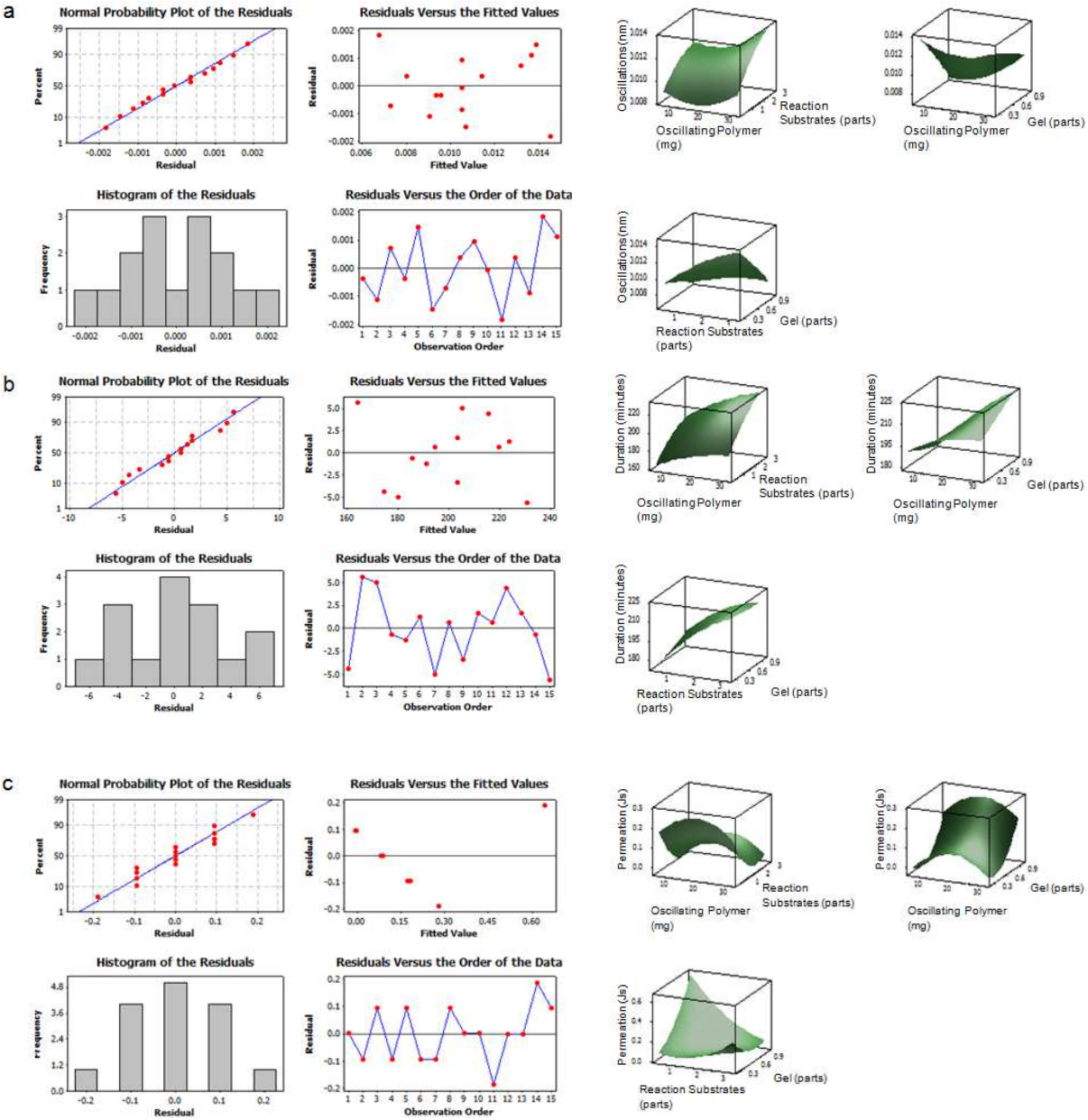

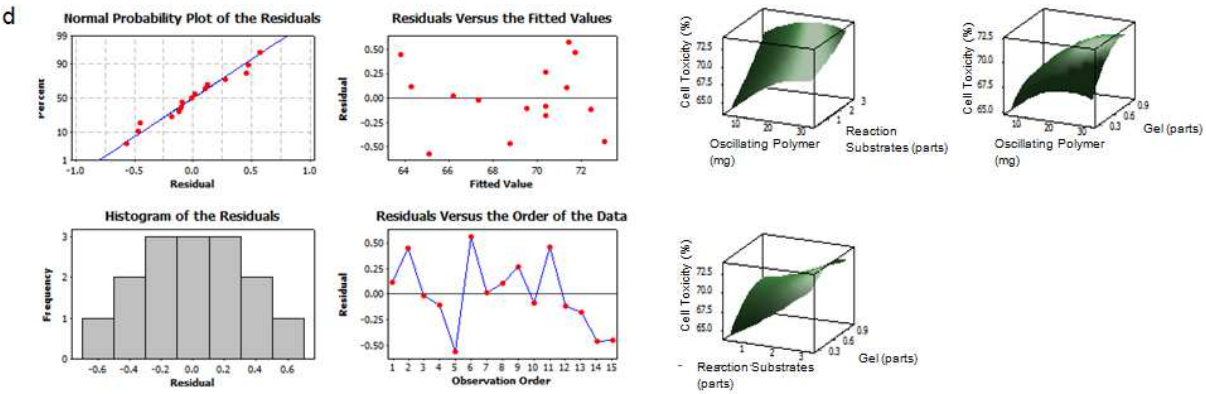


**Figure 5.2:** Residual (left panel) and surface plots (right panel) of a) average oscillation amplitude; b) duration of oscillations; c) permeation rate; d) cell toxicity.

### 5.3.3. Cube-shaped copper nanocrystals synthesized by dual surfactant mediated adsorption

Geometric CuNPs were employed in this study primarily due to the ability of cubic nanoparticles to internalize at a higher rate as compared its counterpart nano-shapes. Nano-cubes were synthesized using CTAB and SDS at specified concentrations during the reduction of the copper salt using ascorbic acid resulting in cube shaped crystalline CuNPs which has been adapted for use in drug delivery. In our previous research, nano-shapes studied for uptake kinetics included 90nm spheres, rods, pyramids, 5nm spheres and cubes in which each nano-shape displayed its own mechanism of cell entry and rate of internalization in human keratinocyte cells. A notable variation in uptake kinetics as a function of nano-shape resulted in 200x200nm cubes having the highest rate of cellular internalization followed by 5nm spheres, pyramids, 90nm spheres and rods, respectively, over a 24 hour incubation period.

The TEM micrograph showing cubic CuNPs (Figure 5.3a) was analyzed under high-resolution for crystallinity evaluation of lattice fringe spacing (Figure 5.3b) which correlates with the 1.811Å spacing of the (100) plane. Growing from the cuboctahedron precursor nucleus, the surfactants adsorb preferentially on the {100} facets resulting in this face becoming the dominant slow growing face while the {111} facets become fast growing and eventually the smallest faces on the nanocrystal, ceasing to appear. The lattice fringes also confirm crystallinity of the copper and promote its characteristics in order to be used as an active agent. Toxicity studies confirmed the use of the CuNPs as a cytotoxic agent and are targeted in this study at the keratinocytes which form the hyper-keratinized plaque of the autoimmune disease. In the inflammatory environment, copper is cytotoxic at 25µg/ml by superoxide and hydroxyl ion production initiating cell death by DNA and cell membrane damage.

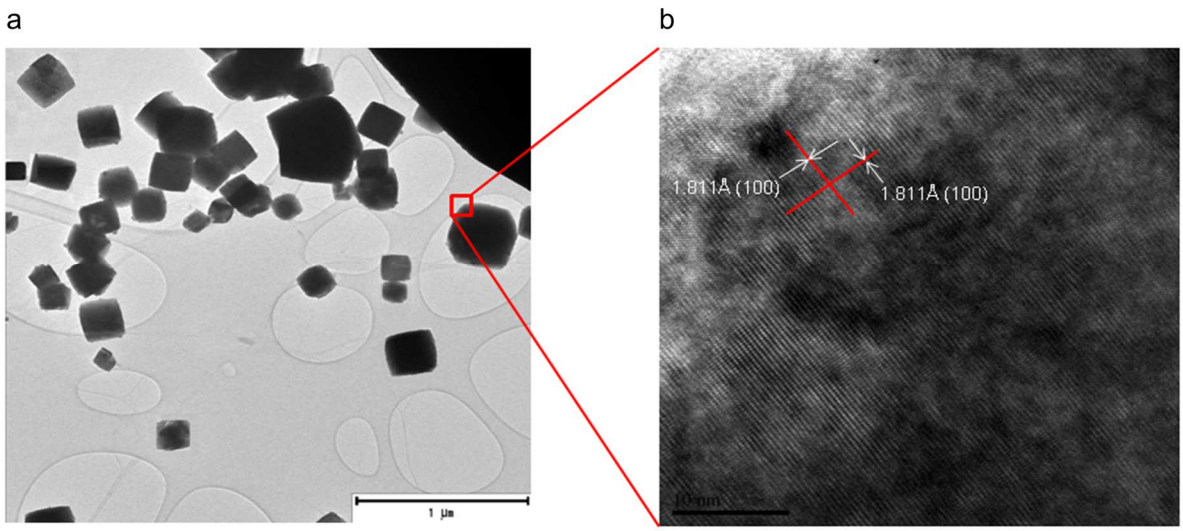


**Figure 5.3:** a) cube-shaped copper nanocrystals; b) lattice fringes and spacing of 1.811Å (100).

### 5.3.4. Chemical synthesis validation of the responsive synthesized self-oscillating polymeric network

The polymerization of NIPAM with $Ru(bpy)^3$ resulted in a PNIPAM-like polymer of which FTIR investigated the differences in the synthesis of the self-oscillating cross-linked polymer. Figure 5.4 compares the synthesized SOPN with its native polymers and desired PNIPAM characteristics. The peaks attributed to the N–H stretching vibration and bending vibration were observed at 3500–3100$cm^{-1}$ and indicate PNIPAM and NIPAM resemblance with the SOPN. The $sp^3$ C–H and C—O stretching vibrations also appeared at 2971 and 1650$cm^{-1}$, respectively, further corroborating PNIPAM characteristics of the synthesized polymer. The similar characteristic peaks of PNIPAM and the SOPN share desirable, necessary properties in order for the SOPN to feature similar activity as the thermo-responsive PNIPAM with sensitivity to hydrophobic phase changes.

Essentially, MBAam and APS as the initiator and cross-linker are not detected in the synthesized SOPN as required and served the only purpose of its functionality. MBAam and APS were used completely during the polymerization reaction and residual amounts were removed during dialysis of the synthesized polymer.

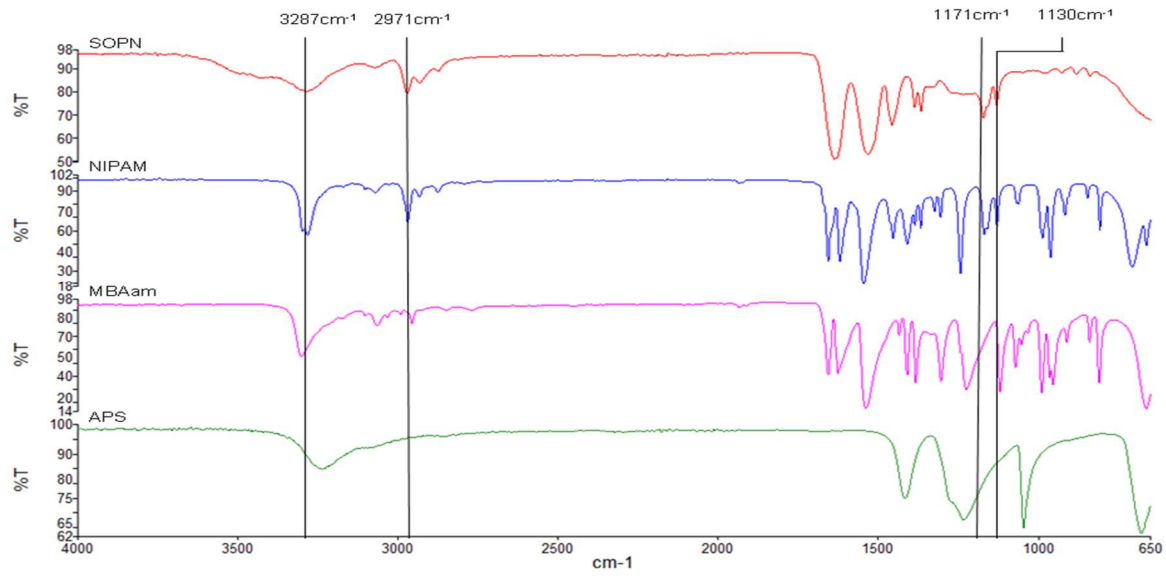


**Figure 5.4:** FTIR spectra of the synthesized SOPN and native polymers.

### 5.3.5. Lower critical solution temperature measurements of the oscillating polymer

DSC was employed to determine the LCST of the synthesized polymer and subsequent sensitivity to thermal change. The LCST is observed in the reduced state of the polymer only and is related to the solubility of the polymer chain (Hara and Yoshida, 2005). The temperature-responsive property of the self-oscillating polymer can be investigated by the determination of cloud points, that is, LCST (Figure 5.5). The appearance of LCST depends on the aggregation of the hydrophobic portions of the co-polymers at a certain temperature. The hydrophobic/hydrophilic properties of the polymer are pertinent in creating the mechanical oscillations of the SOPN. Thermo-sensitivity is attributed to the hydrophilic/hydrophobic balance of the polymer chains which will subsequently be responsible for the swelling/deswelling action in the SOPN.

The endothermic transition at 27-35°C of the synthesized SOPN in the thermogram (Figure 5.5c) gives an indication of the LCST. In Figure 5.5a, NIPAM has a distinct transition at 66°C while native PNIPAM exhibits a broad transition at 80-90°C (Figure 5.5b). Having polymerized the NIPAM with Ru changed the thermal properties and gave the required characteristics for thermal sensitivity. These results indicate that the self-oscillating polymer has been successfully synthesized from NIPAM incorporating Ru ions and possess temperature-responsive behaviour. The LSCT within this range allows the system to function optimally at skin temperature affirming its use as a topical drug delivery system.

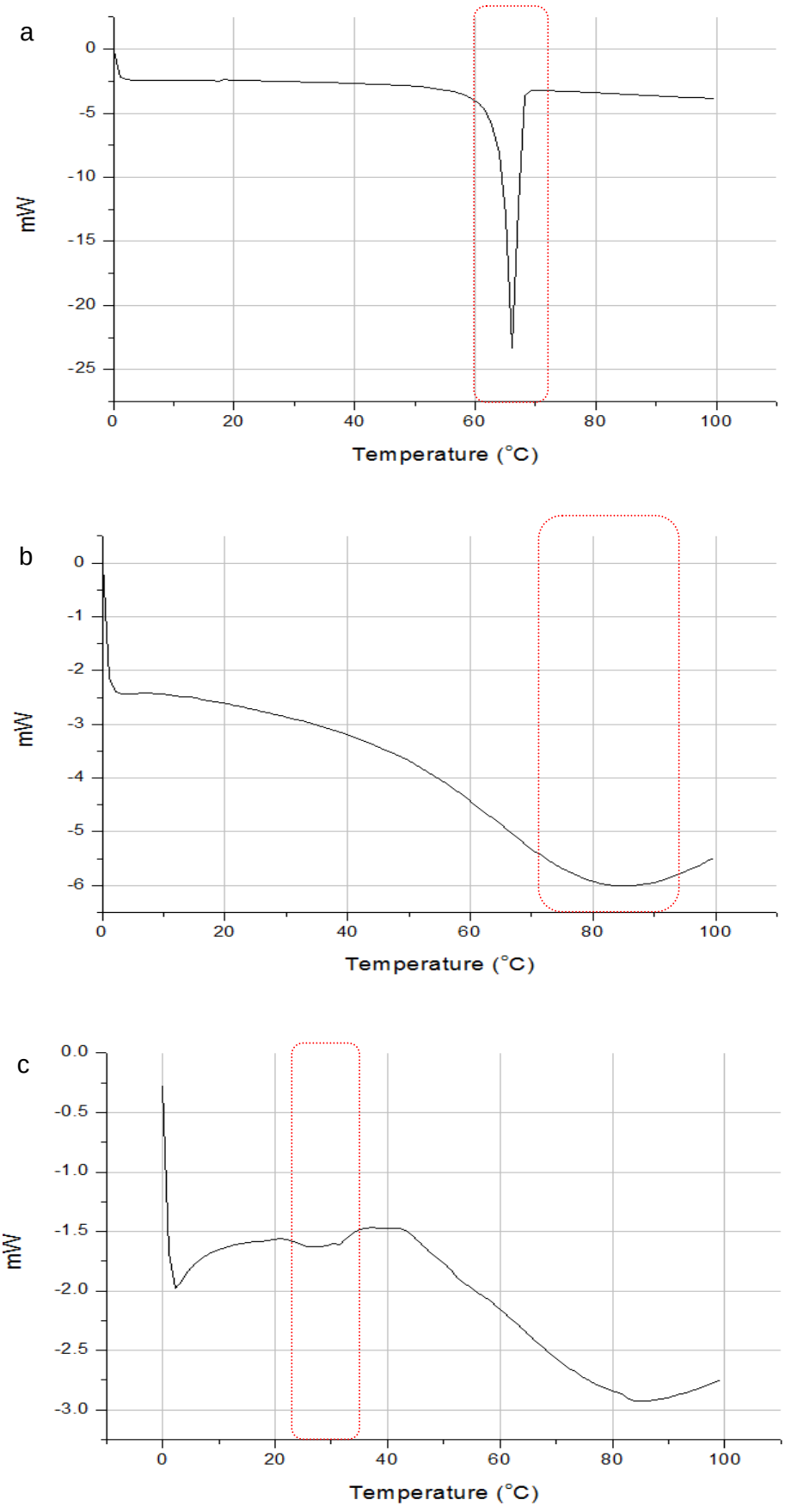


**Figure 5.5:** DSC thermograms of the a) NIPAM; b) PNIPAM; c) synthesized SOPN

### 5.3.6. X-Ray diffraction analysis to determine crystallinity changes

XRD investigated the change in crystallinity properties between NIPAM and the polymerized SOPN. In addition, native PNIPAM was compared to the SOPN to elucidate possible similarities with the new polymer to assess its amorphous-crystalline chemical structure. The XRD spectra of NIPAM (Figure 5.6a) shows distinct, sharp peaks of a highly crystalline polymer while that of PNIPAM shows an amorphous polymer. An analysis of the polymerized SOPN (Figure 5.6c) indicates the polymer to exhibit properties of the PNIPAM (Figure 5.6b) of an amorphous nature. This change in polymerization will therefore lend its thermo-responsive characteristics allowing for the swelling/deswelling of the gel.

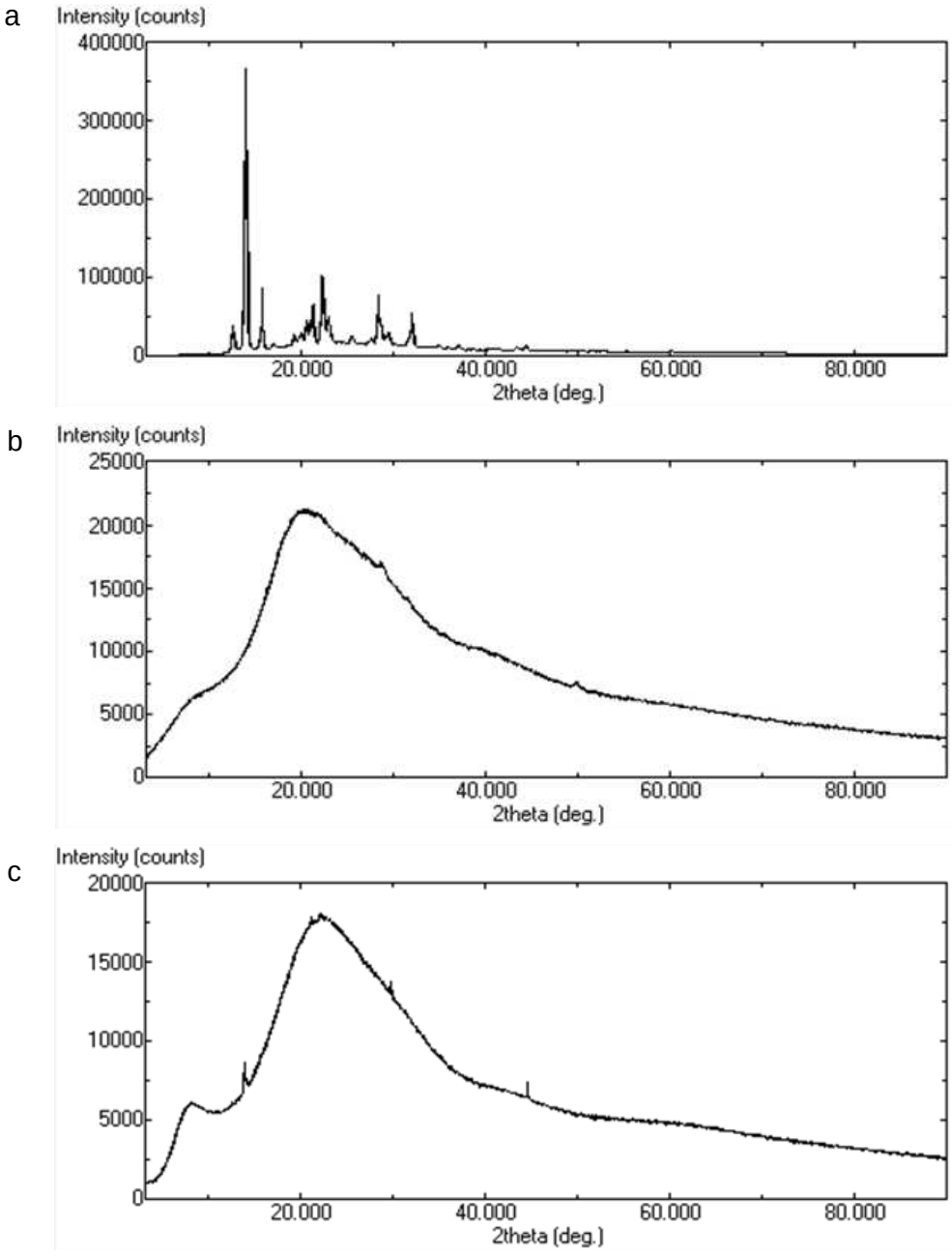


**Figure 5.6:** XRD spectra of a) NIPAM; b) PNIPAM; c) SOPN

### 5.3.7. Measurement of optical vibrations to detect oscillations

This self-oscillating phenomenon characterized by the BZ reaction creates a system of autonomous change in the gel without external stimuli. Reaction substrates driving the reaction potentiate the swelling and deswelling properties of the polymerized polymer and metal ion catalyst. In this investigation, exploiting the swelling-deswelling action of the gel makes functional use of the system in drug delivery by creating microscopic motion in the system enhancing drug delivery through a physical barrier. Dermal delivery of nanoparticles have shown to be unsuccessful whereby the nanoparticles deposit on the external surface of the stratum corneum and do not penetrate the deeper stratum corneum layers (Gamer *et al*., 2006; Cross *et al*., 2007; Larese *et al*., 2009). Hence, the adoption of the BZ reaction to create a self-oscillating mechanism which may stimulate the motion and permeation of nanoparticles through the outermost surface of the epidermal layer due to the physical disturbance in the system. After the incorporation of the oscillating polymer, reaction substrates, gel part and geometric CuNPs, the reaction promotes the oscillations as a result of the reduction and oxidation of the Ru ions causing changes in the hydrophobic phase of the PNIPAM which stimulate the swelling and deswelling properties of the polymer (Figure 5.7).

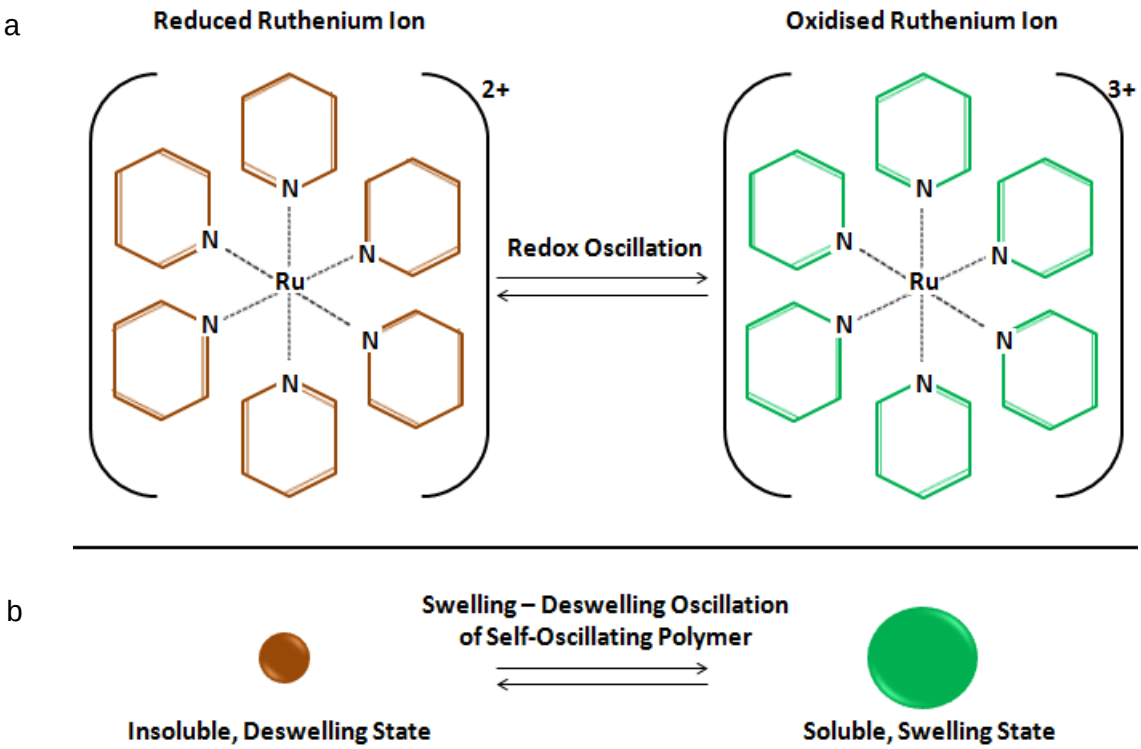

c

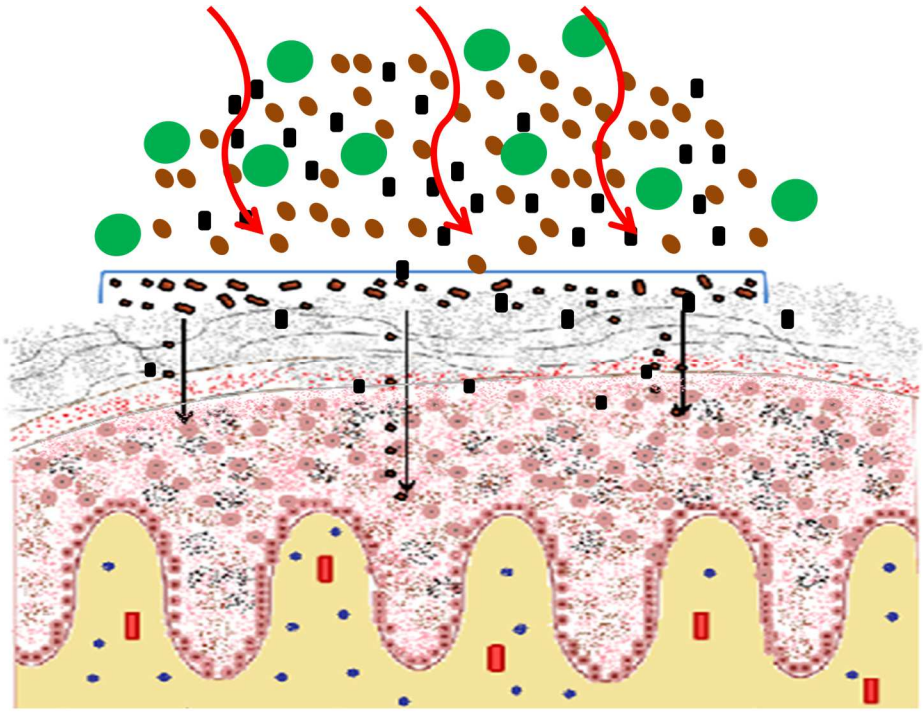

**Figure 5.7:** Redox function of the BZ reaction creating an oscillatory action within the polymer showing a) reduction-oxidation reaction of the ruthenium catalyst ion; b) swelling-deswelling action of the SOPN as a result of the BZ reaction; c) resultant oscillations of the CuNP-loaded SOPN promoting movement in the system and subsequent permeation of CuNPs across the stratum corneum.

The oscillatory amplitude was investigated to identify and optimize the formulation variables for maximum oscillation while taking into consideration other formulation responses. As is with the 15 formulations, the wave-like nature of the oscillations and volume changes of the polymer is clearly visible in Figures 5.7 and 5.8. Essentially, to potentiate the redox reaction, nitric acid forms the acid component of the system; however, its toxic properties are detrimental when used biologically. In the psoriasis application of the SOPN, psoriatic keratinocytes forming the bulk of epidermis express the neuronal form isoform of nitric oxide synthase (NOSI) (Kadam *et al*., 2010) providing the acidic component to drive the reaction allowing for the exclusion of nitric acid from the SOPN gel promoting biocompatibility.

As the SOPN shrinks as a result of the oxidised state of the Ru ions, the transmittance decreases and increases upon reduction of the ion (Figure 5.8). Measuring the oscillations at a wavelength of 570nm attributes the conformational change of the PNIPAM component (Pullela *et al*., 2013) of the SOPN illustrating the volume change of the polymer and subsequent macroscopic oscillation of the whole SOPN. Figure 5.8 shows the oscillations at 570nm and depicts the change in amplitude and duration of the oscillations based on the variables at differing concentrations. The formulations vary in the oscillatory amplitude showing the effect on concentration of the SOPN in response to changes in reaction

substrate concentration and CMC, especially where amplitude reduction is noted upon higher CMC concentrations. Table 5.2 compiles the data analyses of the oscillations for all 15 formulations and includes the average oscillation amplitude for each formulation.

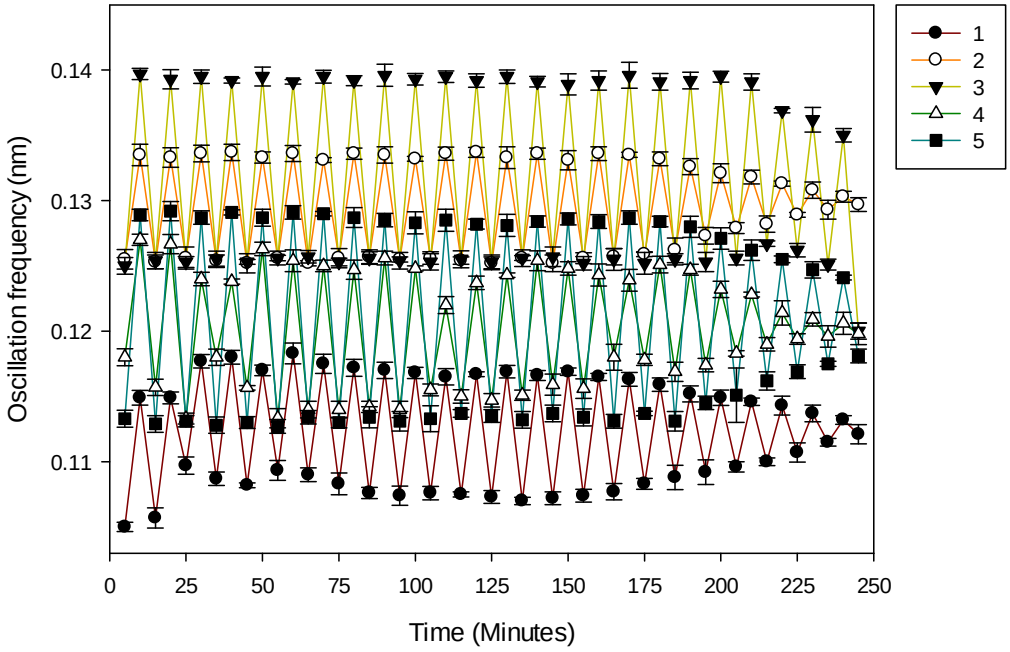


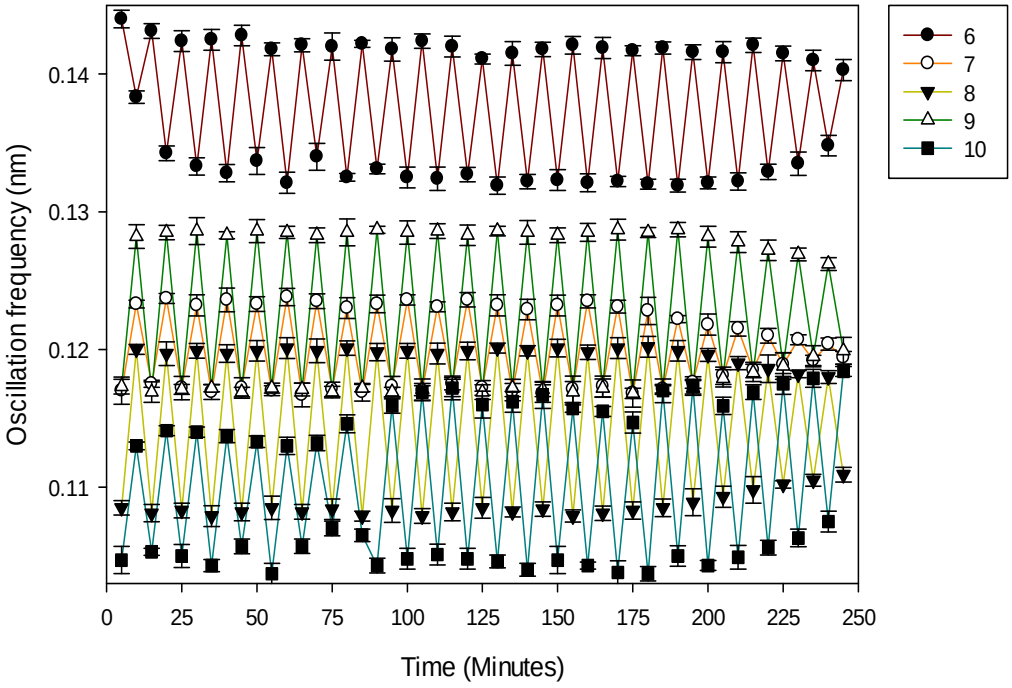

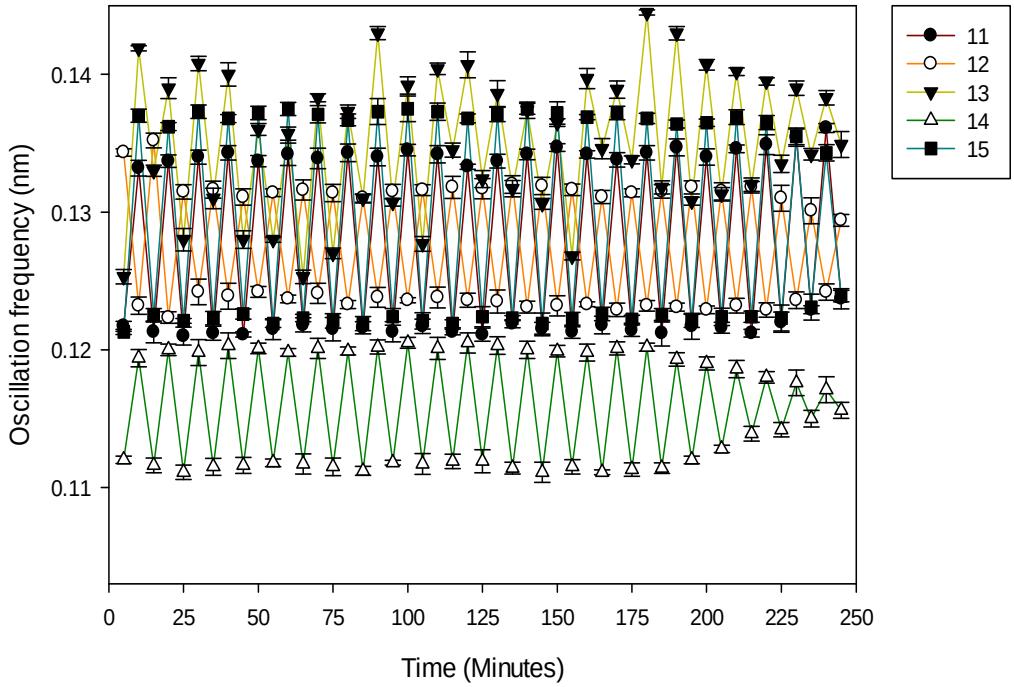


**Figure 5.8:** Self-oscillating vibrational frequency of the 15 Box-Behnken Design formulations. Data presented are mean ± SE of 3 experiments performed in duplicate. *$p$ ≤0.05 versus control.

Formulations 3, 5 and 15 have the highest average oscillations of 13.88, 15.34 and 14.76E$^{-3}$nm, respectively, indicating a trend of the highest oscillating polymer concentration, highest substrate reaction concentration or lowest gel concentration. Conversely, formulations 2, 7 and 12 have the lowest average oscillations of 7.94, 6.53 and 8.38E$^{-3}$nm, respectively, containing the lowest oscillating polymer and reaction substrate concentrations or highest gel concentration, decreasing the oscillatory vibrations of the SOPN system and reducing the duration of the oscillatory phenomenon. Theoretically modelling the BZ reaction, Yashin and Balazs (2007) employed the Tyson and Fife version of the Oregonator model in the following sequence of reactions:

$$A + Y \xrightarrow{k_1 H^2} X + P,$$

$$X + Y \xrightarrow{k_2 H} 2P,$$

$$A + X \xrightarrow{k_3 H} 2X + 2Z,$$

$$X + X \xrightarrow{k_4} A + P,$$

$$B + Z \xrightarrow{k_5} 1/2fY ,$$

where A=[$BrO^{3-}$], B=[all oxidisable organic species], H=[$H^+$], P=[HOBr], X=[$HBrO^2$], Y=[$Br^-$], and Z=[$M_{ox}$]. The stoichiometric factor f is considered as a model parameter. The Oregonator treats the concentrations of the major reactants A, B, and P, as well as the concentration of the hydrogen ion H, as constants. The reaction rate equations for the species X, Y, and Z are

$$dX/dt = k_1H^2AY - k_2HXY + k_3HAX - 2k_4X^2, \quad \text{(Equation 5.1)}$$

$$dY/dt = - k_1H^2AY - k_2HXY + 1/2\ fk_5BZ, \quad \text{(Equation 5.2)}$$

$$dZ/dt = 2k_3HAX - k_5BZ \quad \text{(Equation 5.3)}$$

In a swollen SOPN gel, the self-oscillating polymer network with the attached metal-ion catalyst occupies a volume fraction of the total system. The remaining BZ reaction substrates and CMC gel form the volume fraction (1-ø). The variable concentrations X, Y, and Z are defined with respect to the total volume of the system. In contrast, the concentrations of the reactants are more convenient to define with respect to the volume of the solvent. Recalculating sodium bromate, malonic acid, and nitric acid relative to the total volume is achieved through multiplication by the factor (1-ø). As a result, the following substitutions should be made in the right-hand sides of the reaction rate equations 5.1-5.3

$k_1H2A \rightarrow k_1\,(1\text{-}ø)^3H^2A,$

$k_2H \rightarrow k_2\,(1\text{-}\ ø)H,$

$k_3HA \rightarrow k_3\,(1\text{-}\ ø)^2HA,$

$k_5B \rightarrow k_5\,(1\text{-}ø)B$

Thus, in the derived model, the polymer acts as a diluent (Yashin and Balazs, 2007) which affects the reaction rates through changing the concentrations of the reaction substrates explaining the higher oscillatory amplitude in the formulations containing higher SOPN concentrations. The oscillations lasted 170-225 minutes due to the depletion of reaction substrates per formulation. It can be noted that maximum oscillations last during that period with a sudden reduction in amplitude indicating the end of the reaction. The duration of the oscillations also depend on the formulation variables and can be tailored to output the longest duration which would improve drug delivery through a barrier as time is a consideration.

**Table 5.2:** Experimental design formulation analysis of the oscillating phenomenon and biocompatibility of the SOPN. Data presented are mean ± SE of 3 experiments performed in duplicate. *$p$ ≤0.05 versus control.

| Formulation | Oscillating Polymer (mg) | Reaction Substrate (parts) | Gel (parts) | Average Oscillation Amplitude (nm * $E^{-3}$) | Duration of Oscillations (Minutes) | Permeation (Js)(mg.cm-2.hr-1) | Cell Toxicity (%) |
|---|---|---|---|---|---|---|---|
| 1 | 17.5 | 0.250 | 0.250 | 08.98 | 170 | 0.0842 | 64.44 |
| 2 | 5.00 | 0.250 | 0.250 | 07.94 | 170 | 0.0825 | 64.26 |
| 3 | 30.0 | 1.625 | 1.625 | 13.88 | 210 | 0.0917 | 67.30 |
| 4 | 30.0 | 0.250 | 0.250 | 09.19 | 185 | 0.0865 | 69.42 |
| 5 | 5.00 | 1.625 | 0.250 | 15.34 | 190 | 0.0923 | 64.56 |
| 6 | 30.0 | 1.625 | 1.000 | 09.22 | 225 | 0.0887 | 71.99 |
| 7 | 5.00 | 1.625 | 1.000 | 06.53 | 175 | 0.0796 | 66.19 |
| 8 | 5.00 | 3.000 | 0.625 | 11.77 | 195 | 0.0906 | 71.40 |
| 9 | 17.5 | 1.625 | 0.625 | 11.43 | 200 | 0.0900 | 70.64 |
| 10 | 17.5 | 1.625 | 0.625 | 10.43 | 205 | 0.0899 | 70.28 |
| 11 | 17.5 | 3.000 | 0.250 | 12.70 | 220 | 0.0916 | 72.14 |
| 12 | 17.5 | 3.000 | 1.000 | 08.38 | 220 | 0.0809 | 72.27 |
| 13 | 17.5 | 1.625 | 0.625 | 09.61 | 205 | 0.0891 | 70.19 |
| 14 | 17.5 | 0.250 | 1.000 | 08.58 | 185 | 0.8300 | 68.29 |
| 15 | 30.0 | 3.000 | 0.625 | 14.76 | 225 | 0.0922 | 72.58 |

### 5.3.8. Appraisal of nanoparticle permeation in relation to the self-oscillating polymeric network

In creating a biocompatible system for mass transport of nanoparticles across a barrier, permeation studies employing the Frans Diffusion Apparatus were imperative. The cellulose membrane served as the rate-limiting barrier component of the stratum corneum while buffer of pH 5 was used to simulate the inflammatory environment of the psoriatic lesion. Translocated CuNPs were quantified to determine the oscillatory effect of the SOPN in the enhancement of drug delivery through a biological barrier. The peristaltic kinetics of the SOPN allows for the permeation of the geometric nanocrystals as seen in Figure 5.9 and clearly shows the peak permeation due to the oscillatory vibrations of the polymer.

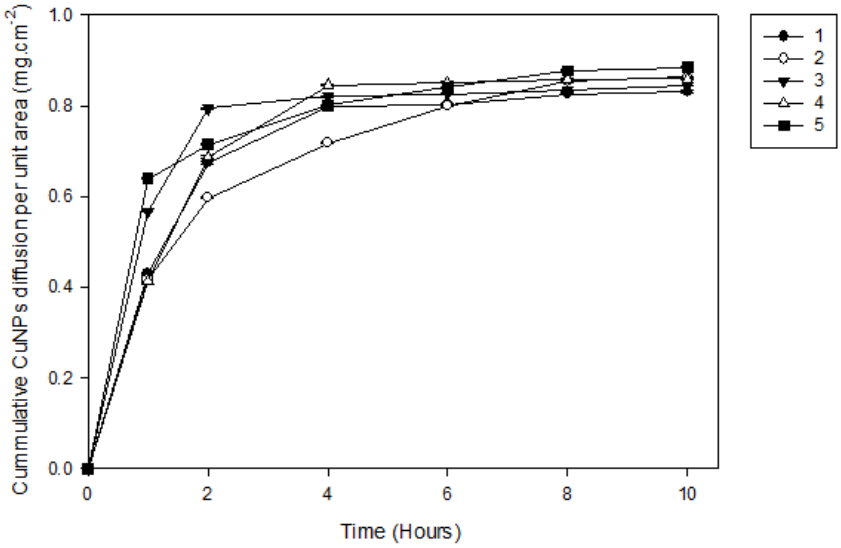


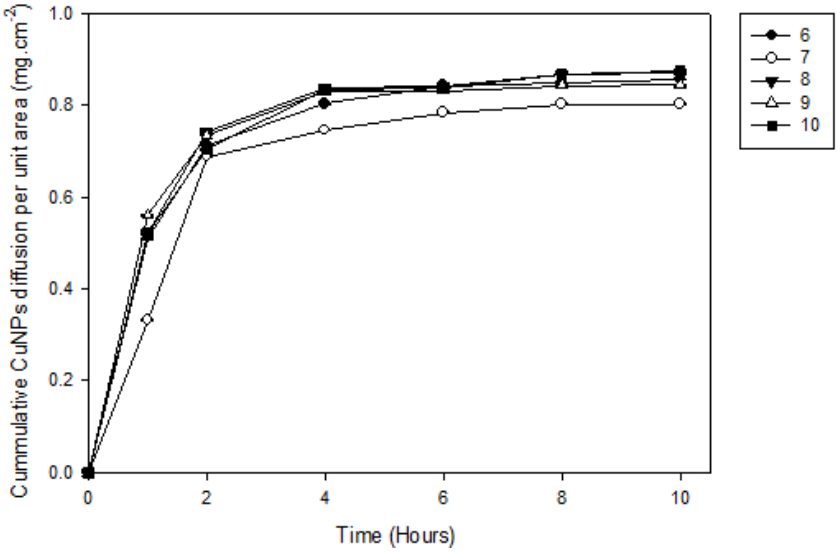

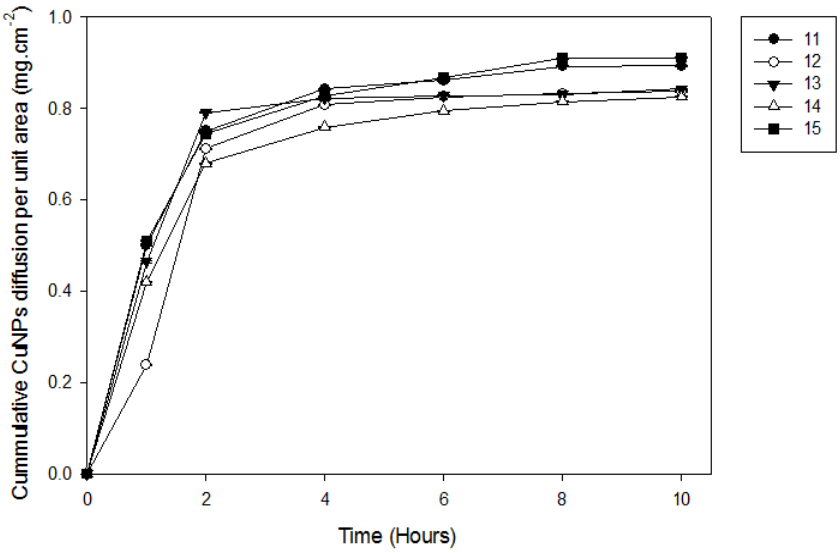


**Figure 5.9:** SOPN potentiated diffusion of CuNPs diffusion through a membrane barrier. Data presented are mean ± SE of 3 experiments performed in duplicate. *$p \leq 0.05$.

It is noted in most formulations that there is a burst CuNP permeation with a slight reduction in flux between the 2nd and 4th hour, thereafter reaching a passive permeation and plateaux due to maximum CuNP translocation and end of the BZ reaction. Slight deviations occur in permeation rates where the flux does not follow the general trend. Formulation 2 has a burst CuNP release in the 1st hour only and steadily decreases in flux which can be accounted for by the use of the minimum concentrations of 5mg of oscillating polymer and 0.250 parts of reduction substrate. The initial burst permeation, however, can be accounted for by the low CMC concentration which does not hinder the oscillations and the duration of the BZ reaction. Similarly, formulation 7 has a fairly linear permeation rate in the first 2 hours before reducing significantly in flux as compared to the other formulations. Also containing 5mg of oscillating polymer explaining the minimum permeation of CuNPs, this formulation has a higher reaction substrate concentration which would ideally potentiate the BZ reaction; however, the higher CMC gel part decreases the amplitude of the oscillations and subsequent flux of CuNPs.

Formulations 3 and 13 show a higher initial CuNP flux by the 2nd hour of permeation studies as compared to other formulations explained by the high oscillation polymer concentration (30mg), intermediate reaction substrate concentration (1.625 parts) and CMC part (1.625) in formulation 3. The derived Tyson and Fife version of the Oregonator model (Yashin and Balazs, 2007) rationalises the higher ratio of oscillating polymer creating larger oscillation amplitudes, therefore having a higher flux during the period of the BZ reaction. Formulation 13 has a lower oscillation polymer concentration of 17mg and a lower CMC concentration of

0.625 parts. Despite having a lower polymer concentration, the high permeation flux is maintained due to the lower CMC in the formulation.

The force created by oscillations of the SOPN is relative to the formulation variables and sufficient to generate energy within the system to stimulate the movement of the geometric CuNPs as the model drug. According to classical physics, the wavefunction associated with the particle requirement movement must be continuous at the barrier. The wavefunction must also be continuous on the far side of the barrier to ensure finite probability of the nanoparticle tunnelling through the barrier. As the nanoparticle approaches the barrier, it is described by a free particle wavefunction. Upon reaching the barrier, it is required to satisfy the Schrodinger equation in the form:

$$-\frac{\hbar 2}{2\mathrm{m}}\frac{\partial 2\Psi(\mathrm{x})}{\partial \mathrm{x}2} = (\mathrm{E} - \mathrm{U}^{\circ})\Psi(\mathrm{x}) \qquad \text{(Equation 5.4)}$$

which has the solution

$$\Psi = \mathrm{A}e^{-\mathrm{ax}} \text{ where } \mathrm{a} = \frac{\sqrt{2\mathrm{m}\,(\mathrm{U}^{\circ}-\mathrm{E})}}{\mathrm{h}^{2}} \qquad \text{(Equation 5.5)}$$

and has a dependence on the fundamental physical constant Planck's constant h.

Murase and associates (2008) discuss the Hertz Contact Theory which can also be adapted for nanoparticles embedded within a loose oscillating gel system. Their research study involved the transport of a cylindrical PAAm gel bead across the surface of an oscillating poly(NIPAAm-co-Ru(bpy)3-co-AMPS) gel sheet. As factors of mass transport, size, gravity, frictional force and contact force play key roles in the design of a transport system, very similar to the kinetics of this study with the exception of the materials for transport loaded within the SOPN. This research group investigated the adsorption of the cargo materials onto the gel surface by an attracting force such as hydrophobic interaction and performance of the peristaltic motion to mass transport materials. Likewise, in the current study, the CuNPs interact with the oscillating polymer and oscillate with the gel. This mechanism constantly disrupts the gel system and forces the movement of the CuNPs across the membrane providing a system useful for drug delivery.

### 5.3.9. Cell toxicity and viability studies

The oscillating phenomenon has previously not been applied for practical biological use possibly due to its toxicity profile. Elucidating the biocompatibility of the system was

necessary, especially for *in vivo* application. The toxicity profile of PNIPAM shows adequate cell viability, biocompatibility and does not elicit a cytotoxic response (Bluestein *et al*., 2017; Guo *et al*., 2017; Li *et al*., 2017), however, when used in combination with other possible cytotoxic polymers the toxicity of the complete system needs to be assessed. In a recent study by Chen and co-workers (2016), their toxicity studies showed the anti-proliferative and cytotoxic activity of ruthenium, in addition to its useful selectivity for cancer cells than normal cells which promotes its use in targeting psoriasis as function of hyperkeratosis. Montani and associates (2016) and Matsui's research group (2016) also proved the reduction in cell viability based on dose dependent concentrations of Ru studied in accordance with anti-cancer drugs. Research also shows the cytotoxic effects of sodium bromate and malonic acid inducing oxidative stress in *in vitro* cellular studies (Al-Sheddi *et al*., 2016; Lazarev *et al*., 2016; Saad *et al*., 2016).

The cell toxicity profiles (Figure 5.10) give an indication of the toxic dose of this system considering all toxic profiles. Using Equation 5.6:

$$\%\ \text{Cell viability} = \frac{\text{Abs(sample)}}{\text{Abs(blank)}} \text{x}\ 100 \qquad \text{(Equation 5.6)}$$

cell toxicity can be ascertained by the difference of 100% and the cell viability %. Differences are small but significant and affect the dosage for *in vivo* use. Using 100µL samples of the complete SOPN gel, toxicity results varied from 64.26 – 72.58%. The results indicate the increase in toxicity as the substrate concentration increased, as was hypothesized. In addition, reduction in the oscillating polymer concentration also resulted in higher cell toxicity due to the cytotoxic profile of ruthenium. However, at the appropriate concentration while still producing mechanical oscillations sufficient to stimulate energy in the system to translocate the geometric CuNPs, the SOPN shows to provide an ideal drug delivery system.

As investigated in our previous research, the CuNPs also has its own toxicity profile which should be taken into consideration apart from the SOPN to prevent excess toxicity to the skin. The geometric CuNPs exerts a mechanism of DNA damage by ROS thereby inducing cell death. Cell toxicity by means of cell membrane damage, change in glutathione production and membrane lipid peroxidation were investigated and a dose dependent toxicity was analyzed. Pertaining to the cube-shaped CuNPs with the highest cellular internalization rates, 25µg/ml has a cell toxicity value of 46%. When 12.5g/ml of the CuNPs incorporated into the SOPN at 50µL were studied after incubated in $1x10^3$ cells/well, toxicity varied from 52.8 – 66.53%. The reduced toxicity accounts for the 50% concentration

decrease of the CuNPs and SOPN which gives an accurate indication of the $LD_{50}$ concentration for *in vivo* application of the CuNP-loaded SOPN.

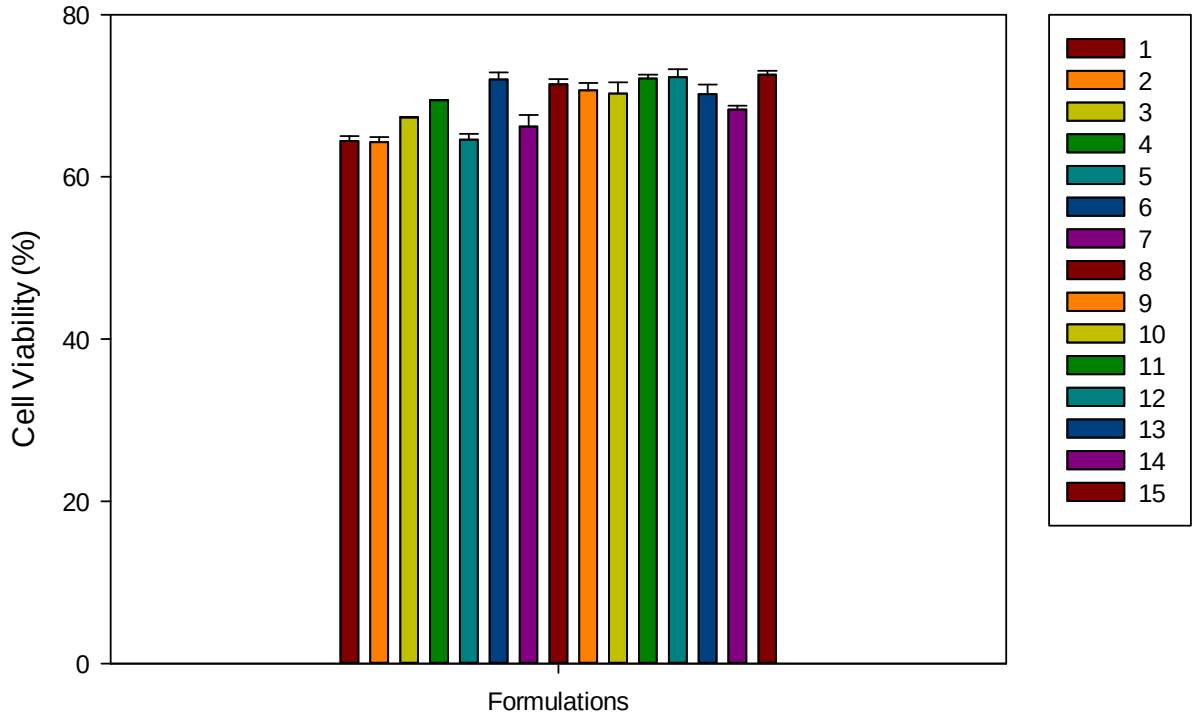


**Figure 5.10:** Cell viability analysis of the SOPN on NHEK cells. Data presented are mean ± SE of 3 experiments performed in duplicate. **p* ≤0.05 versus control.

### 5.3.10. *In vivo* analysis of the geometric copper nanoparticle-loaded self-oscillating polymeric network in the psoriasis model

To investigate the effects of the treatments and control on a psoriasis model, 5% Aldara® was topically applied for 5 days to the shaved backs of BALB/c mice. Imiquimod application induces phenotypic skin changes resembling human psoriasis which includes epidermal hyper-proliferation and acanthosis. The treatment interventions aim to reduce the hyper-proliferative plaque of the induced-psoriasis by cytotoxic mechanisms on the keratinocytes. Figures 5.11a and b, respectively, demonstrates the visual difference between healthy skin and imiquimod-induced psoriasis which presents with inflammation, scaling and thickening of the affected skin. Daily application of the imiquimod cream over a period of 5 days leads to an increased immune response resulting in erythema, swelling and scales (Figure 5.11b). The induction was visibly noticed on the third day of imiquimod application and reached the highest scoring according to the PASI system rendering the model ideal for the beginning of respective treatments.

#### 5.3.10.1. Gross observation of the treated psoriatic lesions by photographic analysis and PASI scoring

After adequate induction of the psoriasis, treatments were applied according to group specifications of CuNPs-loaded aqueous cream, unmedicated aqueous cream, CuNPs-loaded SOPN, unmedicated SOPN and corticosteroid cream application. In the analysis of the effect of treatment, a combination of visual and PASI scoring was utilised as the primary characterization on the induced-psoriasis model. PASI was scored on a scale of 0 to 4 where 0-none; 1-slight; 2-moderate; 3-marked and 4-very severe inflammation with 12 being the maximum possible total score considering the three scoring factors which comprises erythema, scaling and thickening. A hallmark of psoriasis is epidermal hyperplasia which was evident in the induced psoriasiform skin with representative images (Figure 5.11c), the feeling of skin thickness and roughness upon application of the treatments and the PASI scoring evaluation (Table 5.3). The macroscopic presentation of the treated skin after 3, 7 and 14 days of treatment shows effectiveness of the different interventions (Figure 5.11c).

By the end of Phase 1 (day 3) of the treatment interventions, slight differences in erythema, scaling and thickening were already noted according to the visual analysis and PASI scoring. Group 1, 4 and 5 which were the CuNPs-loaded aqueous cream, unmedicated SOPN and corticosteroid cream, respectively, indicated a higher PASI score. The lower PASI score of the CuNPs-loaded SOPN as compared to the CuNPs-loaded aqueous cream and SOPN can be accounted for by its higher cell toxicity profile. The images at the end of Phase 2 (day 7) of all treatment interventions show reduced erythema, scaling and thickening at varying scores. At this time point, according to PASI scoring, the CuNPs-loaded aqueous cream, CuNPs-loaded SOPN and the corticosteroid cream proved to be slightly more effective than the unmedicated aqueous cream and SOPN. There was also slight hair growth indicating effectiveness of the treatments with the most growth in the groups with the lowest PASI scoring. Over the course of the following 7 days (Phase 3), the PASI scoring approached 0, visual analysis indicated complete healing of the plaque and hair growth increased significantly. The time periods, however, varied with the unmedicated aqueous cream maintaining thickened skin. Histological evaluation gives better insight into plaque resolution at a cellular level amongst all treatment interventions. Essentially, these results show Group 3 in which the intervention included the application of the CuNPs-loaded SOPN exhibiting the lowest average PASI score, effectively reducing epidermal thickening and inflammation; and superseding the plaque resolution of Group 5 which was the comparative group.

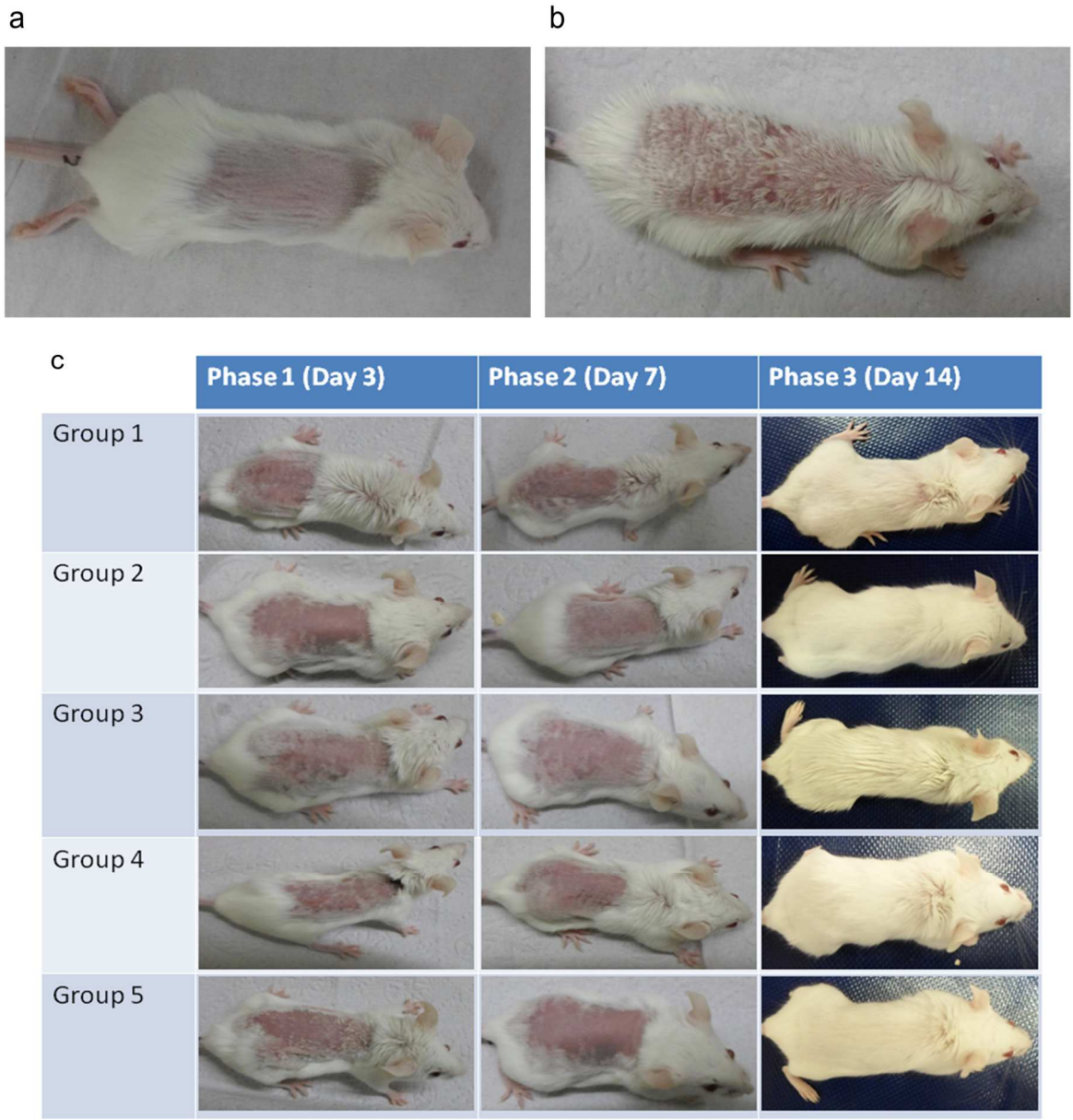


**Figure 5.11:** Macrological transition in the psoriasis model: a) healthy skin; b) imiquimod-induced psoriasis; c) over the 3 phases during treatment interventions for Group1 (CuNPs), Group 2 (aqueous cream), Group 3 (CuNPs-loaded SOPN), Group 4 (SOPN) and Group 5 (corticosteroid cream).

**Table 5.3:** PASI scoring evaluation at 3 phase time points on day 3, 7 and 14 of treatment.

| | **Phase 1 (3 Days)** | **Phase 2 (7 Days)** | **Phase 3 (14 Days)** |
|---|---|---|---|
| Group 1 | 9 | 4 | 0 |
| Group 2 | 8 | 5 | 0 |
| Group 3 | 8 | 4 | 0 |
| Group 4 | 9 | 5 | 0 |
| Group 5 | 9 | 4 | 0 |

**5.3.10.2. Histopathological investigation of the psoriasis interventions**

Histological analysis of healthy skin compares the changes in the induced-psoriasis model with the skin samples from each treatment intervention. In Figures 5.12a and b, respectively, samples of healthy, untreated skin complies with normal appearance while imiquimod-induced psoriatic skin shows severe epidermal hyperplasia with shallow rete pegs and formation of psoriasiform-type hyperplasia. Figure 5.12b shows serocellular crusts in the keratin and acanthosis also extends similarly to the follicular infundibulae where increased mitosis is also visible in the basal layers. The skin shows severe orthokeratotic hyper-keratosis and the dermis shows a diffuse interstitial inflammatory reaction consisting predominantly of neutrophils, lymphocytes, plasma cells and few mast cells and eosinophils.

The results (Figure 5.12c) show a change with each treatment over each time period, however, the extent of change varies. It should also be noted that the healing of the induced psoriasis is also time- and imiquimod-dependent. The cessation of the stimuli automatically results in cessation of the immune disorder. Therefore, effect of the treatment interventions were analyzed based on differences between samples and extent of healing; and not related to the chronic condition of psoriasis but rather the psoriasiform condition presented by the model.

In the first phase of the treatment interventions where samples were taken at day 3 of application, an improvement is noted. At day 3, treatment Group 1 shows moderate epidermal hyperplasia with mild shallow rete pegs. Moderate acanthosis extending mildly into some of the follicular infundibulae and mild interstitial inflammation in the dermis with few neutrophils is evident. The aqueous cream Group 2 shows moderate epidermal hyperplasia and the presence of mitotic figures. Acanthosis is present in slight undulation in the basal layer and mild oedema was observed. Mild dermal inflammation is observed with mild hypergranulosis in the granular layer. The skin samples from Group 3 where the CuNPs-loaded SOPN was applied shows mild to moderate epidermal hyperplasia without rete peg presence or psoriasiform appearance. Small serocellular crusts are visible in the keratin. Mild acanthosis and inflammation is visible in very few areas of the samples and hair follicles appear normal. Skin samples from the unmedicated SOPN treatment Group 4 shows moderate epidermal hyperplasia with features similar to Group 3 with the exception of the hair follicles showing mild infundibular acanthosis. The commercial product treatment Group 7 shows moderate hyperplasia with few mitotic figures present. There are few areas with mild dermal inflammation and moderate hypergranulosis is evident in the epidermis. Acanthosis extending to the follicular infundibulae are prominent with follicles showing perifollicular inflammation. The treatment group 1 and 3 were compared with 2, 4 and 5 and

obvious differences are noted where the changes in Group 5 are not as progressive as the other groups as was expected. Group 3 showed fair changes with the best outcome at this phase of treatment.

In the second phase of the treatment interventions at day 7, the CuNP-loaded aqueous cream Group 1 shows a mild acanthotic dermis with moderate thickening. No dermal rete peg presence or psoriasiform changes are visible and mild to minimal inflammation is observed. In the unmedicated aqueous cream group, mild hyperplasia is noted with mild hypergranulosis and mild interstitial inflammation. Skin samples from Group 3 (CuNPs-loaded SOPN) show mild epidermal hyperplasia without rete peg presence or psoriasiform appearance. The skin appears normal mild inflammation and active hair follicles. The samples from the unmedicated SOPN treatment Group 4 shows mild epidermal hyperplasia with fairly normal occurring epidermal layers, mild to minimal inflammation and active hair follicles. The application of the commercial product after 7 days results in mild epidermal hyperplasia, areas of acanthosis, mild hypergranulosis, single mitotic figures in the basal layer and mild interstitial inflammation with active hair follicles. Similar to phase 1, it is obvious that the copper nanoparticles have a positive effect on the psoriasis model, especially when in use with the SOPN for enhanced cellular delivery. It can be assumed that this drug delivery system potentiates its cytotoxic properties in the presence of inflammation and does reduce epidermal hyperplasia to a higher extent than it commercial counterpart.

After 14 days (Phase 3) of applying the respective treatments, treatment Group 1 shows mildly increased thickness of the epidermis with normal three cell layer thick epidermis and few single lymphocytes in the interstitium. Group 2 shows mild acanthosis and mild flaking orthokeratotic hyperkeratosis. Further, few granular cells were present in addition to odd lymphocytes and mast cells interstitially. Group 3 showed normal appearance of the epidermis and active hair follicles except for few single lymphocytes in the interstitium. Similarly, Group 4 also showed healthy skin appearance but with few granular cells and lymphocytes. Group 5 showed a mild orthokeratotic keratosis and presence of few interstitial lymphocytes. It is deduced from these results that the novel systems have a significant role in psoriasiform conditions, more so than a moisturising aqueous cream and the current commercial gold standard. It is also noted that the CuNPs in combination with the SOPN is a system that reduced the typical features of the induced dermal condition. The CuNPs-loaded aqueous cream and unmedicated SOPN also elicited a positive effect and even though it was to a higher extent than the aqueous cream application (Group 2), it was minimal compared to the CuNPs-loaded SOPN. The dual toxicity and inflammation-selective properties of the optimized system CuNPs-loaded SOPN reflects an optimal drug delivery

system and surpassed the expectations of the commercial product. The commercial product maintained the inflammation longer than the experimental formulations, in contrast to its mechanism of action which includes inflammation reduction. It was noted that the unmedicated SOPN did elicit an anti-psoriasiform effect due to the presence of the cytotoxic ruthenium, however, not as significant to the CuNPs-loaded SOPN and slightly lagged behind the CuNPs-loaded aqueous cream.

In essence, the both CuNPs systems had positive outcomes and proves its use as an agent for use in hyper-proliferative conditions. It should also be considered that the CuNPs has an optimum mechanism in the presence of the SOPN for its own toxic properties in addition to its ability to oscillate the system and stimulate the movement of active ingredient across the innate barrier.

a b

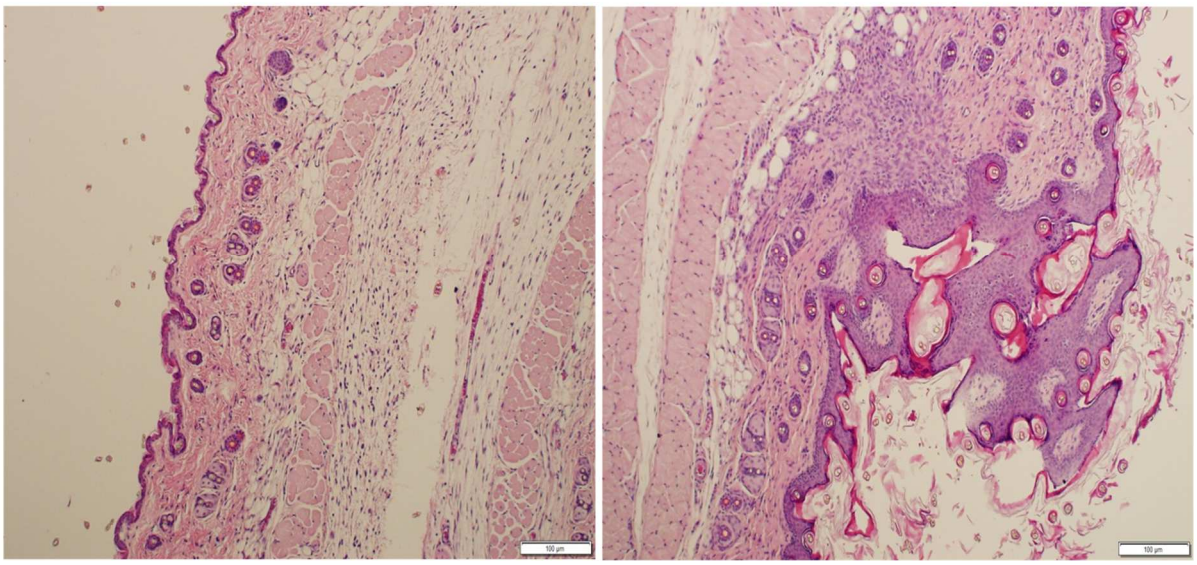

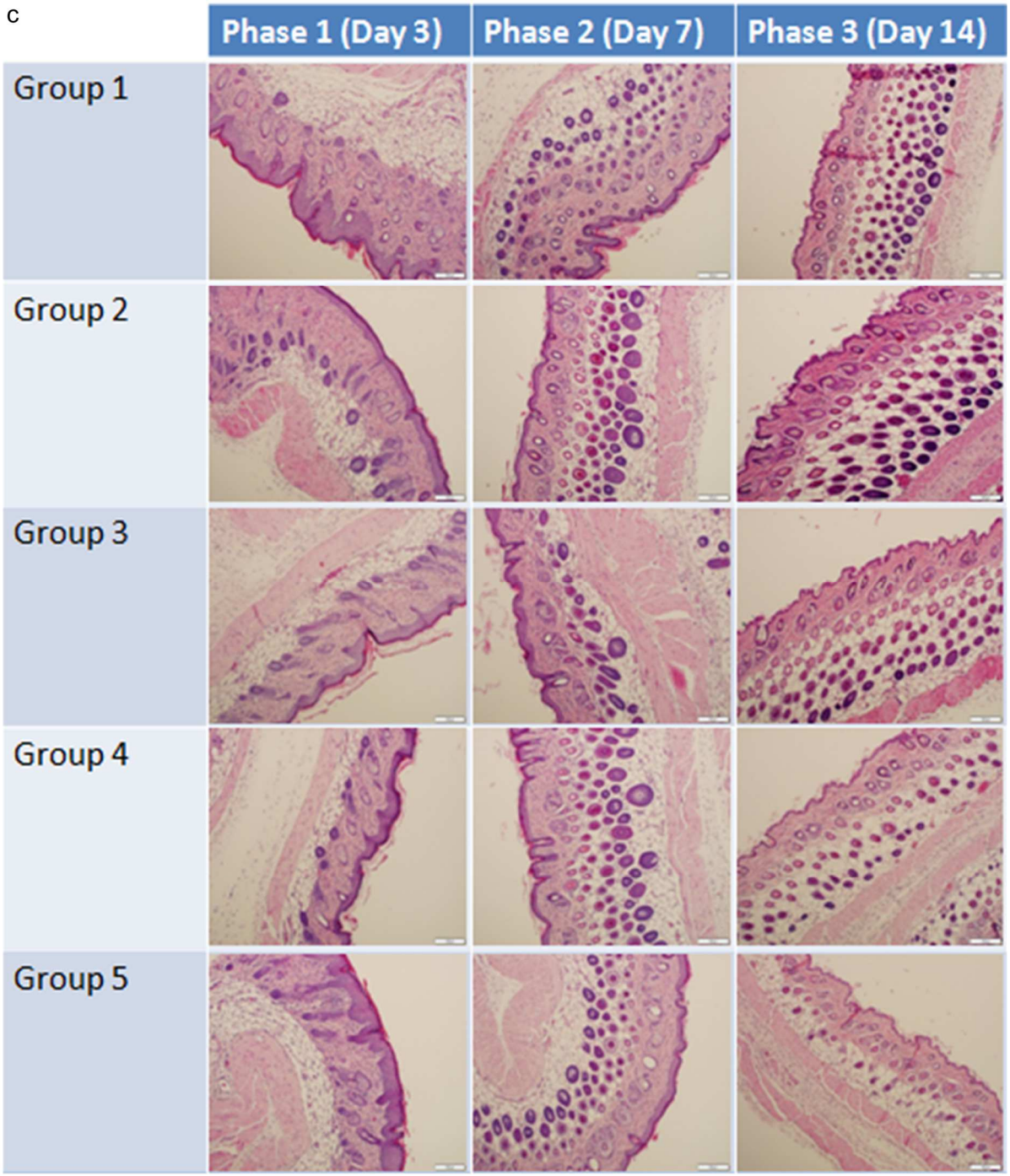


**Figure 5.12:** Histology pictographs comparing mice skin samples from a) Group A (CuNPs-loaded aqueous cream); b) Group B (Unmedicated aqueous cream); c) Group C (CuNPs-loaded SOPN); d) Group D (Unmedicated SOPN); e) Group E (commercial product) at days 3, 7 and 14.

### 5.3.10.3. Quantification of copper retention in dermal skin and blood

Copper has increased toxicity in the inflammatory environment due to the acidic components and converted ionic copper is manipulated in the reduction of the hyper-proliferative keratinocytes of the psoriasiform-plaque. In healthy, physiological concentrations, copper is an essential trace element used in cellular oxidative phosphorylation in energy production

pathways (Ruiz *et al*., 2016). The geometric CuNPs at a $LD_{50}$ dose exhibited cytotoxicity leading the cell death via oxidative stress. After dissolution of the CuNPs, high intracellular concentrations of redox active copper ions induces lactate dehydrogenase and lipid peroxidation activity and reduces glutathione. In addition to cell death by DNA damage, loss of membrane integrity resulted in the toxicity initiated by anion superoxide production. Anion superoxide formation leads to generation of radical hydroxyl ions responsible for interference in physiological cellular integrity.

Used in the process of toxicity to reduce the psoriatic lesion, the excess copper is disposed into peripheral blood supply and excreted by the kidneys. As seen in Figure 13a and b, the measured copper in the blood and skin at days 3, 7 and 14 of topical application increases steadily within the first 3 days and thereafter stabilises, reaching a steady plateau after 7 days as the body compensates for and excretes the influx of copper within the therapeutic range. The relative concentration of copper detected in the skin via ICP-OES is higher than that of the detection in the blood indicating excretion from the blood once in systemic circulation. At 3 days of application of the CuNPs-loaded aqueous cream, 3.031µg/g of copper was detected in the blood and 3.140µg/g of copper was detected in the skin, The lower amount of copper detection in the blood compared with the skin is constant until the $14^{th}$ day of sampling where 3.238 µg/g and 3.300µg/g was detected in the blood and 3.360µg/g and 3.410µg/g was detected in the skin on the $7^{th}$ and $14^{th}$ days, respectively. By the $3^{rd}$ day of application of the CuNPs-loaded SOPN, the copper concentration detected in the blood was minimally higher at 2.873µg/g as compared to the 2.870µg/g detected in the skin. However, this trend did not continue and similar to the CuNPs-loaded aqueous cream analyses; the application of the CuNPs-loaded SOPN resulted in reduced copper concentrations in the blood and skin until the $14^{th}$ day. 3.006µg/g and 3.050µg/g copper detection in the blood and 3.040µg/g and 3.100µg/g copper detection in the skin on days 7 and 14, respectively showed the healthy metabolism and excretion of the copper.

Higher concentrations found in the skin also promote the copper nanosystem as an efficient material drug delivery system due to its retention, thus prolonging its effect in the target area. The increased copper detected in the blood and skin with the application of the CuNPs-loaded aqueous cream is due to the higher concentration of copper loading. The $LD_{50}$ concentration of the CuNPs are reduced when incorporated into the SOPN as the SOPN exhibits its own level of toxicity. The nanosystem embedded in the corresponding vehicles show to be biocompatible entities at copper doses sufficient for its designated role in cell death while maintaining healthy concentrations in the well-being of the *in vivo* model.

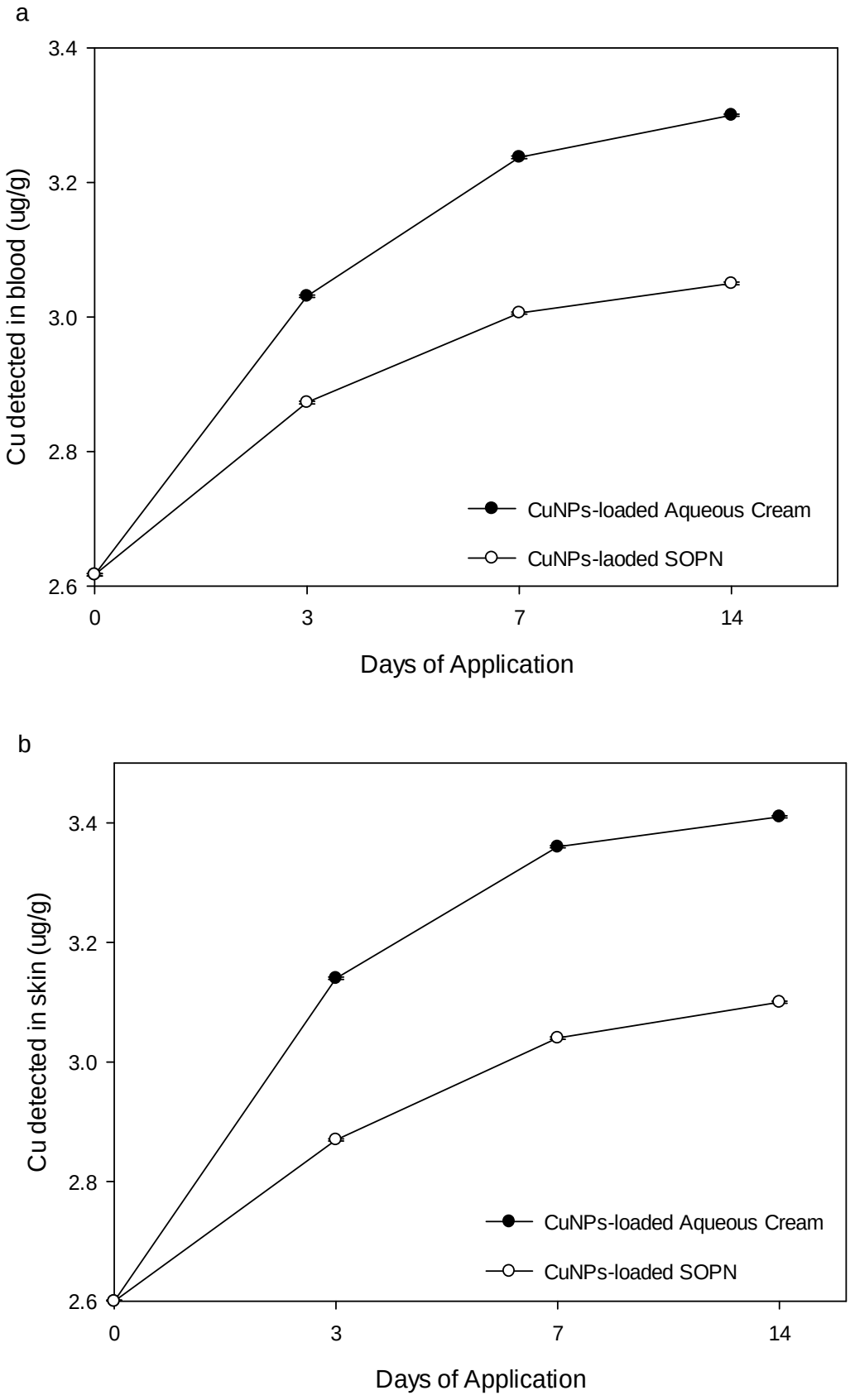


**Figure 5.13:** Copper retention in a) blood; b) skin. Data presented are mean ± SE of 3experiments. *$p$ ≤0.05 versus control.

## 5.4. Concluding Remarks

The successful synthesis of geometric CuNPs and a SOPN drug delivery vehicle has been applied *in vivo* in the imiquimod-induced BALB/c mouse model. It has been shown that the geometry of nanoparticles affects internalization rates and by designing geometric CuNPs and determining the nano-shape with the highest uptake in keratinocytes, we were able to determine optimum nano-shape for uptake in addition to its use as a cytotoxic agent in the treatment of psoriasis. Cellular internalization investigations proved cube-shaped CuNPs to have the highest rate of uptake and were therefore used in the study. The novel SOPN was also studied for its biological compatibility and was adapted for use as a vehicle and nanoparticle-stimulus to cross the stratum corneum of the skin. *In vitro*, the CuNPs-loaded SOPN was optimized to ensure optimal oscillations at the ideal duration for enhanced permeation of the CuNPs across a barrier. Utilizing the toxic profiles of the CuNPs and SOPN at ideal concentrations and the chemical-mechanical oscillations from the SOPN, the system showed promising results as a new topical drug device for psoriasiform and hyper-keratotic conditions which includes warts caused by the human papilloma virus. The BZ reaction has been applied *in vivo* with excellent results and nitric acid being present in the psoriasiform model allows for the safe use of the SOPN. The multi-novel designed system exploits geometric CuNPs as a drug delivery system for cellular internalization and the SOPN for stimulated movement of the CuNPs defeating a strong biological barrier and treating a chronic condition at a faster rate than the commercial gold-standard.

## 5.6. References


Al-Sheddi, E.S., Farshori, N.N., Al-Oqail, M.M., Musarrat, J., Al-Khedhairy, A.A. and Siddiqui, M.A., 2016. Protective effect of Lepidium sativum seed extract against hydrogen peroxide-induced cytotoxicity and oxidative stress in human liver cells (HepG2). *Pharmaceutical biology*, *54*(2), pp.314-321.

Bluestein, B.M., Reed, J.A. and Canavan, H.E., 2017. Effect of substrate storage conditions on the stability of “Smart” films used for mammalian cell applications. *Applied Surface Science*, *392*, pp.950-959.

Boehncke, W.H., 2015. Etiology and pathogenesis of psoriasis. *Rheumatic Disease Clinics of North America*, *41*(4), pp.665-675.

Chen, L.M., Peng, F., Li, G.D., Jie, X.M., Cai, K.R., Cai, C., Zhong, Y., Zeng, H., Li, W., Zhang, Z. and Chen, J.C., 2016. The studies on the cytotoxicity in vitro, cellular uptake, cell cycle arrest and apoptosis-inducing properties of ruthenium methylimidazole complex [Ru (MeIm) 4 (p-cpip)] 2+. *Journal of inorganic biochemistry*, *156*, pp.64-74.

Cross, S.E., Innes, B., Roberts, M.S., Tsuzuki, T., Robertson, T.A. and McCormick, P., 2007. Human skin penetration of sunscreen nanoparticles: in-vitro assessment of a novel micronized zinc oxide formulation. *Skin pharmacology and physiology*, *20*(3), pp.148-154.

Gamer, A.O., Leibold, E.V. and Van Ravenzwaay, B., 2006. The in vitro absorption of microfine zinc oxide and titanium dioxide through porcine skin. *Toxicology in vitro*, *20*(3), pp.301-307.

Gattu, S. and Maibach, H.I., 2010. Modest but increased penetration through damaged skin: an overview of the in vivo human model. *Skin pharmacology and physiology*, *24*(1), pp.2-9.

Guo, Z., Li, S., Wang, C., Xu, J., Kirk, B., Wu, J., Liu, Z. and Xue, W., 2017. Biocompatibility and cellular uptake mechanisms of poly (N-isopropylacrylamide) in different cells. *Journal of Bioactive and Compatible Polymers*, *32*(1), pp.17-31.

Hara, Y. and Yoshida, R., 2005. Control of oscillating behavior for the self-oscillating polymer with pH-control site. *Langmuir*, *21*(21), pp.9773-9776.

Ito, Y., Hara, Y., Uetsuka, H., Hasuda, H., Onishi, H., Arakawa, H., Ikai, A. and Yoshida, R., 2006. AFM observation of immobilized self-oscillating polymer. *The Journal of Physical Chemistry B*, *110*(11), pp.5170-5173.

Ito, Y., Nogawa, M. and Yoshida, R., 2003. Temperature Control of the Belousov− Zhabotinsky Reaction Using a Thermoresponsive Polymer. *Langmuir*, *19*(23), pp.9577-9579.

Kadam, D.P., Suryakar, A.N., Ankush, R.D., Kadam, C.Y. and Deshpande, K.H., 2010. Role of oxidative stress in various stages of psoriasis. *Indian journal of clinical biochemistry*, *25*(4), pp.388-392.

Kang, D., Li, B., Luo, L., Jiang, W., Lu, Q., Rong, M. and Lai, R., 2016. Curcumin shows excellent therapeutic effect on psoriasis in mouse model. *Biochimie*, *123*, pp.73-80.

Larese, F.F., D'Agostin, F., Crosera, M., Adami, G., Renzi, N., Bovenzi, M. and Maina, G., 2009. Human skin penetration of silver nanoparticles through intact and damaged skin. *Toxicology*, *255*(1), pp.33-37.

Lazarev, V.F., Nikotina, A.D., Semenyuk, P.I., Evstafyeva, D.B., Mikhaylova, E.R., Muronetz, V.I., Shevtsov, M.A., Tolkacheva, A.V., Dobrodumov, A.V., Shavarda, A.L. and Guzhova, I.V., 2016. Small molecules preventing GAPDH aggregation are therapeutically applicable in cell and rat models of oxidative stress. *Free Radical Biology and Medicine*, *92*, pp.29-38.

Li, J., Liu, J., Xu, L. and Chen, J., 2017. Preparation of thermoresponsive fluorescent carbon dots for cellular imaging. *Polymer International*, *66*(1), pp.92-97.

Matsui, T., Sugiyama, H., Nakai, M. and Nakabayashi, Y., 2016. DNA Interaction and Cytotoxicity of Cyclometalated Ruthenium (II) Complexes as Potential Anticancer Drugs. *Chemical and Pharmaceutical Bulletin*, *64*(3), pp.282-286.

Montani, M., Pazmay, G.V.B., Hysi, A., Lupidi, G., Pettinari, R., Gambini, V., Tilio, M., Marchetti, F., Pettinari, C., Ferraro, S. and Iezzi, M., 2016. The water soluble ruthenium (II) organometallic compound [Ru (p-cymene)(bis (3, 5 dimethylpyrazol-1-yl) methane) Cl] Cl suppresses triple negative breast cancer growth by inhibiting tumor infiltration of regulatory T cells. *Pharmacological research*, *107*, pp.282-290.

Murase, Y., Maeda, S., Hashimoto, S. and Yoshida, R., 2008. Design of a mass transport surface utilizing peristaltic motion of a self-oscillating gel. *Langmuir*, *25*(1), pp.483-489.

Perera, G.K., Di Meglio, P. and Nestle, F.O., 2012. Psoriasis. Abbas AK, Galli, SJ, Howley, PM. *Annual Review of Pathology: Mechanisms of Disease*, *72012*, pp.385-422.

Pullela, S.R., Wang, Q. and Cheng, Z., 2013. Self-oscillating structural polymer gels. *Advanced Nanoparticles,* 2, pp.94-98.

Ruiz, L.M., Jensen, E.L., Rossel, Y., Puas, G.I., Gonzalez-Ibanez, A.M., Bustos, R.I., Ferrick, D.A. and Elorza, A.A., 2016. Non-cytotoxic copper overload boosts mitochondrial energy metabolism to modulate cell proliferation and differentiation in the human erythroleukemic cell line K562. *Mitochondrion*, *29*, pp.18-30.

Saad, H.B., Driss, D., Chaabouni, S.E., Boudawara, T., Zeghal, K.M., Hakim, A. and Amara, I.B., 2016. Vanillin mitigates potassium bromate-induced molecular, biochemical and histopathological changes in the kidney of adult mice. *Chemico-biological interactions*, *252*, pp.102-113.

Sala, M., Elaissari, A. and Fessi, H., 2016. Advances in psoriasis physiopathology and treatments: Up to date of mechanistic insights and perspectives of novel therapies based on innovative skin drug delivery systems (ISDDS). *Journal of Controlled Release*, *239*, pp.182-202.

Stewardson, D.J. and Whitfield, R.I., 2004. A demonstration of the utility of fractional experimental design for finding optimal genetic algorithm parameter settings. *Journal of the Operational Research Society*, *55*(2), pp.132-138.

Vogt, A., Wischke, C., Neffe, A.T., Ma, N., Alexiev, U. and Lendlein, A., 2016. Nanocarriers for drug delivery into and through the skin—Do existing technologies match clinical challenges?. *Journal of Controlled Release*, *242*, pp.3-15.

Yashin, V.V. and Balazs, A.C., 2007. Theoretical and computational modeling of self-oscillating polymer gels. *The Journal of chemical physics*, *126*(12), p.124707.

# CHAPTER 6

# CONCLUSIONS AND RECOMMENDATIONS

## 6.1. Conclusions

The advancement in the field of drug delivery is a continuous avenue of growth in confronting treatment limitations. Merging various aspects of this field drastically aids the cause of improving drug delivery due to the different views and is therefore able to satisfy several aims within one system. Furthermore, as is with this study, the integration of a multitude of fields serves as the ideal outcome to solve the challenge of chronic diseases and patient compliance. Material science, polymer science and drug delivery is an apt combination and its innovation proves beneficial in progressing each field.

Numerous breakthrough psoriasis treatment strategies have been designed to surpass current models, however, the common limitations continue to exist and no system is fully efficient. Hence, the design of the geometric CuNPs for enhanced cellular uptake and cytotoxic effects against hyper-proliferative cells of the plaque in addition to the self-oscillating mechanism of the SOPN to stimulate the transport of the CuNPs across the stratum corneum which acts as a biological barrier and impediment to dermal drug delivery.

90nm spherical, rod, pyramidal, cubic and 5nm spherical CuNPs were synthesized using two distinctive surfactants as shape-dictating parameters. The novelty of the concept, practice and experiment resulted in the geometric, controlled growth of copper nanocrystals. Post *in vitro* characterization, the nanocrystals were confirmed to exist as pure copper corresponding to the theoretical description of the metal. The key surfactants, CTAB and SDS, formed a catanionic complex which coated the CuNPs during synthesis. The coating was adsorbed dependent on surface energy of the growing nanoparticle and selectivity of the adsorption based on minimising the energy in the system. The surfactant adsorption assisted with preventing oxidation of the copper when exposed to air and maintained its crystallinity.

In the determination of the cytotoxic range and $LD_{50}$ of the CuNPs, *ex vivo* analyses included investigation against a human keratinocyte cell line and human cervical cell line. The difference in toxicity between the two cell lines allowed for distinguishing the activity of copper on normal and cancerous cells. Showing more toxicity against the cancer cell line, it was concluded that the copper will be suitable in the hypothesised model. In addition, the

effect of shape on the internalization kinetics of the nanoparticles showed higher uptake with the cubic CuNPs as opposed to the rods, pyramids and spheres (5 and 90nm). The uptake was independent of surface charge and relied on orientation to the cell membrane. Sharp aspects played a role in the attachment and endocytosis rates which were confirmed by imaging and ICP-OES analysis.

Additional *ex vivo* studies included permeation kinetics of the geometric CuNPs across epidermal mice skin samples. The transport across the simulated barrier showed delayed results as the copper was retained in the skin and exited the barrier upon saturation. This system proved to be promising seeing as the copper is required to exert its effects within the epidermal skin layer. Delayed flux of the CuNPs at 2-4 hours after incubation exhibited burst release and reached plateaux after 12-16 hours. The *ex vivo* environments were insufficient to fully investigate the effects of a geometric copper nanosystem; hence *in vivo* analysis was pursued.

The SOPN was synthesised to serve as a vehicle for the geometric CuNPs and to stimulate the movement of the nanoparticles across the stratum corneum of the skin. This barrier is the source of several limitations to dermal drug delivery and the SOPN aimed to overcome the limitation of the barrier being a rate limiting factor hindering the permeation of nanoparticles. Using the inflammatory environment of the psoriasis and acidic mediators, the reaction stimulating the oscillations are initiated by exploiting the existing condition. On-off changes in the oxidative state of the catalyst ion promote hydrophilic changes in the responsive polymer it is cross-linked to which results in the oscillating mechanism of the network. *In vitro* investigations of the synthesized polymer determined the amplitude and duration of the oscillations which when applied to *ex vivo* permeation studies corresponded to the enhanced permeation rates of the CuNPs which were embedded in the SOPN. Inclusive *ex vivo* analyses probed the toxicity of the SOPN and further changes to the CuNPs-SOPN system were made to ensure biocompatibility and maintenance of skin integrity with minimal irritation.

Psoriasis was induced in the BALB/c mouse by applying imiquimod on the shaved dorsal aspect of each mouse for 5 consecutive days. An immune reaction cascade resulted in the psoriasis-like plaque at the site of application which acted as the disease model for the *in vivo* investigation of the CuNPs-SOPN drug delivery system. CuNPs embedded in an aqueous cream base, aqueous cream, CuNPs-loaded SOPN, unmedicated SOPN and a commercial corticosteroid were the treatment groups used for investigation of the synthesised systems and comparison. The CuNPs-aqueous cream, CuNPs-loaded SOPN

and commercial product showed higher plaque healing than their counterpart groups with the CuNPs-loaded SOPN showing highest resolve. Essentially, the optimized SOPN proved to be a successful therapeutic option and should be considered for further trials in the control of psoriasis.

In summary, this thesis focused on the formulation of geometric CuNPs ensuring increased cellular internalization as a function of shape and cytotoxicity based on the copper *in vivo* reaction. Cube-shaped nanoparticles showed the best results with regards to the discussed and an SOPN gel vehicle for enhanced dermal drug delivery fulfilled the role as a mediator for the aim. The SOPN also exhibited its own toxicity allowing for a reduction in the active CuNPs concentration. In essence, the limitations and barriers to improved psoriasis treatment was addressed by improving target cell uptake, increasing the rate of cell uptake of nanoparticles, dose reduction due to targeted intracellular delivery, elimination of drug-associated side-effects and enhanced permeation through the stratum corneum as a biological barrier to dermal drug delivery. Thus, this invention is a novel and innovative addition to the treatment strategies of psoriasis and supersedes benefits to the patient.

### 6.2. Recommendations

The formulation of the CuNPs-loaded SOPN resulted in a system that satisfied the aims and objectives of the study. *In vitro*, *ex vivo* and *in vivo* analysis showed the fabrication of a system that is significant enough, however, additions to the study may have enhanced the data output.

An addition to Chapter 2 in *ex vivo* characterization of the CuNP internalization using human keratinocyte cells should include TEM image investigation to elucidate the movement of CuNPs within the cell. Observation of the trafficking the internal location of CuNPs may give more insight into the site of activity induced by the copper and the preferential location of stability for the CuNPs. In addition, live-time imaging of the internalization process will further add to the interest upon viewing the endocytosis of the CuNPs and dissect the orientation dependence on the internalization.

Furthermore, in the permeation analysis of the SOPN in Chapter 5, a cellulose membrane was used as the simulated barrier of the stratum corneum. Complementing the study on permeation kinetics of the SOPN based on the oscillations, epidermal mice skin could be used to determine if the flux of the CuNPs through the epidermis CuNPs was maintained or

if the increased trans-stratum corneum transport stimulated the permeation through the entire skin layer. These results would compare to that of the geometric CuNPs in Chapter 3.

Although the *in vivo* animal study model proved to be efficient, additional analyses of samples could have been included. Results obtained include imaging of the psoriatic plaque throughout the 14 day treatment period, PASI score recording of the degrees of inflammation, histology analysis of the treated skin samples for a thorough investigation into the effects of the treatments applied, blood and skin sampling at 3, 7 and 14 day intervals to determine the *in vivo* fate of the CuNPs and confirm biocompatibility of the systems at systemically non-toxic doses. To enhance the current study, mouse urine should be collected daily or at the end of each phase (days 3, 7 and 14) for further elucidation using ICP-OES to detect and quantify copper excretion and tracking of the rate of copper metabolism.

### 6.3. Future Outlook

The crucial goal of this research was to develop a geometric CuNPs system for enhanced intracellular drug delivery with toxic properties embedded in a self-oscillating gel for promoted delivery across the skin barrier with the focal-point honing in on the improvement of patient compliance and reduction of the thickness of the psoriatic plaque. Ultimately, the optimum benefit of the CuNPs-loaded SOPN will be experienced if the system is employed in its entirety; however, in the application of other disease conditions, each system may be employed individually. Therefore, owing to the immense promise of the geometric CuNPs and the SOPN, disease applications may include but not limited to the following conditions:

- Cancer therapy: the concept of the nanoparticles can be applied to other hyper-proliferative cells, especially in a systemic *in vivo* model. The geometric property of the CuNPs promotes the ideology of enhanced cell uptake when compared to standard CuNPs intended for cancer drug delivery. This research shows the toxic activity of the copper while maintaining healthy copper blood levels, showing a biocompatible system. The nanoparticles can be tailored by surface-coating adjuvant chemo drugs in addition to the surfactants and targeting moieties for cancer cells. The dose administered will therefore differ depending on the toxicity of the chemo drug.

- Skin cancer: as is with the geometric CuNPs in the systemic application of chemotherapy, it can be applied topically in the treatment of skin cancer. This would

call for the dual use of the SOPN to penetrate the stratum corneum barrier and target the epidermal hyperplasia. Topical therapy of the CuNPs coated with chemo drugs facilitates reduced side effects due to a lower concentration of chemo drug and a possible reduced therapeutic time due to intracellular delivery of the copper and drug. Similar to psoriasis, the geometric CuNPs would exert the same effects.

- Warts: employing the CuNPs-loaded SOPN in the treatment of warts could be significantly effective in the prognosis of the condition. Current wart therapy has deleterious side effects and affects patient compliance due to the irritation of healthy skin exposed to the treatment or specific instructions for application. Imiquimod is used in wart therapy and prolonged use initiates an immune response which may lead to lifelong effects. In this research study, imiquimod was used as the inducing agent for psoriasis indicating the toxicity of the drug. Application of the CuNPs prevents the onset of these side effects and the cytotoxic effects are exerted on the hyper-keratinized lesion. The SOPN assists with potentiating the transport of the CuNPs lesion and exposure to healthy skin will not be detrimental to the patient.

- Keratin disorders: epidermal thickening, keratinocyte proliferation, ichthyosiform dermatoses and acanthosis are dermal conditions which suit the application of the CuNPs-loaded SOPN. Current therapy focuses on reducing inflammation and challenges to the therapy exist as these are chronic therapies. Similar to psoriasis, these conditions have proliferation presentation and the cytotoxic mechanism of plaque resolve applies.

- Calluses and corns: hypertrophy of the stratum corneum and accelerated proliferation of dermal cells result in callus formation commonly found on the feet. Also occurring on the feet, corn formation is a condition of hyperkeratosis. Conservative treatments for calluses and corns include corticosteroids leading to surgical removal. The ease of employing the CuNPs-loaded SOPN to treat these conditions could promote reduction of the proliferating lesion.

- Dermal bacterial conditions: the neo-geometric CuNPs can be investigated for its activity against bacterial strains in its future use as a topical anti-bacterial agent in the aim of preventing antibiotic resistance by using an alternate active agent. The varied nano-shapes may have differed toxic effects and can be applied for its anti-bacterial properties in the treatment of dermal bacterial conditions. In addition, the CuNPs

embedded in an aqueous cream base may be a suitable vehicle for the delivery of the nanosystem.

## 7. Appendices

### 7.1. Research Publications

#### 7.1.1. Review Article 1

International Journal of Nanomedicine

Dovepress

REVIEW

# Parameters and characteristics governing cellular internalization and trans-barrier trafficking of nanostructures

This article was published in the following Dove Press journal:
International Journal of Nanomedicine
18 March 2015
Number of times this article has been viewed

Karmani Murugan
Yahya E Choonara
Pradeep Kumar
Divya Bijukumar
Lisa C du Toit
Viness Pillay

Wits Advanced Drug Delivery Platform Research Unit, Department of Pharmacy and Pharmacology, School of Therapeutic Sciences, Faculty of Health Sciences, University of the Witwatersrand, Johannesburg, South Africa

**Abstract:** Cellular internalization and trans-barrier transport of nanoparticles can be manipulated on the basis of the physicochemical and mechanical characteristics of nanoparticles. Research has shown that these factors significantly influence the uptake of nanoparticles. Dictating these characteristics allows for the control of the rate and extent of cellular uptake, as well as delivering the drug-loaded nanosystem intra-cellularly, which is imperative for drugs that require a specific cellular level to exert their effects. Additionally, physicochemical characteristics of the nanoparticles should be optimal for the nanosystem to bypass the natural restricting phenomena of the body and act therapeutically at the targeted site. The factors at the focal point of emerging smart nanomedicines include nanoparticle size, surface charge, shape, hydrophobicity, surface chemistry, and even protein and ligand conjugates. Hence, this review discusses the mechanism of internalization of nanoparticles and ideal nanoparticle characteristics that allow them to evade the biological barriers in order to achieve optimal cellular uptake in different organ systems. Identifying these parameters assists with the progression of nanomedicine as an outstanding vector of pharmaceuticals.

**Keywords:** nanoparticles, transport mechanisms, cellular uptake, size, shape, charge

## Introduction

The emergence of nanomedicine provides a strategic, therapeutic tool that aims to increase drug targeting to site-specific areas within the body. Nanoparticle (NP) research has identified the crossing of mucosal barriers and cellular uptake to support NP utilization, as well as NP surface properties that affect these phenomena.[1] In the design of NPs for biological use, significant factors to overcome limitations associated with insufficient drug delivery to targeted sites include NP size, surface charge, shape, chemical composition, and stability.[2,3] Manipulating these pertinent NP characteristics may facilitate various applications and enhanced cellular and trans-barrier internalization of NPs into the target sites. These sites innately have a biological barrier to prevent the entry of foreign objects, thus resulting in decreased drug concentrations at the intended site. Ideally, nanomedicine should circumvent the biological barriers and enhance drug targeting and NP uptake.[4]

Figure 1 illustrates different transport mechanisms across and into the biological membrane for the internalization of NPs; key terms related to NP internalization and trans-barriers are provided in Table 1. According to Kumari et al[5] NP internalization occurs mainly through intracellular, paracellular, and transcellular pathways. However, endocytosis pathways are poorly understood regardless of their clinical significance and continued research.[5] Continued research in this paradigm, coupled

Correspondence: Viness Pillay
Department of Pharmacy and Pharmacology, School of Therapeutic Sciences, Faculty of Health Sciences, University of the Witwatersrand, 7 York Road, Parktown, Johannesburg, South Africa
Tel +27 11 717 2274
Fax +27 11 642 4355
Email viness.pillay@wits.ac.za



© 2015 Murugan et al. This work is published by Dove Medical Press Limited, and licensed under Creative Commons Attribution – Non Commercial (unported, v3.0) License. The full terms of the License are available at http://creativecommons.org/licenses/by-nc/3.0/. Non-commercial uses of the work are permitted without any further permission from Dove Medical Press Limited, provided the work is properly attributed. Permissions beyond the scope of the License are administered by Dove Medical Press Limited. Information on how to request permission may be found at: http://www.dovepress.com/permissions.php

### 7.1.2. Research Paper 1

Cum Laude

Academy of Pharmaceutical Sciences



Kamani Murugan

# Surfactant directed synthesis and self-assembly of geometric cytotoxic copper nanocrystals

Kamani Murugan, Yahya E. Choonara, Pradeep Kumar, Lisa C du Toit, Viness Pillay

Wits Advanced Drug Delivery Platform Research Unit, Department of Pharmacy and Pharmacology, School of Therapeutic Sciences, Faculty of Health Sciences, University of the Witwatersrand, Johannesburg, 7 York Road, Parktown, 2193, Johannesburg, South Africa. Kamani Murugan is the winner of the 2015 Boehringer Ingelheim Young Scientist award (Laboratory Science category).

## Introduction

The versatility of copper nanoparticles (CuNPs) facilitates its biomedical applications as a cytotoxic agent via oxidative stress, exerts antibacterial activity, functions as an *in vivo* agent for imaging as well as for advanced drug delivery applications [1,2]. In the last decade, researchers have proven that by manipulating the physicochemical, physicomechanical and morphological properties of CuNPs its application expands. In particular, the geometrical shape of CuNPs has gained much interest. By further controlling the shape of CuNPs, cellular internalisation can be dictated thereby enhancing copper delivery into target cells. The self-assembly control process is able to maintain the nano-shape within the colloidal dispersion by minimal chemical, physical or mechanical modification during synthesis, however, despite advances it is still highly complex to optimise the shape of CuNPs. This study focused on the novel synthesis of CuNPs of four different geometries by manipulating surfactant concentrations with homogeneity throughout each colloidal solution.

## Materials and Methods

The thermal-reduction method of synthesizing nanocrystals included a standard $CuSO_4.5H_2O$ solution added to varied molar concentrations of aliquot hexadecetyl trimethylammonium bromide (CTAB) and sodium dodecyl sulphate (SDS) solutions heated at 50°C. Solution was further heated between 85-90°C and a standard ascorbic acid solution was added as the reducing agent in a drop-wise manner to allow for spontaneous copper formation. The dual surfactants of various concentrations served as shape-directing parameters.

TEM (FEI T12 Spirit Transmission Electron Microscope (120kV), Hillsborough, USA) and High-Resolution TEM (JEOL JEM 2100F (200kV), Oregan, USA) confirmed the synthesis of self-assembled neo-geometrical NPs. A powder X-Ray diffractometer (XRD) (MiniFlex 600, Tokyo, Japan) was used to monitor diffraction patterns of the CuNP samples to validate the synthesis of crystalline copper. Samples were also subjected to TEM-Energy Dispersive Spectroscopy (EDS) for high-speed elemental analysis. Thermogravimetric Analysis (TGA) using a 4000 TGA (PerkinElmer Inc., Massachusetts, USA) evaluated the polymer-coating of the CuNP samples as the function of temperature in nitrogen atmosphere under a flow of 40mL/min and heating rate of 10°C/min from 30-900°C.

## Results and Discussion

The scope for change and sensitivity to an external parameter was ascertained to determine the geometries that could be derived from the crystalline structure of nanocrystals and assist with the synthesis of uniform neogeometric CuNPs. After the nucleation of the crystal, the growth of the nanocrystal facets is controlled to synthesize the various shapes. In this study, the major influence involved in shape dictation is the organisation of the surfactant molecules on specific faces to preferentially grow facets of certain dimensions and the induction of truncation of the CuNPs as shown in Fig. 1. The surfactants adsorb on the solid–liquid interface of particular nanocrystal facets imparting various energies on the different facets and the controlled reaction temperature allow for the deviation from the shape formation [3,4].

The structure of the rod-shaped NP grows from a decahedron and exists with a 5-fold symmetry [5]. The induction of the decahedron formation is mediated by the truncation of the five subunit edges of the decahedra nucleus in the (111) planes and additional intermediate faces in the (100) planes. Growth along the facet of the (100) surface results in an elongated structure with two 5-fold symmetry points on either end (Fig. 2a). The stable tetrahedral geometry with a threefold axis acts as the precursor nucleus in the formation of the pyramidal-shaped NPs (Fig. 2b) [5]. The facets are dominated by {111} suggesting that the growth of the tetrahedral geometry is directed by this facet unlike the decahedron and cuboctahedron geometries. It can be assumed that the spherical NPs are formed from the truncated polyhedral precursor nuclei and are composed of several {100} and {111} face (Fig. 2c). The

### 7.1.3. Research Paper 2

materials

MDPI

Article

# Neo-Geometric Copper Nanocrystals by Competitive, Dual Surfactant-Mediated Facet Adsorption Controlling Skin Permeation

**Karmani Murugan, Yahya E. Choonara, Pradeep Kumar, Lisa C. du Toit and Viness Pillay ***

Wits Advanced Drug Delivery Platform Research Unit, Department of Pharmacy and Pharmacology, School of Therapeutic Sciences, Faculty of Health Sciences, University of the Witwatersrand, Johannesburg, 7 York Road, Parktown 2193, South Africa; karmani.murugan@students.wits.ac.za (K.M.); yahya.choonara@wits.ac.za (Y.E.C.); pradeep.kumar@wits.ac.za (P.K.); lisa.dutoit@wits.ac.za (L.C.d.T.)
* Correspondence: viness.pillay@wits.ac.za; Tel.: +27-11-717-2274

Academic Editor: Ilaria Fratoddi
Received: 14 October 2016; Accepted: 21 November 2016; Published: 28 November 2016

**Abstract:** Neogeometric copper nanoparticles (CuNPs) have various applications yet its synthesis still proves to be challenging with regards to self-assembly and uniformity control. This study aimed to synthesize shape-specific CuNPs in the biomedical application of ascertaining skin permeation and retention of the CuNPs as a drug delivery system. The approach to the shape design involved the dual control of two surfactants to direct the shape organisation of the nanoparticles (NPs) while an interesting aspect of the study showed the competitive adsorption of the surfactants onto the nanocrystal facets to direct facet growth. The resulting copper nanoparticles were characterised using X-ray diffraction (XRD) and electron diffraction spectra analysis (EDS) for elemental and crystalline analysis. Thermogravimetric Analysis (TGA) identified the degradation of the surfactant coat and the synthesis of a novel copper-polymer complex and extensive transmission electron microscopy (TEM) was conducted to determine the nanoparticle morphology. Epidermal skin tissue served as the model for permeation studies of five idealistic nano-geometries and investigated its application in drug delivery with regards to cellular internalisation and transbarrier transport of the geometric CuNPs. A mechanistic consideration for shape control is discussed.

**Keywords:** nanocrystals; nanoparticles; copper; geometric structure; self-assembly; transdermal; drug delivery

## 1. Introduction

Copper nanoparticles (CuNPs) have gained considerable research interest in the recent years for investigation in the biomedical and pharmaceutical sciences. The versatility of CuNPs facilitates its biomedical applications as a cytotoxic agent via oxidative stress [1,2], an antibacterial agent [3], an in vivo agent for imaging [4] as well as for advanced drug delivery applications [5]. In the last decade, researchers have proven that by manipulating the physicochemical, physicomechanical and morphological properties of CuNPs its industrial application expands and its extent of use. In particular, the geometrical shape and size of CuNPs has gained much interest [6]. Variation in the shape of CuNPs can be controlled via modification of synthesis processes and methods such as microemulsion [7], reverse micelle method [8], chemical reduction [9], electrochemical reduction [10], metal vaporisation [11], sonochemical processing [12], solution plasma methods [13] and microwave-assisted synthesis [14].

However, utilizing these methods does not ensure specificity in controlling the shape of CuNPs. In the bottom-up synthesis of shape controlled inorganic nanocrystals, studies have proven that colloidal solutions and key parameters such as temperature fluctuation, concentration of polymers and

### 7.1.4. Research Paper 3

Materials Science and Engineering: C
Volume 78, 1 September 2017, Pages 376–388



# Cellular internalisation kinetics and cytotoxic properties of statistically designed and optimised neo-geometric copper nanocrystals

Kermani Murugan, Yahya E. Choonara, Pradeep Kumar, Lisa C. du Toit, Viness Pillay
Show more

https://doi.org/10.1016/j.msec.2017.04.087

Get rights and content

## Highlights

- The concentrations of CTAB and SDS acted as the shape-directing parameters for the neo-geometric copper nanoparticles.
- Copper nanoparticles had a $LD_{50}$ of 25 μg/ml (keratinocytes) and 12.5 μg/ml (HeLa) indicating sensitivity in toxicity.
- *Ex vivo* studies on mechanisms of toxicity confirmed that nano-shape served as a primary determinant for extent of toxicity.
- Cube-shaped copper nanoparticles displayed the highest cellular internalisation.

## Abstract

This study aimed to highlight a statistic design to precisely engineer homogenous geometric copper nanoparticles (CuNPs) for enhanced intracellular drug delivery as a function of geometrical structure. CuNPs with a dual functionality comprising geometric attributes for enhanced cell uptake and exerting cytotoxic activity on proliferating cells were synthesized as a novel drug delivery system. This paper investigated the defined concentrations of two key surfactants used in the reaction to mutually control and manipulate nano-shape and optimisation of the geometric nanosystems. A statistical experimental design comprising a full factorial model served as a refining factor to achieve homogenous geometric nanoparticles using a one-pot method for the systematic optimisation of the geometric CuNPs. Shapes of the nanoparticles were investigated to determine the result of the surfactant variation as the aim of the study and zeta potential was studied to ensure the stability of the system and establish a nanosystem of low aggregation potential. After optimisation of the nano-shapes, extensive cellular internalisation studies were conducted to elucidate the effect of geometric CuNPs on uptake rates, in addition to the vital toxicity assays to further understand the cellular effect of geometric CuNPs as a drug delivery system. In addition to geometry; volume, surface area, orientation to the cell membrane and colloidal stability is also addressed. The outcomes of the study demonstrated the success of homogenous geometric NP formation, in addition to a stable surface charge. The findings of the study can be utilized for the development of a drug delivery system for promoted cellular internalisation and effective drug delivery.

### 7.1.5. Research Paper 4

**Transport of a novel geometric copper nanosystem across the skin barrier employing a self-oscillating polymeric network in the topical treatment of psoriasis**

Karmani Murugan, Yahya E. Choonara, Pradeep Kumar, Lisa C. du Toit and Viness Pillay

Wits Advanced Drug Delivery Platform Research Unit, Department of Pharmacy and Pharmacology, School of Therapeutic Sciences, Faculty of Health Sciences, University of the Witwatersrand, Johannesburg, 7 York Road, Parktown, 2193, South Africa

**Correspondence:** Professor Viness Pillay
Tel: +27-11-717-2274
Fax: +27-11-642-4355
Fax2Email: +27-86-553-4733
Email: viness.pillay@wits.ac.za

**Abstract**

This study focused on the synthesis of novel geometric copper nanoparticles (CuNPs) in the treatment of psoriasis as a function of nano-shape for enhanced cellular internalisation. The nanosystem is embedded in an innovative self-oscillating polymeric network (SOPN) to stimulate the permeation of the CuNPs across the stratum corneum of the psoriasiform-plaque in a BALB/c mouse model. TEM and SAED confirmed the geometric structure and crystalline properties of the CuNPs. FTIR, DSC and XRD characterised the molecular transitions, its LSCT and crystalline properties of the SOPN, respectively. The design of the SOPN included the amplitude and duration of the oscillations; and the rate of the permeation through a barrier based on chemical-mechanical oscillations and its biocompatibility of the 15 formulations generated. The results confirmed an optimized CuNPs-loaded SOPN topical system with promising plaque thickness reduction when compared with a commercial gold standard.

Keywords: copper, nanoparticles, cytotoxicity, self-oscillating gel, BZ reaction, permeation, stratum corneum, topical application, psoriasis

## 7.2. Research Presentations

### 7.2.1. Poster presentation – 2015

**School of Therapeutic Sciences Research Day, University of the Witwatersrand, Johannesburg, South Africa, September 08, 2015**

**Synthesis of superstable neo-geometric cytotoxic copper nanocrystals by competitive, dual surfactant-mediated facet adsorption**

**Karmani Murugan, Yahya Choonara, Pradeep Kumar, Lisa du Toit, Viness PillayWits**
**Advanced Drug Delivery Platform Research Unit, Department of Pharmacy and Pharmacology, School of Therapeutic Sciences, Faculty of Health Sciences, University of the Witwatersrand, Johannesburg, 7 York Road, Parktown, 2193, South Africa**

**Purpose:**
The versatility of copper nanoparticles (CuNPs) facilitates its biomedical applications as a cytotoxic agent via oxidative stress, an antibacterial agent, an *in vivo* agent for imaging as well as for advanced drug delivery applications. By further controlling the shape of CuNPs, intracellular internalization can be dictated thereby enhancing copper delivery to target cells. The aim of the study was to synthesize homogenous, shape-specific CuNPs to promote cellular uptake of the cytotoxic nanocrystal.
**Methods:**
*Preparation of CuNPs:* The synthesis of stable CuNPs of various monodisperse structural geometries was achieved using a bottom-up thermo-chemical reduction method. Standard $CuSO_4.5H_2O$ solution was added to varied molar concentrations of two aliquot surfactant solutions heated at 50°C and thereafter reduced by ascorbic acid at 80°C.
*Confirmation of synthesis of neo-geometric nanocrystals:* TEM and High-Resolution TEM were conducted to confirm the synthesis of self-assembled neo-geometric NPs.
*Confirmation of crystalline copper formation:* Samples were subjected to TEM-EDS and SAED for high-speed elemental analysis and powder XRD was used to monitor diffraction patterns of the CuNP samples to validate the synthesis of crystalline copper.
*Synthesis of stable CuNPs:* The zeta potential was used to measure the surface charge of the CuNPs, thus indicating the stability and aggregation potential of the NPs.
*Validation of surface adsorption and coating:* FTIR analysis of ascorbic acid, both surfactants and synthesized polymer-coated CuNPs was undertaken to evaluate, ascertain and compare vibrational characteristics of the chemical functional groups in response to infrared light interactions. TGA was conducted to evaluate the polymer-coating of the CuNP samples.
**Results:**
The approach to the shape design involved the control of dual surfactants to direct the shape organization of the nanoparticles while an interesting aspect of the study showed the competitive adsorption of the surfactants onto the nanocrystal facets to direct facet growth. By surfactant competition for facet adsorption, various nano-geometries including spheres (90nm), rods, cubes, pyramids and spheres (5nm) were orientated while maintaining homogeneity. Additionally, it was discovered that the highest geometrical control occurred at a surfactant1 concentration of 0.02M and 0.04M achieving high shape uniformity throughout the solution. XRD, SAED and EDS confirmed 100% pure crystalline nano-structures. FTIR and TGA established the coating of the CuNPs produced with surfactant serving as a geometry control factor and a coat to prevent oxidation and aggregation of the CuNPs.
**Conclusion:**
This approach in the synthesis of neo-geometric copper nanocrystals offers the controlled shape formation of copper nanocrystals and reproducibility of heterogeneous and homogenous shape-formation based on the surfactant concentration. The CuNPs will be further used as a cytotoxic agent in drug delivery due to its shape-specificity and enhanced internalization properties.

**7.2.2. Podium presentation – 2015**

**36th Annual Conference of the Academy of Pharmaceutical Sciences of South Africa (APSSA) and the South African Association of Pharmacists in Industry (SAAPI), Ingelheim Boehringer Young Scientist Competition, CedarWood Conference Centre, Sandton, South Africa, September 18, 2015**

**Surfactant directed synthesis and self-assembly of geometric cytotoxic copper nanocrystals**

*Karmani Murugan, Yahya Choonara, Pradeep Kumar, Lisa du Toit, Viness Pillay*Wits Advanced Drug Delivery Platform Research Unit, Department of Pharmacy and Pharmacology, School of Therapeutic Sciences, Faculty of Health Sciences, University of the Witwatersrand, Johannesburg, 7 York Road, Parktown, 2193, Johannesburg, South Africa

**Purpose:** The versatility of copper nanoparticles (CuNPs) facilitates its biomedical applications for advanced drug delivery applications. By further controlling the shape of CuNPs, intracellular internalization can be dictated thereby enhancing copper delivery to target cells. The aim of the study was to synthesize homogenous, shape-specific CuNPs to promote cellular uptake of the cytotoxic nanocrystal.

**Methods:** *Preparation of CuNPs:* The synthesis of stable CuNPs of various monodisperse structural geometries was achieved using a bottom-up thermo-chemical reduction method utilizing dual surfactants as shape-directing parameters.
TEM and High-Resolution TEM were conducted to confirm the synthesis of self-assembled neo-geometric NPs. Samples were subjected to TEM-EDS and SAED for high-speed elemental analysis and powder XRD was used to monitor diffraction patterns of the CuNP samples to validate the synthesis of crystalline copper. Zeta potential was used to measure the surface charge of the CuNPs, thus indicating the stability and aggregation potential of the NPs. FTIR analysis of ascorbic acid, both surfactants and synthesized polymer-coated CuNPs was undertaken to evaluate, ascertain and compare vibrational characteristics of the chemical functional groups in response to infrared light interactions. TGA was conducted to evaluate the polymer-coating of the CuNP samples.

**Results:** The approach to the shape design involved the control of dual surfactants to direct the shape organization of the nanoparticles while an interesting aspect of the study showed the competitive adsorption of the surfactants onto the nanocrystal facets to direct facet growth. By surfactant competition for facet adsorption, various nano-geometries including spheres (90nm), rods (decahedrons), cubes (cuboctahedrons), pyramids (tetrahedrals) and spheres (polyhedrons) (5nm) were orientated while maintaining homogeneity. Additionally, it was discovered that the highest geometrical control occurred at a surfactant1 concentration of 0.02M and 0.04M achieving high shape uniformity throughout the solution. XRD, SAED and EDS confirmed 100% pure crystalline nano-structures. FTIR and TGA established the coating of the CuNPs produced with surfactant serving as a geometry control factor and a coat to prevent oxidation and aggregation of the CuNPs.

**Conclusion:** This approach in the synthesis of neo-geometric copper nanocrystals offers the controlled shape formation of copper nanocrystals and reproducibility of heterogeneous and homogenous shape-formation based on the surfactant concentration. The CuNPs will be further used in drug delivery due to its shape-specificity, thereby enhancing cellular internalization and resulting in elevated drug concentrations to the target area.

**7.2.3. Poster presentation – 2015**

**2015 American Association of Pharmaceutical Scientists – Annual Meeting and Exposition, Orange County Convention Centre, Orlando, Florida, United States of America, October 25, 2015**

**Synthesis of superstable neo-geometric cytotoxic copper nanocrystals by competitive, dual surfactant-mediated facet adsorption**

**Karmani Murugan, Yahya Choonara, Pradeep Kumar, Lisa du Toit, Viness Pillay**

**Wits Advanced Drug Delivery Platform Research Unit, Department of Pharmacy and Pharmacology, School of Therapeutic Sciences, Faculty of Health Sciences, University of the Witwatersrand, Johannesburg, 7 York Road, Parktown, 2193, South Africa**

## Purpose:

The versatility of copper nanoparticles (CuNPs) facilitates its biomedical applications as a cytotoxic agent via oxidative stress, an antibacterial agent, an *in vivo* agent for imaging as well as for advanced drug delivery applications. By further controlling the shape of CuNPs, intracellular internalization can be dictated thereby enhancing copper delivery to target cells. The aim of the study was to synthesize homogenous, shape-specific CuNPs to promote cellular uptake of the cytotoxic nanocrystal.

## Methods:

*Preparation of CuNPs:* The synthesis of stable CuNPs of various monodisperse structural geometries was achieved using a bottom-up thermo-chemical reduction method. Standard $CuSO_4.5H_2O$ solution was added to varied molar concentrations of two aliquot surfactant solutions heated at 50°C and thereafter reduced by ascorbic acid at 80°C.

*Confirmation of synthesis of neo-geometric nanocrystals:* TEM and High-Resolution TEM were conducted to confirm the synthesis of self-assembled neo-geometric NPs.

*Confirmation of crystalline copper formation:* Samples were subjected to TEM-EDS and SAED for high-speed elemental analysis and powder XRD was used to monitor diffraction patterns of the CuNP samples to validate the synthesis of crystalline copper.

*Synthesis of stable CuNPs:* The zeta potential was used to measure the surface charge of the CuNPs, thus indicating the stability and aggregation potential of the NPs.

*Validation of surface adsorption and coating:* FTIR analysis of ascorbic acid, both surfactants and synthesized polymer-coated CuNPs was undertaken to evaluate, ascertain and compare vibrational characteristics of the chemical functional groups in response to infrared light interactions. TGA was conducted to evaluate the polymer-coating of the CuNP samples.

## Results:

The approach to the shape design involved the control of dual surfactants to direct the shape organization of the nanoparticles while an interesting aspect of the study showed the competitive adsorption of the surfactants onto the nanocrystal facets to direct facet growth. By surfactant competition for facet adsorption, various nano-geometries including spheres (90nm), rods, cubes, pyramids and spheres (5nm) were orientated while maintaining homogeneity. Additionally, it was discovered that the highest geometrical control occurred at a surfactant1 concentration of 0.02M and 0.04M achieving high shape uniformity throughout the solution. XRD, SAED and EDS confirmed 100% pure crystalline nano-structures. FTIR and TGA established the coating of the CuNPs produced with surfactant serving as a geometry control factor and a coat to prevent oxidation and aggregation of the CuNPs.

## Conclusion:

This approach in the synthesis of neo-geometric copper nanocrystals offers the controlled shape formation of copper nanocrystals and reproducibility of heterogeneous and homogenous shape-formation based on the surfactant concentration. The CuNPs will be further used as a cytotoxic agent in drug delivery due to its shape-specificity and enhanced internalization properties.

**7.2.4. Poster presentation – 2015**

**Molecular Biosciences Research Thrust Postgraduate Research Day 2015, University of the Witwatersrand, Johannesburg, South Africa, December 03, 2015**

**Ordered Synthesis of Geometric Copper Nanocrystals for Enhanced Drug Delivery**

**Murugan, K.[1], Choonara, YE.[1], Pradeep, K[1]. and Pillay, V[1].**
[1] Department of Pharmacy and Pharmacology, School of Therapeutic Sciences, Faculty of Health Sciences, University of the Witwatersrand.

Neo-geometric copper nanoparticles (CuNPs) have various applications yet its synthesis still proves to be challenging with regards to self-assembly and uniformity control. The synthesis of stable CuNPs of various monodisperse structural geometries was achieved using a bottom-up thermo-chemical reduction method. The approach to the shape design involved the control of dual surfactants to direct the shape organization of the nanoparticles while an interesting aspect of the study showed the competitive adsorption of the surfactants onto the nanocrystal facets to direct facet growth. By surfactant competition for facet adsorption, various nano-geometries including spheres (polyhedrons, 90nm), rods (decahedrons), cubes (cuboctahedrons), pyramids (tetrahedrals) and spheres (polyhedrons, 5nm) were orientated while maintaining homogeneity. Additionally, it was discovered that the highest geometrical control occurred at a surfactant1 concentration of 0.02M and 0.04M achieving high shape uniformity throughout the suspension. X-Ray Diffraction, Selected Area Electron Diffraction and Energy Dispersion Spectroscopy confirmed 100% pure crystalline nanocrystals. Fourier-Transform Infrared and Thermogravimetric Analysis established the coating of the CuNPs produced with surfactant serving as a geometry control factor and a coat to prevent oxidation and aggregation of the CuNPs. This approach in the synthesis of neo-geometric copper nanocrystals offers the controlled shape formation of copper nanocrystals and reproducibility of heterogeneous and homogenous shape-formation based on the surfactant concentration. The CuNPs will be further used in drug delivery due to its shape-specificity, thereby enhancing cellular internalization and resulting in elevated drug concentrations to the target area.

***Word count: 236 words***

**Acknowledgements:** This research has been funded by the National Research Foundation of South Africa.

### 7.2.5. Podium presentation – 2016

**Wits 7th Postgraduate Symposium, University of the Witwatersrand, Johannesburg, South Africa, March 01, 2016**

**MURUGAN, KARMANI**
Choonara Yahya, Kumar Pradeep, du Toit Lisa, Pillay Viness
School of Therapeutic Sciences

**Dual surfactant-mediated synthesis of self-assembled geometric cytotoxic copper nanocrystals**

Neo-geometric copper nanoparticles (CuNPs) have various applications yet its synthesis still proves to be challenging with regards to self-assembly and uniformity control. The synthesis of stable CuNPs of various monodisperse structural geometries was achieved using a bottom-up thermo-chemical reduction method. The approach to the shape design involved the dual control of two surfactants to direct the shape organization of the nanoparticles while an interesting aspect of the study showed the competitive adsorption of the surfactants onto the nanocrystal facets to direct facet growth. Formulations at various concentration combinations resulted in heterogeneous or homogenous samples of geometries. By surfactant competition for facet adsorption, various nano-geometries including spheres (90nm), rods (decahedrons), cubes (cuboctahedrons), pyramids (tetrahedrals) and spheres (polyhedrons) (5nm) were orientated while maintaining homogeneity. Additionally, it was discovered that the highest geometrical control occurred at a surfactant1 concentration of 0.02M and 0.04M achieving high shape uniformity throughout the solution. XRD, SAED and EDS confirmed 100% pure crystalline nano-structures. FTIR and TGA established the coating of the CuNPs produced with surfactant serving as a geometry control factor and a coat to prevent oxidation and aggregation of the CuNPs. This approach in the synthesis of neo-geometric copper nanocrystals offers the controlled shape formation of copper nanocrystals and reproducibility of heterogeneous and homogenous shape-formation based on the surfactant concentration. The CuNPs will be further used in drug delivery due to its shape-specificity, thereby enhancing cellular internalization and resulting in elevated drug concentrations to the target area.

**7.2.6. Poster presentation – 2016**

**13th International Conference on Nanosciences & Nanotechonologies (NN16), Porto Palace Conference Centre, Thessaloniki, Greece, July 5, 2016**

## Surfactant directed synthesis and self-assembly of novel neo-geometric cytotoxic copper nanocrystals for enhanced cellular internalization

K. Murugan[1], Y.E Choonara[1], P. Kumar[1], L.C du Toit[1], V. Pillay[1]

*[1]Wits Advanced Drug Delivery Platform Research Unit, Department of Pharmacy and Pharmacology, School of Therapeutic Sciences, Faculty of Health Sciences, University of the Witwatersrand, Johannesburg, 7 York Road, Parktown, 2193, Johannesburg, South Africa*

**Aim:** The versatility of copper nanoparticles (CuNPs) facilitates its biomedical applications for advanced drug delivery applications. By further controlling the shape of CuNPs, intracellular internalization can be dictated thereby enhancing copper delivery to target cells. The aim of the study was to synthesize homogenous, shape-specific CuNPs to promote cellular uptake of the cytotoxic nanocrystal and investigate the internalization and toxicity profiles of the CuNPs based on its geometric structures. **Methods & Results:** The approach to the shape design involved the control of dual surfactants to direct the shape organization of the nanoparticles while an interesting aspect of the study showed the competitive adsorption of the surfactants onto the nanocrystal facets directed CuNP growth. TEM confirmed various monodisperse nano-geometries including spheres (90nm), rods (decahedrons), cubes (cuboctahedrons), pyramids (tetrahedrals) and spheres (5nm) (Figure 1). Additionally, it was discovered that the highest geometrical control occurred at a surfactant1 concentration of 0.02M and 0.04M achieving high shape uniformity throughout the solution. XRD, SAED and EDS confirmed 100% pure copper crystalline nano-structures. FTIR and TGA established a 3-5% coating on the CuNPs produced with surfactant serving as a geometry control factor and preventing oxidation and aggregation of the CuNPs. Following the cell studies, it was conclusive that nano-shape significantly affects the rate at which nanostructures internalize human keratinocyte cell line over 24 hours, as well as the effect that shape has on cytotoxicity profiles especially differing between the human keratinocyte and HeLa cell lines. **Conclusion:** This approach in the synthesis of neo-geometric copper nanocrystals offers the controlled shape formation of copper nanocrystals and reproducibility of heterogeneous and homogenous shape-formation based on the surfactant concentration. The CuNPs will be further used in drug delivery due to its shape-specificity, thereby enhancing cellular internalization and resulting in elevated drug concentrations to the target area. **Conclusion:** This approach in the synthesis of neogeometric copper nanocrystals offers the controlled shape formation of copper nanocrystals and reproducibility of heterogeneous and homogenous shape-formation based on the surfactant concentration. The CuNPs will be further used in drug delivery due to its shape-specificity, thereby enhancing cellular internalization and resulting in elevated drug concentrations to the target area.

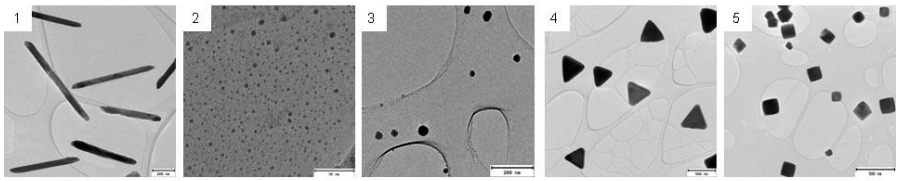


Figure 1. TEM micrographs of monodisperse neo-geometric copper nanoparticles. 1) Rods, 2) 5nm spheres, 3) 100nm spheres, 4) 500nm pyramids, 5) 200nm cubes

### 7.3. Research Awards

#### 7.3.1. Winner of the Boehringer Ingelheim Young Scientist Award, 2015, South Africa



The Academy of Pharmaceutical Sciences of the Pharmaceutical Society of South Africa

hereby commends

Karmoni Murugan

As the winner of the Young Scientist award for Pharmaceutical Sciences 2015

Chairman

Secretary

**7.3.2. Winner of the Young Researcher Award, 2016, Greece**

## 7.4. Animal Ethics Declaration

**STRICTLY CONFIDENTIAL**

**ANIMAL ETHICS SCREENING COMMITTEE (AESC)**

**CLEARANCE CERTIFICATE NO.** 2014/48/B

**APPLICANT:** Ms K Murugan

**SCHOOL:** Pharmacy & Pharmacology

**LOCATION:** Faculty of Health Sciences

**PROJECT TITLE:** *In vivo topical delivery of a neogeometrical copper nanoparticle based system for psoriasis treatment in the BALB/c model*

**Number and Species**

**66 Mice**

Approval was given for to the use of animals for the project described above at an AESC meeting held on 26 August 2014. This approval remains valid until 25 August 2016.

The use of these animals is subject to AESC guidelines for the use and care of animals, is limited to the procedures described in the application form and is subject to any additional conditions listed below.

None.

Signed: _____ (Chairperson, AESC) Date: 12th Sept. 2014

I am satisfied that the persons listed in this application are competent to perform the procedures therein, in terms of Section 23 (1) (c) of the Veterinary and Para-Veterinary Professions Act (19 of 1982)

Signed: _____ (Registered Veterinarian) Date: 11th September 2014

cc: Supervisor: Prof V Pillay
Director: CAS

Works 2000/lain0015/AESCCert.wps